MODULATION OF GRAPHENE AND ITS HYBRID NANOSTRUCTURES TOWARD THE DEVELOPMENT OF HYBRID ENERGY STORAGE DEVICES

NAVPREET

A thesis submitted for the partial fulfilment of

the degree of Doctor of Philosophy

Institute of Nano Science and Technology (INST) Mohali

Knowledge City, Sector 81, SAS Nagar, Manauli, P.O. 140306 Punjab, India

Indian Institute of Science Education and Research (IISER) Mohali

Knowledge City, Sector 81, SAS Nagar, Manauli, P.O. 140306 Punjab, India

March 2022

Dedicated to

My parents & family

Declaration

The work presented in this thesis has been carried out by me under the guidance of Dr. Ramendra Sundar Dey at the Institute of Nano Science and Technology, Mohali. This work has not been submitted in part or in full for a degree, a diploma, or a fellowship to any other university or institute. Whenever contributions of others are involved, every effort is made to indicate this clearly, with due acknowledgement of collaborative research and discussions. This thesis is a bonafide record of original work done by me and all sources listed within have been detailed in the bibliography.

Navpreet

In my capacity as the supervisor of the candidate's thesis work, I certify that the above statements by the candidate are true to the best of my knowledge.

Dr. Ramendra Sundar Dey
Scientist-D
INST Mohali

Acknowledgement

Date: *Navpreet*

Abbreviations

LIG	*Laser-irradiated graphene*
GO	*Graphene oxide*
rGO	*Reduced graphene oxide*
TMO	*Transition metal oxides*
TMPs	*Transition metal phosphides*
IPA	*Isopropyl alcohol*
PVA	*Poly(vinyl) alcohol*
Cuf	*Copper foam*
EES	*Electrochemical energy storage*
CV	*Cyclic voltammetry*
LSV	*Linear sweep voltammetry*
GCD	*Galvanostatic charge discharge*
EIS	*Electrochemical impedance spectroscopy*
XRD	*X-ray Diffraction*
FTIR	*Fourier transform infrared spectrophotometer*
BET	*Brunauer Emmett Teller*
XPS	*X-Ray Photoelectron Spectroscopy*
SEM	*Scanning electron microscopy*
TEM	*Transmission electron microscopy*
HRTEM	*High resolution transmission electron microscopy*
SAED	*Selected area electron diffraction*
EDX	*Energy dispersive X-ray spectroscopy*
C_{sp}	*Specific capacitance*
R_{ct}	*Charge transfer resistance*
C_{dl}	*Double layer capacitance*
OCP/OCV	*Open circuit potential/voltage*
J_{sc}	*Short circuit current density*
E_A	*Area normalized energy density*
P_A	*Area normalized power density*
ECSA	*Electrochemically active surface area*
DHBT	*Dynamic hydrogen bubble template*
AWIS	*Acetonitrile/Water-in-salt*

Abstract

On account of the intermittent nature of renewable resources, electrochemical energy storage systems (EESs) are realized as crucial divisions in energy technologies that have the capability to store the energy from renewable energy resources when not needed and make it utilized for later use. The commonly known EES systems are battery receiving high energy density and supercapacitors (SCs) *i.e.,* full of power, are the main components in an energy-efficient hardware network. The distinct features of battery and SCs are due to their charge storage mechanisms: diffusion-controlled process responsible for high energy density in battery and surface-controlled process brings the high-power output in SCs. The strategy to design the electrode materials should focus on the device performance in terms of capacity output, sufficient energy-power density correlation, and stability factor which in turn are dependent on the material's electrical conductivity and porosity characteristics. Nanostructured graphene as an electrode material is emerging in the storage field due to its remarkable electrical, optical and mechanical properties. The present study is focused on the exploration of such electrode material with the facile synthetic process, their morphological advances and can be utilized as metal-free planar structured solid EES system. Finally, the mixed kinetics of battery and SCs were utilized to develop a hybrid energy device i.e., BSH (battery-supercapacitor hybrid) system with optimum energy and power density values. The versatile systems developed in each and every project gives a new avenue for the development of sustainable energy storage system for the continuous power run.

TABLE OF CONTENT

Chapter 4 Graphene/polypyrrole based metal-free microsupercapacitor using "Organic/Water-in-salt" electrolyte   111-142

List of figures

List of tables

Chapter 1

Introduction

Abstract: This chapter describes the numerous universal challenges due to the current energy scenario and their alternatives to fulfill the demand. The energy storage devices like supercapacitors and batteries are the main highlights of this chapter. The chapter started with a brief introduction of energy storage devices, their demand and types of storage devices. Different types of energy storage devices based on their charge storage kinetics like electric double layer capacitance (EDLC), pseudocapacitance and their geometrical configurations such as stacked structure or planar geometry has been highlighted in details. A complete survey of carbonaceous materials, pseudocapacitive materials, battery type materials and their electrochemistry in electrochemical cell has been discussed in the later sections. The various quantification parameters of supercapacitor and the improvements executed based on such limited electrochemical responses is given in next sub-sections. The role of electrolytes and their types with their advantageous and disadvantageous features are also included. A complete historical background of battery system of different generation, the electrochemistry involved, benefits and limitations are also described in details. Some embodiments also include the scientific development in the field of Li-ion battery and Ni-Zn battery till date. In order to approach the next-generation energy technology, the importance of hybrid structure of battery and supercapacitor (BSH) system is impactfully interpreted. The rational designing and engineering of electrode materials in supercapacitors as well as batteries is been highlighted in a sub-section. At the end, an objective, the background motivation and the future perspectives of the present experimental investigations in the field of energy storage system is discussed briefly.

1.1 Current energy scenario and demand of energy storage systems

Modern civilization is completely dependent upon energy and sustainable production of energy resources is indeed important. The urgent energy scenario of the world towards its demand, supply and limited availability of fossil fuels is slowly taking a serious concern for the environmentalist and researchers. The Statistical Review of World Energy 2020 states that the primary energy source i.e. oil has the highest share of 33% of the total energy consumption[1] and the other share of global energy consumption contributes from coal (27%), natural gas (24%), hydropower (6%), nuclear power (4%), and renewable energy resources. (6%).[2] The data suggests, nearly, 84% of the total energy demand is fulfilled by the burning of fossil fuels, which eventually causes global warming and climatic changes. So, it is highly desirable to search for an alternative energy converter or energy storage system. In the modern digital world, technological advancement is an essential parameter to meet the global growing demand for green and affordable energy resources.[3] Simultaneously, diversification in electronic devices involves the incorporation of various chip size sensors into a single device taking into consideration the two facts such as system on chip (SOC) and system in package (SIP). The additional functionality in electrical devices like smartphones, computers, aircraft gadgets, etc. requires more power, known as "more-than-Moore technology".[4] By taking the advantageous characteristics of energy storage devices (which have the ability to quick charge/discharge), the energy storage systems are considered as the primary resource for sustainable power delivery.

1.2 Electrochemical energy storage systems and their classifications

The progress in science and technology is crucial for the development of civilization. In the current century, electronic devices like cellular phones, i-pad, machinery, laptops and hybrid vehicles are frequently required in our daily lives, they are just dead dummies without their energy components. Numerous initiatives have been dedicated by the scientific community towards spontaneous production of energy from renewable resources (like solar, wind etc.) These resources are meant to be applicable for consumer optoelectronics to hybrid electric vehicles (HEVs) and the integration of conversion systems to large-scale power grid systems. Due to the intermittent nature of renewable resources, electrical energy storage systems are realized as crucial divisions in energy technologies. These systems are capable of quantitative storage of the produced energy from renewable energy resources when not needed and make it

utilized for later use. Among a broad range of energy storage technologies like chemical, thermal, thermochemical, mechanical, electrolytic, electrochemical etc., the best provision for the energy storage mechanism is by electrochemical means. Hence, electrochemical energy storage (EES) systems are the intermediate joint in between electrical energy production systems and power grid systems as spontaneous powered equipment. The diversity in the charge storage mechanism of electrochemical energy storage systems leads to distinguished energy and power delivery of the systems.[5] The inevitable growth of flexible devices, consumer electronics and electrified transport systems, encourages the substantial growth of EES technologies in the current energy market. The well-known EES technologies are featured on the commercial ground with tremendous performance for consumer utility and many more are under progress on laboratory scale. The functioning of EES systems can be broadly explained based on two major classifications:

    (a) Charge storage mechanisms

    (b) Geometrical features

The EES system combines the energy production systems to the demanding systems in two possible ways:

(i) *via* storing the bulk energy from the renewable resource and releasing at the time of energy demand (battery system).

(ii) providing a stable power with a faster rate by supercapacitors.

      The detailed description of the charge storage mechanism in EES technologies is given in the next sub-divisions.

1.2.1 Charge Storage Mechanism: Surface-controlled and Diffusion-controlled

The type of storage device can be classified based on their charge storage mechanism as follows:

    (a) Electric double layer capacitors (EDLCs)

    (b) Pseudocapacitors

    (c) Battery systems

1.2.1.1 Electric double layer capacitors

When a charged electrode material is placed in liquid electrolyte medium, an electric double-layered structure appeared at the interface of electrolyte and electrode. Several theories or models are discussed earlier in order to understand the spatial charge distribution at electrode and electrolyte interface. The approximation theories are Helmholtz-Perrin or parallel plate condenser model,[6] Gouy-Chapman model or diffuse

charge model,[7,8] and the Stern model[9] are well illustrated in Fig. 1.1. The Helmholtz model explains that a double layer with opposite charges (positive and negative) exists across the electrified interface (electrode and electrolyte interface) as shown in Fig. 1.1a. According to this approximation, the electric double layer potential ψ varies linearly with the distance "d", where 'd' is the distance from the electrode surface to the other charged layer ions center. The exerted potential difference in between the two charged layers[10] is defined as equation 1.1 :

$$dV = \frac{4\pi d}{\varepsilon}\, dQ \qquad \ldots\ldots\ldots\ldots\ldots (1.1)$$

Where 'dQ' is the collection of charge on each layer, 'ε' is dielectric constant of the electrolytic medium. The major limitation of this model is the prediction of constant capacity of electric double layer but experimentally it cannot be true. However, the properties of double layer vary with the variation of electrolyte concentration and temperature conditions. For an adequate explanation of charge storage, Guoy and Chapman developed a theory, which suggests that a diffuse electric double layer form at the interface rather than a sharp layer and ions is considered to be a point charge. The oppositely charged ions are not rigidly attached to the electrode surface. The variation of potential from one charged layer to another diffused layer is no longer linear now; it behaves exponentially (Fig. 1.1b) and is represented in equation (1.2):

$$\psi_x = \psi_o e^{-\kappa x} \qquad \ldots\ldots\ldots\ldots (1.2)$$

Where, $'\psi_x'$ is the potential at a distance 'x' in the liquid phase, $'\psi_o'$ is the potential at x = 0, 'κ^{-1}' is the thickness inverse of the oppositely charged diffused layer. According to this theory, the dependence of capacitance on potential difference shows the inverted parabolic pattern. The Guoy and Chapman theory fails at high concentration solutions. Simply, we can say that when the charged concentration increases, this theory does not work. After the failure of Guoy-Chapman's theory, a new approach for the charge distribution was introduced and called as 'Stern Theory'. According to this theory, one charged layer is fixed at the electrode whereas, the other charged layer is divided into two parts; one is stern layer specifically include the adsorbed ion, forming the inner Helmholtz plane (IHP) and second is a diffuse layer, forming outer Helmholtz plane (OHP). Hence, the Stern model (Fig. 1.1c) is the combination of the above two models (Helmholtz-Perrin model and Guoy-Chapman model). This theory validates under all electrolytic conditions (High or low). The total capacitance of the double is explained as equation 1.3:
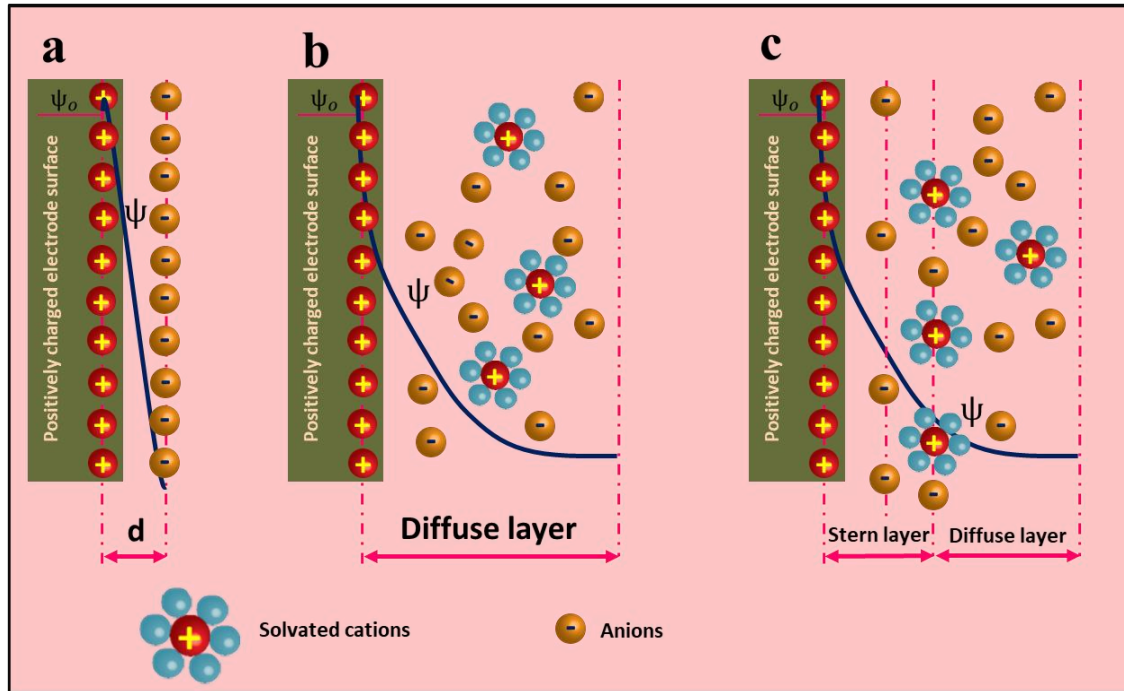
Figure 1.1 Electric double layer models, (a) Helmholtz Model, (b) Guoy –Chapman Model, and (c) Stern Model

$$C_T = C_H + C_G \qquad \ldots\ldots\ldots\ldots\ldots. (1.3)$$

Where, $'C_H'$ is the Helmholtz region capacitance and $'C_G'$ is the diffuse layer region capacitance.

1.2.1.2 Pseudocapacitors

Pseudocapacitors acquire non-electrostatic capacitance as a consequence of faradaic redox reaction mechanism or electrochemical charge-transfer reaction at the electrode surface. Pseudocapacitance is completely dependent on the collection of charges crossing the double layer and on the varying potential.[11] The pseudocapacitance 'C' is the derivative of collective charge 'ΔQ' and changing potential 'ΔV' *i.e.* represented in equation (1.4):

$$C = \frac{d\Delta Q}{d\Delta V} \qquad \ldots\ldots\ldots\ldots\ldots. (1.4)$$

Several faradaic charge storage mechanisms involve pseudocapacitive features such as:

    (a) One kind of metal's ions form a single layer on different metal's surfaces above its electrochemical redox potential limit, called 'underpotential deposition'.[12]

    (b) When a charge-transfer reaction occurred by electrochemically absorbed ions on the surface of the electrode or near to the surface, named as 'redox pseudocapacitance' (preferably occurred in transition metal oxides).

(c) Charge transfer reaction can be possible after intercalation of absorbed ions into the layers of redox-active species without any structural phase change, defined as 'intercalation pseudocapacitance' as shown in Fig. 1.2 a-c.

Conclusively, pseudocapacitors involve surface-controlled charge storage mechanism. Two processes (faradaic and EDL) existing together give rise to the specific capacitance of the pseudocapacitor (10-100 times greater) than EDLC but the slower faradaic response lowers the output power performance. Despite many advantages like sufficient charge storage capability of pseudocapacitors and so on, pseudocapacitive materials are susceptible to volume expansion and reduction during charge/discharge process which in turn hampers the cyclic stability of the device.[13] Generally, transition metal-oxides like RuO_2,[14] V_2O_5,[15] MnO_2,[16] conducting polymers such as polyaniline (PANI),[17] Polypyrrole (PPy), hetero-atom doped carbon network, electrosorbed hydrogen atoms on nanoporous carbon skelton follows pseudocapacitive charge storage mechanism. The surface-
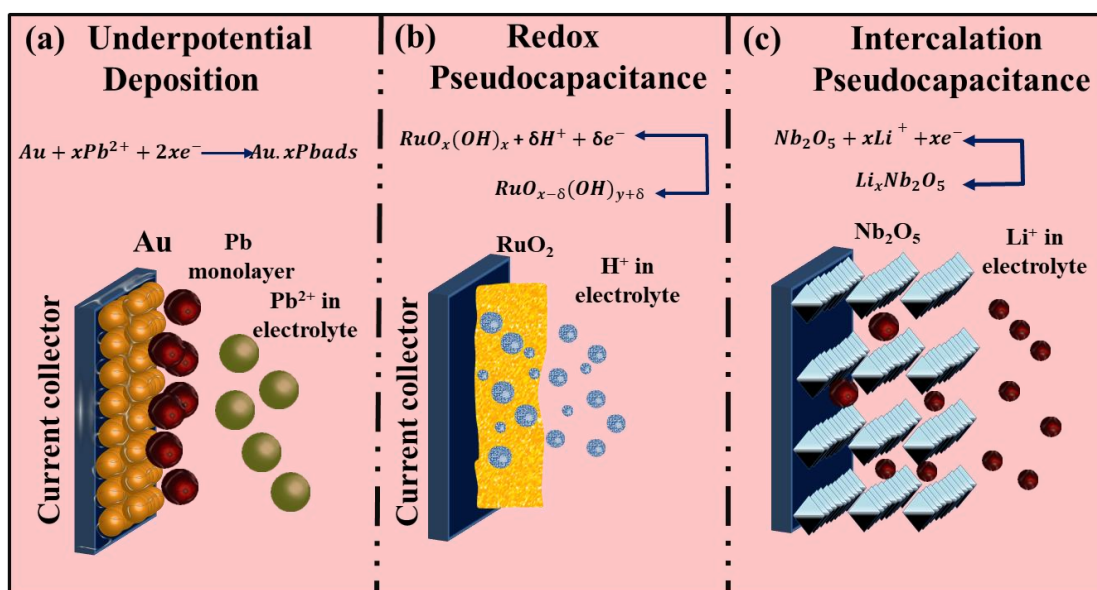
Figure 1.2 Redox reaction mechanisms in pseudocapacitors, (a) Underpotential deposition, (b) Redox pdeudocapacitance, (c) Intercalation pseudocapacitance.

controlled characteristics of pseudocapacitive materials can be analyzed by performing cyclic voltammetry at different sweep scan rates (Trasatti and Dunn method). The current response according to the scan rate is as given in equation 1.5:

$$i = av^b \qquad \qquad ....(1.5)$$

Where 'i' is the current, 'v' is the scan rate and '$a,$ and b' are modified parameters. The slope of log(i) vs log(v)curve ensures the value of 'b'. The b-value approximately near or equal to 1, generally indicates a surface-controlled process a value of 0.5 indicates

the diffusion-controlled intercalation process (kind of battery). The similar characteristics of the intercalation pseudocapacitance and battery systems may create a confusion, so the basic difference among them can be understand by considering two important points:

(a) Intercalation psedocapacitance process does not accompany a phase transformation in the active material as battery electrode does.

(b) The b-value should be near or equal to one.

1.2.1.3 Diffusion controlled charge storage mechanism in batteries:

The well-known battery devices work on the basic principle of galvanic cell and the electrochemical energy is stored via an electrochemical diffusion-controlled redox reaction. The capacity that occurs by the semi-infinite diffusion process, varies with the (negative) square root of the scan rate *i.e.,* $v^{-\frac{1}{2}}$ (means 'b' value is -0.5).

Battery was first invented 100 years ago by an Italian scientist named "Alessandro Volta". Batteries are accompanied by the same components that of supercapacitors such as anode, cathode, current collector, liquid or solid electrolytic medium and a separator to isolate both the electrodes. Batteries are classified into two generations:

(a) Primary/Non-Rechargeable battery

(b) Secondary/Rechargeable battery

(a) Primary/Non-Rechargeable battery: These kinds of batteries are of one time use with various advantages like good shelf life, easily scale up to fit for application, sufficient energy and power density, reasonable price and reliability. A variety of anode and cathode combinations were selected initially to achieve practical success,

these are listed as: Zinc-carbon (Leclanche) battery, Zinc/Alkaline/MnO_2 system, Zinc/Mercury oxide battery, Zinc/Air battery, Zinc/Silver battery, and so on. The corresponding advantages, their applications and limitations are listed in Table 1.1. The recharging of primary battery is not permissible because charging could lead to the release of such gasses that could be very harmful.

(b) Secondary/Rechargeable battery: As the name suggest, secondary batteries are those which can be recharged. In the secondary batteries, the charge and discharge cycle should undergo reversibly. In the discharge state, electron deriving from anode electrode are collected at cathode electrode and electrons flow through the outer circuit. Whereas, in

Table 1.1 *A brief study of different type of primary batteries, their characteristics, applications and limitations.*

Sr. No	Primary battery	Characteristics	Applications	Limitations
1	Zinc-carbon (Leclanche) cell	Simple, low-cost; Easily shaped and sized	Flashlight, toys like car, drums etc. portable radios,	Less performance characteristics
2	Magnesium (Mg/MnO_2)	High-capacity primary battery with extremely long shelf life	Military purpose receiver/transmitters, aircraft emergency transmitters	High gassing (H_2) on discharge; delayed voltage
3	Mercury (Zn/HgO)	Highest volume capacity, flat discharge potential; fair shelf life	pacemakers, cameras, detectors, military equipment's	environmental hazard of mercury
4	Alkaline ($Zn/$ alkaline $/MnO_2$)	Can be operated at high current drains; good low-temperature and excellent rate capability; acceptable cost	used in cameras, smoke alarms and consumer electronics	Moderate cost
5	Silver / zinc (Zn/Ag_2O)	Highest capacity (by weight) of conventional types; flat discharge; good shelf life	Hearing aids, electric watches, missiles, space application	Very costly
6	Zinc / air (Zn/O_2)	Highest energy density, low cost	Special applications, hearing aids, medical device, portable small electronics	Sensitivity to extreme temperature conditions, humidity effects, poor shelf life
7	Lithium / solid cathode	High energy density; good rate capability and low-temperature performance; long shelf life;	Replacement for conventional button and cylindrical cell applications, communications devices	High cost, major safety concerns, low-power solid state battery
8	Lithium / solid electrolyte	Extremely long shelf life	Medical electronics, memory circuits, battery backups	low-power solid state battery

charging state, the above reaction was reversed by applying an external potential at both the electrodes as represented in Fig 1.3 a and b, respectively.[18]

These kinds of batteries are feasible for two categories of practical applications: the first category includes an uninterruptible energy source for automotive and aircraft systems where battery systems can be charged priory by energy source and delivers energy depending on the demand. The second category of practical application is automobiles, electric vehicles, and consumer electronics where at first the battery system is completely discharged and charged it again in the same device or after taking it off. The usual characteristics possessed by secondary batteries are their high specific energy, flat discharge plateau profiles, good reversibility of the device, no deterioration of cell
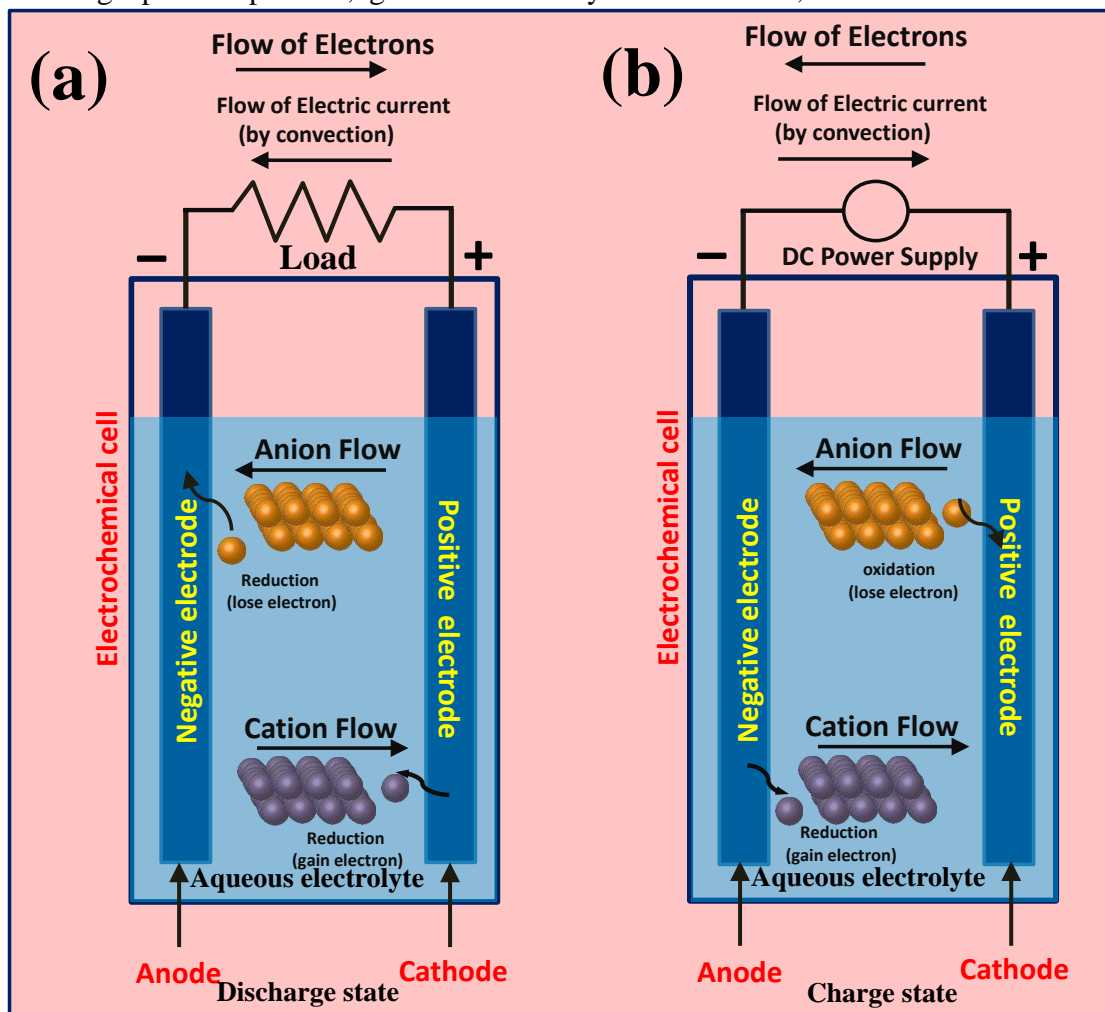
Figure 1.3 *Electrochemical battery in (a) Discharge state, (b) Charge state.*

components during chemical reaction, stability under severe temperature conditions and so on.[19] Few examples of secondary batteries are lead-acid battery, Nickel-metal hydride battery, Ni-Cd battery, Ni-Zn battery, Zn-Air battery and Li-ion battery and are listed in Table 1.2 according to their progress.

1.2.2 Hybrid storage systems

Generally, hybrid systems are introduced in order to enhance the energy density to a range of 20-30 Wh kg^{-1}. Initially, a basic approach was in limelight for the enhancement

Table 1.2 *Classifications of secondary batteries, their characteristics, applications and limitations.*

Sr. No	Secondary batteries	Characteristics	Applications	Limitations
1	**Lead-Acid batteries**	Cost-effective secondary battery, high-rate, and low-temperature performance	golf carts, lawn mowers, tractors, aircraft, marine, in mining equipment's	moderate specific-energy
2	**Nickel-cadmium (Alkaline secondary battery)**	Good high-rate, low-temperature operation capability, flat voltage, excellent cycle life, various possible configurations (button, cylindrical and coin cell)	Aircraft batteries, industrial and emergency power applications, railway signalling, communication equipment	Limited specific capacity and energy density
3	**Nickel-metal hydride**	Sealed, maintenance-free, higher capacity than nickel-cadmium batteries	Consumer electronics, portable electronic applications; electric and hybrid vehicles	Costly
4	**Nickel-iron**	Durable, rough construction, long life,	Materials handling, stationary applications, rail road cars	Low specific energy, high self-discharge, unstable at low temperature condition, high manufacturing cost
5	**Silver-zinc**	Highest specific energy, very good high-rate capability,	Lightweight portable electronic; training targets, drones, submarines, other military equipment, launch vehicles and space probes	high-cost low cycle life
6	**Silver-cadmium**	moderate specific energy, good charge retention	Portable equipment requiring a light weight,high-capacity battery; space satellites	lower cycle life, high cost
7	**Zn-MnO$_2$ rechargeable battery**	Low cost, good capacity retention, sealed and maintenance-free, limited cycle life and rate capability	Cylindrical cell applications, rechargeable replacement for zinc-carbon and alkaline primary batteries, consumer electronics (ambient-temperature systems)	Limited cycle stability and rate capability

8	Nickel-zinc batteries	High specific energy, extended cycle life and rate capability	Bicycles, scooters, trolling motors	Dendrite's formation over zinc electrode
9	Lithium-ion batteries	High specific energy and energy density, High operating voltage long cycle life	Portable and consumer electronic equipment, electric vehicles, and space applications	Safety concerns under over-charge conditions

of energy density which was developed by coupling an EDLC material with some redox-active material (graphene, carbon nanotubes, metal oxide, polymers etc.) and the modifications in the electrolytes (hybrid electrolytes, bi-redox electrolytes etc.) was practiced.

The concept was brought to overcome the limited energy density generated from individual EDLC and pseudocapacitor systems. The first class of hybrid systems includes composite electrodes of EDLC type material (carbon, graphene, activated carbon) and pseudocapacitive material (conducting polymers), known as hybrid supercapacitors. The second class of hybrid systems includes two different electrode materials *i.e.;* one is capacitive in nature and the other is pseudocapacitive in nature. The storage principle for hybrid supercapacitors is ruled by the collective features of EDLC and pseudocapacitors charge storage principles. These hybrid supercapacitors can be symmetric and asymmetric in configuration (Fig. 1.4 a and b). Symmetric hybrid supercapacitors are those which occupy both similar types of positive and negative electrodes.[20] For example, a symmetric hybrid supercapacitor is assembled with two electrodes of activated carbon (AC) in organic electrolytes holding a potential window of 2.7 V.[21] The asymmetric hybrid supercapacitors include two different electrodes where one is of EDLC behaviour and the second electrode is pseudo in nature *e.g.* AC as one electrode and MnO_2 in AC-$Ni(OH)_2$ is the another electrode,[22] AC is one electrode and conducting polymer is another electrode etc. [23] The assembly of capacitive electrode with conducting polymer is of greatest interest over a market trade. The charge transfer redox reactions undergoes at the conducting polymer electrode. The oxidation process pushes the ions to flow towards the polymer and they get back into the solution during the reduction process. A prototype of a hybrid supercapacitor using conducting polymer was demonstrated in 2002 by M. Mastragostino *et al.* which delivers a high specific capacity of 39 F g^{-1}. [24]

The hybrid supercapacitors consist of an EDLC component, which delivers high output power density and a pseudocapacitive component imparts greater energy density. The
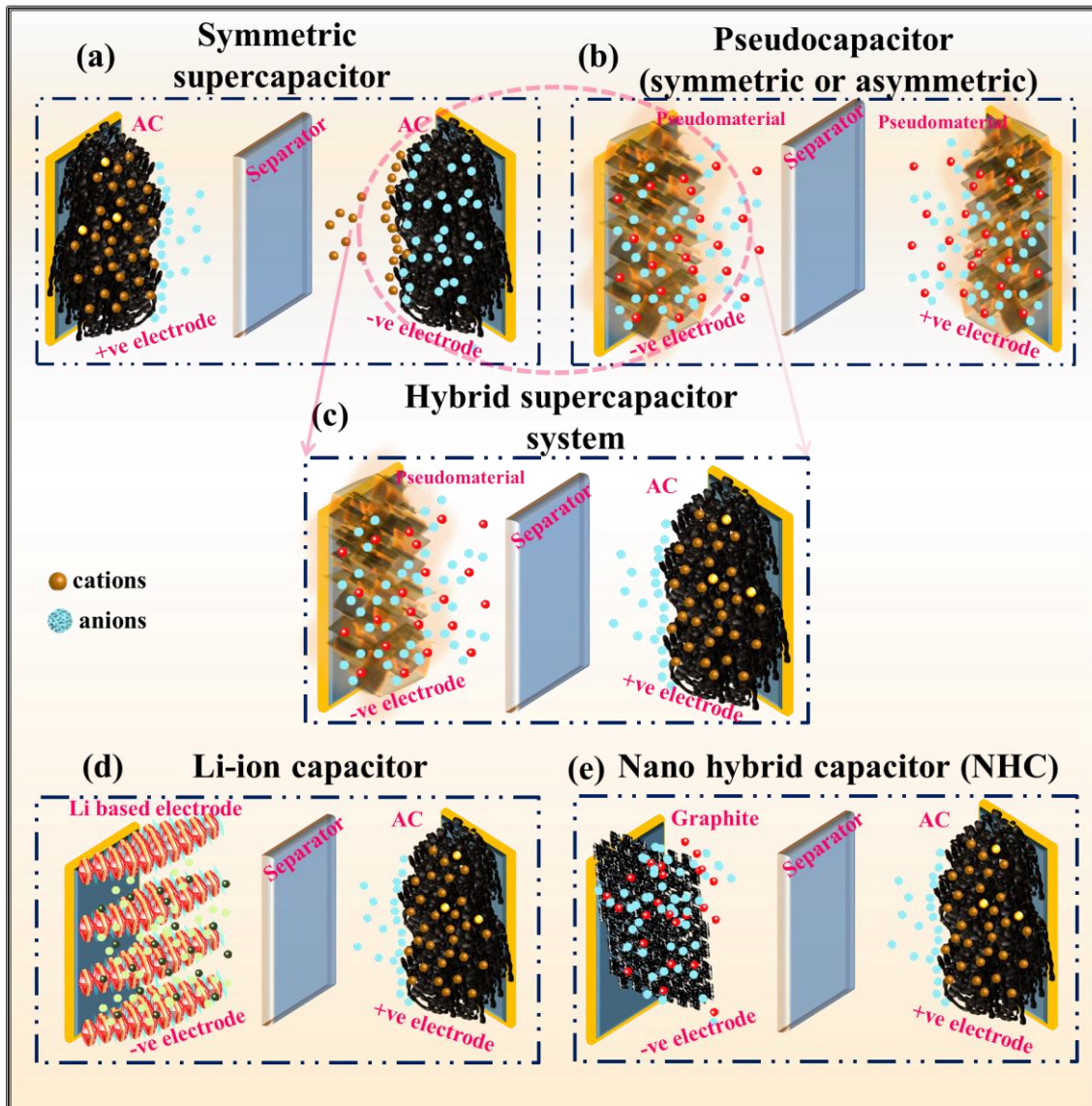
Figure 1.4 *Energy storage mechanism in different hybrid energy storage systems, (a) symmetric supercapacitors, (b) symmetric or asymmetric pseudocapacitors, (c) hybrid supercapacitor systems, (d) Li-ion capacitor, (e) Nano hybrid capacitors (NHCs).*

incorporation of both the components into a hybrid structure exhibits extremely high-rate performances.

Further advancements in the hybrid technology have been done *via* replacing pseudocapacitive electrode with a battery-type electrode and EDLC material as the other electrode. It is an internal series configuration of the hybrid system. The battery component undergoes a slow process of faradaic redox reaction, which gives elevated energy characteristics over charge/discharge cycles. Whereas, the EDLC electrode with fast kinetics impedes excellent power density (Fig. 1.4c). The combination of both i.e.,

battery-supercapacitor hybrid (BSH) systems impede tremendous energy and power density characteristics, which are useful for commercial applications. The class of battery-supercapacitor hybrid systems is further classified in two sections: (i) metal-ion capacitors as shown in Fig. 1.4 d (where metals are Li, Na, Mg etc.) consists of the
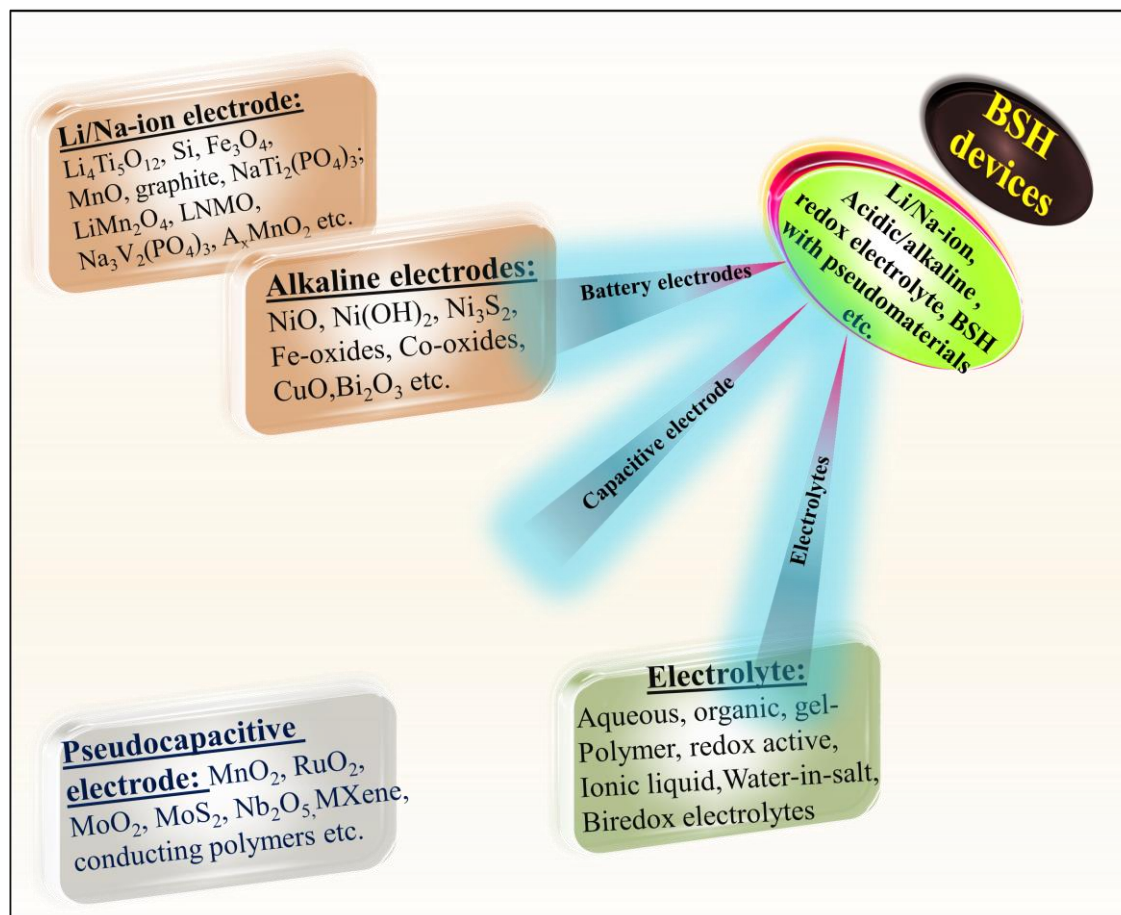
Figure 1.5 Schematic shows BSHs electrodes and electrolyte materials.

negative electrodes for metal's (Li, Na, Mg etc.) intercalation like $Li_4Ti_5O_{12}$, TiO_{2-x}/G aerogel, $Na_2Ti_2O_4(OH)_2$ etc. and other capacitive electrode like activated carbon, graphene, reduced graphene oxide etc. The second class of BSH system (ii) is nanohybrid capacitors (NHCs), which exhibit graphite as negative electrodes where intercalation of ions can be possible (Fig. 1.4e). The BSHs system can be classified based on the type of battery electrode and the kind of electrolyte ions used. The numerous BSHs system's electrode and electrolytes are listed in Fig. 1.5.

1.3 The structural modelling of storage devices

Storage devices (battery and supercapacitors) are further classified on basis of their device structural configuration; (a) Vertical sandwich configuration, (b) Planar configuration. Generally, the sandwich configuration was supposed to be more

convenient for scalable production, but intense care had to be followed while preparing the device (Fig 1.6a). Such configuration accompanies several limitations like heavyweight of the device, larger size, greater chances of short circuit, need of separator and sluggish ion transport. An appropriate distance has to be maintained to keep both the electrode to get isolated to each other. A higher mass concentration is required for the delivery of sufficient energy density, which in turn increases the thickness of the electrode. The greater thickness eventually increases the resistance for the easy ionic
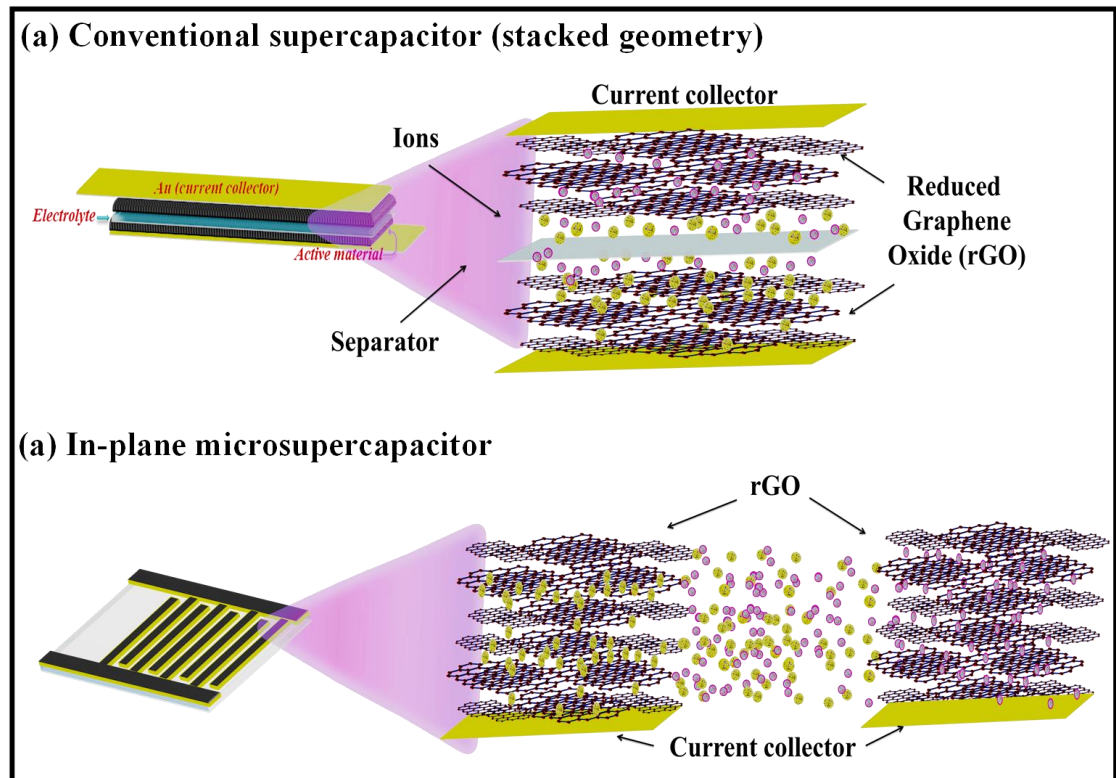
Figure 1.6 Schematic illustration of (a) sandwich geometry and (b) In-plane geometry in supercapacitors.

transportation, hampers the reversible reactions and fast power delivery. The integration and miniaturization with such bulky configuration become a hectic task with the inferior electrochemical response. Later on, to resolve the issue researchers convert this bulky configuration to a simple two-dimensional design, called as "planar configuration" and more profound for the 2D-layered active materials like graphene, MXenes for the lateral flow of ions from one layered electrode to another electrode. The in-plane structure (Fig. 1.6 b) includes that the electrodes are situated side by side with a minimum optimum separation distance to isolate from each other. This configuration has several advantages over sandwich-type such as less possibility of short circuit, less mass loading is required, narrow gap between the electrode (in microscale), light-weight, easy ion transport, lesser

charge-transfer resistance, excellent rate performance and delivers power at a faster rate. The planar structure of the device can be designed in several shapes like interdigitated finger electrodes; linear shape; circular; square shape; spiral shape and many more can be designed. Generally, On-chip electrical technologies use such advanced in-plane layout of the integrated circuits. Hence, in-plane microsupercapacitors/microbatteries could be a powerful tool for integrated miniature on-chip portable electronics devices.

As already discussed, the basics of the energy storage devices (supercapacitors and batteries), their storage mechanisms and their device architectures. It is essential to know how to quantify the quality of supercapacitors and batteries with respect to their output electrochemical performances and their response on a commercial scale. The discussion regarding this will be highlighted in the next section. Furthermore, a complete explanation on supercapacitors, batteries and hybrid systems regarding the active material selection, use of efficient electrolytes and the research breakthroughs till now is also focused on the coming section.

1.4 Electrochemical profile quantization parameters

The assessment in the electrochemical profile of the storage device (supercapacitor/battery) can be realized *via* determination of open-circuit voltage, electrochemical stability window, charge-transfer resistance (R_{ct}), specific capacitance/capacity, energy density, power density and cycling stability study with respect to specific current density. These measurements can be done by various electrochemical techniques; cyclic voltammetry (CV), Galvanostatic charge-discharge (GCD), and electrochemical impedance spectroscopy (EIS). These quantified parameters are described as follows:

1.4.1 Open circuit potential (OCP): It is defined as the attained potential of the device when it is disconnected from the external load. When the electrodes are immersed in electrolytes, it adopts an open circuit potential (OCP). The OCP value decides whether the electrode will undergo oxidation or reduction.

1.4.2 Specific capacitance: The specific capacitance can be measured by performing both the techniques: cyclic voltammetry and galvanostatic charge-discharge techniques. The capacitance value of the device can be quantified in areal, gravimetric and volumetric measures. As CV curve provides a correlation of current versus potential. The mass normalized specific capacitance 'C_{sp} (F g^{-1})' can be measured by the following equation 1.6:

$$C_{sp} = \frac{\int_{V_i}^{V_f} IdV}{m \times v \times (V_f - V_i)} \qquad \ldots\ldots\ldots\ldots..(1.6)$$

Where, 'I (A g^{-1})' is the output current generated in the device, 'm (g)' is the mass loading of the active material, 'v (mV s^{-1})' is the scan rate, $V_f - V_i$ (V) is the difference in the final potential to initial potential (potential window).

Similarly, the specific capacitance can be calculated from the GCD profile (Potential versus time correlation at constant current density) according to the formula 1.7:

$$C_{sp} = \frac{d_t \times I}{m \times (\Delta V - V_{IR})} \qquad \ldots\ldots\ldots\ldots (1.7)$$

Where 'I (A g^{-1})' is the applied current generated in the device, 'm (g)' is the mass loading of the active material, $V_f - V_i = \Delta V$ (V) is the potential window, V_{IR} is the potential drop due to internal resistance (IR).

1.4.3 Normalized energy density: The mass normalized energy density 'E_m (Wh kg^{-1})' of the device is defined as the amount of energy storage per unit volume/area/mass in the system. It can be calculated using the formula 1.8:

$$E_m = \frac{1}{2} C_{sp} \times \Delta V^2 \qquad \ldots\ldots\ldots\ldots (1.8)$$

The energy density is directly proportional to two quantified parameters i.e the capacitance value and cell voltage. The capacitance in turn is dependent upon the type of capacitive material used (whether it is capacitive, pseudocapacitive or battery type) and the effective surface area of the electrode. Hence, porous structured materials exhibiting greater effective surface provide subsequent high energy density.

1.4.4 Normalized power density: The normalized power density 'E_m (W kg^{-1})' is defined as the rate of energy flow per unit volume/area/mass. It is calculated by the formula 1.9

$$P_m = \frac{E_{sp}}{d_t} \qquad \ldots\ldots\ldots\ldots..(1.9)$$

Where 'd_t' is the discharge time under fast charge/discharge rate. The power density is directly dependent upon the energy stored in the device and inversely on the time taken by the device to get fully discharged. Hence, the lesser is the discharge time, the higher would be the power delivery but it is also true that when the device is working at higher power the energy density will be less.

1.5 Evolution of active electrode materials in supercapacitors

As explained above, supercapacitors are super-fast rechargeable storage devices, accompanying advantageous features like high charge storage capability and extremely high output power density without any damage. Preliminary, researchers were using metals to collect the charge and let them flow to the external circuit. As metals (gold, copper, aluminium, tin etc.) get corroded in aqueous electrolytes which can affect the stability of the device. The addition of metals as current collector components also increases the total weight of the microsupercapacitor devices. In order to maintain the trademark properties of the supercapacitors, efficient electrode materials are required because active material has significant impacts on the performance of the supercapacitors and also, the elimination/replacement of metals from the supercapacitor structure is mandatory. Therefore, we need such materials which can work as active material as well as a current collector to replace the metals from the device. Hence, the electrical conductivity of the active electrode should be comparable to metals so that they have the ability of collection of sufficient charge. Moreover, the active electrode material not only acquires good electrochemical properties but should also exhibit high mechanical strength upon stretching, bending and folded pose; closely packed powered material, diverse structural features and lightweight properties. Among all kind of electrodes materials, carbonaceous materials are of utmost importance due to their several intrinsic features and ability to replace the metals. The charge storage mechanism further classifies the materials as mentioned in earlier sub-sections described as electric double layer capacitive (EDLC) or pseudocapacitive types. In the next sub-sections, we have focused on the evolution of carbonaceous electrode materials (EDLC type and pseudo/carbon-polymer or carbon-pseudo composite materials) for the development of metal-free flexible microsupercapacitors.

1.5.1 Carbonaceous materials and their significances

Carbon materials, exhibiting EDLC characteristics, are studied as the ideal materials in storage applications due to their high surface area, good electrical properties, extreme chemical stability, cheapness, wide operating temperature range and facile applicability.[19] High surface area mesoporous carbon materials and activated carbon were widely used in supercapacitors due to their high surface area (approximately 1000-2000 m^2 g^{-1}).[25] Ideally, the calculated capacitance value for the material with an effective surface of 1000 m^2 g^{-1} should be very high (more than 500 F g^{-1}), which actually does

not happens. Practically, few tens of the capacitance are covered by these carbon materials. Activated carbon also lacked behind in high capacitance value because of their pore size distribution on a micropore scale.[19,26] Generally, the pores with this much size are non-accessible for the electrolytes ions and hence, not capable to form the double layer.[27] Sometimes, the modification in the structures increases the pore size distribution but the volume of the pores still remains less which is also responsible for the limited capacitance in such materials. Therefore, a new class of alternative materials is required to overcome the discrepancies generated in activated carbon-based supercapacitors. The classification of carbon materials is shown in Fig. 1.7. Nanostructured carbon materials like graphene, three-dimensional (3D) reduce graphene oxides, carbon nanotubes (CNTs) became promising materials in SCs applications owing to their superior properties such as high surface area, greater mesoporosity and good ionic accessibility. Graphene is defined as a two dimensional (2D) structured material *i.e.* a single atom thick layer of sp^2 carbon atoms densely packed into a honeycomb lattice configuration and also a building unit for other nanocarbons such as 0D fullerene, one dimensional (1D) CNTs,
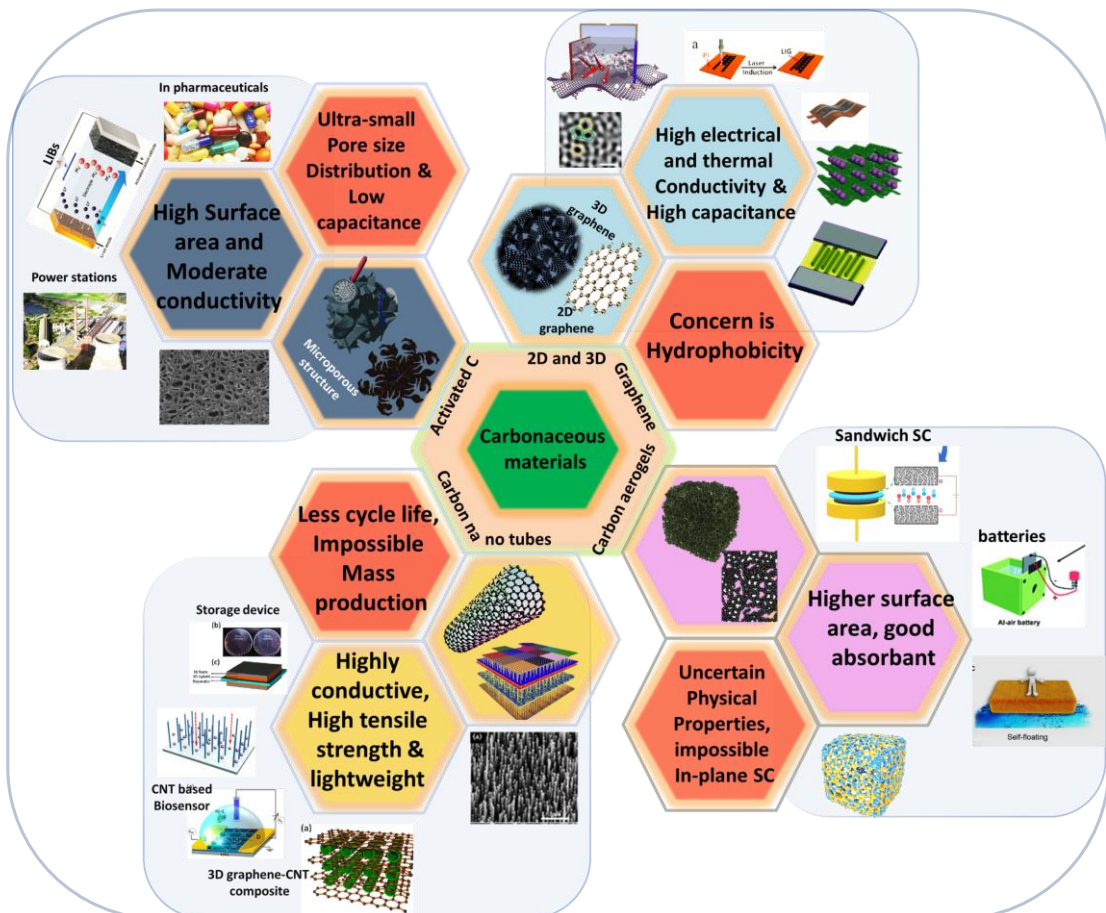
Figure 1.7 *Classifications of carbon nanomaterials in supercapacitor applications.*

3D graphite (stacking of graphene sheets) and 3D reduced graphene oxide (rGO).[28–30] The electrical conductivity of rGO is not that sufficient (~100 order) who can replace metals and delivers high capacitance. The complicated synthesis procedure and their vertical alignment architecture is quite a difficult approach. Among all kinds of carbon nano structures, graphene is the promising material to be utilized for the capacitive application independently and very efficiently.

1.5.2 Graphene: an emerging material in supercapacitive technology

Figure 1.8 The superior properties of graphene.

Recent scientific studies in the field of storage technology emphasize on the unique properties of graphene, structural modulation and their extraordinary performance in supercapacitors as well as in batteries. Defining graphene as a 2D carbon monolayer arranged with all sp^2-hybridized carbon atoms accumulating many fascinating properties; like lightweight, high electrical and thermal conductivity, highly modulated surface area (up to 2675 m^2 g^{-1}), and strong mechanical stability, chemical and electrochemical stability (as represented in Fig. 1.8). [31–33] These extraordinary features make graphene and its nanocomposite materials more profound selection for diverse applications such as in consumer electronics, for environmental safety and also in energy devices including

both energy generation and storage.[34–41] Graphene and graphene-based nanocomposite materials have shown tremendous performance in electrochemical energy generation and storage devices like Li-ion batteries, supercapacitors, fuel cells, and photovoltaic cells.[42] Basically, it is essential to study the reason behind the good electronic and outstanding electrochemical properties of graphene-based supercapacitors. The electrochemical properties of graphene depend upon its structure as it has a finite sheet-like structure with terminating edges, which acts as active sites.[43],[44] The basal and edge planes are the major surface responsible for the flow of electrons in heterogeneous electron transfer phenomenon.[45,46] The dimensionality of graphene can be categorized into Z-axis and x-y axes, which is also responsible for tuning the electronic properties of graphene. Due to the high electrical conductivity of graphene nanomaterials, they can be considered as charge collectors in supercapacitors or battery applications. They have the ability to replace metals with comparable electrical conductivity values ($\sim 10^5$ S m^{-1}). Obviously, these electrical features may vary with different synthetic procedures, which arise due to the tuning of the graphene with different structural properties. Many synthetic approaches are reported for the development of graphene film, but the as modified graphene film contains some advantageous facets and with few limitations. These

Synthesis Methods	Advantages	Disadvantages
Mechanical Exfoliation	High quality graphene; Cheap equipment; easy operation	Low yield; small size graphene; time-consuming
CVD/Arc discharge	High quality single layer graphene	Low yield; Expensive; Energy consuming
Chemical Derived /Epitaxial Growth on SiC	Mass synthesis; graphene composites	Impurities; defects; toxic reducing agents; hard to obtain single layer graphene
Electrochemical Method	No use of toxic chemical; Quality better than chemical derived	Less defects; hard to obtain single layer graphene
Laser-irradiation assisted graphene	large scale-up; Excellent quality; No Damage; no reducing agents	Hard to obtain single layer graphene

Figure 1.9 Advantages and disadvantages of various synthesis techniques of graphene

synthetic methods include: physical methods like peeling of graphene sheet from highly ordered pyrolytic graphite (HOPG),[47] mechanical exfoliation,[48] chemical vapor

deposition method,[44,49] chemical derived/epitaxial growth on SiC,[50] thermal reduction of GO,[51,52] solvothermal approach, electrochemical deposition methods,[53] laser-irradiation assisted process[54–56] and many more. Each process is described in Fig. 1.9 highlighting its advantages and disadvantages. The capacitive response depends upon the quality of the graphene film related to its conductivity, porosity and defect density. The mass-production of high-quality graphene is the main concern with many of the approaches like CVD technique and micromechanical exfoliation. Therefore, it is important to search for such methods, which do not involve high-end instruments and costly reducing agents and also require less time-consuming techniques. The electrochemical deposition method which involves the deposition of rGO and reduction of GO simultaneously, yields a highly porous 3D network in a short time span. Among all various graphene fabrication methods as above discussed, laser scribed/irradiation/induction method for the fabrication of graphene from graphene oxide (GO) is preferable as it can yield mass production of graphene in a short time period with premium quality. The combination of both electrochemical deposition of rGO and later on the laser-reduction method was followed in order to synthesize a highly porous and conductive graphene sheet which can be used as current collector as well as active material. We have also opted for this method (electrochemical deposition followed by laser-irradiation method) and fabricated a laser-irradiated graphene (LIG) film, which was further utilized to make metal-free On-chip microsupercapacitor (MSC) for the first experimental work of the thesis (will be explained in chapter 3). Since, graphene-based MSCs acquire EDLC property only, hence it can attain limited capacitance and energy density. Therefore, modification of graphene with some redox-active materials encourages pseudocapacitive response and increases the capacitance value, which in turn enhances the energy density.

1.5.3 Pseudocapacitive materials for capacitance enhancement

The basic mechanisms for the pseudocapacitance are already discussed in section 1.2.1.2. Typically, transition metal compounds (TMCs) like metal oxides, metal nitrides, metal sulfides and carbides[57] possess intriguing benefits for high energy applications. They have the ability to store energy through a reversible redox mechanism. The specific intercalation-type pseudo materials like Nb_2O_5,[58] MoO_3,[59] Co_3O_4,[60] and MXenes,[61] are more susceptible to organic electrolytes. More strikingly, RuO_2 has attracted much attention as a pseudocapacitive material due to its high theoretical specific capacitance and good chemical stability but its toxic impacts on the environment and high cost restrict its further application in storage devices.[62,63] Other than RuO_2, other metal oxides like

V_2O_5, Co_3O_4, ZnO, SnO_2 and MnO_2 have been explored as capacitive pseudocapacitors due to their high natural abundance. Although these materials show moderate pseudocapacitance, they suffer from sluggish reaction kinetics, less conductivity, moderate rate capability, and poor cycling stability. In recent years, metal nitrides (TiN, VN, and FeN)[64–67] and carbides like Ti_3C_2 have received marvelous research interest because of their high electrical conductivity and extreme chemical stability but they follow very complicated synthesis procedures. Apart from many metals-based pseudo materials, conductive polymers are considered most appropriate for storage purposes because of their low cost, high conductivity, environmentally benign, easy polymerization processing and robust nature. The most studied conductive polymers are Polyaniline (PANI), Polypyrrole (PPy), Poly(3, 4-ethylenedioxythiophene) (PEDOT), Polythiophenes etc.[68–70] During charge/discharge process the polymers undergo contraction, fracture and expansion which may degrade the conductivity and in response cycling stability of the electrode. Forming composite structure by combining polymer with some other conductive networks like graphene, CNTs and so on[71–73], the generated synergistic effect is so beneficial for the improvement in the specific capacitance and cycling stability. In my second work, we have opted for this concept and utilized the graphene-polymer composite film in planar MSC with successful enhancement in the specific capacitance as compared to LIG-based MSC (will be discussed in chapter 4).

1.6 Electrolytes for supercapacitors

Electrolytes are an essential component in any storage device and act as a transport medium for the charges towards the electrodes. The electrolyte concentration, size of the ions, their boiling and freezing conditions, type and nature of the electrolyte, and internal resistance are the key factors that influences the performance of the supercapacitors in terms of the potential window, specific capacitance and thermal conditions of the device. The basic properties that are held by the electrolyte for best capacitive performance are:

(a) Wide electrochemical stability window
(b) Fine chemical and electrochemical stability
(c) Superior ionic conductivity
(d) Low volatility and non-flammable
(e) Comparable size of electrolytic ions for the electrode pore
(f) Resource-efficient.

It is quite a difficult task to carry all requirements for some particular electrolyte as each of type holds its own advantage and disadvantage. The conventional electrolytes are categorized as aqueous, non-aqueous (ionic liquid) and organic electrolytes, supersaturated (Water-in-salt) that are described in the coming sections.

1.6.1 Aqueous electrolytes

In an aqueous electrolyte, generally, water is the polar solvent in which salt ions are dissolved. Aqueous electrolytes have better conductivity rather than other classes of electrolytes (organic or ionic-liquid), are easily accessible to the pores of the electrodes, are low cost and can be easily used without inert atmosphere conditions. Due to the higher conductivity, the electrochemical equivalent series resistance (ESR) between electrode and electrolyte interface is minimum which results in an increment in the power density. Despite of many advantages, since the aqueous electrolytes restrict the potential window up to 1.23, beyond this value the decomposition of water takes place. The aqueous electrolytes are further classified into acidic electrolytes (such as H_2SO_4, H_3PO_4, $HCLO_4$),[74] basic (KOH, NaOH, LiOH), and neutral electrolytes (Na_2SO_4, NaCl, K_2SO_4). Acidic electrolyte *i.e.,* H_2SO_4 is most preferable for EDLC type of electrode materials due to its high ionic conductivity with less ESR value as compared to neutral electrolytes. But the acidic nature of H_2SO_4 electrolyte causes degradation of the electrode which hampers the cycle stability of the device. To such redox-active electrodes like metal oxides, the alkaline medium is enormously used instead of using the acidic electrolytes. In asymmetric supercapacitors, the charge storage mechanism undergoes intercalation and desorption of ions *via* decomposing of the electrode internal structure which influences the cycle life of the electrode, in such instances, neutral electrolytes are mostly used. Neutral electrolytes are better than acidic or basic electrolytes due to their wide operating potential window, less corrosion and more secure as compared to acidic electrolytes.

1.6.2 Ionic-liquid and organic electrolytes

Ionic liquid electrolytes are also known as solvent-free electrolytes have taken attention due to their large potential window, non-flammable and chemically stable. The aprotic, protic and zwitterionic are the further categorized terms of ionic liquid electrolytes. Few examples of ionic liquid electrolytes are N-butyle-N-methylpyrrolidinium bis(trifluoromethansulfony)imide (PYR14TFSI), ethylammonium nitrate [EtNH3][NO3], 1-alkyl-3-methylimidazolium etc. The high viscosity of the ionic liquid electrolytes

promotes sluggish ionic kinetics. More studies need to carry out to develop efficient ionic liquid electrolytes with a wide stability windows and lower molecular weight.

Organic electrolytes are dominating the battery market due to their wide electrochemical stability window (~ 2.5 -3.0 V). The large potential window gives enormously high energy density. The organic electrolyte is prepared by dissolving salt acquiring good conductivity into some organic solvent like acetonitrile (ACN), Propylene carbonate (PC), ethylene carbonate (EC). Some commonly used organic solvents are: tertraetheyleneammonium tetrafluoroborate [TEABF$_4$], tetraethylenephosphonium tetraborate [TEPBF$_4$], and tetraethylmethyammonium tetrafluoroborate [TEMABF$_4$]. Since these organic electrolytes acquire wide operating potential window, still they are not the best choice due to their ESW significant limitations such as expensive, less conductivity, major safety concerns due to toxic and flammable nature and limited specific capacitance.

1.6.3 Water-In-Salt electrolytes

The safety and cost of the electrolytes are two major concerns for their applicability in an energy storage device. As discussed above, the aqueous electrolytes have a limit of 1.23 V ESW due to water decomposition at that potential. To enlarge the potential window in aqueous electrolytes, another alternative approach is required to be explored. Recently, the "Water-in-salt" (WIS) electrolytes are emerging due to their large electrochemical stability window capability. The high concentration WIS electrolytes, which includes that the salt concentration outnumbers water molecules in terms of volume as well in mass. They are also called "supersaturated electrolytes", which have the capability to extend the potential window upto ~3V (Suo *et. al*. in 2015).[75] The internal properties like safety, environmental friendliness, sufficient ionic conductivity of the traditional aqueous electrolytes do not disturb as the concentration of the salt increases in WIS electrolytes. Numerous efforts have been done to establish the solvation structure formation mechanism and their application in SCs and batteries.[76] The working mechanism of WIS needs to be understood in order to explain the increment in the potential window and development in the performance of the storage system with respect to the undergoing processes salt ion solvation,[77] solvated ion transport[78] and solid electrolyte interphase (SEI)[79] at the surface of the electrode. The commonly used WIS type electrolytes are bis(trifluoromethanesulfonyl)imide (LiTFSI), sodium perchlorate (NaClO$_4$), LiCl, potassium acetate (CH$_3$COOK), K$_2$CO$_3$ and many more. To understand the solvation structure in "Salt in water" (SIW) electrolyte and WIS electrolyte, LiTFSI

is considered as an example. The dilute condition (*i. e.* SIW) of LiTFSI states that Li^+ cation is fully surrounded with four water molecules in the first solvation sheath, and the free $TFSI^-$ anions. The primary solvation sheath is known as "solvent-separated ions pairs". As LiTFSI concentration increases, the amount of Li^+ and $TFSI^-$ ions increases and anions starts interacting with cations, forming contact-ions pairs (CIPs). With further increase in the LiTFSI (21m), almost all the H_2O molecules are bound to Li^+ cations and the coordination of $TFSI^-$ anions in massive amounts leads to the formation of ion aggregates (AGGs). The water activity reduces due to the negligible amount of free water molecules in WIS electrolyte system. But the high concentration in WIS electrolytes increase the viscosity of the electrolyte, which in turn slows down the ion transport. The ionic conductivity in 21 m LiTFSI electrolyte is comparable to the conventional aqueous systems but still not sufficient. Therefore, some improvements are much needed to improve the ionic conductivity, operating temperature conditions and viscosity of the electrolyte.

Diluting supersaturated WIS with some solvent helps in easy ionic dynamics, decreases viscosity and increases the ionic conductivity of the electrolyte. Mostly organic solvents are used for diluting the WIS electrolyte to simultaneously modify the working temperature conditions of the electrolyte, named "organic/water-in-salt". The commonly used organic solvent is Acetonitrile (ACN). We have also designed the next work of thesis based on this concept and fabricated a supercapacitor device in "Organic/water-in-salt" type of electrolyte. Moreover, the capacitance can be increased by adding some redox-active species in WIS electrolyte, e.g. 1 m LiCl is added into 21 m LiTFSI which undergoes the redox process of $Cl_2/2Cl^-$, which has the theoretical capacity of 766 mAh g^{-1}.[80] The modification with WIS electrolytes gives highlight achievements in both batteries and SCs.

We have already gone through all the basic mechanisms of charge storage, supercapacitor components and their classifications responsible for the great performance of supercapacitors. The following sections include the scientific breakthroughs in graphene-based microsupercapacitors technology and their advantages and limitations.

1.7 Scientific breakthrough in graphene-based supercapacitors

As already discussed, the benefits of fabrication of graphene by laser irradiation process. The laser irradiation method does not need any expensive chemical and does not require

any photoresist mask-like used in the lithography technique.[81–84] The graphene can be directly synthesized by this facile and cost-effective laser processing technique. The synthesis of graphene and patterning for the supercapacitor electrode can be done
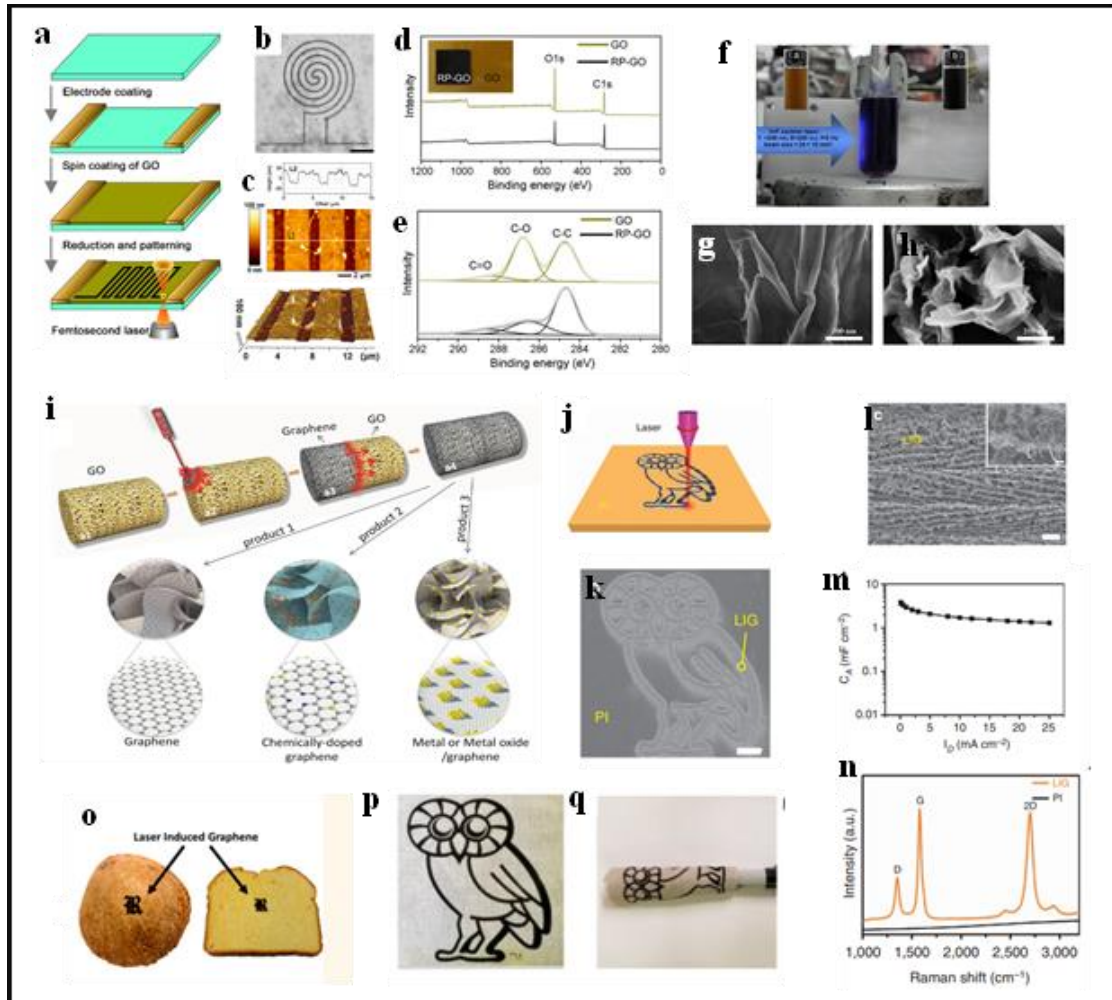
Figure 1.10. *(a) Illustration of the development of graphene nanostructures by laser scribing method. (a) The preparative procedure of LSG microcircuit on GO film. (b-c) atomic force microscope (AFM) image of LSG microcircuit on GO film, the height profile along the white line (L2), and its 3D image; (d) Survey X-ray photoelectron spectra of GO and LSG, inset is a photograph of an LSG square on a GO film; (e) C1s x-ray photoelectron spectroscopy (XPS) spectra of GO and LSG, (f) A representation of the experimental setup of pulsed laser reduction system. The inset is optical images of GO solution (15 mL, 0.1 mg/mL) before and after pulsed laser irradiation, SEM photos of (g) GO and (h) pulsed laser irradiated GO dispersion in ethanol (0.05 mg/mL), (i) A schematic illustration of the preparation of graphene bulks and its functional composites. a) Schematic illustration of the preparation process of graphene bulks and functional counterparts induced by a laser shot within milliseconds. The enlarged schematic shows the constituent structures of graphene (product 1), chemically-doped graphene (product 2), or graphene composites with metal or metal oxide (product 3). (j) Schematic of the fabrication procedure of LIG from PI. (b), SEM image of LIG patterned into an owl shape. (c), SEM image of the porous LIG film, inset is the corresponding higher magnification SEM image; scale bar, 1 mm, (m) Raman spectrum of PI and LIG, (o-r) The letter "R" in LSG induced from bread and picture of LSG patterned into an "R" on a coconut (2 cm tall). (p) LSG on cloth in the shape of an owl (60 mm in height) (q) and the wrapped cloth.*

simultaneously in a short period. This section includes the scientific breakthroughs in the

development of laser-induced graphene for supercapacitor applications. In the preliminary studies, Xiao et al., fabricated laser scribed graphene (LSG) microcircuits by laser irradiation on spin-coated GO films using a femtosecond laser.[85] Figure 1.10a shows the synthesis steps of GO films and the scanning electron microscopy (SEM) images of patterned LSG (Fig. 1.10b). The laser writing turns the brown colour GO sheet into black. An obvious removal of oxygen components can be observed as indicated in AFM and XPS results in Fig. 1.10(c-e). The mechanism of laser reduction of GO is completely dependent on the photochemical and photothermal effect of the laser.[86] Laser light having a wavelength of <390 nm, the induced photochemical effect weakens the C-O bond on graphene oxide structure and removes the oxygen functionalities. Laser source provides a local temperature of ~ 2700 K at the GO film surface which can easily break the C-O and C=O bonds.[87] This whole laser induction process surpasses two processes that are: sp^3 carbon to sp^2 carbons conversion[88] and simultaneous exfoliation with the removal of oxygen functionalities which yields reduced graphene oxide (rGO). Not only GO solution, GO fibers and aerogels also can be reduced using the laser activation method. As shown in Fig. 1.10f, when a GO solution mixed with ammonia is laser irradiated, the brown colour of GO changes to black which indicated the reduction of GO.[89] The SEM images also show the structural comparison of GO vs LSG as shown in Fig. 1.10g-h. To make a flexible fiber-based supercapacitor device, a region-specified GO fiber is laser irradiated to make reduced GO electrodes.[90] The aerogel solution can also be laser-treated, reduced and converted to bulky graphene (Fig. 1.10i).[88] The fabrication of GO gels *via* focused femtosecond laser source on air/GO interface was purposed by Ibrahim *et al.* The major limitation of such methodology for the fabrication of graphene from GO solution is the possibilities of stacking of graphene layers which may decrease the effective surface area of the film. Besides using GO solution as a starting material, polymers like polyimides (PIs) and polyetherimide can be used for the growth of highly conducting graphene sheets with unique porosity. Prof. Tour and his group in 2014 introduced a one-step laser scribing method using CO_2 laser to make a highly porous 3D graphene as shown in (Fig. 1.10j-l) from commercial polymer film *i.e.,* Polyimide sheet.[91] The resulting porous LIG sheet exhibits a uniform pore distribution with a high effective surface area (~340 m^2 g^{-1}) and a high degree of graphitization examined by Raman spectrum (Fig. 1.10n). The Raman spectrum of LSG (as shown in Fig. 1.10n) includes a sharp 2D band indicating 2D graphitic features. The origin of the decrease in the intensity of the D-band and the appearance of a sharp 2D band is the

removal of oxygen functionalities upon laser impact. The resulting highly conductive ((5 –25 S·cm^{-1}) LSG film was used as electrode material and patterned into the interdigitated electrode to make a metal-free planar micro supercapacitor which gives a high C_{sp} of > 4 mF cm^{-2} (Fig. 1.10m). Similarly, Zhang et al., develop laser-induced graphene from phenolic resin (PR) on a large scale.[92] The resulting LIG comprises superior properties like 3D porous morphology, lower sheet resistance and strong mechanical properties. The resulting LIG can act as the binder-free electrode to make all in one solid-state metal-free micro supercapacitor.[93] Besides GO solution and polymers, natural precursors like wood,[94] cloth, normal paper, potato skins, coconut shells, and lignin's,[95] which are cost-effective, abundant reserve, and also biodegradable, can also be used for the fabrication of graphene, as shown in Fig. 1.10(o-q). Later on, Prof. Kaner's group. converted carbon nanodots (CNDs) into high-surface area 3D graphene networks with excellent electrochemical properties by irradiation with an infrared laser.[96] The fabricated 3D LSG electrodes show high specific volumetric capacitance of 27.5 mF·cm^{-3} and extremely fast charging rates with a relaxation time of 3.44 ms. The produced laser irradiated graphene comes up with numerous advantageous features like high conductivity, unique porosity, low sheet resistance and high degree of graphitization, which can be a benchmark for the development of highly efficient metal-free energy storage devices

1.8 Advantages and disadvantages of supercapacitors

In the last few decades, extensive research progress has been carried out in field of supercapacitors and its performances. The main advantages of supercapacitors are listed below:

(a) High energy density and power density as compared to conventional capacitors

(b) Fast charge/discharging process

(c) Longer life cycle upto 10 to 15 years

(d) Offers high specific capacitance

(e) Greater performance reliability

(f) Can be lightweight, pocket size on-chip device

(g) Stable at low temperature conditions

(h) Eco-friendly

Although there are many advantages, supercapacitors also have a few limitations, as explained below

(a) Lower energy density as compared to batteries

(b) Less storage capacity compared to batteries

(c) Higher self-discharge rate

(d) Voltage reduces to half as supercapacitor discharge 50% rather in case of battery, voltage does not drop at battery discharge 50%

(e) Cannot be used in high frequency circuits.

Despite many beneficial features, supercapacitors could not replace batteries on a large-scale energy application. Therefore, batteries are highly desired for high-energy applications. The basic concepts of Li-ion batteries and their upgradation in recent studies will be discussed in the next section.

1.9 Li-ion battery: An introduction and basic mechanism

In the past few decades, Li-ion batteries (LIB) are the most advanced rechargeable battery due to their characteristic features of high energy density, long cycling stability, high-temperature viability, specific power, low self-discharge rate, etc. Only Li-ion batteries are the most powerful energy resources anticipating for widespread replacement of energy sources based on fossil fuel and they are on the verge to convert the fuel-based transport system into electric buses, scooters, and cars. LIBs are the main component in portable electronics such as cell phones and laptops to power the cell continuously. From the time when Li-ion batteries were commercialized to the present date, only LIBs are the power pack tool for the digital electronic revolution in modern society. The demand for the growth of LIB is rapidly increased with the development of electric-powered vehicles. An important concern for the LIBs is their safety and toxicity of lithium. This provides a motivation for extensive scientific development in the field of safe and high-energy Li-ion batteries. Although lithium metal batteries have higher theoretical energy densities than that of Li-ion batteries, but their poor reversibility of cathode material, dendritic formation on Li metal, and susceptibility to catching fire, even explosive behaviour; are hazardous drawbacks. Also, LIBs do not suffer from memory effect problems and the operating voltage is nearly three times the values corresponding to other rechargeable batteries. The high voltage of single unit cell would reduce cells quantity in a battery module. The self-discharge rate is very low in Li-ion batteries. These advantages over other rechargeable batteries make Li-ion batteries a better choice in storage applications. A brief overview of the history of the yearly development of Li-ion batteries is provided in Fig. 1.11.

1.9.1 Reaction mechanism in LIB

The Li-ion cell consists of a cathode and anode connected by an electrolyte and keep insulated by a separator between the electrodes. The separator is a microporous polymer membrane that can allow Li ions to pass through and at the same time block electrons. The most commonly used anode materials are graphite and petroleum coke. It is interesting to note that the three leading cathodes such as spinel oxides like $LiMn_2O_2$, layered oxides like $LiCoO_2$, and polyanion ($Li_xFe_2(XO_4)_3$) groups are the derived materials by Prof. John Goodenough's group at Oxford University and at Texas university. Later on, in 2019 John Goodenough, Akira Yoshino, and Stanley Whittingham were awarded by Nobel Prize to embolden the claim. The different mechanisms followed by Li-ion charge carriers to interact the electrode's active materials which are explained as:

    (a) Insertion or de-insertion

    (b) Alloying/de-alloying

    (c) Conversion reactions. [97–99]

When the charging state occurs, Li ions get migrate from the anode (negative charge electrode) towards the cathode (positive graphitic carbon electrode) via oxidation of $LiMO_2$ anode and release number of electrons. The electrons flow through the external circuit towards the positive electrode to reduce the graphitic electrode and form lithium carbide. It is a non-spontaneous process and the process is schematically shown in Fig. 1.12. The corresponding reactions (1.10 and 1.11) are as follows:

$$LiMoO_2\ (anode)\ \longrightarrow\ Li_{1-x}MO_2 + xLi^+ + xe^- \qquad (1.10)$$

$$yC + xLi^+ + xe^- \longrightarrow\ Li_xC_y \qquad (1.11)$$
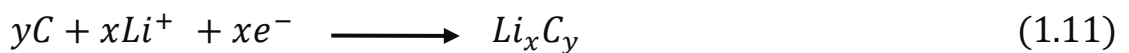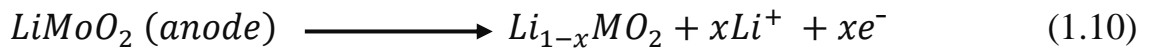
Under discharging conditions (refer to Fig. 1.12), the above reactions get reversed *i.e.,* graphite will act as anode and $LiMO_2$ act as cathode. Lithium carbide release the lithium ions which recombine with metal oxide crossing through the electrolyte to reform $LiMO_2$. The reaction at the discharge state are as follows (1.12) and (1.13):

$$Li_xC_y\ (anode) \longrightarrow yC + xLi^+ + xe^- \qquad (1.13)$$

$$Li_{1-x}MO_2 + xLi^+ + xe^- \longrightarrow LiMoO_2 \ (cathode) \qquad (1.14)$$
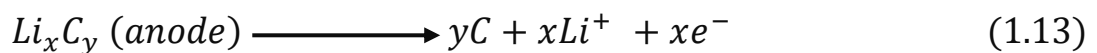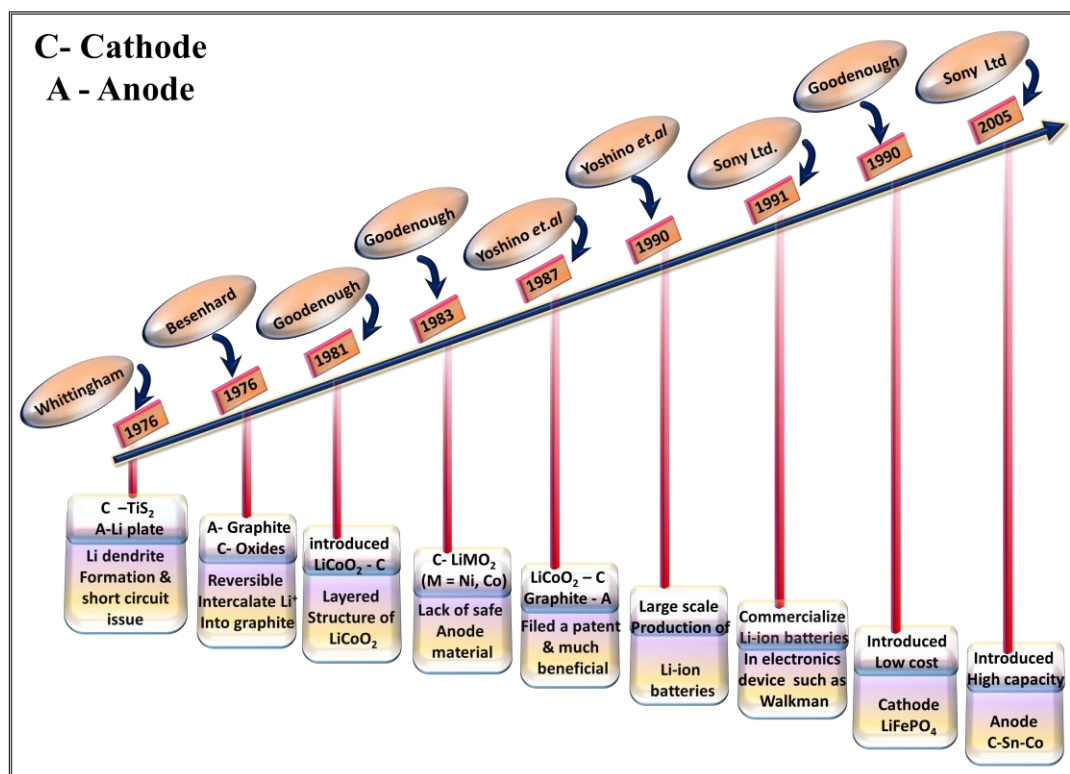
Figure 1.11 *The history of the development of Li-ion battery*

1.9.2 Research progress in Li-ion batteries

The current idea of present lithium-ion batteries is based on the combination of a lithium-ion positive electrode *i.e.,* "cathode" and a negative electrode "anode" these are separated by a membrane sodden with a lithium-ion conducting electrolyte. Important efforts have been dedicated to discovering advanced energy density electrode materials to meet the condition for EV's application. Currently, $LiCoO^2$,[100] layered metal oxides like $LiNi_{1/3}Co_{1/3}Mn_{1/3}O_2$ (NCM),[101,102] and $LiNi_{0.8}Co_{0.15}Al_{0.05}O_2$ (NCA),[103,104] olivine-kind of electrode $LiFePO_4$[105] and spinel-shaped electrode $LiMn_2O_4$,[106] and are the current active cathode materials, well proved themselves in Li-ion storage field. However, they deliver short practical capacities typically in the range of 100–180 mAh g^{-1} in a lithium-ion cell. Clearly, it is important to advance new strategies to strategy alternative high-energy cathode materials that are greater to those attainable with standard $LiMn_2O^{4-}$, $LiCoO^{2-}$, and $LiFePO^{4-}$ type electrodes upholding the physical stability, rate capability as well as long cycle life of the device.

An Additional effective method of growing the energy density of lithium-ion batteries is to pursue for high-capacity anode materials. As mentioned earlier, graphite is

definitely the most widely used anode active material in the commercial Li-ion cells due
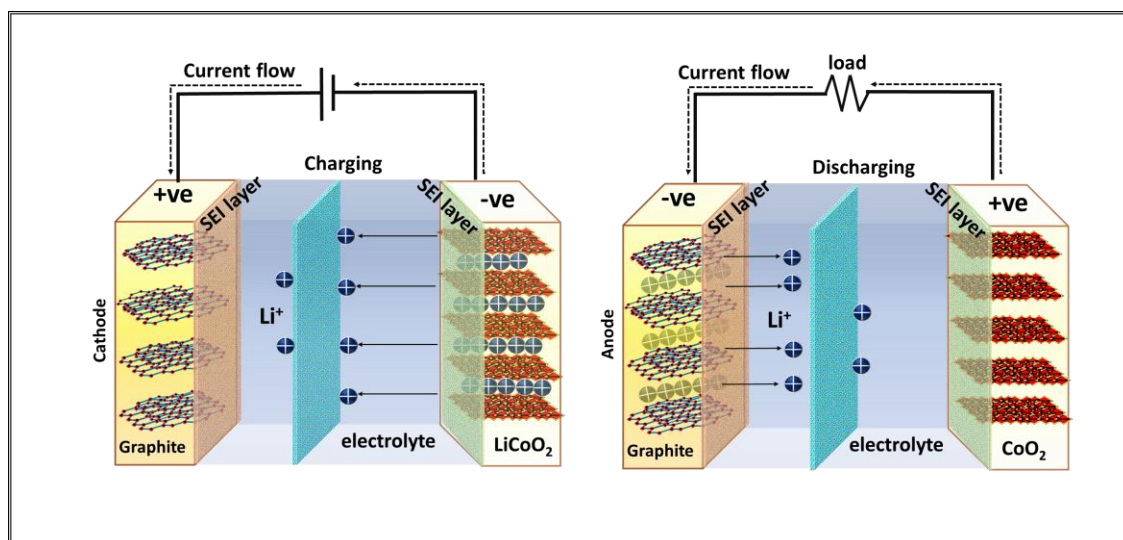
Figure 1.12 *Reaction mechanism in Li-ion battery utilising LiCoO₂ and graphite electrodes under charge and discharge conditions.*

to its outstanding properties including low working potential, low cost and good cycle life.[107] However, graphite only delivers a relatively low capacity of 372 mAh g⁻¹ since it lets the intercalation of only one lithium for six carbon atoms form a stoichiometric LiC_6. In addition, battery with graphite anode usually has moderate power density because of relatively slow diffusion rate of lithium-ion into carbon materials (between 10^{-12} and 10^{-6} cm² s⁻¹).[108] Therefore, there is an urgency to find alternative anode materials with high-capacity and high lithium-ion diffusion rate that assists the improvement of energy and power densities of the cell. An ideal anode for Li-ion battery should fulfill the necessity of high reversible gravimetric and volumetric capacity; a low potential against cathode materials; high-rate capability; long cycle life; small cost; excellent tolerance; and environmental compatibility. Both carbon and non-carbon materials for high-performance anode have been intensively examined, including but not limited to carbon nanotubes,[109] carbon nanofibers,[110] graphene,[111–113] porous carbon, [114] silicon,[115] and silicon monoxide,[116,117] tin,[118] germanium,[119,120] and transition metal oxides,[121] phosphides,[116]sulfides,[122] and nitrides.[123] The redox potentials versus Li/Li⁺ and the consistent specific capacity of these materials are shown in Fig. 1.13a, which clearly shows that the choice of appropriate anode materials has an important influence on improving the energy density of the Li-ion cell.

Extensive research in the past 15 years is done on LIBs anode to replace graphite, which needs to be explored furthermore. Rational research on anodes for LIBs is focused

toward the materials that can perform via three specific mechanisms: (a) Intercalation−deintercalation, (b) Elements (A) or metals (M) that can form alloys with Li metal (Li_xA or Li_xM accept separate crystal structures and display physical properties different than that of Li, A, and M) and (c) Redox or "conversion" reaction accompanying Li. The schematic illustration of three different types of anodes based on the lithium storage mechanism and their advantages and disadvantages are tabulated in Fig. 1.13a. Figure 1.13b depicts the schematic illustration of active anode materials for the next-generation lithium batteries.

(a) **Anodes based on intercalation-deintercalation:** The intercalation of an ion, atom, or molecule into a crystal lattice of the base compound is integration of the visitant species without abolishing the crystal structure. The anodes based on intercalation-deintercalation are generally consist of binary oxides, Ternary Oxides of Ti and Nb. Enormous research has been performed in the search of anode material based on binary oxides and ternary oxides. For example, binary oxide such as TiO_2, is an attractive material for its use as an anode because of its admirable properties such as low-cost, availability, and environmental-friendliness. TiO_2 imparts numerous polymorphic amendments: anatase, rutile, brookite, TiO_2-R (ramsdellite), TiO_2-B (bronze), TiO_2-II (columbite), TiO_2-H (hollandite), and TiO_2-III (baddeyite). Yang et al.[124] and Froschl et al.[125] have highlighted, Li cycling properties of different titanium oxides in their recent review. A substantial exertion has been made on the production of 2D TiO_2 materials. For example, Iversen et al.,[126] demonstrated TiO_2 anatase and rutile nanoparticles (Fig. 1.13c-d) are synthesized by facile, scalable, low-temperature precipitation, and the capacity loss in the first cycle is significantly reduced by simple treatments of the particles with LiOH or NaOH. Furthermore, these treatments inhibit crystal growth during heating. Figure 1.13e-f shows two examples of galvanostatic cycling of half cells with rutile (RL0.5) and anatase (A400N) electrodes. The maximal Li extractions of 210 mAh g^{-1} or ~0.63 Li/TiO_2 in anatase at low charge rates (0.5 C) and 120 mA g^{-1} at 5 C were delivered, which is at the best of many other reported ones. Many ternary titanium and niobium oxides containing 2D or 3D network structures that attained good Li cycling stability via intercalation−deintercalation way without hampering the structure of host material. They are of potential interest because their cycling potential occurs in the range of 1.3−1.8 V *vs* Li. The materials fall in this class are $Li_4Ti_5O_{12}$ (LTO), $MgTi_2O_5$,

LiTiNbO$_5$, TiNb$_2$O$_7$ etc., Li$_4$Ti$_5$O$_{12}$ (LTO), which has been extensively examined for Li storage and cyclability by the groups of Thackeray, Dahn, Ohzuku etc.[127–129] Yang *et al.*[124] and Yi *et al.*[130] have recently reviewed its exceptional Li cycling properties, which show that pure and modified LTO are feasible anodes for LIBs.

(b) Anodes based on alloying-dealloying reaction: By virtue of alloying and dealloying reactions, elements like Si, Sb, Sn, In and Cd are highly favourable for Li storage and cycling stability at a potential, V ≤ 1 V *vs* Li metal and suited best for
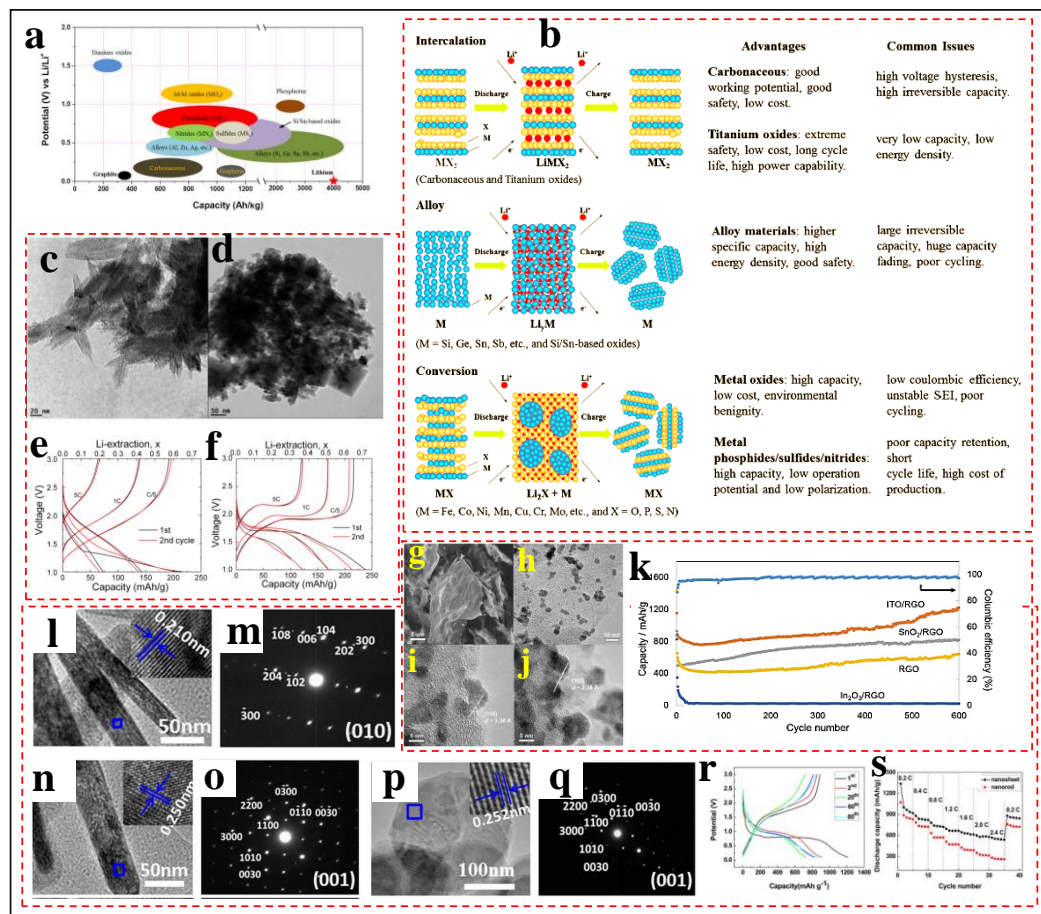
Figure 1.13 *(a) Schematic illustration of active anode materials for the next-generation lithium batteries. Potential (vs. Li/Li$^+$) and the corresponding capacity density, (b) Schematic illustration of three different types of anodes based on the lithium storage mechanism and their advantages and disadvantages, (c and d) TEM images of (left) anatase heated to 300 °C (A300), (middle) rutile dried at 120 °C (R120), and (right) rutile autoclaved with a stoichiometric ratio of LiOH at 180 °C (RL1), (e and f) Charge-discharge curves for (left) RL0.5 and (right) A400N samples, (g)) SEM image of graphene. Low-magnification TEM image (h) and HRTEM images (i, j) of ITO/RGO, (k) Cycling performance of ITO/RGO, SnO$_2$/RGO, In$_2$O$_3$/RGO and RGO electrodes and Columbic efficiency of ITO/RGO electrode, (l) The TEM image of a Fe$_2$O$_3$ nanosheet, inset shows the lattice fringes and (m) the corresponding SAED pattern; (n,o) The TEM image of Fe$_2$O$_3$ nanorod with {001} plane, inset shows the lattice fringes and the corresponding SAED pattern; (p,q) The TEM image of Fe$_2$O$_3$ nanorods with {010} plane, inset shows the lattice fringes and the corresponding SAED pattern. (r) Fe$_2$O$_3$ nanosheets in the 1st, 2nd, 20th, 60th and 80th cycles at the rate of 0.2 C, respectively. (s) The rate performances of Fe$_2$O$_3$ nanorods and Fe$_2$O$_3$ nanosheets.*

anode material in LIBs. In this context, binary Tin oxide (SnO), Ternary Tin Oxides (M_2SnO_4 (M = Metal), $ASnO_3$ (A = Ca, Sr, Ba, Co, and Mg), Li_2SnO_3, $A_2Sn_2O_7$ (A = Y or Nd), $K_2(M,Sn)_8O_{16}$ (M = Li, Mg, Fe, Mn, Co, or In), SnP_2O_7, $LiSn_2P_3O_{12}$, $Sn_2P_2O_7$, and $Sn_3P_2O_8$) have been enormously studied. [131–136] For example, Mustain et al.,[137] have designed a SnO_2@rGO anode material in which SnO_2 nanoparticles are uniformly distributed on a reduced graphene oxide network as shown in Fig 1.13 g-j. It was found that the incorporation of Indium (In) into SnO_2 reduces the charge transfer resistance during cycling, prolonging cycle life. It is also stated that the increased conductivity allows the tin oxide conversion and alloying reactions to both be reversible, leading to a very high capacity near 1200 mAh g^{-1}. Finally, the electrodes show excellent rate capability with a capacity of over 200 mAh g^{-1} at 10 C as shown in Fig. 1.13k.

(c) Anodes based on conversion (Redox reactions)

Binary oxides (MO; M = Mn, Fe, Co, Ni, or Cu as anode materials), is primarily reported by the group of Tarasco via the "conversion reaction".[138–140] The type like M_3O_4, (M = Co, Fe, or Mn) like Co_3O_4. Co_3O_4 group of Tarascon, highlighting its cycling stability. Oxides, M_2O_3, with Corundum Structure (M=Fe, Cr or Mn), like α-Fe_2O_3, Cr_2O_3, Metal Dioxides, MO_2 (M=Mn, Mo or Ru), MoO_2, RuO_2 have also been researched under the category of binary oxides as an anode material via redox process.[140–143] For example, Chen et. al.,[144] have shown the effects of crystal faces of Fe_2O_3 on the electrochemical performance of Li-ion batteries. Fe_2O_3 nanorods exposing (001) and (010) plane as well as Fe_2O_3 nanosheets exposing (001) plane have been successfully synthesized. Fe_2O_3 nanosheets exhibit better cycling performance and the rate capabilities than that of Fe_2O_3 nanorods (Fig. 1.13l-q). The discharge capacity of Fe_2O_3 nanosheets can stabilize at 865 mAh g^{-1} at the rate of 0.2C (1C=1000 mA g^{-1}) and 570 mAh g^{-1} at the rate of 1.2 C after 80 cycles, which increased by 90% and 79% compared with 456 mAh g^{-1} and 318 mAh g^{-1} of Fe_2O_3 nanorods. In comparison with (010) plane, the (001) plane of hematite possesses larger packing density of Fe^{3+} and O^{2-}, which is responsible for the superior electrochemical performances of Fe_2O_3 nanosheets than that of Fe_2O_3 nanorods (Fig. 1.13 r and s). Many scientific breakthroughs have already been done in the past decades and many more are in queue, which is still going on.

1.10 Advantages and disadvantages of LIBs

The Li-ion batteries are popular source of energy for a small- and large-scale electronics like cell phones, laptops, and electric vehicles etc. due to their advantages that are listed as follows:

(a) High energy density

(b) Lighter and smaller in shape than other rechargeable batteries

(c) Minimum memory effect

(d) Large open-circuit potential

(e) Huge service life cycle

(f) Lower self-discharge

(g) Easy processability and maintenance

(h) Availability of numerous models of LIB for distinct purposes

Although LIB acquire so many advantageous features, it also shares some limitations that are listed below:

(a) Sensitive to high temperature

(b) Demands protection circuitry

(c) Relatively expensive

(d) Difficult transportation in airlines

(e) Aging issue

(f) Higher maintenance cost

(g) Use of toxic Li metal

(h) Limited power density due to slow charge/discharge process

(i) If the separator gets damaged, the LIB can be explosive

1.11 New generation rechargeable batteries: Ni-Zn battery

The huge safety concern analogous with limited abundance of Li, expensive maintenance and complicated production technology,[145,146] restricts the scope of LIB in high-power applications.[147,148] Currently, multivalent ions such as Zn^{2+}, Mg^{2+}, Al^{3+} based battery systems are progressing as new generation rechargeable battery systems in order to take the position of LIBs for high energy storage technologies. Among these, rechargeable Zn-ion batteries are of particular interest in storage technology due to their worldwide abundance, less redox potential, high theoretical capacity (825 mAh g^{-1}),[149] intrinsically safe and comparable specific energies with Li-ion batteries.[150] Preliminary a number of Zn-based secondary batteries were used such as $Zn-MnO_2$, $Zn-Ni_3Se_2$, $Zn-Co_3O_4$, Zn-

NiCo hydroxide, Zinc-air battery and so on.[151–156] Among all kinds of cathodes, Nickel based cathodes are taking advantage over other cathode materials due to their great quality features. Particularly, numerous Ni-based cathodes are reported like nickel oxides, hydroxides, selenides and phosphides having characteristics like wide electrochemical stability window (~1.8 V), [157–159] great abundance of both Ni and Zn, good reversibility and high normalized specific capacity. Considerable efforts have been made by the scientific community to establish the field of Ni-Zn battery *via* numerous
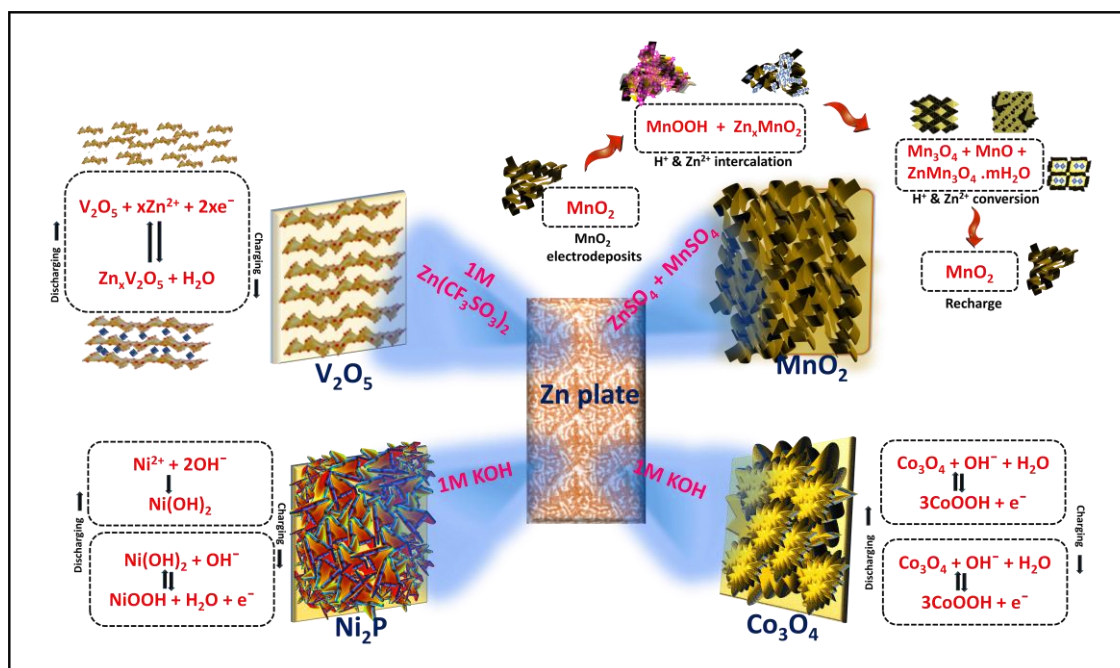
Figure 1.14 *Various cathode materials in Zn-based batteries and their reaction mechanism.*

designing approaches such as (1) formation of hybrid nanostructures through conductive reinforcement, (2) compositional and morphological modification like Ni_3S_2 nanosheet (NS) [153,156,160,161], Ni oxide nanoflakes, cobalt-doped $Ni(OH)_2$ on Ni nanowire array (NAA@CNH), (3) Ni-NiO hetrostructures, and (4) Ni-based compounds *e.g.* NiAlCo-LDH/CNT.

1.11.1 Reaction mechanism in Zn-based battery systems

The most commonly used cathode for zinc ion batteries (ZIBs) is manganese oxide (MnO_2) accompanied by diverse crystal structures. The electrochemical performance and cycling stability of a MnO_2 cathode in ZIBs are strongly dependent on their crystal structure. MnO_2 exists in several crystalline forms that are α-MnO_2, β-MnO_2, and γ-MnO_2 and so on. Although Zn-MnO_2 battery system acquire many advantageous features, but the large irreversible structural transformation and lower open circuit

potential value are the biggest challenges for Zn-MnO$_2$ battery. Vanadium-based cathodes offer good performance than Mn-based cathodes like good stability and diversity in the structures. Vanadium oxides share V-O coordination and can be designed in different units like tetrahedron, square pyramid, trigonal bipyramid, regular octahedron, and distorted octahedron etc.[148,162] The capacity and stability of Zn-V systems are much better than Zn-Mn systems, but the complex reaction kinetics and lower cell voltage (~ 0.75 V) need more improvements in V-based cathodes. Nowadays, Ni-Zn are batteries are on extensive trend due to their high open circuit potential (~1.8 V) and good reversibility of Ni-based cathodes.[163] Co-based system has very easy kinetics and large open circuit potential and good reversibility and more studies are carried out to explore the reaction kinetics of zinc-cobalt oxide (Zn-Co$_3$O$_4$) battery system in different electrolyte systems. So far, zinc-cobalt oxide systems use an alkaline solution like 1.0 M KOH as an electrolyte which results limited discharge capacities, and poor cycling performance. This particular system are reported to show best performance in mild electrolyte medium.[155,164]

The complete reaction kinetics of ZIB system with different cathode materials is shown in Fig. 1.14 with possible reaction occurs at cathode and anode electrodes.

1.11.2 Research progress in Ni-Zn battery till date

Various Ni-based materials such as hydroxides and oxides (α- Ni(OH)$_2$, NiO), sulfides (Ni$_3$S$_2$), phosphides (Ni$_3$P), and their compounds (NiCo$_2$O$_4$) have been explored as a cathode material in Ni-Zn battery. The scientific community has done substantial efforts to achieve great processes in the field of Ni-Zn battery systems. In this section, we highlight the recent advances on rationally designed Ni-based electrodes for Ni-Zn batteries. Initially, Ni(OH)$_2$ in alpha or beta phase was commonly used cathode material in Ni-Zn battery due to the its high diffusion coefficient, cost-effectiveness, and high energy. The possible redox reaction involved at Ni(OH)$_2$ cathode material in Ni-Zn battery is

$$Ni(OH)_2 + 2\,OH^- \longrightarrow 2NiOOH + 2H_2O + 2e^- \qquad (E^0 = 0.49 \text{ V versus SHE})$$
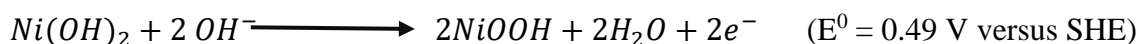
At the initial times of the Ni-Zn battery, Zinc five Ltd has devoted their substantial efforts to commercializing the Ni-Zn battery utilizing β-Ni(OH)$_2$. Later on, in 2015 Huang *et al.* developed a Ni-Zn system with commercial β-Ni(OH)$_2$ cathode and Zn-Al-LDH (layered double oxide) anode which delivers a discharge capacity of 460 mAh g^{-1} and 100% capacitive retention after 1000 cycles. In 2016, Cao and his fellows have designed a prototype of a Ni-Zn battery with a specific capacity of 510 mAh g^{-1}, but it faded up to 120 mAh g^{-1} after 300 cycles. In order to increase the cycling stability of nickel hydroxides, plenty of experimental studies have been done. Among them, one approach is to partially substitute Ni ion from the Ni(OH)$_2$ lattice by any other metal ions like
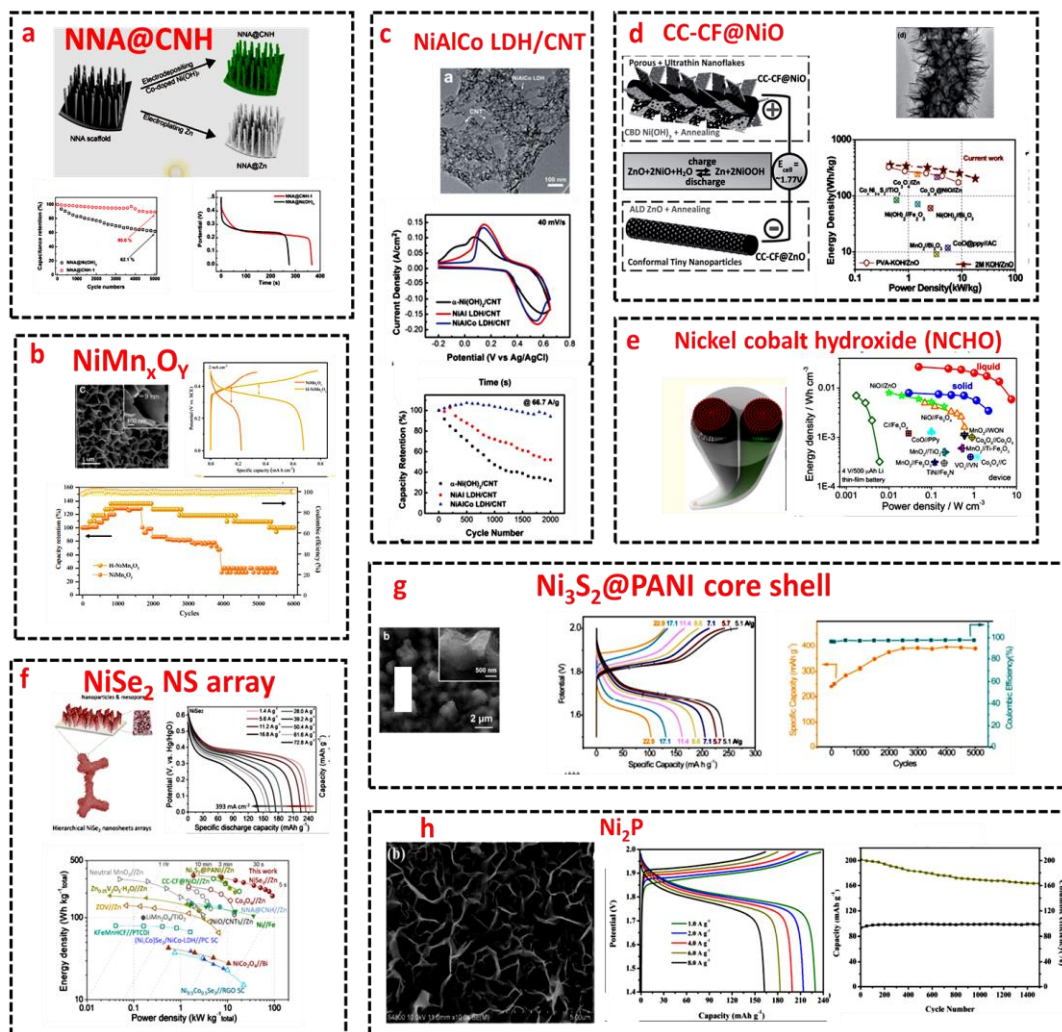
Figure 1.15 *Various cathode materials in Zn-based batteries and their reaction mechanism.*

Al^{3+},[165,166] Fe^{3+},[167] Mn^{4+}, Zn^{2+}, [168] and Co^{2+}. [169] The doped ions in the structure of α-Ni(OH)$_2$ influence the physical and chemical properties of the layer in a positive way, and thus improved the electrochemical behaviour. Indira *et al.* have synthesized a hydrotalcite-like compounds (Ni$_{1-x}$Al$_x$(OH)$_2$(CO$_3$)$_{x/2}$.nH$_2$O {x = 0.1 to 0.25}). The

fabricated compound has prolonged stability in an alkaline medium and delivered 240 mAh g^{-1} specific capacity.[170] Other than Al^{3+} element substitutes, Co^{2+} is considered to be the most effective dopant element to increase the compound stabilizing ability. Recently, in 2016 Wu *et al.* constructed a rechargeable Ni-Zn battery with a cathode material of electrochemically grown Co-doped Ni(OH)$_2$ (named as CNH) as shown in Fig. 1.15a. It was observed that the doped compound shows an increased capacity (~27%) as compared to pristine Ni(OH)$_2$ and 88% capacity retention even after 5000 continuous galvanostatic charge/discharge cycles (Fig. 1.15a).[160] Recently, Liang *et al.* have fabricated H-NiMn$_x$O$_y$ nanosheet via H$_2$ annealing process (Fig. 1.15b). The electrode yield an areal capacity of 0.68 mAh cm^{-2} and extraordinary cycling stability of 6000 cycles, whereas the Ni-Zn battery system display a capacity of 0.68 mAh cm^{-2} and capacity retention of 88.5% after 5500 cycles.[171] Not only single ion doping, two or more metal ions doping simultaneously also have shown tremendous electrochemical response due to the collaborative effect of both the dopants. Gong *et al.* in 2014 introduced a cathode material *i.e.,* NiAlCo-layered double hydroxide nanoplates (LDH) connected to carbon nanotubes "NiAlCo LDH/CNT" for a rechargeable Ni-Zn battery system. It can be seen from Fig. 1.15c, CNTs were well attached to the NiAlCo LDH. Furthermore, Al doping in the structure suggests high specific capacity as compared to undoped sample, it is due to that Al doping decrease the difference between reduction and oxidation potential and increases the area under the CV curve. Figure 1.15c illustrates that the specific capacity retains approximately 94% in NiAlCo-LDH/CNT, 50% in NiAl-LDH/CNT, and 40% in undoped α-Ni(OH)$_2$/CNT. The extreme stability in NiAlCo LDH material could be attributed to the synergistic effect of Co-doped Al and Co.[172]

Liu et al. have shared a Ni-Zn system with an OCP of 1.77 V by designing NiO nanoflakes on a 3D hierarchical carbon-cloth nanofibers cathode. The highly porous structure of NiO (Fig. 1.15d) enables easy electrolytic ionic dynamics and fast ion-mass transportation. The assembled solid-state CC-CF@NiO//CC-CF@ZnO (Fig. 1.15d) yields a high energy density of 323.3 Wh kg^{-1}. [153] In 2017, Huang *et al.* fabricate a wearable Ni/Co-Zn battery system with electrodeposited nickel-cobalt hydroxide (NCHO) and Zn on conductive yarns. They acquire both battery level capacity and energy density as well as compete for power density as supercapacitors. They deliver high specific capacity of 5 mAh cm^{-3} and energy densities of 0.12 mWh cm^{-2} and endows excellent power density of 32.8 mW cm^{-2} (Fig. 1.15e). [173]

Nowadays, the sulfides, phosphides, and selenide structure of nickel are also showing their potential in the Ni-Zn battery system. Recently, Zhou et al. have proposed a hierarchical $NiSe_2$ nanosheet array (Fig. 1.15f) as a cathode electrode. This unique structure of $NiSe_2$ endows a remarkable specific capacity of 245.1 mAh g^{-1} and an excellent rate capability of 58% capacity retention even at a very high current density of 72.8 A g^{-1} and 10,000 cycle stability without any capacity degradation. The as-prepared $NiSe_2$//Zn battery acquires record-high power density (91.22 kW kg^{-1}), and superior energy density (328.8 Wh kg^{-1}) (Fig. 1.15f).[163] Similarly, Lu et al. developed a new binder-free Ni_3S_2@polyaniline (PANI) core-shell structure as a robust cathode electrode that can deliver a high reversible capacity of 242.8 mAh g^{-1} in Ni-Zn system and 100% capacity stability after 5000 cycles (Fig. 1.15g).[174] Wan et al. have synthesized hierarchical porous structure of Ni_2P via a phosphorization process and employed it as cathode material in Ni-Zn battery showing excellent electrochemical performance such as the high operating voltage of 1.78 V (Fig. 1.15h), the specific capacity of 231 mAh g^{-1}, and energy density of 318 Wh Kg^{-1}. Additionally, this system maintains specific capacity retention of ~ 80% even after 1500 continuous cycles. [175]

1.12 Advantages and drawbacks of Ni-Zn battery

The generalized advantages and disadvantages of Ni-Zn battery system are described in Table 1.3:

Table 1.3 The advantages and disadvantages of Ni-Zn battery system

1.13

Battery-supercapacitor Technology and its research highlights

Sr. No.	Advantages	Disadvantages
1.	Fast recharge capability	Relatively low volumetric energy density
2.	Good specific energy	Higher cost than lead-acid
3.	Low environmental impact	Self-discharge rate after 40-50 cycles
4.	Good cycle life	
5.	Abundant raw material	
6.	Sealed maintenance-free design	
7.	Excellent stability of Ni electrode	

As explained earlier in section 1.2.2, battery-supercapacitor hybrid system acquires both merits of both supercapacitor with extreme rate capability and battery high energy density. As discussed, variety of work has already been done in this field of metal-ion capacitor and BSH system which is explained in Table 1.4 and 1.5.

Table 1.4 *Scientific research highlights and the output electrochemical performance of various metal-ion capacitors with different cathode materials.*

Sr. No.	Cathode	Anode	Pot. window	Separator	Electrolyte	Capacity/capacitance	ED	PD	Cycle stability	Reference
1	Kelp-carbon	Zn plate	0-1.7 V	Polypropylene film (MPF30, NKK)	2 M $Zn(CF_3SO_3)_2$	196.7 mAh g^{-1} at 0.1 A g^{-1}	8.2 µWh cm^{-2}		4000 (90%)	176
2.	Activated carbon (AC)	Thin walled zinc (TW Zn)	0.2-1.8 V	-	2 M $ZnSO_4$	421 F g^{-1} at 0.5 A g^{-1}			3000 (94%)	177
3.	AC	V_2O_5 (Zn/FTO/ Ag/V_2O_5) photoanode	0-1.7 V	Whatman glass microfiber filter paper	3 M $Zn(CF_3SO_3)_2$	~90 mAh g^{-1}	53.13 Wh Kg^{-1}	1384 W Kg^{-1}	4000 (99%)	178
4.	$Ti_3C_2T_x$/ $BiCuS_{2.5}$	Zn foil	-1.4 - 0.6 V in 3 electrode)		2 M $ZnSO_4$	746 C g^{-1}	298.4 Wh Kg^{-1}	7200 W Kg^{-1}	10,000 (82%)	179
5.	Porous carbon nanoflakes	Zn foil	0.1 – 1.7 V	Used a separator (coin cell)	2 M $ZnSO_4$	-	142 Wh	15390 W Kg^{-1}	10,000 (90%)	180

							Kg^{-1}			
6	AC (ZIC) V$_2$O$_5$ (ZIB)	Zn@CNTs	0.2 - 1.8 V (ZICs) 0.2- 1.6 V (ZIBs)	Air-laid paper	2 M Zn(CF$_3$SO$_3$)$_2$	(277 mAh g^{-1} at 0.1 A g^{-1}			7000 (ZIC) 2000 (ZIB)	181
7.	MXene		0.01-1 V (3 Electrode system)	---	ZnSO$_4$	82 mAh g-1 at 20 A g-1)	----	----	1000	182
8.	Molten salt assisted Porous carbon (MSPC)	Zn foil	0-1.7 V	---	2 M ZnSO$_4$	136 mAh g-1 at 0.68 A g-1	36.5 Wh Kg^{-1}	376 W Kg^{-1}	10000 (85 %)	183
9.	Mesoporous AC	Zn foil	0.3-1.8 V		2 M ZnSO$_4$	176 mAh g^{-1}	188 Wh kg^{-1}	10,666 W kg^{-1}	40,000 at 10 A g-1 (78 %)	184
10.	AC	Modified Zn	0.3-1.8 V		2 M ZnSO$_4$	353 F g^{-1} at 0.5 A g^{-1}	125 Wh kg^{-1}	8000 W kg^{-1}	2000 (99 %)	185
8.	Molten salt assisted Porous carbon (MSPC)	Zn foil	0-1.7 V	---	2 M ZnSO$_4$	136 mAh g-1 at 0.68 A g-1	36 Wh Kg^{-1}	376 W Kg^{-1}	10000 (85 %)	183

ZIC- Zinc ion capacitor, AC- activated carbon, CNT – carbon

Table 1.5 *Scientific research highlights of various BSH systems.*

Sr. No.	Anode	Cathode	Electrolyte	window	capacity	Energy density	Power density	Cycle stabiity	Ref.
1	Co-Cd-Se on Ni foam	AC	2 M KOH	2.2 V	124 mAh g^{-1} at 20 A g-1	68 Wh kg^{-1}	1.20 kW kg^{-1}	1000 (80.9%)	186
2	Ni-MOF	CNTs-COOH	3 M KOH +0.1 M K$_4$Fe(CN)$_6$	1.4 V	--	55.8Wh kg^{-1}	7000 W Kg^{-1}	--	187
3	MoSe$_2$ in carbon fibre	AC	0.8 M KPF$_6$ K-ion battery coin cell	3 V	316 mAh g$_{-1}$ for single electrode 81 mAh g$_{-1}$ at 100 mA g-1 in hybrid	--	--	100	188
4	Fe$_3$O$_4$-C	CNTs	3M KOH	1.7 V	7776.36 C cm^{-3} (247.5 mAh g$_{-1}$)	1.56 mWh cm$_{-3}$	0.028 W cm$_{-3}$	2000 (83%), 5000 (64%)	189
5	Ni$_{12}$P$_5$	AC	6M KOH	1.6 V	707.2 C g^{-1}	108.2 Wh kg^{-1}	8.96 k W kg^{-1}	1000	190
6	S-Co$_3$O$_4$@NiCo$_2$S$_4$	AC	6 M KOH	1.5 V	10.9 mAh cm^{-2}			5000 (97.3%)	191
7	NiS/SnS$_2$ @CC	Fe$_2$O$_3$/rGO@CC	6 M KOH	1.6 V	430.38 mAh g^{-1}	104.23 Wh kg^{-1}	301 W kg^{-1}	1000 (82%)	192

8	GF@Bi$_2$O$_3$-NCs	GF@NS-CAG	1M KOH	2.3 V	103 mAh g^{-1}	118 Wh kg^{-1}	--	10,000 (95.7%)	193
9	CoCo$_2$O$_4$	CNT	KOH	-	206 mAh g^{-1}	26.8 Wh kg^{-1}	775.4 W kg^{-1}	8000 (82.3%)	194
10	NiCoSe-1	AC	1M KOH	1.7 V	164.4 mAh g^{-1}	37.54 Wh kg^{-1}	842.7 W kg^{-1}	3000 (89.5%)	195

AC- activated carbon, MOF-metal organic framework, C-carbon, CC- carbon cloth, NC- N-doped carbon, CNT- carbon Nanotube

1.14 Objective and outlook of the thesis

For the development of portable electronics and miniature devices for commercial trade, an energy storage system with full of power and high energy density is in high demand. Graphene macrostructures as an electrode material are emerging in this field due to their remarkable properties. The present study is focused on the exploration of such electrode materials with the facile synthetic process, their morphological advances and utilization in metal-free planar structured solid energy storage systems. The present study also includes the development of hybrid systems with optimum energy density and power density and making them commercially viable in the storage technology.

The presently supercapacitors have a major drawback in respect of their poor life span and low energy density. Numerous efforts have been realized in the direction of electrode designing, electrolyte modification, and dealing with mixed kinetic of battery and supercapacitor to enhance the energy density, power density and cycling stability. The present investigation includes the development of high-quality graphene film, which has the ability to replace metals from the energy device and exhibits high effective surface area in order to increase the charge storage capacity.

Chapter 1 gives brief introduction about electrochemical energy storage systems and their need. How the different storage kinetics (i.e., diffusion-controlled and surface-controlled processes) influence the electrode material electrochemical performance, are briefly discussed. The criteria for the selection of electroactive material and device performance are well explained.

In ***Chapter 3***, a new synthesis strategy scheme opted for the fabrication of conductive graphene film with unique structural features *i.e.,* electrochemical reduction followed by

laser-irradiation method. The resulting graphene sheet was utilized to make a metal-free, robust microsupercapacitor in order to achieve extraordinary cycling stability.

The prepared metal-free graphene-based microsupercapacitor was although of best cycling stability, but the specific capacitance and energy density of the device was not sufficient.

In order to improve the charge storage capacity, a conductive polymer *i.e.,* polypyrrole (PPy) having pseudocapacitive properties was added with electric double-layer capacitive graphene material *i.e.*

LIG-PPy and a "Organic/Water-in-salt" type electrolyte ($^{7\ m\ LiTFSI}$AWIS) was chosen to increase the electrochemical stability window, highlighted in ***Chapter 4.***

Chapter 5 of the thesis include the fabrication of rechargeable Ni-Zn battery system with $Ni_3P@CC*$ as a cathode and $Zn@CC*$ as an anode material. A thorough electrochemical study was carried out to check the performance of Ni-Zn battery system.

Since, the response of Ni-Zn battery system was moderately good in terms of its stability performance, a Li-ion battery (LIB) system was explored in ***Chapter 6*** of this thesis with mix phase $SnO-SnO_2@rGO$ electrode and investigated the electrochemical performance in both half-cell and full cell. It is satisfying to note that the resulting LIB shows tremendous reversible specific capacity and cycling stability.

Chapter 7 of the thesis includes an in-plane solid-state hybrid system of battery and supercapacitor was investigated via combining LIG-PPy as supercapacitive material and LIG-MnO_2 as battery-type material.

Finally, the conclusions of the thesis work are discussed in ***Chapter 8*** and the possibilities of the future work based on the thesis work are given.

1.15 References

1   B. Looney, *Rev. World Energy data*, 2021, **70**, 8–20.

2   M. T. Islam, S. A. Shahir, T. M. I. Uddin and A. Z. A. Saifullah, *Renew. Sustain. Energy Rev.*, 2014, **39**, 1074–1088.

3   S. Dahlke, J. Sterling and C. Meehan, ed. A. K. B. T.-A. in C. E. T. Azad, Academic Press, 2021, pp. 451–485.

4   J. Shalf, *Philos. Trans. R. Soc. A Math. Phys. Eng. Sci.*, 2020, **378**, 20190061.

5   L. L. Zhang and X. S. Zhao, *Chem. Soc. Rev.*, 2009, **38**, 2520–2531.

6   H. Helmholtz, *Ann. Phys.*, 1853, **165**, 211–233.

7   M. Gouy, *J. Phys. Theor. Appl.*, 1910, **9**, 457–468.

8   D. L. Chapman, *London, Edinburgh, Dublin Philos. Mag. J. Sci.*, 1913, **25**, 475–481.

9   O. Stern, *Zeitschrift für Elektrochemie und Angew. Phys. Chemie*, 1924, **30**, 508–516.

10   B. E. Conway, ed. B. E. Conway, Springer US, Boston, MA, 1999, pp. 67–86.

11   B. E. Conway, ed. B. E. Conway, Springer US, Boston, MA, 1999, pp. 221–257.

12   E. Herrero, L. J. Buller and H. D. Abruña, *Chem. Rev.*, 2001, **101**, 1897–1930.

13   V. Khomenko, E. Raymundo-Piñero and F. Béguin, *J. Power Sources*, 2010, **195**, 4234–4241.

14   J. P. Zheng, P. J. Cygan and T. R. Jow, *J. Electrochem. Soc.*, 1995, **142**, 2699–2703.

15   A. Ghosh, E. J. Ra, M. Jin, H.-K. Jeong, T. H. Kim, C. Biswas and Y. H. Lee, *Adv. Funct. Mater.*, 2011, **21**, 2541–2547.

16   T. Cottineau, M. Toupin, T. Delahaye, T. Brousse and D. Bélanger, *Appl. Phys. A*, 2006, **82**, 599–606.

17   J. Hu, H. Wang and X. Huang, *Electrochim. Acta*, 2012, **74**, 98–104.

18   A. Ponrouch, J. Bitenc, R. Dominko, N. Lindahl, P. Johansson and M. R. Palacin, *Energy Storage Mater.*, 2019, **20**, 253–262.

19   K. Bradbury, *Energy Storage Technol. Rev. Duke Univ. Durham, NC, USA*, 2010, 1–34.

20   C. Romanitan, P. Varasteanu, I. Mihalache, D. Culita, S. Somacescu, R. Pascu, E. Tanasa, S. A. V Eremia, A. Boldeiu, M. Simion, A. Radoi and M. Kusko, *Sci. Rep.*, 2018, **8**, 9654.

21   X. Sun, X. Zhang, H. Zhang, D. Zhang and Y. Ma, *J. Solid State Electrochem.*, 2012, **16**, 2597–2603.

22   Y. Wang, L. Yu and Y. Xia, *J. Electrochem. Soc.*, 2006, **153**, A743.

23   P. Gómez-Romero, O. Ayyad, J. Suárez-Guevara and D. Muñoz-Rojas, *J. Solid State Electrochem.*, 2010, **14**, 1939–1945.

24   M. Mastragostino, C. Arbizzani and F. Soavi, *Solid State Ionics*, 2002, **148**, 493–498.

25   K. Kierzek, E. Frackowiak, G. Lota, G. Gryglewicz and J. Machnikowski, *Electrochim. Acta*, 2004, **49**, 515–523.

26   E. Raymundo-Piñero, K. Kierzek, J. Machnikowski and F. Beguin, *Carbon N. Y.*, 2006, **44**, 2498–2507.

27   B. Kastening and S. Spinzig, *J. Electroanal. Chem. Interfacial Electrochem.*, 1986, **214**, 295–302.

28   R. Raccichini, A. Varzi, S. Passerini and B. Scrosati, *Nat. Mater.*, 2015, **14**, 271–279.

29   M. F. El-Kady and R. B. Kaner, *Nat. Commun.*, 2013, **4**, 1475.

30   N. A. Kyeremateng, T. Brousse and D. Pech, *Nat. Nanotechnol.*, 2017, **12**, 7–15.

31   J. Xia, F. Chen, J. Li and N. Tao, *Nat. Nanotechnol.*, 2009, **4**, 505–509.

32   T. J. Booth, P. Blake, R. R. Nair, D. Jiang, E. W. Hill, U. Bangert, A. Bleloch, M. Gass, K. S. Novoselov, M. I. Katsnelson and A. K. Geim, *Nano Lett.*, 2008, **8**, 2442–2446.

33   C. Lee, X. Wei, J. W. Kysar and J. Hone, *Science*, 2008, **321**, 385–388.

34   J. Liang, Y. Huang, L. Zhang, Y. Wang, Y. Ma, T. Guo and Y. Chen, *Adv. Funct. Mater.*, 2009, **19**, 2297–2302.

35   C. Liu, Z. Yu, D. Neff, A. Zhamu and B. Z. Jang, *Nano Lett.*, 2010, **10**, 4863–4868.

36   X. Huang, X. Qi, F. Boey and H. Zhang, *Chem. Soc. Rev.*, 2012, **41**, 666–686.

37   K. S. Kim, Y. Zhao, H. Jang, S. Y. Lee, J. M. Kim, K. S. Kim, J.-H. Ahn, P. Kim, J.-Y. Choi and B. H. Hong, *Nature*, 2009, **457**, 706–710.

38   Z. Yin, S. Sun, T. Salim, S. Wu, X. Huang, Q. He, Y. M. Lam and H. Zhang, *ACS Nano*, 2010, **4**, 5263–5268.

39   X. Xie, L. Qu, C. Zhou, Y. Li, J. Zhu, H. Bai, G. Shi and L. Dai, *ACS Nano*, 2010, **4**, 6050–6054.

40   D. A. C. Brownson, D. K. Kampouris and C. E. Banks, *J. Power Sources*, 2011, **196**, 4873–4885.

41   M. Pumera, *Chem. Soc. Rev.*, 2010, **39**, 4146–4157.

42   P. Simon and Y. Gogotsi, *Nat. Mater.*, 2008, **7**, 845–854.

43   T. Ohta, A. Bostwick, T. Seyller, K. Horn and E. Rotenberg, *Science*, 2006, **313**, 951–954.

44   N. G. Shang, P. Papakonstantinou, M. McMullan, M. Chu, A. Stamboulis, A. Potenza, S. S. Dhesi and H. Marchetto, *Adv. Funct. Mater.*, 2008, **18**, 3506–3514.

45   L. Jiao, L. Zhang, X. Wang, G. Diankov and H. Dai, *Nature*, 2009, **458**, 877–880.

46   A. Ambrosi, T. Sasaki and M. Pumera, *Chem. Asian J.*, 2010, **5**, 266–271.

47   N. K. S., G. A. K., M. S. V., J. D., Z. Y., D. S. V., G. I. V. and F. A. A., *Science*, 2004, **306**, 666–669.

48   C. Berger, Z. Song, T. Li, X. Li, A. Y. Ogbazghi, R. Feng, Z. Dai, A. N. Marchenkov, E. H. Conrad, P. N. First and W. A. de Heer, *J. Phys. Chem. B*, 2004, **108**, 19912–19916.

49   Y. H. Kwon, S. Kumar, J. Bae and Y. Seo, *Nanotechnology*, 2018, **29**, 195404.

50   X. Li, G. Zhang, X. Bai, X. Sun, X. Wang, E. Wang and H. Dai, *Nat. Nanotechnol.*, 2008, **3**, 538–542.

51   S. L. Kim, J.-H. Hsu and C. Yu, *Nano Energy*, 2018, **48**, 582–589.

52   H. Zhang, V. V Bhat, N. C. Gallego and C. I. Contescu, *ACS Appl. Mater. Interfaces*, 2012, **4**, 3239–3246.

53   N. Liu, F. Luo, H. Wu, Y. Liu, C. Zhang and J. Chen, *Adv. Funct. Mater.*, 2008, **18**, 1518–1525.

54   Y. Yuan, L. Jiang, X. Li, P. Zuo, C. Xu, M. Tian, X. Zhang, S. Wang, B. Lu, C. Shao, B. Zhao, J. Zhang, L. Qu and T. Cui, *Nat. Commun.*, 2020, **11**, 6185.

55   Q. Liu, Q. Shi, H. Wang, Q. Zhang and Y. Li, *RSC Adv.*, 2015, **5**, 47074–47079.

56   M. R. R. Abdul-Aziz, A. Hassan, A. Abdel-Aty, M. Saber, R. Ghannam, B. Anis, H. Heidari and A. Khalil, *IEEE Access*, , DOI:10.1109/ACCESS.2020.3035828.

57   M. Naguib, J. Halim, J. Lu, K. M. Cook, L. Hultman, Y. Gogotsi and M. W. Barsoum, *J. Am. Chem. Soc.*, 2013, **135**, 15966–15969.

58   V. Augustyn, J. Come, M. A. Lowe, J. W. Kim, P.-L. Taberna, S. H. Tolbert, H. D. Abruña, P. Simon and B. Dunn, *Nat. Mater.*, 2013, **12**, 518–522.

59   T. Brezesinski, J. Wang, S. H. Tolbert and B. Dunn, *Nat. Mater.*, 2010, **9**, 146–151.

60   X.-H. Xia, J.-P. Tu, X.-L. Wang, C.-D. Gu and X.-B. Zhao, *Chem. Commun.*, 2011, **47**, 5786–5788.

61   P. Forouzandeh and S. C. Pillai, *Curr. Opin. Chem. Eng.*, 2021, **33**, 100710.

62   T. N. Jebakumar Immanuel Edison, R. Atchudan and Y. Lee, *Int. J. Hydrogen Energy*, , DOI:10.1016/j.ijhydene.2018.02.018.

63   J. Xu, Q. Wang, X. Wang, Q. Xiang, B. Liang, D. Chen and G. Shen, *ACS Nano*, 2013, **7**, 5453–5462.

64   C. Zhu, P. Yang, D. Chao, X. Wang, X. Zhang, S. Chen, B. K. Tay, H. Huang, H. Zhang, W. Mai and H. J. Fan, *Adv. Mater.*, 2015, **27**, 4566–4571.

65   Y. Wu, Y. Yang, X. Zhao, Y. Tan, Y. Liu, Z. Wang and F. Ran, *Nano-Micro Lett.*, 2018, **10**, 63.

66   S. Ghosh, S. M. Jeong and S. R. Polaki, *Korean J. Chem. Eng.*, 2018, **35**, 1389–1408.

67   P. Pande, P. G. Rasmussen and L. T. Thompson, *J. Power Sources*, 2012, **207**, 212–215.

68   J. Huang, K. Wang and Z. Wei, *J. Mater. Chem.*, 2010, **20**, 1117–1121.

69   H.-P. Cong, X.-C. Ren, P. Wang and S.-H. Yu, *Energy Environ. Sci.*, 2013, **6**, 1185–1191.

70   B. Anothumakkool, R. Soni, S. N. Bhange and S. Kurungot, *Energy Environ. Sci.*, 2015, **8**, 1339–1347.

71   R. K. Sharma, A. C. Rastogi and S. B. Desu, *Electrochim. Acta*, 2008, **53**, 7690–7695.

72   A. Moyseowicz and G. Gryglewicz, *Electrochim. Acta*, 2020, **354**, 136661.

73   J. Cao, Y. Wang, J. Chen, X. Li, F. C. Walsh, J.-H. Ouyang, D. Jia and Y. Zhou, *J. Mater. Chem. A*, 2015, **3**, 14445–14457.

74   G.-Y. Yu, W.-X. Chen, Y.-F. Zheng, J. Zhao, X. Li and Z.-D. Xu, *Mater. Lett.*, 2006, **60**, 2453–2456.

75   S. Liumin, B. Oleg, G. Tao, O. Marco, H. Janet, F. Xiulin, L. Chao, W. Chunsheng and X. Kang, *Science*, 2015, **350**, 938–943.

76   A. Eftekhari, *Adv. Energy Mater.*, 2018, **8**, 1801156.

77   X. Chen, X. Zhang, H. Li and Q. Zhang, *Batter. Supercaps*, 2019, **2**, 128–131.

78   O. Borodin, L. Suo, M. Gobet, X. Ren, F. Wang, A. Faraone, J. Peng, M. Olguin, M. Schroeder, M. S. Ding, E. Gobrogge, A. von Wald Cresce, S. Munoz, J. A. Dura, S. Greenbaum, C. Wang and K. Xu, *ACS Nano*, 2017, **11**, 10462–10471.

79   L. Suo, D. Oh, Y. Lin, Z. Zhuo, O. Borodin, T. Gao, F. Wang, A. Kushima, Z. Wang, H.-C. Kim, Y. Qi, W. Yang, F. Pan, J. Li, K. Xu and C. Wang, *J. Am. Chem. Soc.*, 2017, **139**, 18670–18680.

80   X. Yan, X. Zhao, C. Liu, S. Wang, Y. Zhang, M. Guo, Y. Wang, L. Dai and X. Yang, *J. Power Sources*, 2019, **423**, 331–338.

81   S. Kang, K. Lim, H. Park, J. B. Park, S. C. Park, S.-P. Cho, K. Kang and B. H. Hong, *ACS Appl. Mater. Interfaces*, 2018, **10**, 1033–1038.

82   L. Zhang, D. DeArmond, N. T. Alvarez, R. Malik, N. Oslin, C. McConnell, P. K. Adusei, Y.-Y. Hsieh and V. Shanov, *Small*, 2017, **13**, 1603114.

83   J. Ye, H. Tan, S. Wu, K. Ni, F. Pan, J. Liu, Z. Tao, Y. Qu, H. Ji, P. Simon and Y. Zhu, *Adv. Mater.*, 2018, **30**, e1801384.

84   Y. Zhang, L. Shi, D. Hu, S. Chen, S. Xie, Y. Lu, Y. Cao, Z. Zhu, L. Jin, B.-O. Guan, S. Rogge and X. Li, *Nanoscale Horizons*, 2019, **4**, 601–609.

85   Y. Zhang, L. Guo, S. Wei, Y. He, H. Xia, Q. Chen, H.-B. Sun and F.-S. Xiao, *Nano Today*, 2010, **5**, 15–20.

86   D. S. Bergsman, B. A. Getachew, C. B. Cooper and J. C. Grossman, *Nat. Commun.*, 2020, **11**, 3636.

87   G. Wang, Z. Yang, X. Li and C. Li, *Carbon N. Y.*, 2005, **43**, 2564–2570.

88   Z. Wan, S. Wang, B. Haylock, J. Kaur, P. Tanner, D. Thiel, R. Sang, I. S. Cole, X. Li, M. Lobino and Q. Li, *Carbon N. Y.*, 2019, **141**, 83–91.

89   L. Huang, Y. Liu, L.-C. Ji, Y.-Q. Xie, T. Wang and W.-Z. Shi, *Carbon N. Y.*, 2011, **49**, 2431–2436.

90   Y. Hu, H. Cheng, F. Zhao, N. Chen, L. Jiang, Z. Feng and L. Qu, *Nanoscale*, 2014, **6**, 6448–6451.

91   J. Lin, Z. Peng, Y. Liu, F. Ruiz-Zepeda, R. Ye, E. L. G. Samuel, M. J. Yacaman, B. I. Yakobson and J. M. Tour, *Nat. Commun.*, 2014, **5**, 5714.

92   Z. Zhang, M. Song, J. Hao, K. Wu, C. Li and C. Hu, *Carbon N. Y.*, 2018, **127**, 287–296.

93   A. Lamberti, M. Serrapede, G. Ferraro, M. Fontana, F. Perrucci, S. Bianco, A. Chiolerio and S. Bocchini, *2D Mater.*, 2017, **4**, 35012.

94   R. Ye, Y. Chyan, J. Zhang, Y. Li, X. Han, C. Kittrell and J. M. Tour, *Adv. Mater.*, 2017, **29**, 1702211.

95   W. Zhang, Y. Lei, F. Ming, Q. Jiang, P. M. F. J. Costa and H. N. Alshareef, *Adv. Energy Mater.*, 2018, **8**, 1801840.

96   V. Strauss, K. Marsh, M. D. Kowal, M. El-Kady and R. B. Kaner, *Adv. Mater.*, 2018, **30**, 1704449.

97   J. Cabana, L. Monconduit, D. Larcher and M. R. Palacín, *Adv. Mater.*, 2010, **22**, 170–192.

98   B. Scrosati, *Electrochim. Acta*, 2000, **45**, 2461–2466.

99   Y. Gogotsi and P. Simon, *Science*, 2011, **334**, 917–918.

100   J. Cho, Y. J. Kim and B. Park, *Chem. Mater.*, 2000, **12**, 3788–3791.

101   Z. Wang, Y. Sun, L. Chen and X. Huang, *J. Electrochem. Soc. - J Electrochem SOC*, , DOI:10.1149/1.1740781.

102   C. Venkateswara Rao, A. Leela Mohana Reddy, Y. Ishikawa and P. M. Ajayan, *ACS Appl. Mater. Interfaces*, 2011, **3**, 2966–2972.

103   S.-W. Song, G. V Zhuang and P. N. Ross, *J. Electrochem. Soc.*, 2004, **151**, A1162.

104   H. Y. Tran, G. Greco, C. Täubert, M. Wohlfahrt-Mehrens, W. Haselrieder and A. Kwade, *J. Power Sources*, 2012, **210**, 276–285.

105   S.-Y. Chung, J. T. Bloking and Y.-M. Chiang, *Nat. Mater.*, 2002, **1**, 123–128.

106   J. M. Tarascon, W. R. McKinnon, F. Coowar, T. N. Bowmer, G. Amatucci and D. Guyomard, *J. Electrochem. Soc.*, 1994, **141**, 1421–1431.

107   J. W. Long, B. Dunn, D. R. Rolison and H. S. White, *Chem. Rev.*, 2004, **104**, 4463–4492.

108   S. Goriparti, E. Miele, F. De Angelis, E. Di Fabrizio, R. Proietti Zaccaria and C. Capiglia, *J. Power Sources*, 2014, **257**, 421–443.

109   B. J. Landi, M. J. Ganter, C. D. Cress, R. A. DiLeo and R. P. Raffaelle, *Energy Environ. Sci.*, 2009, **2**, 638–654.

110   L. Qie, W.-M. Chen, Z.-H. Wang, Q.-G. Shao, X. Li, L.-X. Yuan, X.-L. Hu, W.-X. Zhang and Y.-H. Huang, *Adv. Mater.*, 2012, **24**, 2047–2050.

111   F. Su, Y.-B. He, B. Li, X.-C. Chen, C.-H. You, W. Wei, W. Lv, Q.-H. Yang and F. Kang, *Nano Energy*, 2012, **1**, 429–439.

112   A. Ambrosi, C. K. Chua, A. Bonanni and M. Pumera, *Chem. Rev.*, 2014, **114**, 7150–7188.

113   Y. Fang, Y. Lv, R. Che, H. Wu, X. Zhang, D. Gu, G. Zheng and D. Zhao, *J. Am. Chem. Soc.*, 2013, **135**, 1524–1530.

114   A. Stein, Z. Wang and M. Fierke, *Adv. Mater.*, 2009, **21**, 265–293.

115   H. Wu, G. Chan, J. W. Choi, I. Ryu, Y. Yao, M. T. McDowell, S. W. Lee, A. Jackson, Y. Yang, L. Hu and Y. Cui, *Nat. Nanotechnol.*, 2012, **7**, 310–315.

116   C.-M. Park, J.-H. Kim, H. Kim and H.-J. Sohn, *Chem. Soc. Rev.*, 2010, **39**, 3115–3141.

117   M. Miyachi, H. Yamamoto, H. Kawai, T. Ohta and M. Shirakata, *J. Electrochem. Soc.*, 2005, **152**, A2089.

118   I. Yoshio, K. Tadahiko, M. Akihiro, M. Yukio and M. Tsutomu, *Science*, 1997, **276**, 1395–1397.

119   D.-J. Xue, S. Xin, Y. Yan, K.-C. Jiang, Y.-X. Yin, Y.-G. Guo and L.-J. Wan, *J. Am. Chem. Soc.*, 2012, **134**, 2512–2515.

120   M.-H. Seo, M. Park, K. T. Lee, K. Kim, J. Kim and J. Cho, *Energy Environ. Sci.*, 2011, **4**, 425–428.

121   K. Lee, A. Mazare and P. Schmuki, *Chem. Rev.*, 2014, **114**, 9385–9454.

122   L. Ji, Z. Lin, M. Alcoutlabi and X. Zhang, *Energy Environ. Sci.*, 2011, **4**, 2682–2699.

123   J. L. C. Rowsell, V. Pralong and L. F. Nazar, *J. Am. Chem. Soc.*, 2001, **123**, 8598–8599.

124   Z. Yang, D. Choi, S. Kerisit, K. M. Rosso, D. Wang, J. Zhang, G. Graff and J. Liu, *J. Power Sources*, 2009, **192**, 588–598.

125   T. Fröschl, U. Hörmann, P. Kubiak, G. Kučerová, M. Pfanzelt, C. K. Weiss, R. J. Behm, N. Hüsing, U. Kaiser, K. Landfester and M. Wohlfahrt-Mehrens, *Chem. Soc. Rev.*, 2012, **41**, 5313–5360.

126   M. Søndergaard, Y. Shen, A. Mamakhel, M. Marinaro, M. Wohlfahrt-Mehrens, K. Wonsyld, S. Dahl and B. B. Iversen, *Chem. Mater.*, 2015, **27**, 119–126.

127   J.-F. Colin, V. Pralong, V. Caignaert, M. Hervieu and B. Raveau, *Inorg. Chem.*, 2006, **45**, 7217–7223.

128   S. Patoux and C. Masquelier, *Chem. Mater.*, 2002, **14**, 5057–5068.

129   M. A. Reddy, M. S. Kishore, V. Pralong, V. Caignaert, U. V. Varadaraju and B. Raveau, *Chem. Mater.*, 2008, **20**, 2192–2197.

130   T.-F. Yi, L.-J. Jiang, J. Shu, C.-B. Yue, R.-S. Zhu and H.-B. Qiao, *J. Phys. Chem. Solids*, 2010, **71**, 1236–1242.

131   N. Sharma, G. V Subba Rao and B. V. R. Chowdari, *J. Power Sources*, 2006, **159**, 340–344.

132   N. Sharma, J. Plévert, G. V Subba Rao, B. V. R. Chowdari and T. J. White, *Chem. Mater.*, 2005, **17**, 4700–4710.

133   Y. W. Xiao, J. Y. Lee, A. S. Yu and Z. L. Liu, *J. Electrochem. Soc.*, 1999, **146**, 3623–3629.

134   I. A. Courtney and J. R. Dahn, *J. Electrochem. Soc.*, 1997, **144**, 2045–2052.

135   Y. Sharma, N. Sharma, G. V Subba Rao and B. V. R. Chowdari, *Chem. Mater.*, 2008, **20**, 6829–6839.

136   F. Belliard, P. A. Connor and J. T. S. Irvine, *Solid State Ionics*, 2000, **135**, 163–167.

137   Y. Liu, A. Palmieri, J. He, Y. Meng, N. Beauregard, S. L. Suib and W. E. Mustain, *Sci. Rep.*, 2016, **6**, 25860.

138   S. Grugeon, S. Laruelle, L. Dupont and J.-M. Tarascon, *Solid State Sci.*, 2003, **5**, 895–904.

139   P. Poizot, S. Laruelle, S. Grugeon, L. Dupont and J.-M. Tarascon, *J. Power Sources*, 2001, **97–98**, 235–239.

140   P. Poizot, S. Laruelle, S. Grugeon, L. Dupont and J.-M. Tarascon, *Nature*, 2000, **407**, 496–499.

141   D. Larcher, C. Masquelier, D. Bonnin, Y. Chabre, V. Masson, J.-B. Leriche and J.-M. Tarascon, *J. Electrochem. Soc.*, 2003, **150**, A133.

142   P. Balaya, H. Li, L. Kienle and J. Maier, *Adv. Funct. Mater.*, 2003, **13**, 621–625.

143   M.-S. Wu, P.-C. J. Chiang, J.-T. Lee and J.-C. Lin, *J. Phys. Chem. B*, 2005, **109**, 23279–23284.

144   M. Chen, E. Zhao, Q. Yan, Z. Hu, X. Xiao and D. Chen, *Sci. Rep.*, 2016, **6**, 29381.

145   D. Chao, W. Zhou, F. Xie, C. Ye, H. Li, M. Jaroniec and S.-Z. Qiao, *Sci. Adv.*, 2020, **6**, eaba4098.

146   K. Liu, Y. Liu, D. Lin, A. Pei and Y. Cui, *Sci. Adv.*, 2018, **4**, eaas9820.

147   G. Zubi, R. Dufo-López, M. Carvalho and G. Pasaoglu, *Renew. Sustain. Energy Rev.*, 2018, **89**, 292–308.

148   M. Song, H. Tan, D. Chao and H. J. Fan, *Adv. Funct. Mater.*, 2018, **28**, 1802564.

149   H. Kim, G. Jeong, Y.-U. Kim, J.-H. Kim, C.-M. Park and H.-J. Sohn, *Chem. Soc. Rev.*, 2013, **42**, 9011–9034.

150   Y. Zeng, Y. Han, Y. Zhao, Y. Zeng, M. Yu, Y. Liu, H. Tang, Y. Tong and X. Lu, *Adv. Energy Mater.*, 2015, **5**, 1402176.

151   G. G. Yadav, J. W. Gallaway, D. E. Turney, M. Nyce, J. Huang, X. Wei and S. Banerjee, *Nat. Commun.*, 2017, **8**, 14424.

152   C. Li, Q. Zhang, J. Sun, T. Li, S. E, Z. Zhu, B. He, Z. Zhou, Q. Li and Y. Yao, *ACS Energy Lett.*, 2018, **3**, 2761–2768.

153   J. Liu, C. Guan, C. Zhou, Z. Fan, Q. Ke, G. Zhang, C. Liu and J. Wang, *Adv. Mater.*, 2016, **28**, 8732–8739.

154   Y. He, P. Zhang, H. Huang, X. Li, X. Zhai, B. Chen and Z. Guo, *Electrochim. Acta*, 2020, **343**, 136140.

155   L. Ma, S. Chen, H. Li, Z. Ruan, Z. Tang, Z. Liu, Z. Wang, Y. Huang, Z. Pei, J. A. Zapien and C. Zhi, *Energy Environ. Sci.*, 2018, **11**, 2521–2530.

156   X. Wang, M. Li, Y. Wang, B. Chen, Y. Zhu and Y. Wu, *J. Mater. Chem. A*,

2015, **3**, 8280–8283.

157   F. Beck and P. Rüetschi, *Electrochim. Acta*, 2000, **45**, 2467–2482.

158   G. Bronoel, A. Millot and N. Tassin, *J. Power Sources*, 1991, **34**, 243–255.

159   J. Jindra, *J. Power Sources*, 2000, **88**, 202–205.

160   C. Xu, J. Liao, C. Yang, R. Wang, D. Wu, P. Zou, Z. Lin, B. Li, F. Kang and C.-P. Wong, *Nano Energy*, 2016, **30**, 900–908.

161   P. Hu, T. Wang, J. Zhao, C. Zhang, J. Ma, H. Du, X. Wang and G. Cui, *ACS Appl. Mater. Interfaces*, 2015, **7**, 26396–26399.

162   P. Y. Zavalij and M. S. Whittingham, *Acta Crystallogr. B.*, 1999, **55**, 627–663.

163   W. Zhou, J. He, D. Zhu, J. Li and Y. Chen, *ACS Appl. Mater. Interfaces*, 2020, **12**, 34931–34940.

164   P. Tan, B. Chen, H. Xu, W. Cai, W. He and M. Ni, *Appl. Catal. B Environ.*, 2019, **241**, 104–112.

165   V. Ganesh Kumar, N. Munichandraiah, P. Vishnu Kamath and A. K. Shukla, *J. Power Sources*, 1995, **56**, 111–114.

166   L. Indira, M. Dixit and P. V. Kamath, *J. Power Sources*, 1994, **52**, 93–97.

167   L. Demourgues-Guerlou and C. Delmas, *J. Power Sources*, 1993, **45**, 281–289.

168   M. Dixit, P. V. Kamath and J. Gopalakrishnan, *J. Electrochem. Soc.*, 1999, **146**, 79–82.

169   C. Faure, C. Delmas and P. Willmann, *J. Power Sources*, 1991, **36**, 497–506.

170   P. V. Kamath, M. Dixit, L. Indira, A. K. Shukla, V. G. Kumar and N. Munichandraiah, *J. Electrochem. Soc.*, 1994, **141**, 2956–2959.

171   X. Liang, X. Zou, X. Ren, B. Xiang, W. Li, F. Chen, J. Hao, Q. Hu and L. Feng, *J. Colloid Interface Sci.*, 2020, **578**, 677–684.

172   M. Gong, Y. Li, H. Zhang, B. Zhang, W. Zhou, J. Feng, H. Wang, Y. Liang, Z. Fan, J. Liu and H. Dai, *Energy Environ. Sci.*, 2014, **7**, 2025–2032.

173   Y. Huang, W. S. Ip, Y. Y. Lau, J. Sun, J. Zeng, N. S. S. Yeung, W. S. Ng, H. Li, Z. Pei, Q. Xue, Y. Wang, J. Yu, H. Hu and C. Zhi, *ACS Nano*, 2017, **11**, 8953–8961.

174   L. Zhou, X. Zhang, D. Zheng, W. Xu, J. Liu and X. Lu, *J. Mater. Chem. A*, 2019, **7**, 10629–10635.

175   J. Wen, Z. Feng, L. HR, T. Chen, Y. YQ, L. SZ, S. Sheng and F. GJ, *Appl. Surf. Sci.*, 2019, **485**, 462–467.

176   J. Zeng, L. Dong, L. Sun, W. Wang, Y. Zhou, L. Wei and X. Guo, *Nano-Micro*

Lett., 2020, **13**, 19.

177 G. An, *Curr. Appl. Phys.*, 2020, **20**, 605–610.

178 B. D. Boruah, B. Wen, S. Nagane, X. Zhang, S. D. Stranks, A. Boies and M. De Volder, *ACS Energy Lett.*, 2020, **5**, 3132–3139.

179 Y. Li, W. Zhang, X. Yang, J. Zhang, Z. Wang and H. Zhu, *Nano Energy*, 2021, **87**, 106136.

180 Z. Pan, Z. Lu, L. Xu and D. Wang, *Appl. Surf. Sci.*, 2020, **510**, 145384.

181 L. Dong, W. Yang, W. Yang, H. Tian, Y. Huang, X. Wang, C. Xu, C. Wang, F. Kang and G. Wang, *Chem. Eng. J.*, 2020, **384**, 123355.

182 P. A. Maughan, N. Tapia-Ruiz and N. Bimbo, *Electrochim. Acta*, 2020, **341**, 136061.

183 S. Zeng, X. Shi, D. Zheng, C. Yao, F. Wang, W. Xu and X. Lu, *Mater. Res. Bull.*, 2021, **135**, 111134.

184 G.-H. An, *Appl. Surf. Sci.*, 2020, **530**, 147220.

185 G.-H. An, S. Cha and J. I. Sohn, *Appl. Surf. Sci.*, 2019, **467**–**468**, 1157–1160.

186 Z.-B. Zhai, K.-J. Huang and X. Wu, *Nano Energy*, , DOI:10.1016/j.nanoen.2018.02.059.

187 Y. Jiao, J. Pei, C. Yan, D. Chen, Y. Hu and G. Chen, *J. Mater. Chem. A*, 2016, **4**, 13344–13351.

188 Q. Shen, P. Jiang, H. He, C. Chen, Y. Liu and M. Zhang, *Nanoscale*, 2019, **11**, 13511–13520.

189 R. Li, Y. Wang, C. Zhou, C. Wang, X. Ba, Y. Li, X. Huang and J. Liu, *Adv. Funct. Mater.*, 2015, **25**, 5384–5394.

190 Y. Gan, C. Wang, X. Chen, P. Liang, H. Wan, X. Liu, Q. Tan, H. Wu, H. Rao, H. Wang, J. Zhang, Y. Wang, P. A. van Aken and H. Wang, *Chem. Eng. J.*, 2020, **392**, 123661.

191 Y. Ouyang, H. Ye, X. Xia, X. Jiao, G. Li, S. Mutahir, L. Wang, D. Mandler, W. Lei and Q. Hao, *J. Mater. Chem. A*, 2019, **7**, 3228–3237.

192 S. Guan, X. Fu, B. Zhang, M. Lei and Z. Peng, *J. Mater. Chem. A*, 2020, **8**, 3300–3310.

193 C. Yang, Q. Jia, Q. Pan, W. Qi, R. Ling and B. Cao, *Nanoscale Adv.*, 2021, **3**, 593–603.

194 Y. Sun, X. Sun, J. Zhang, S. Liu, L. Guo, J. Bi and N. Huang, *Sustain. Energy Fuels*, 2021, **5**, 3918–3928.

195 Y.-L. Liu, C. Yan, G.-G. Wang, F. Li, Q. Kang, H.-Y. Zhang and J.-C. Han, *Nanoscale*, 2020, **12**, 4040–4050.

Chapter 2

Material synthesis procedures and characterization techniques

Abstract: The thesis work involves the development of various materials that can be applied for energy storage applications. The exploration of the chemical states, the structure properties and many other benefitted characteristics of the materials toward the manufacturing of device having excellent performance is essential in the frontier of research domains. Therefore, the following chapter gives a brief overview of the synthesis procedures as well as the different instrumentation used for the material characterizations with adequate details.

2.1 Introduction

This chapter gives the detailed information of the chemicals/reagents from qualitative and quantitative point of view, the instruments used with adequate details of the model number and experimental conditions, experimental techniques and the procedures with proper formulae of various evaluation parameters of supercapacitors and batteries for e. g. specific capacitance, specific capacity, energy and power density etc.[1,2] Various analytical characterization techniques are listed in the following chapter with details study about the techniques for the investigation of physical properties of the materials. The different analytical methods have been used for the development of graphene and modulated graphene-based nanostructures are listed in the following chapter.

It also includes the brief overview regarding materials, methods, formulae and characterization techniques used in this thesis work.

2.2 Reagents and materials

Chemicals	Purity (%)	Source
Acetone	$\geq$99.5%	Merck Chemicals India
Ammonium persulfate		Sigma Aldrich
Bis(fluorosulfonyl)imide	99.9% trace metals basis	Sigma Aldrich
Carbon Cloth (CC)		Kanopy Techo Solutions Pvt Ltd.
Copper sulphate pentahydrate ($CuSO_4.5H_2O$)	$\geq$99%	Sigma Aldrich
Copper foil	99%	Gelon LIB group, China
Copper wire (d = 0.25 mm)		Local market
Graphite powder	<20 μm	Sigma Aldrich
Hydrochloric acid (HCl)	37%	Merck Chemicals India
Hydrogen peroxide (H_2O_2) 30%		Sigma Aldrich
Holey carbon coated Cu grid for TEM analysis		Agar Scientific Ltd. (UK)
Isopropyl alcohol (IPA)	97%	Merck Chemicals India

Lithium salt (LiTFSI)		
Mangenese sulfate monohydrate ($MnSO_4.H_2O$)	>99%	TCI chemicals
Mica disc for AFM analysis		Agar Scientific Ltd.
Nickel chloride ($NiCl_2 \cdot 6H_2O$)		Sigma Aldrich
Nitric acid (HNO_3)		CDH, India
Orthophosphoric acid (H_3PO_4)	85%	Merck chemicals
Perchloric acid ($HClO_4$)	70%	Merck chemicals
Phosphorous pentoxide (P_2O_5)	≥98.5%	Sigma Aldrich
Potassium hydroxide (KOH)		Sigma Aldrich
Potassium chloride (KCl)		Sigma Aldrich
Polyvinyl alcohol (PVA)	98-99% (M.W.= 89000-98000)	Sigma Aldrich
Potassium permanganate ($KMnO_4$)	97%	Sigma Aldrich
Polyethylene terephthalate (PET sheet)		Local market
Polyethylene oxide (M.W.= 200,000)		Sigma Aldrich
Pyrrole	≥99%	TCI chemicals
Sodium dihydrogen phosphate ($NaH_2PO_4 \cdot H_2O$)		Sigma Aldrich
Sulphuric acid (H_2SO_4)	≥99%	Merck chemicals
Sodium sulfate (Na_2SO_4)		Sigma Aldrich
Sodium hypophosphite ($NaH_2PO_2 \cdot H_2O$)		Sigma Aldrich
Tin Powder	100 mesh, ≥99.9% trace metal basis	Sigma Aldrich

Zinc sulfate monohydrate ≥99.9%   Sigma Aldrich
(ZnSO$_4$.H$_2$O)

Zinc acetate   Sigma Aldrich

2.3 Experimental synthesis procedures

2.3.1 Synthesis of graphene oxide (GO)

 The modified Hummer's method was opted for the synthesis of graphene oxide (GO).[3] This procedure for the fabrication of GO involves two steps as shown in Fig. 2.1a and b: 1.) oxidation of graphite powder in order to obtain the pre-oxidised graphene oxide and 2.) includes exfoliation process for the development of highly dispersed and well-separated graphene oxide sheets. Initially, Graphite powder was slowly mixed into
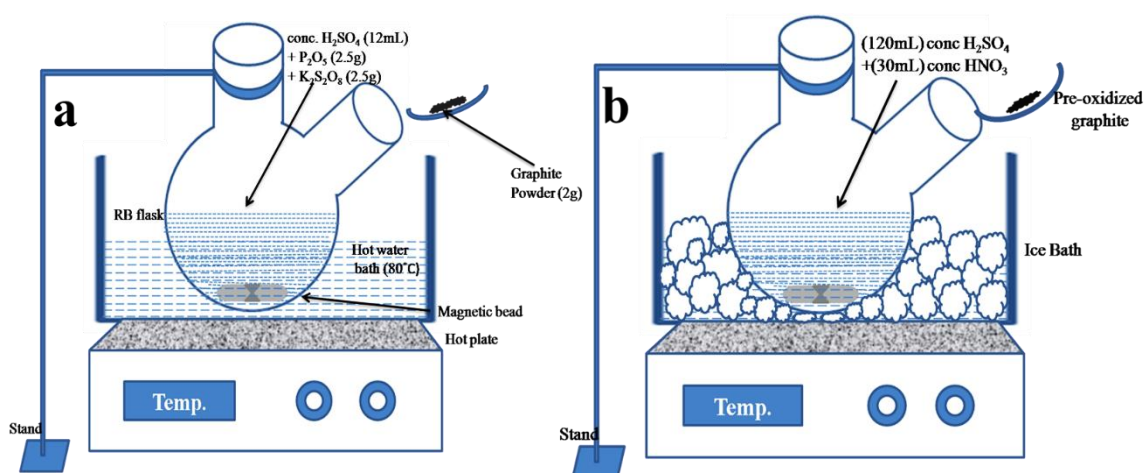
Figure 2.1. *Schematic representation depicting the formation of (a) pre-oxidized graphite (b) graphene oxide.*

concentrated H$_2$SO$_4$ solution which contains P$_2$O$_5$ and K$_2$S$_2$O$_8$ and kept in a hot water bath (80°C) under strong stirring for 3 h. Diluting with Milli-Q water maintaining the temperature 25°C (room temperature), a dark green mixture was obtained. The mixture was then washed several times under centrifugation until pH of waste solutions became neutral. Pre-oxidized graphite powder was collected and dried in oven (at 70°C) overnight. In the second and final step, pre-oxidized graphite powder was slowly added to concentrated H$_2$SO$_4$ maintaining the temperature at 0 °C in an ice bath. Solid KMnO$_4$ was then slowly added to the mixture under slow stirring while maintaining the temperature below 20 °C. After removing the ice-water bath, the mixture was heated at 35 °C under continuous stirring for 2 h, to which Milli-Q water was then added. After a few minutes, Milli-Q water and 30% H$_2$O$_2$ solution were further added to the mixture

and observed the solution colour changed rapidly to bright yellow. The mixture was then washed with 20% HCl solution followed by washing with 15% HCl and 5% HCl solution. After acid washing, the washed product was neutralized with Milli-Q water under centrifugation at a high rotation speed (12000 rpm). To remove residual salts and acids, the sample was further dialyzed using a dialysis tube (with a cut-off molecular weight of 12000-14000) for 7 days by regularly replacing water bath with fresh Milli-Q water 2-3 times per day. The dialyzed GO solution can be stored in a reagent bottle.

2.3.2 Galvanostatically grown copper foam (Cuf) using dynamic hydrogen bubble template (DHBT) method

Electrochemical preparation of Cuf using the hydrogen bubbling mechanism in DHBT method is considered to be most fascinating process to modulate the three-dimensional structures and morphology of the deposited metals.[4] The porous architecture of Cuf can further acts as a template for the development of supercapacitive electrode material with
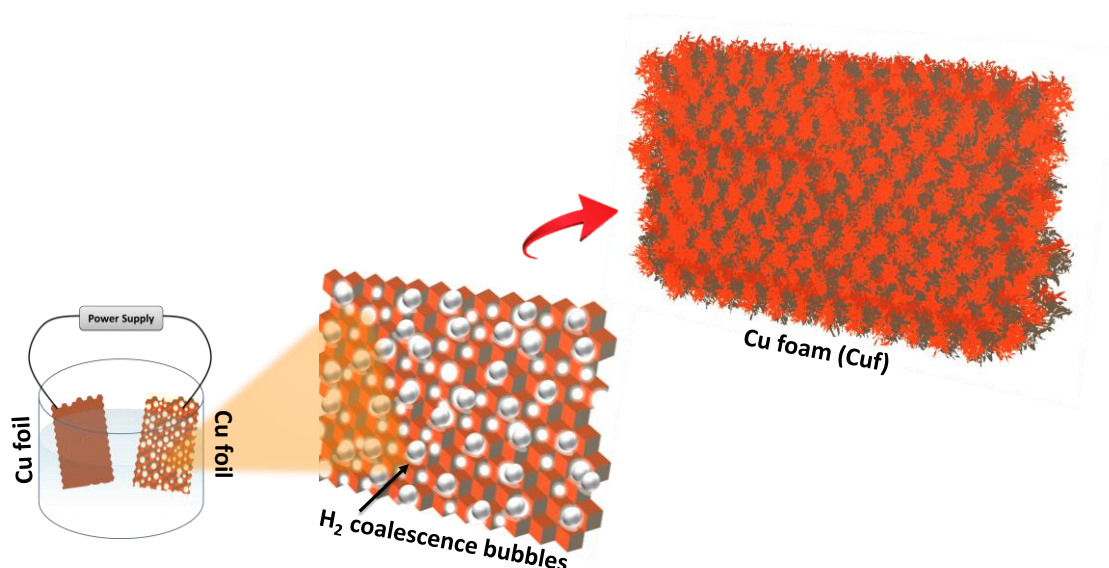
Figure 2.2*. Schematic representation depicting the formation mechanism of electrodeposited copper foam.*

unique porosity and 3D-morphological architectures.[5–9] The Cuf can be grown using two-electrode where copper foil acts as a working electrode and an another copper foil is used as counter electrode. In the three-electrode synthesis procedure, copper foil acts as cathode as well as anode and an Ag/AgCl as reference electrode in a mixture solution of acid and copper sulphate as shown in Fig. 2.2. At a certain current density/potential value, a co-reduction process occurs along with the evolution of hydrogen gas bubbles at the surface by the hydrogen ion supplied by supporting electrolyte. The possible reaction involved in the process are shown in the following equations 2.1 and 2.2

$$2H^+(aq) + 2e^- \rightleftarrows H_2(g) \tag{2.1}$$

$$CuSO_4 + 2e^- \rightarrow Cu_{metal} + SO_4^{-2} \tag{2.2}$$

The bubble formation on the electrode undergoes through three basic steps: nucleation, growth and detachment. The small bubbles get fused to each other to form large sized bubble on the surface and gets detached when it reaches upto a critical size *i.e.* "break-off diameter" which solely depends on the surface energy and morphology of the surface at which the reduction is taking place.[10] As the critical size of the bubble reaches to its extreme value, the bubble breaks on the electrode surface leaving behind a void which forms the foam like morphology of the Cuf. The metal surface grow around these bubbles, acting as a dynamic template.

The galvanostatic electrodeposition was carried out for the deposition of Cuf in the aqueous suspension at room temperature. Briefly, an aqueous solution of 0.4 M $CuSO_4$ in 1.5 M H_2SO_4 was used. Commercially available high-purity copper sheet (>99%) with specified dimensions was used as the substrate (cathode) for Cuf deposition and another copper sheet of equal area was used as counter electrode (anode) as shown in Fig. 2.2. Both copper sheets were cleaned with 30 % HNO_3 followed by washing with Millipore water 3-4 times and finally washed with ethanol. When not in use, the cleaned copper sheets were kept in argon atmosphere to avoid atmospheric oxidation. Cuf deposition was carried out with a constant current density of 1 A cm^{-2} for 45 sec using a DC voltage supply system. A gap of 2 cm was maintained between the electrodes. The as-deposited Cuf sheet was finally cleaned with Millipore water repeatedly. The formation process of the foam structure can be mechanistically described as a reason of hydrogen gas evolution explained very well as above.[11]

2.3.3 Electrodeposition of reduced graphene oxide (ErGO)

Electrochemically reduced graphene-oxide (ErGO) networks were grown by electrolysis of GO aqueous solution on the Cuf (Fig. 2.3)[11]. In a typical procedure, bulk electrolysis of GO aqueous suspension (3 mg ml^{-1}) in 0.5 M perchloric acid (HClO$_4$) was carried out at an applied potential of -1.0 V against Ag/AgCl reference for 60-120 seconds on Cuf electrode. After electrochemical deposition of ErGO, any unreduced GO suspension or physically absorbed rGO attached to the surface was removed by repeatedly washing the film with DI water. Electro-reduction of the oxygen containing groups in GO leads to the formation of the conductive rGO sheets in the form of three-dimensional porous networks. ErGO membrane deposited on to Cuf was separated by etching Cuf/Cu with

10% ammonium persulfate solution. Typically, the rGO/Cuf/Cu was placed in the $(NH_4)_2S_2O_8$ solution (with the rGO side facing up) for overnight under ambient conditions. A stable copper sulfate formed during oxidation of copper by persulfate to form soluble copper sulfate as represented in equation 2.4,

$$Cu + S_2O_8^{2-} \longrightarrow CuSO_4 + SO_4^{2-} \qquad (2.4)$$

After complete etching of copper, the rGO membrane starts floating onto the surface of the solution and the solution turns blue in color. The rGO film was then transferred by

Cuf@Cu

Electrochemical deposition

ErGO
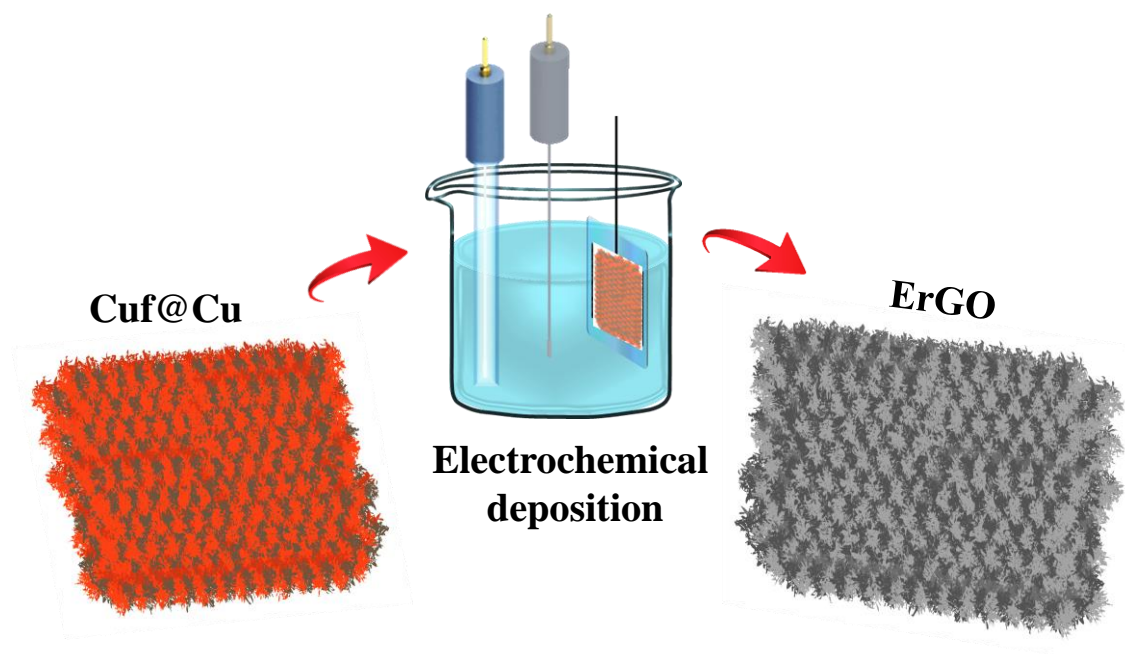
Figure 2.3 Electrodeposition setup of electrochemically reduced graphene oxide in set up in a three-electrode system.

scooping up on to a PET sheet (poly ethylene terephthalate) and then washed in Millipore water several times for the complete removal of Cu^{+2} ions that may have adsorbed in the ErGO networks. The transferred ErGO sheet was kept for drying in desiccator.

2.3.4 Laser-irradiation method to develop highly conducting graphene (LIG)

The laser-irradiation process is carried out by CO_2 laser with a wavelength of 10.6 μm and 2-inch focal length. The mechanism of laser-irradiation (LI) process is well known for the development of highly conducting graphene film. It is reported that the LI process is responsible to make huge change in the local temperature (>2500°C) on the surface of the material, which could easily break the bonds (C-O and C=O) present in ErGO surface.[12–15] Then, the released small atoms/molecules either can recombine to form gases or the edge group can undergoes rearrangement process to form graphitic structures.[16] The LI process involves two-step reduction pathways, first the
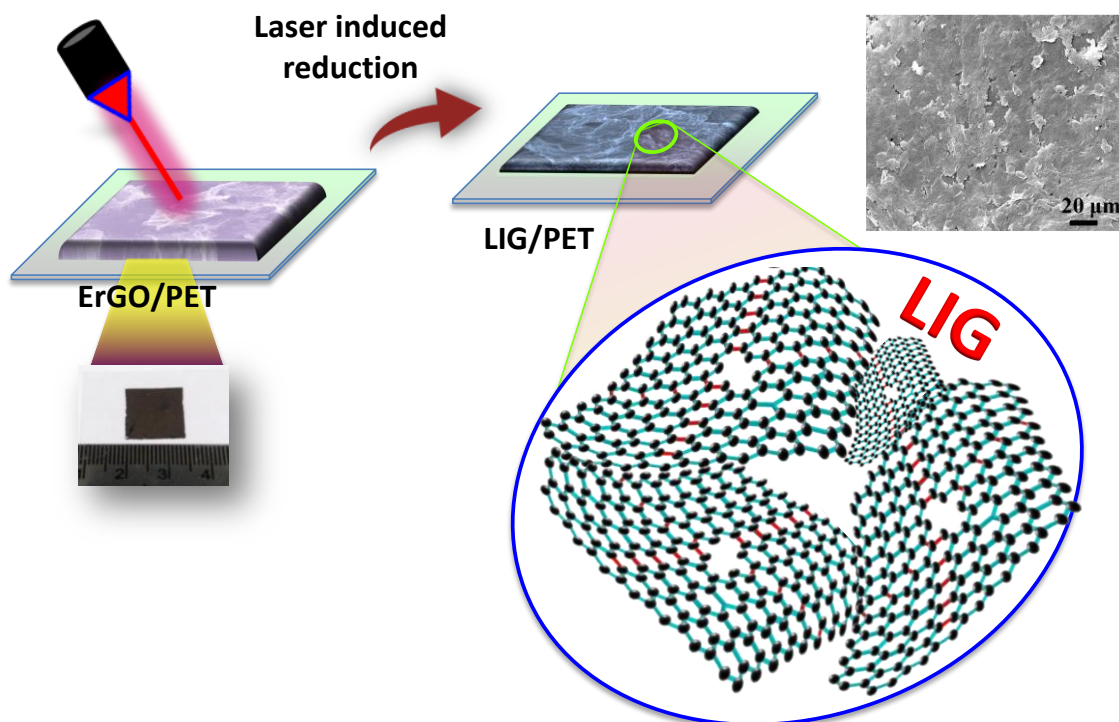
Figure 2.4 *Laser-irradiation process for the fabrication of highly conducting laser-irradiated graphene (LIG) film.*

photochemical removal of oxygen was realized on the surface followed by the thermal restoration of π-electron cloud in graphene networks.[17] The depth of penetration mainly depends on the wavelength of laser radiation, laser output power and duration of exposure, which was optimised in the present study. The degree of graphitization is the consequence of photothermal process, which is proportional to the laser power and exposer time. Therefore, more degree of graphitization takes place with more laser power. The laser speed also has direct influence in the formation of local temperature.[17] In this case, by decreasing scan rate the exposer time of the laser beam per unit area increases, which is certainly increasing the local temperature. Therefore, the LI process results in restoration of the sp^2 carbons and make the film more compact and flattened due to removal of oxygen functionalities present in the surface (Fig. 2.4).

2.3.5 Hydrothermal synthesis method

This particular method is utilised for the fabrication of crystallizing substances from high-temperature aqueous solutions at a high vapor pressures.

2.3.6 Interdigitated patterning of the electrodes

To pattern the electrodes in an energy storage device in order to make a planar geometry of the device, a near-infrared (NIR) laser of 1.06 μm wavelength is utilised. The laser power, speed and exposure time are optimized to completely etch the material between

the electrode to keep them completely insulating to each other. For example, in our case the LIG film was patterned to interdigital structures of 5 positive and 5 negative microelectrodes having actual width, length and inter-finger distance of about 670 µm, 5000 µm and 200 µm, respectively. Patterning was carried out by 1.06 µm NIR laser source of power 30 W, speed 0.5 m/sec and 20,000 Hz frequency in one pass. The laser-engraving process took about 30 sec to pattern a single device.

2.3.7 Solid-state gel electrolyte fabrication

To fabricate the solid-state MSC, a clear solution of PVA/H_3PO_4 gel electrolyte was prepared by successively adding H_3PO_4/KOH and PVA into 10 mL deionized water and heating to 85° C under continuous stirring for 2 hours. The transparent PVA/H_3PO_4 or PVA/KOH gel electrolyte was drop casted on the active interdigital electrode areas and kept for drying for 24 hours under ambient conditions. The gel electrolyte is ionically conducting but electrically insulating. The as-fabricated supercapacitor device should be properly dried before testing.

2.3.8 Battery set-up

A battery set-up includes three components that are cathode, anode and an electrolyte medium. In the discharge state, electron deriving from anode electrode are collected at cathode electrode and electrons flows through the outer circuit whereas in charging state, the above reaction was reversed by applying an external potential at both the electrodes.

2.4 The calculation and formulas for supercapacitor/battery device performance evaluation

The assessment in the electrochemical profile of the storage device (supercapacitor/battery) can be realized *via* determination of open-circuit voltage, electrochemical stability window, charge-transfer resistance (R_{ct}), specific capacitance/capacity, energy density, power density and cycling stability study with respect to specific current density. These measurements can be done by various electrochemical techniques; cyclic voltammetry (CV), Galvanostatic charge-discharge (GCD), and electrochemical impedance spectroscopy (EIS). These quantify parameters are described as follows:

2.4.1 Open circuit potential (OCP): is defined as the attained potential of the device when it is disconnected from external load. When the electrodes are immersed in electrolyte, it adopts an open circuit potential (OCP). The OCP value decides whether the electrode will undergo oxidation or reduction.

2.4.2 Specific capacitance: The specific capacitance can be measured by performing both the techniques: cyclic voltammetry and galvanostatic charge-discharge techniques. The capacitance value of the device can be quantified in areal, gravimetric and volumetric measures. As CV curve provide a corelation of current versus potential. The mass normalized specific capacitance 'C_{sp} (F g^{-1})' can be measured by the following equation 2.5:

$$C_{sp} = \frac{\int_{V_i}^{V_f} IdV}{m \times v \times (V_f - V_i)} \qquad (2.5)$$

where 'I (A g^{-1})' is the output current generated in the device, 'm (g)' is the mass loading of the active material, 'v (mV s^{-1})' is the scan rate, $V_f - V_i$ (V) is the difference in the final potential to initial potential (potential window).

Similarly, the specific capacitance can be calculated from GCD profile (Potential versus time correlation at constant current density) according to the formula shown in the equation 2.6:

$$C_{sp} = \frac{d_t \times I}{m \times (\Delta V - V_{IR})} \qquad (2.6)$$

where 'I (A g^{-1})' is the applied current generated in the device, 'm (g)' is the mass loading of the active material, $V_f - V_i = \Delta V$ (V) is the potential window, V_{IR} is the potential drop due to internal resistance (IR).

2.4.3 Normalized energy density: The mass normalized energy density 'E_m (Wh kg^{-1})'of the device is defined as the amount of energy storage per unit volume/area/mass in the system. It can be calculated from the equation 2.7:

$$E_m = \frac{1}{2} C_{sp} \times \Delta V^2 \qquad (2.7)$$

The energy density is directly proportional to two quantified parameters i.e the capacitance value and cell voltage. The capacitance in turn is dependent upon the type of capacitive material used (whether it is capacitive, pseudocapacitive or battery type) and the effective surface area of the electrode. Hence, porous structured materials exhibiting greater effective surface are provides subsequent high energy density.

2.4.4 Normalized power density: The normalized power density 'E_m (W kg^{-1})' is defined as the rate of energy flow per unit volume/area/mass. It is calculated by the formula as given in equation 2.8:

$$P_m = \frac{E_{sp}}{d_t} \qquad (2.8)$$

Where 'd_t' is the discharge time under fast charge/discharge rate. The power density is directly dependent upon the energy stored in the device and inversely on the time taken by the device to get fully discharge. Hence, lesser is the discharge time, higher would be the power delivery but it is also true that when the device is working at a higher power the energy density will be less.

2.4.5 Electrochemically active surface area calculation (ECSA)

To calculate the normalized specific capacitance of the device, the electrochemically active surface area (ECSA) of the active material is essential to measure. ECSA can be measured from its electrochemical double layer capacitance (C_{dl}) which in turn can be calculated by performing the cyclic voltammetry (CV) at different scan rates by choosing a non-Faradaic region in the corresponding electrolyte medium. The double-layer charging current "i_c" is equal to the product of the scan rate "v" and the electrochemical double-layer capacitance, "C_{dl}" as given by equation 2.9:

$$i_c = vC_{dl} \tag{2.9}$$

The difference in the fitted slopes of charging and discharging CV scans was used to determine the C_{dl},.[18] ECSA is then calculated *via* dividing the C_{dl} by the specific surface capacitance (C_{sp}) of electrode surface as depicted in equation 2.10:

$$ECSA = C_{dl}/C_{sp} \tag{2.10}$$

2.4.6 Mass loading measurements of the electroactive material *via* electrochemical quartz crystal microbalance (EQCM)

Various experiments include mass loading calculation using a piezoelectric electrochemical quartz crystal microbalance (EQCM) analysis. The EQCM measurements were performed with 302N computerized time-resolved quartz crystal microbalance in Metrohm Autolab system. A quartz crystal coated with Au on Cr layer, acquiring a 6 MHz fundamental resonant frequency, was used as working electrode. The geometrical area of Au covered quartz crystal is 0.196 cm^2. A single-compartment cell comprising a platinum wire counter electrode and Ag/AgCl (3M KCl) reference electrodes was utilised. The working electrode was electrochemically pre-treated by sweeping potential from 0 to 1.4 V in 0.1 M H$_2$SO$_4$ at a scan rate of 200 mV s^{-1} for continuous 50 cycles. The electrode was used for EQCM studies after washing with deionized (DI) water. The mass change is related with the frequency change at the electrode surface by represented by Sauerbrey's equation 2.11:

$$\Delta f = \frac{-2\,f_0^2\,\Delta m}{A\sqrt{\rho_q\mu_q}} \qquad\qquad (2.11)$$

Where, "f_0" is the resonant frequency of the fundamental mode of the crystal (6MHz), "A" is the area of Au disk coated on the crystal, "μ_q" is shear modulus of quartz (2.947 $\times$ 10^{11} g cm^{-1} s^{-2}), "ρ_q" is density of the crystal (2.684 g cm^{-3}), "Δf" is net change in frequency (Hz), and "Δm" is the net change in mass (mg).

2.5 Instrumentation

2.5.1 X-ray diffraction (XRD)

The crystallinity of the material, its crystal structure, the number of phases and the type pf phase present in the sample can be investigated by X-ray diffraction analysis. It is a non-destructive technique to characterize other parameters apart from above mentioned like average grain size, tension and crystal defects in the material. When a monochromatic X-ray beam incident on the surface of the sample, it gets diffracted from
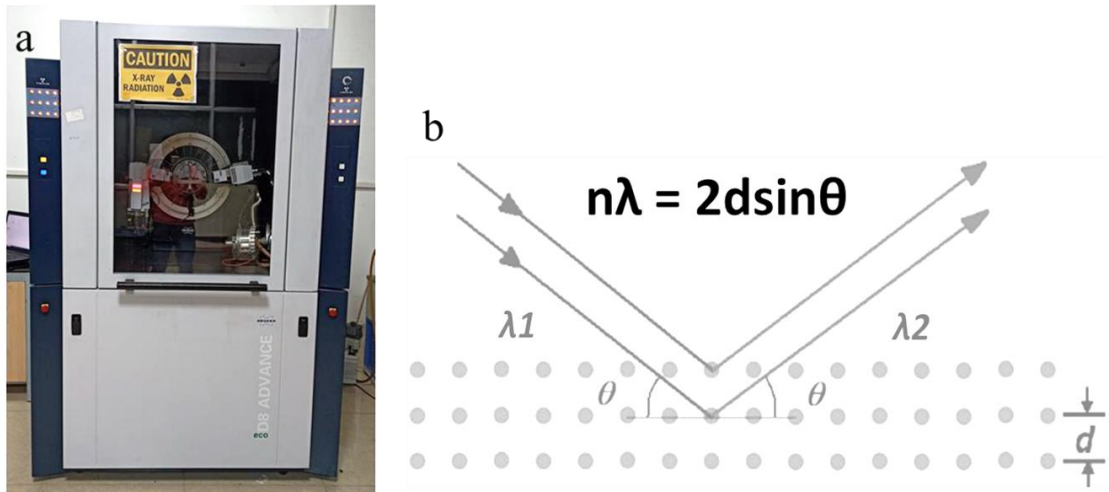
Figure 2.5 (a) A typical view of PXRD instrument (b) X-ray generation geometry.

the unique crystal planes and analysed the scattered X-ray beam through detector (a digital image of the instrument is shown in (Fig. 2.5a). It is an elastic scattering process which gives rise to an increase in the interference of the fringe patterns of more ordered materials. W. L. Bragg in 1912 introduces Bragg's equation *i.e.,* nλ=2dsinθ, where θ, λ are the incident angle and wavelength of the radiation (1.5418 Å for Cu Kα), 'd' is the perpendicular distance between adjacent planes (Fig. 2.5b)[19] to investigate the crystal structure of the material.

The XRD analysis was carried out on a Bruker D8 Advances instrument using a Cu- Kα (λ = 1.5406 Å) radiation source in the 2θ range from 5° to 80° with an acceleration voltage of 40 KV.

2.5.2 Scanning electron microscopy (SEM)

The scanning electron microscope (digital image shown in Fig. 2.6a) is a kind of electron microscope that give the exact trace image of the sample when a focused beam of electron falls at the surface of the sample. Figure 2.6 b and c shows the digital images of detector
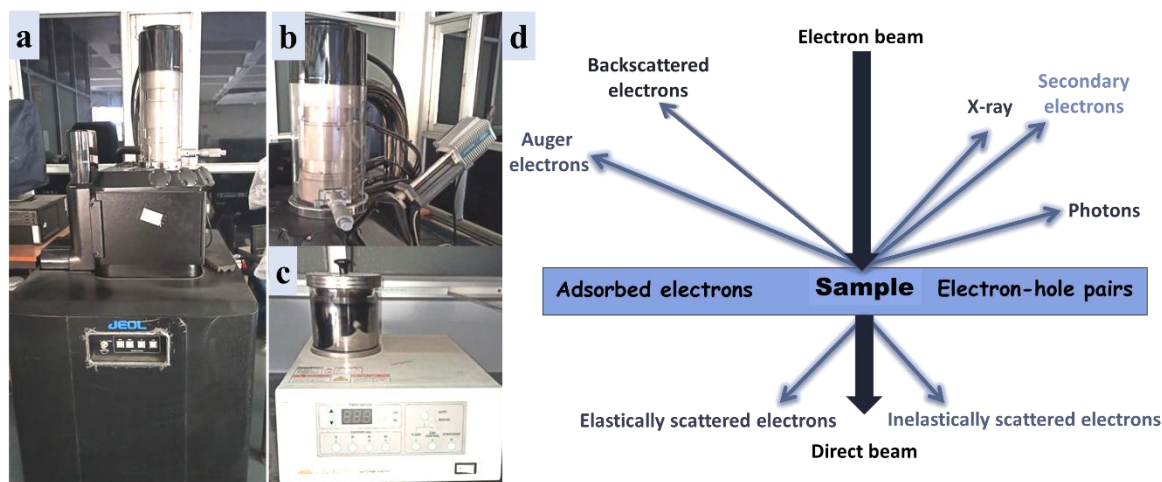
Figure 2.6 (a) A typical view of SEM column (left), (b) the EDX detector (backside of column, upper right) (c) gold coater unit (lower right). (d) different signal of generated from specimen upon the interaction with e-beam.

chamber and gold coater system. The typical working principle of SEM include the interaction of electrons with atoms in the sample producing various signals like secondary electrons (SE), back scattered electrons (BSE), characteristics X-ray and transmitted electrons that contains information about the surface topography and distribution of the elements present in the sample (Fig. 2.6d). The electron microscope encompasses very high resolution compared to optical microscope and capture the content at the atomic level.[20] The SEM instrument works in high vacuum conditions.

Surface morphology was investigated using Scanning Electron Microscopy (SEM Jeol JSMIT300) at an acceleration voltage of 10-15 KV.

2.5.3 Field-emission scanning electron microscopy (FE-SEM)

To take the topographical images at ultra-high-resolution range, Field Emission Scanning Electron Microscope (FE-SEM) is used. The major difference between FE-SEM and SEM is its emission source, the SEM utilizes thermionic emitter whereas FE-SEM uses field-emitter.[21] The FE-SEM analysis was performed using JEOL JSM-7600F (FESEM).

2.5.4 Raman spectroscopy

Raman spectroscopy gives detailed information about the phase of the material, chemical structure, crystallinity and the possible molecular interactions in the material. It is a non-destructive phenomenon. The corresponding technique involves light scattering phenomenon, whereby the incident light from an intensified laser light source gets scattered through the molecules present in the materials. A quantitative amount of scattered light is of same wavelength as of the laser source and in meaningless, which is called "Rayleigh scattering". The Raman spectrum comes in the anti-stoke region, giving a number of peaks corresponding to specific molecular bond vibration, also including individual bonds like C-C, C=C, N-O, C-H etc., and groups of bonds such as benzene ring breathing mode, polymer chain vibrations, lattice modes, etc.

The Raman spectroscopy was performed on a WITEC Focus Innovations Alpha-300 Raman confocal microscope at a laser wavelength of 532 nm.

2.5.5 Transmission electron microscopy (TEM)

TEM is an analytical morphology characterization technique which is extremely

Figure 2.7 Digital image of transmission electron microscopy.

mandatory characterization in material science studies. The working principle is explained as: high voltage electron beam is transmitted through the thin sample (< 100 nm thickness) and collect the high resolution morphological information at micro as well

as nanoscale.[22] The image was taken after the interaction of the e-beam with the sample on the fluorescent screen after coupling with the CCD camera.

Transmission Electron Microscopy (TEM) analysis was investigated out on a JEM2100 instrument suitable for High-Resolution TEM (HRTEM) studies (Fig. 2.7). The instrument was armed with digital micrograph software for investigating selected area electron diffraction (SAED) pattern of the sample surface. Holey carbon-coated copper grids (Agar Scientific Ltd.) were used as the sample grid in the measurements.

2.5.6 Energy-dispersive X-ray spectroscopy (EDX) and elemental mapping

The atomic information of the material is obtained from EDX analysis coupled with SEM/TEM instrument. EDAX can easily detect the elements having the atomic number higher than that of boron. Elemental mapping can be used to check the distribution of the elemental entities in the sample using the same instrument as mentioned in sections 2.4.3 and 2.4.4.[23,24]

2.5.7 Brunauer Emmett Teller (BET) surface area analysis
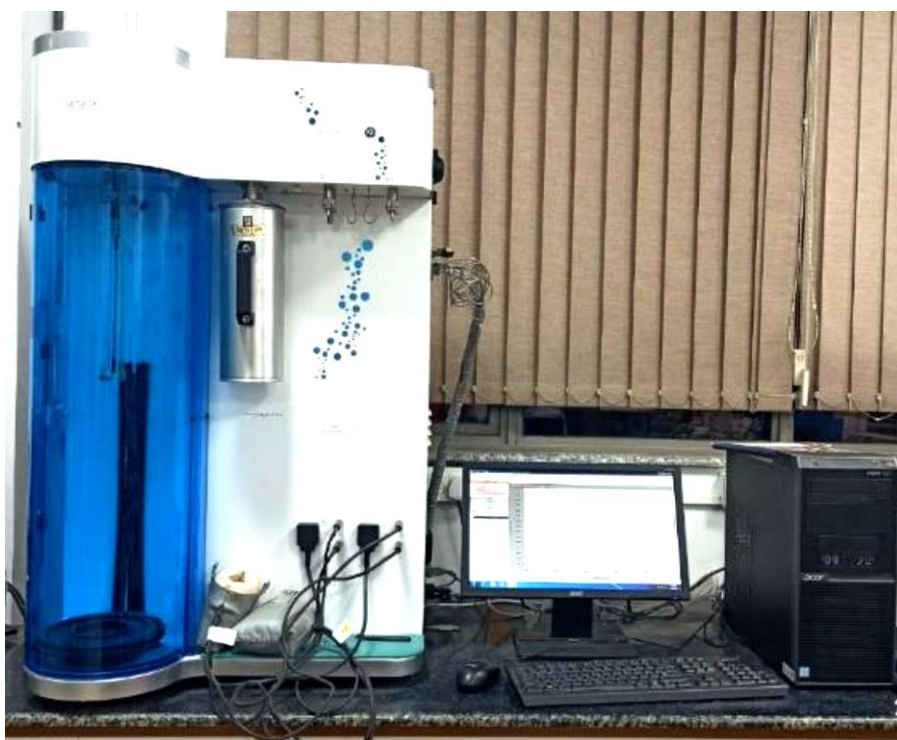
Figure 2.8 A typical image for surface area analyser instrument.

This is a common technique for the determination of specific surface area, pore size distribution and pore volume in the material. In a typical BET analysis, the specific surface area can be calculated from the volume of N_2 gas absorbed in the infinite layers of the material (digital image of the instrument is shown in Fig. 2.8). The porous

behaviour of the material can be analysed by volumetric N_2 adsorption-desorption isotherm at 77K. International Union of Pure and Applied Chemistry (IUPAC) classified a total six types of adsorption isotherms (Type I to VI) according to their pore size distribution characteristics. The type I isotherm is classified for the microporous materials (pore size < 2nm) owing to high adsorption of adsorbent molecules at relatively low partial pressure. Type II isotherm is found in mesoporous (pore size 2-50 nm) materials and beyond this range, the isotherm is found to be non-porous or macroporous.[25,26]

Nitrogen adsorption-desorption analysis was done at 77 K on an Autosorb iQ2 instrumental setup to examine the surface area by Brunauer Emmett Teller (BET) method. The samples were degassed at 150 °C for more than 12 h under vacuum conditions.

2.5.8 X-Ray photoelectron spectroscopy (XPS)

The X-ray photoelectron spectroscopy (XPS) is a surface sensitive quantitative technique which gives the identification of elements, their chemical states, the overall electronic structure and density of electronic configuration in the material. This technique is purely
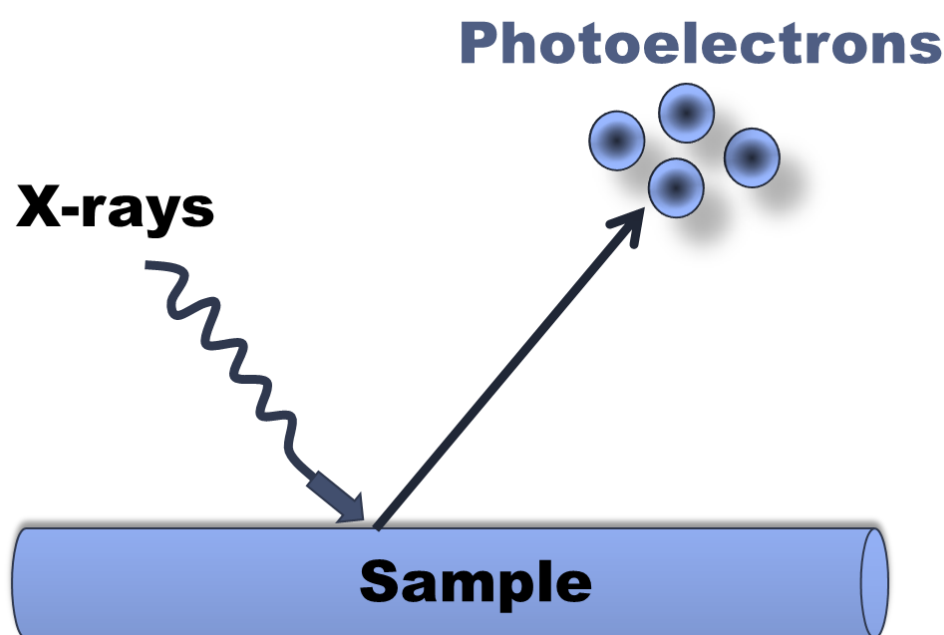
Figure 2.9 *Fundamental of X-Ray Photoelectron Spectroscopy (XPS)*

based on the photoelectric effect and can also be performed on electrically conducting as well as non-conducting material surface. A monochromatic X-ray having low-energy (Al Kα or Mg Kα) under high vacuum condition is irradiated over the sample surface and X-ray photon hits the core level electron present in the material, transfers its energy to the

electron which results in the ejection of the electron from its initial ground state with certain kinetic energy associated with it (Fig. 2.9).[27,28] The photo-emitted core electron is been analysed as a function of binding energy and give the detailed information about its chemical environment and states with their composition.

X-Ray photoelectron (XPS) spectroscopy was executed on a K-Alpha plus XPS system of ThermoFisher Scientific instruments in an ultrahigh vacuum chamber (7×10^{-9} torr) using Al-K radiation (1486.6 eV).

2.5.9 Attenuated total reflectance (ATR) spectral measurements

ATR works on the basis of vibration of the molecular functional groups. Each and every functional group has their own and unique vibrational energy, which actually helps in the identification of the bonds present in the sample. This spectroscopy technique gives the idea about the bonds present in the sample which are infrared active.[29]

ATR spectral measurements were recorded Bruker FTIR-ATR spectrometer (VERTEX-70). Au-coated quartz crystals were used as substrate for ATR spectral measurements. Before measurements, the Au-coated quartz crystal platform was washed with absolute ethanol and Millipore water.

2.5.10 Fourier transform infrared spectrophotometer (FTIR)

Fourier transform Infrared (FTIR) spectroscopy was carried out on an Agilent technology Cary 600 series FTIR instrument at room temperature. For FTIR analysis, all the samples were mixed with KBr (KBr as a reference) and then finely ground to make a pellet.

2.5.11 Contact angle measurements through drop shape analyser

The drop size analyser, was used to investigate the surface wettability properties like hydrophilicity or hydrophobicity[30] nature of the material surface and performed using KRUSS (DSA25E, 100 watt) instrument at room temperature.

2.5.12 Electrical conductivity measurements through sourcemeter B2902A

This instrument is used for the measurement of electrical conductivity of the material *via* two-probe and four probe technique. In two probes, the two connections are the only input and output sources whereas four probe method have two connections for input voltage source and the other two connections corresponds to the output current source.

A source meter (Model No. B2902A) is used as a power supply source to analyse the electrical conduction in the material.

2.5.13 Nuclear magnetic resonance (NMR) technique

This technique is a spectroscopic technique to identify the monomolecular organic compounds and also investigate the local magnetic fields around the atomic nuclei. The

sample produces the NMR signals while placing in a magnetic field region *via* the excitation of the nuclei sample through radio waves into the NMR spectra which is detected with radio receivers. The changes in the resonance frequency through intramolecular magnetic field given the details explanation of the electronic structure of a molecule and its functional groups. The basic principle of NMR involves three steps: 1.) The aligned polarization of the nuclear spin under the application of magnetic field B_0, 2.) The perturbation of these nuclear spin polarization by a weak oscillating magnetic field (known as radio-frequency pulse), 3.) The emitted electromagnetic waves detection and analysis.

The ^{1}H NMR spectra is taken from 400MHz Bruker Advance II400 NMR spectrometer.

2.5.14 Atomic force microscopy (AFM)

AFM is a surface analysis method which is used for micro/nanostructured coated materials. It is used to take the high-resolution nanoscale images and thickness measurements of nanoparticles and nanomaterials

AFM was done on a Bruker Multimode 8 instrument for the investigation of the surface topologies and thickness of the material.

2.5.15 Electrochemical measurements through electrochemical workstations

Electrochemical measurement techniques such as cyclic voltammetry (CV), linear sweep voltammetry (LSV), galvanostatic charge discharge (GCD), Electrochemical Impedance Spectroscopy (EIS), chronoamperometry (CA), chronopotentiometry (CP) etc. were performed on electrochemical workstation CHI 660 and CHI 760E as shown in Figure 2.10a (CH Instruments, USA) and Metrohm Autolab PGSTAT (302N) (Fig. 2.10b) in order to understand the mechanism happening on the surface of the electrode material.
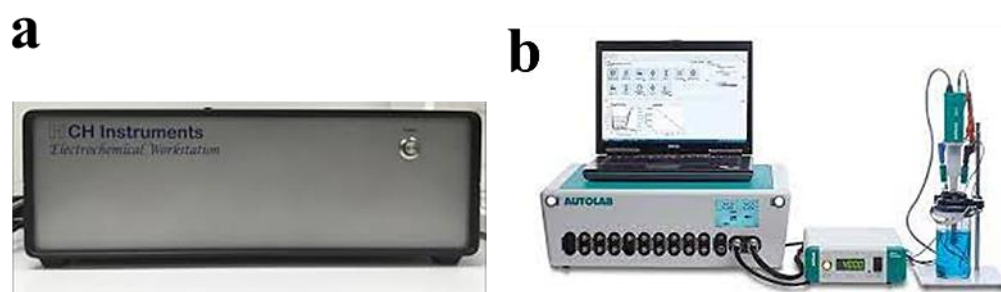
Figure 2.10 *Electrochemical workstations (a) CHI 760E (b) Metrohm Autolab PGSTAT (302N).*

The analysis is basically done using two processes; Faradaic as well as non-Faradaic

process. Faradaic process involves the transfer of the electron/charge through the electrode/electrolyte interface following the Faraday law in contrast other is termed as a non-Faradaic process. The occurrence of the redox reaction (oxidation and reduction) is due to the transfer of charge through the interfaces.

2.5.15.1 Two-electrode and three-electrode system configuration

The electrochemical studies were done in a standard three/two-electrode system electrochemical cell. The as prepared electrode material worked as working electrode, Ag/AgCl (3.0 M) as the reference electrode and graphite rod/Platinum rod as the counter electrode under ambient atmospheric conditions. In contrast, two-electrode system the electrochemical measurement is done between the identical patterned working electrodes.

2.5.15.2 Linear sweep voltammetry and cyclic voltammetry

Within a fixed potential window, the sweeping of potential is recorded at a certain scan rate is termed as linear sweep voltammetry (LSV). The revert back of the LSV one or many times to complete the redox process is termed as cyclic voltammetry (CV).

2.5.15.3 Galvanostatic charge/discharge (GCD) profile

The GCD profile is studied through chronopotentiometry technique where a constant anodic and cathodic currents are applied in either a potential bounded region or time bounder region.

2.5.15.4 Impedance measurements

The electrochemical impedance spectroscopy (EIS) for three/two electrode system were conducted at a particular potential in a frequency range of 10^5-10^{-2} Hz.

2.6 Conclusions

This chapter provides the glimpse of synthesis procedures like electrochemical deposition method, laser-irradiation process etc. for the development of highly efficient electrode materials to be applicable for the storage properties. The material characterizations like XRD, Raman, AFM and many more are briefly discussed and all the device testing techniques such as cyclic voltammetry, charge/discharge, electrochemical impedance spectroscopy are elaborated with adequate details.

2.6 References

1   J. Slotwinski, P. Stutzman, C. Ferraris, S. Watson, M. Peltz and E. J. Garboczi, *AIP Conf. Proc.*, , DOI:10.1063/1.4864954.

2   J. B. Park and R. S. Lakes, Eds., Springer New York, New York, NY, 2007, pp. 41–81.

3   N. I. Zaaba, K. L. Foo, U. Hashim, S. J. Tan, W.-W. Liu and C. H. Voon, *Procedia Eng.*, 2017, **184**, 469–477.

4   R. Abdel-Karim and S. El-Raghy, in *Advanced Materials and their Applications: Micro to nano scale*, 2017, pp. 69–91.

5   Y. K. Kim, S. I. Cha and S. H. Hong, *J. Mater. Chem. A*, 2013, **1**, 9802–9808.

6   T. Bryce C, S. Stephen A and E. P. Luther, *Angew. Chemie - Int. Ed.*, 2010, **49**, 4544–4565.

7   Z. Hua, Y. Deng, K. Li and S. Yang, *Nanoscale Res. Lett.*, 2012, **7**, 1–7.

8   P. S. Liu and G. F. Chen, *Porous Mater.*, 2014, 113–188.

9   K. I. Popov, S. S. Djokić, N. D. Nikolić and V. D. Jović, Morphology of Electrochemically and Chemically Deposited Metals, Springer International Publishing, Cham, 2016.

10   H. C. Shin, J. Dong and M. Liu, *Adv. Mater.*, 2003, **15**, 1610–1614.

11   R. S. Dey, H. A. Hjuler and Q. Chi, *J. Mater. Chem. A*, 2015, **3**, 6324–6329.

12   H. Tomiyasu, H. Shikata, K. Takao, N. Asanuma, S. Taruta and Y.-Y. Park, *Sci. Rep.*, 2017, **7**, 45048.

13   J. Lin, Z. Peng, Y. Liu, F. Ruiz-Zepeda, R. Ye, E. L. G. Samuel, M. J. Yacaman, B. I. Yakobson and J. M. Tour, *Nat. Commun.*, 2014, **5**, 5714.

14   T. N. Lin, K. H. Chih, C. T. Yuan, J. L. Shen, C. A. J. Lin and W. R. Liu, *Nanoscale*, 2015, **7**, 2708–2715.

15   Z. Wan, E. W. Streed, M. Lobino, S. Wang, R. T. Sang, I. S. Cole, D. V Thiel and Q. Li, *Adv. Mater. Technol.*, 2018, **3**, 1700315.

16   J. Lin, Z. Peng, Y. Liu, F. Ruiz-Zepeda, R. Ye, E. L. G. Samuel, M. J. Yacaman, B. I. Yakobson and J. M. Tour, *Nat. Commun.*, 2015, **5**, 1–8.

17   B. S. Yilbas, Z. Yilbas and M. Sami, *Opt. Laser Technol.*, 1996, **28**, 513–519.

18   C. Fisica and U. Milano, *Pure Appl. Chem.*, 1991, **63**, 711–734.

19   E. S. Ameh, *Int. J. Adv. Manuf. Technol.*, 2019, **105**, 3289–3302.

20   K. D. Vernon-Parry, *III-Vs Rev.*, 2000, **13**, 40–44.

21   M. S. El-Eskandarany, ed. M. S. B. T.-M. A. (Third E. El-Eskandarany, William Andrew Publishing, 2020, pp. 13–18.

22   L. E. Franken, K. Grünewald, E. J. Boekema and M. C. A. Stuart, *Small*, 2020, **16**, 1906198.

23   R. Kohli, eds. R. Kohli and K. L. B. T.-D. in S. C. and C. Mittal, William Andrew Publishing, Oxford, 2012, pp. 107–178.

24   S. A. Ghodke, U. Maheshwari, S. Gupta, S. H. Sonawane and B. A. Bhanvase, in *Micro and Nano Technologies*, eds. B. Bhanvase, S. Sonawane, V. Pawade and A. B. T.-H. of N. for W. T. Pandit, Elsevier, 2021, pp. 343–366.

25   M. Thommes, K. Kaneko, A. V. Neimark, J. P. Olivier, F. Rodriguez-Reinoso, J. Rouquerol and K. S. W. Sing, *Pure Appl. Chem.*, 2015, **87**, 1051–1069.

26   K. V. Kumar, S. Gadipelli, B. Wood, K. A. Ramisetty, A. A. Stewart, C. A. Howard, D. J. L. Brett and F. Rodriguez-Reinoso, *J. Mater. Chem. A*, 2019, **7**, 10104–10137.

27   D. R. Baer and S. Thevuthasan, ed. P. M. B. T.-H. of D. T. for F. and C. (Third E. Martin, William Andrew Publishing, Boston, 2010, pp. 749–864.

28   M. H. Engelhard, T. C. Droubay and Y. Du, eds. J. C. Lindon, G. E. Tranter and D. W. B. T.-E. of S. and S. (Third E. Koppenaal, Academic Press, Oxford, 2017, pp. 716–724.

29   M. JANSSENS, ed. V. B. B. T.-F. T. of M. U. in C. Apte Transport and Mining, Woodhead Publishing, 2006, pp. 22–62.

30   M. Das, N. Kamboj, T. Purkait, S. Sarkar and R. S. Dey, *J. Phys. Chem. C*, 2020, **124**, 13525–13534.

Chapter 3

Highly conducting and robust laser-irradiated graphene as high-performance metal-free micro-supercapacitor for an integrated storage device
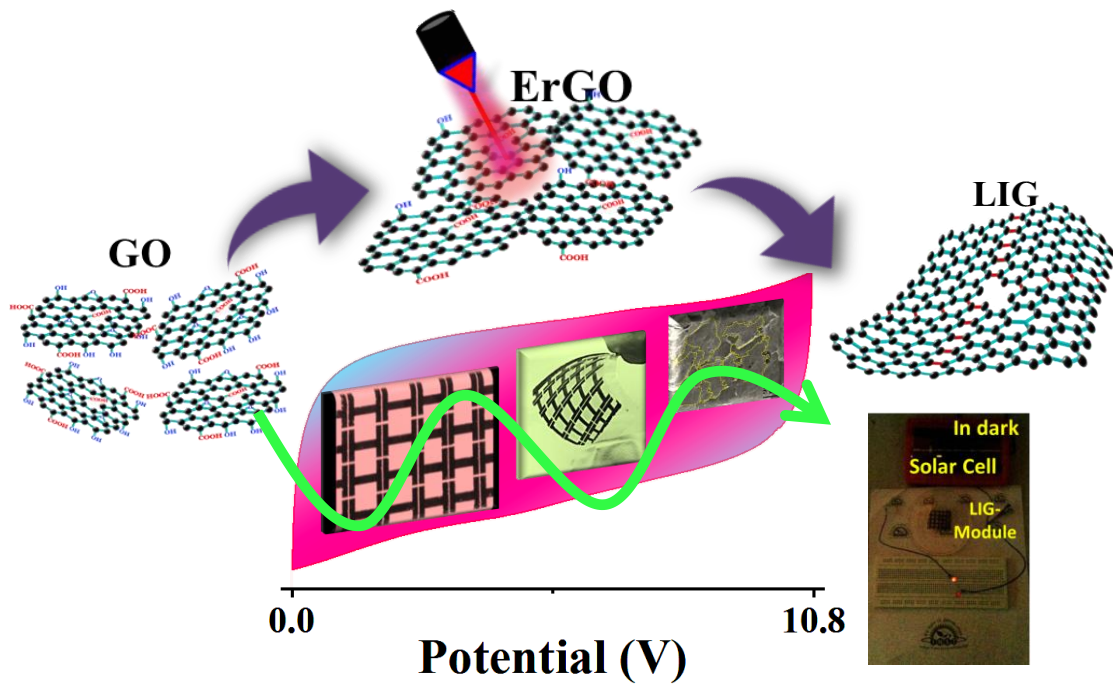
Abstract: Interconnected porous graphene plays a crucial role as supercapacitive material as well as a current collector in developing metal free microsupercapacitor (MSC) because of its unique structure and superior conductivity. Electrochemical reduction followed by use of a laser irradiation method shows advances for the fabrication of the conductive graphene-based robust device. Raman spectra further proves that the laser irradiation method is capable of healing the defects with fused interconnected sheets, as a result of which high conductivity and improved crystallinity of the laser irradiated graphene (LIG) sample is achieved. The LIG film on a flexible substrate was patterned with the aim to develop an on-chip flexible MSC, which offers a large working voltage of 1.2 V in an aqueous solid electrolyte. Interestingly, the MSC, without any metal current collector, shows a unique electrical-double layer behavior and unprecedented cycling stability. It is worth noting that the retention of the initial capacitance after 100,000 continuous cycles was 100%. A large cell voltage of 10.8 V was realized by modularizing the array of devices without much degradation of the rectangular shapes of the voltammogram even at higher scan rates (100 V s^{-1}). The array of LIG-MSC was integrated with a commercial solar cell module for hybrid energy harvesting and as a storage device. This study provides an effective strategy to build a metal free supercapacitor with exceptional cycle life and facilitates progress towards self-sustainable energy in the future.

3.1 Introduction

Because of the continuous production of new technologies and internet of things (IOT), flexible, low cost and high performance integrated energy storage systems are in considerable demand.[1,2] An energy storage device with high cell voltage, high energy density and ultralong cycle life is the fundamental concern for today's technology and has potential for use in the state-of-the-art consumer electronics,[3] microrobots,[4] integrated sensors[5] and hybrid devices. A large working voltage in aqueous media is an age old unresolved problem, because the potential for electrochemical stability of water is 1.23 V.[6] Therefore, to meet the actual demand of high voltage, a numbers of supercapacitor cells have to be connected in series/in parallel. Traditional microscale supercapacitors and batteries with a nonplanar or stacked geometry do not satisfy the rigorous conditions of high-voltage flexible electronic devices.[7] A planar microsupercapacitor (MSC) is a type of miniaturized electrochemical storage device, which can easily be embedded in microelectronic systems offering a large power density (by several fold) than the conventional batteries or supercapacitors for their short ion-diffusion length.[8] However, due to moderate lifetime of the MSCs, they suffer from costly maintenance and periodic replacement, which often damage the embedded electronics. The major drawback of using metal as a current collector in aqueous electrolyte is corrosion[9] that leads to the diminution in their cycle life and also increase the total weight of the supercapacitor. Metal current collector may include the interfacial resistance between metal and active material, which could impede the charge storage properties of supercapacitor. Dissolution, phase change and the side reactions of active material also induce negative effect on cycling performances of the device.[10] To overcome these issues, considerable efforts have been made for the development of a metal-free current collector as well as active material.[11–13] Therefore, the development of highly conductive carbonaceous materials that will work under large voltage window in aqueous electrolyte and perform for a long time, remains a challenge to the researchers in this field.

Carbonaceous materials such as carbon nanotubes (CNTs)[14], carbon nanofiber[15], graphitic carbon nitride[16], onion-like carbon[17], carbide-derived carbon[18], graphene[19] and reduced graphene oxide[20], have been explored for the fabrication of MSCs due to their extraordinary properties such as high effective

surface area, electrical conductivity and mechanical robustness. From material perspective, Graphene stands out as a very promising candidate for supercapacitor owing to its many pleasing properties like good thermal and chemical stability, wide potential window, porous structure and excellent mechanical flexibility.[21] The supercapacitive performance of graphene primarily depends on the quality of graphene, which is directly related to their porosity, conductivity, number of layers and presence of defects. It is established that mass-production of graphene by mechanical exfoliation or chemical vapour deposition methods is not possible due to low yield and high cost though it exhibits ideal properties like negligible defect density and single layer structure and thus not suitable for energy storage application.[22] It is therefore highly desired to look for an inexpensive process that does not involve any reducing agents and high-end equipment to produce high quality graphene-based film with less defects and superior conductivity.

Electrochemical reduction and simultaneous deposition of rGO networks on metal substrate has drawn considerable interest due to its versatile applications in the large-area device.[23,24] Despite of its several advantages, electrochemically reduced graphene oxide (ErGO) has shortcomings as active materials. Firstly, it does not have sufficient conductivity and the surface pores are not open to the electrolyte when it is used as supercapacitor due to significant decrease in the active surface area caused from the re-stacking of ErGO sheets and limits ion transportation through the channels. Furthermore, as the metal current collectors (gold, copper and nickel) are used for the deposition of ErGO, interfacial resistance between the metal and ErGO sometimes is considerably high. Nowadays, laser scribed graphene derived from polyimide sheets shows potential for the development of flexible MSC,[25–27] it fails to achieve large potential window in aqueous electrolyte and high conductivity, as a result, the cycling performance of the devices are not superior for practical applications. Therefore, laser irradiated reduction of rGO or ErGO via computer controlled laser writing methods for the preparation and patterning of electrode has drawn substantial attention because it simplifies the development of on-chip microsupercapacitor (MSC).[7,28,29] The combination of electro-reduction and laser-irradiated reduction to achieve the complete graphitization of the network may revolutionize in the field of storage technology and the challenges are still open.

In this paper, a new strategy is presented, in which highly conductive graphene networks are synthesized that can act as a current collector, by replacing metals with combinations of electrochemical and LI methods for the development of metal free flexible MSCs. The LIG-based MSC is efficient in displaying unique capacitive behaviour and extraordinary life cycle. Furthermore, a laser irradiated graphene (LIG) supercapacitor was extended in series and in parallel to make a high voltage module. In particular, a hybrid structure of a solar cell and a supercapacitor was fabricated to power the supercapacitor module for the demonstration of self-powered small electronics.

3.2 Experimental Section

3.2.1 Simultaneous electrochemical reduction and deposition of a graphene oxide network

The overall synthesis procedure is schematically illustrated in Fig. 3.1a. First of all, a graphene oxide (GO) suspension was prepared from natural graphite powders, using a
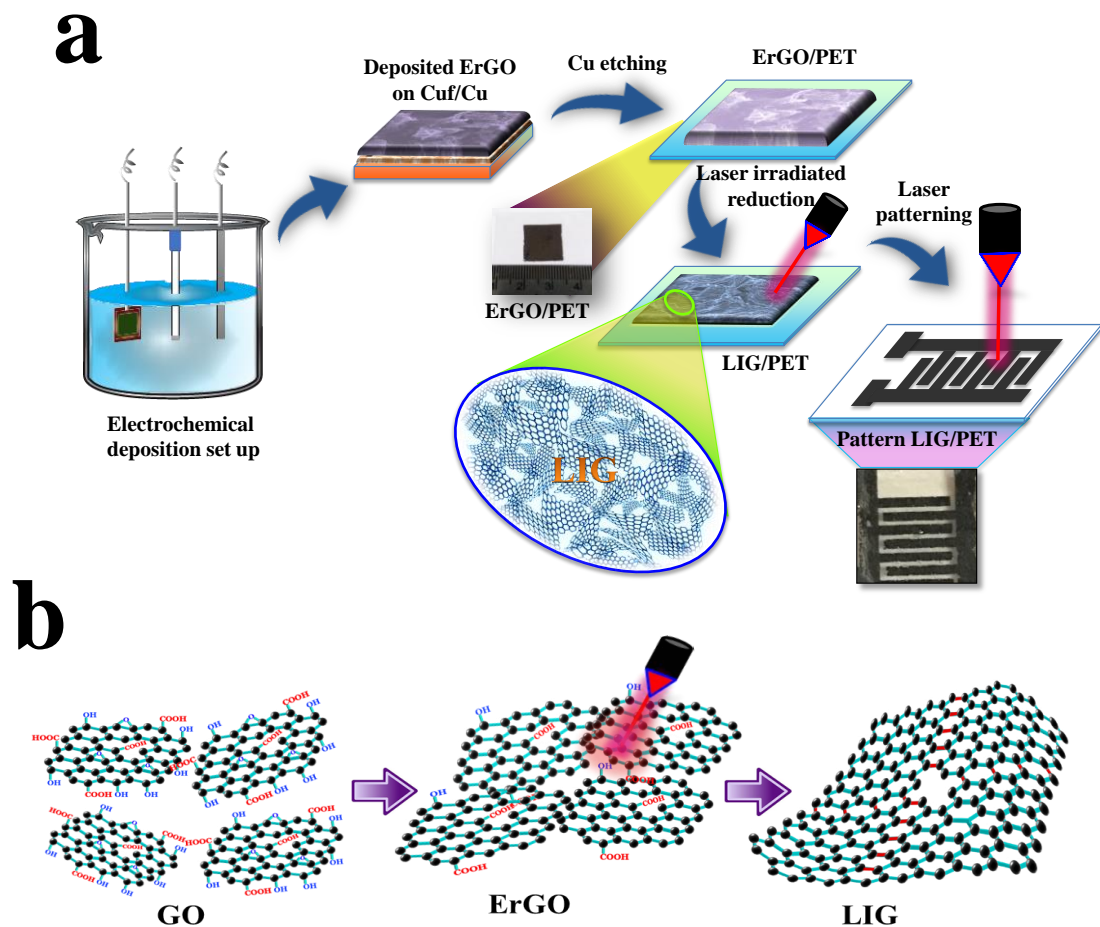
Figure 3.1. (a) Schematic representation of the electrochemical synthesis followed by laser-irradiated reduction used for the preparation of LIG-MSC, (b) Proposed reaction mechanism for the conversion of GO to ErGO and to LIG.

modified Hummers' method as explained in chapter 2 and also reported elsewhere.[30,31] The rGO network was electrochemically grown on galvanostatically deposited copper foam (Cuf) (details are provided in chapter 2) using the electrolysis of GO suspension in perchloric acid at an applied potential of -1.0 V for 60 s to 120 s to obtain the desired thickness. The as-prepared ErGO thin film deposited on the Cuf/Cu was kept in ammonium persulfate solution (with the rGO side facing up) for the etching of Cu from the ErGO film. The freestanding ErGO thin film was washed three to four times with deionized water and finally transferred by scooping it up on to a poly(ethylene terephthalate) (PET) sheet (Fig. 3.1a). The ErGO/PET was kept at ambient conditions overnight (~12 h) to dry the film for further use.

3.2.2 Laser irradiation method for the synthesis of LIG

The LI method was used to further reduce the partially reduced or unreduced functional group present in the ErGO film. Laser irradiation of ErGO/PET was conducted with a 10.6 μm carbon dioxide (CO_2) laser engraver system at various laser pulse powers (48–60W) at room temperature. The LI exposure was made using a circled laser spot with speed of 1.6 m s^{-1}, a focal point of two inches and a frequency of 1000 Hz in one pass. The actual mechanism of the LI process has for a long time not been well known. However, it is reported that the LI process is responsible for making a huge change in the local temperature (> 2500 °C), which could easily break the bonds (C–O and C=O) present in the ErGO surface.[6,32–34] Then, either the released small atoms/molecules recombined to form gases or the edge group undergoes a rearrangement process to form the graphitic structures.[28] The latter path is actually responsible for the fusion/interconnection of two graphene sheets, which may revolutionize the structural and electrical properties of the film as shown in Fig. 3.1b schematically. The LI process involves a two-step reduction pathway. First, the photochemical removal of oxygen was realized on the surface followed by the thermal restoration of the π-cloud in the graphene networks.[35] The depth of penetration mainly depends on the wavelength of the laser radiation, the laser power output and the duration of exposure, which was optimised in the present study. Therefore, the LI process results in the restoration of the sp^2 carbons and makes the film more compact and flattened because of the removal of the oxygen functionalities present in the surface (Fig. 3.1b). Furthermore, the thickness of the film was reduced to 7 μm in LIG from 25 μm in ErGO (Fig. 3.2a-c); in addition, it retains the mechanism of the LI process discussed previously. The laser irradiated GO (LIGO) was
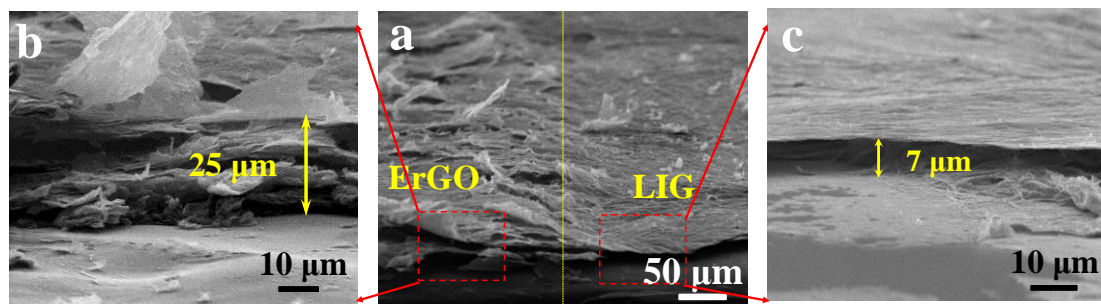
Figure 3.2. *(a) SEM images showing cross-sectional image of a film in which half portion of the film is laser-irradiated and other half is only electrochemically reduced i.e., ErGO, (b) Thickness measurements of (b) ErGO and (c) LIG;ErGO and LIG supported on flexible PET sheet shows a cross-sectional length of 25 µm and 7 µm, respectively.*

prepared using a similar method with drop casting of the GO sample on a flexible substrate for comparison.

3.2.3 Fabrication of flexible interdigitated microsupercapacitor (IMSC)

The LIG film was patterned to interdigital structures of 5 positive and 5 negative microelectrodes having actual width, length and inter-finger distance of about 670 µm, 5000 µm and 200 µm, respectively. Patterning was carried out by 1.06 µm near-infrared (NIR) laser source of power 30 W, speed 0.5 m s^{-1} and 20,000 Hz frequency in one pass. The laser-engraving process took about 30 sec to pattern a single device. To fabricate the solid-state IMSC, a clear solution of PVA/H$_3$PO$_4$ gel electrolyte was prepared by successively adding H$_3$PO$_4$ (600 µl) and PVA (1 g) into 9.4 mL deionized water and heating to 85° C under continuous stirring for 2 hours. The transparent PVA/H$_3$PO$_4$ gel electrolyte was drop casted on the active interdigital electrode areas and kept for drying for 24 h under ambient conditions.

3.3 Results and discussion

3.3.1 Physicochemical characterization of electrode materials

Scanning electron microscopic (SEM) and transmission electron microscopic (TEM) investigations were carried out to investigate the structure and morphology of the ErGO and LIG materials. Fig. 3.3a shows the SEM image of the film containing both ErGO and LIG material as indicated, whereas the ErGO shows a wrinkled morphology that was flattened after laser irradiation. The morphology differences of the film clearly demonstrate the conversion of ErGO to LIG. A comparative SEM analysis was performed for both the ErGO and LIG film and the results are shown in Fig. 3.3b–g. A high-resolution SEM study of the ErGO revealed a networked structure with wrinkled sheets at the pore (Fig. 3.3b), wall (Fig. 3.3c) as well as at the boundary (Fig. 3.3d) of

the pore. The LIG film after laser irradiation was flattened throughout its surface (Fig. 3.3e–g). The detailed SEM study of LIG MSC (Fig. 3.3h and i) confirmed that the graphene sheets were fused together (as marked with the dotted line) and formed a continuous sheet on the surface during the LI. Fig. 3.3j and k are the SEM images of the patterned MSC device, which show the actual width, length and inter-finger distances of about 670 μm, 5000 μm and 200 μm, respectively. High-resolution TEM analysis taken from the edge of a graphene sheet revealed the uniform and transparent nature of the sheet (Fig. 3.3l and m). As shown in the proposed mechanistic pathway (Fig. 3.4), interconnected networks and partially reduced GO were obtained using the electrochemical methods. However, the LI method helped to achieve fully reduced GO with a fused interconnected sheet, as confirmed from the SEM study (Fig. 3.3i). The electrochemical method utilizes the edge functional group of GO to create the network-like structure, whereas the LI method accelerated the generation of the fused sheet-type architecture (Fig. 3.1b) on the surface of the film. It was observed that the C–C bonds present in the ErGO network could absorb the frequency 927–951 cm^{-1}, generally used for a CO_2 laser (10.6 μm), thus it was useful for the complete graphitization of the networks.[36,37] The atomic percentages of C and O were quantified using energy dispersive spectral analysis and mapping results, which is found to be 93.35 % and 6.65 %, respectively (Fig. 3.4). The degree of reduction for oxygen containing functionalities was monitored using Fourier-transform infrared spectroscopy (FTIR) spectra (Fig. 3.5a).
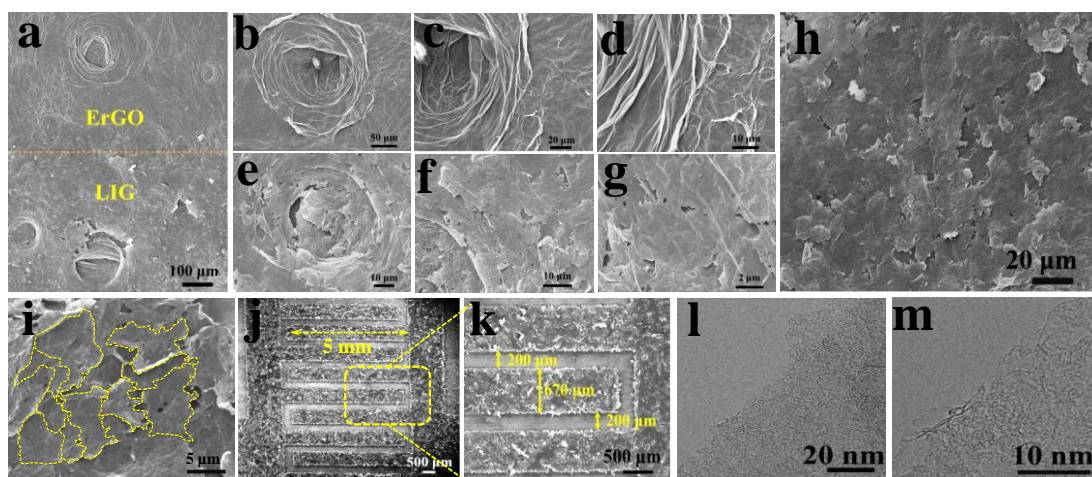
Figure 3.3. The SEM image of the film (a) with ErGO (top half) and LIG (bottom half), the yellow dashed line is used to distinguish the different materials. The SEM images focusing on pore, boundary of pore and planar surface of ErGO (b–d) and LIG (e–g). The SEM images (h and i) of the LIG sheet showing the fused architecture of the film. The SEM images (j and k) of the MSC device taken after laser patterning. High-resolution TEM images (l and m) of the LIG sheet from the edge of the networks.

The FTIR spectra of GO shows peaks for the O–H stretching (3420 cm^{-1}), C=O stretching (1714 cm^{-1}), and stretching of other oxygen functionalities, which was reduced to ErGO and almost disappeared in the LIG sample, confirming the reduction of GO to LIG. [38] The X-ray diffraction pattern (Fig. 3.5b) of GO shows a sharp peak at 2θ=11° with d-spacing of 0.398 nm, whereas ErGO and LIG show a broad peak at 2θ=24.6° (with d-spacing at 0.190 nm). However, a more intense peak observed for LIG indicated the highly crystalline nature of the sample. [39] The X-ray photoelectron spectroscopy (XPS) results further confirmed the effects of laser irradiation on the oxygen functionalities. Fig. 3.5c shows the C1s XPS spectra of ErGO consisted of three peaks at 284.3 eV (C–C/C=C), 286.0 eV (C=O/C–O), and 288.3 eV (O–C=O), whereas LIG contained two peaks at 284.3 eV (C–C/C=C) and 285.5 eV (C=O/C–O). The peak intensities for the oxygen containing groups of LIG were impressively reduced, confirming that the adequate reduction of ErGO using the LI method and transformation of C (sp^3) to C (sp^2) occurred in LIG. To investigate the disorder, defects and crystalline nature of the graphene, Raman spectroscopy was conducted for GO, LIGO, ErGO and LIG thin film samples (Fig. 3.5d-f). The G-band is responsible for the first order scattering of the E_{2g} phonon, whereas the D-band occurred because of the elastic scattering from the defects with a single phonon transition of A_{1g} symmetry and required defect sites for activation.[40] The I_G/I_D ratio, which quantified the defects for GO, was calculated to be 0.71, which was improved compared to the ~0.94 for ErGO, confirming that the smaller defect site of ErGO film appeared after the electrochemical reduction. However, a dramatic increase in the I_G/I_D ratio (~16.1) was observed in the LIG sample, which was ~20

Element	Weight %	Atomic %
Carbon (C)	91.34	93.35
Oxygen (O)	8.66	6.65
Total	100	100

Figure 3.4. Energy dispersive spectra (EDS) for laser irradiated graphene film. (a) EDS spectra obtained from LIG film. (b) Elemental mapping of sample obtained from selected area. Individual elemental distribution of carbon (c) and oxygen (d). Table shows the atomic and weight percent of C and O in the sample.

times larger than that of the GO. Therefore, the LI method helped to greatly reduce the
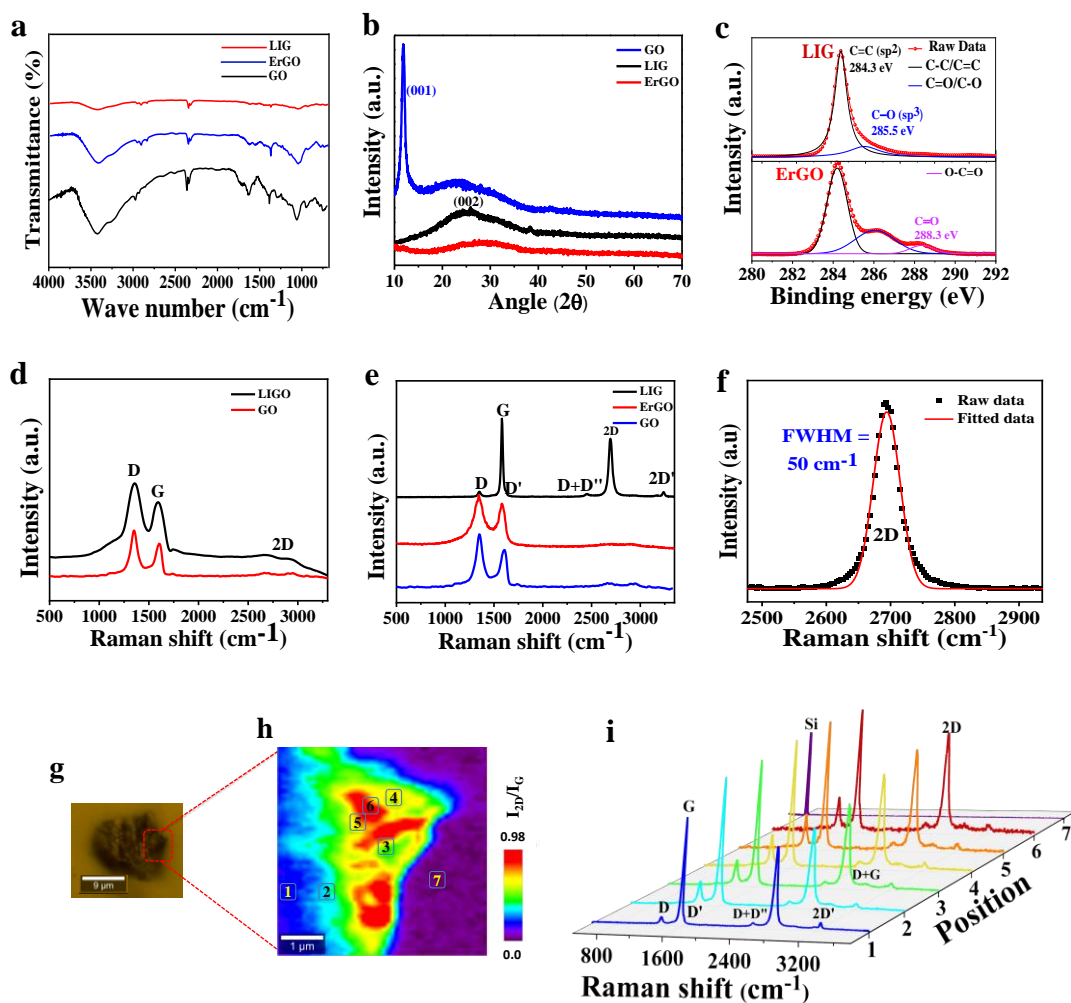
Figure 3.5. *The FTIR spectra (a) of GO, ErGO and LIG samples, (b) XRD analysis of GO, LIG and ErGO. XRD pattern of GO gives a sharp peak at 2θ =11° with d-spacing 0.398 nm. ErGO and LIG shows a broad peak at 2θ=24.6° (d-spacing 0.190 nm). However, the intensity of the peak is sharp for LIG sample, (c) Deconvoluted C1s XPS spectra obtained from ErGO and LIG films. (d) Representative Raman spectra of GO and LIGO, (e) Comparison of Raman spectra obtained from GO, ErGO and LIG, (f) Lorentzian single peak fitting of the 2D band, (g) Optical image of LIG obtained during the Raman measurements. Raman mapping (h) shows the distribution of the 2D peak. Raman spectra (i) of LIG at different positions as described in the mapping, indicating the various intensity ratios of 2D to G.*

defect density n_D (cm^{-2}) from 3.1 (ErGO) to 0.2 (LIG). The degree of graphitization was a consequence of the photothermal process, which was proportional to the laser power and exposure time. Therefore, a higher degree of graphitization occurred with a higher laser power. The laser speed also had a direct influence on the formation of the local temperature.[35] In this case, by decreasing the scan rate, the exposure time of the laser beam per unit area increased, which certainly increased the local temperature. The optimum laser power and speed of the laser were found to be 60 Wand 1.6 ms^{-1}, respectively.

Surprisingly, a very sharp 2D-band occurs only for the LIG sample (Fig. 3.5f) at ~2693 cm^{-1} upon LI, which originated because of a two-phonon transition at the highest optical branch near the **K**.[41] The full width half maxima (FWHM) was calculated to be 50 cm^{-1}. To confirm the uniform distribution of the 2D peak in the LIG sample, Raman mapping analysis was carried out. Fig. 3.5g and h show the optical image and Raman mapping at different positions of LIG, respectively. The corresponding 3D plot of the Raman spectra at seven different regions is shown in Fig. 3.5i. An intense 2D-band was observed in all the positions except point number 7 (on the silica (Si)
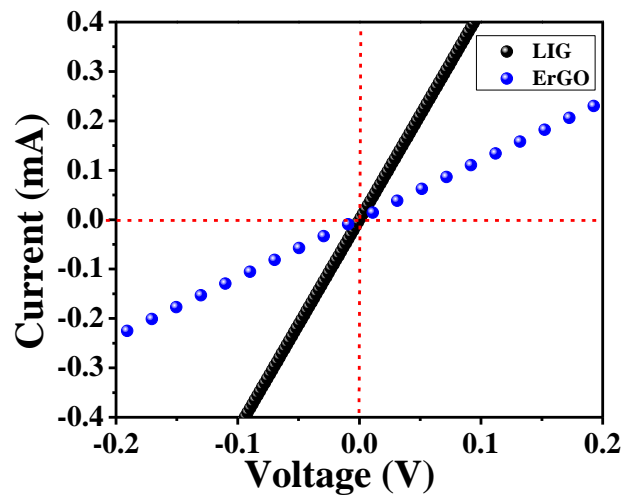
Figure 3.6. *A comparison of electrical conductivity of ErGO and LIG sheet measured by two-probe technique. I-V characteristics for ErGO and LIG shows linear plot, indicating ohmic behavior. The calculated electrical conductivity values for ErGO and LIG are 2123 S m^{-1} and 5963 S m^{-1}, respectively*

substrate), confirming the homogeneous distribution of the 2D peak. Although the LIG sample has a multilayer configuration, it unexpectedly shows an intense 2D peak throughout the sample with single Lorentzian peak fitting, indicating an insignificant interlayer hopping interaction unlike conventional multilayer graphene samples, where a broad 2D peak with multiple Lorentzian peaks are observed.[42] The graphene flakes in the LIG sample were crosslinked to each other in a 3D architecture and after laser irradiation, the film became fused at the surface, and as a result the whole film behaved unitedly as a monolayer graphene film with a very high electrical conductivity. The double resonance peak D' and its overtone 2D' appeared at 1618 cm^{-1} and 3238 cm^{-1}, respectively. These peaks originated from momentum conservation of two phonons with opposite wave vectors.[40] The LIG sample showed the D + D' and the D + G peaks at 2469 cm^{-1} and 2950 cm^{-1}, respectively. The calculated crystalline size (L$_a$) of ErGO was 18.4 nm, and this was improved to 309 nm for LIG, which further proved the improved crystallinity achieved upon LI reduction. The electrical property of the material was investigated to evaluate the performance of the LIG material as an active material as well as a current collector. The conductivity of the LIG was calculated (Fig. 3.6) to be 5963 S m^{-1}, which was almost three times larger than that of the ErGO (2123 S m^{-1}) material.

The electrical conductivity of the LIG film was much higher than that of activated carbon (10–100 S m^{-1}), [43] rGO (100–2000 S m^{-1}) [11] and also that of the laser-scribed graphene
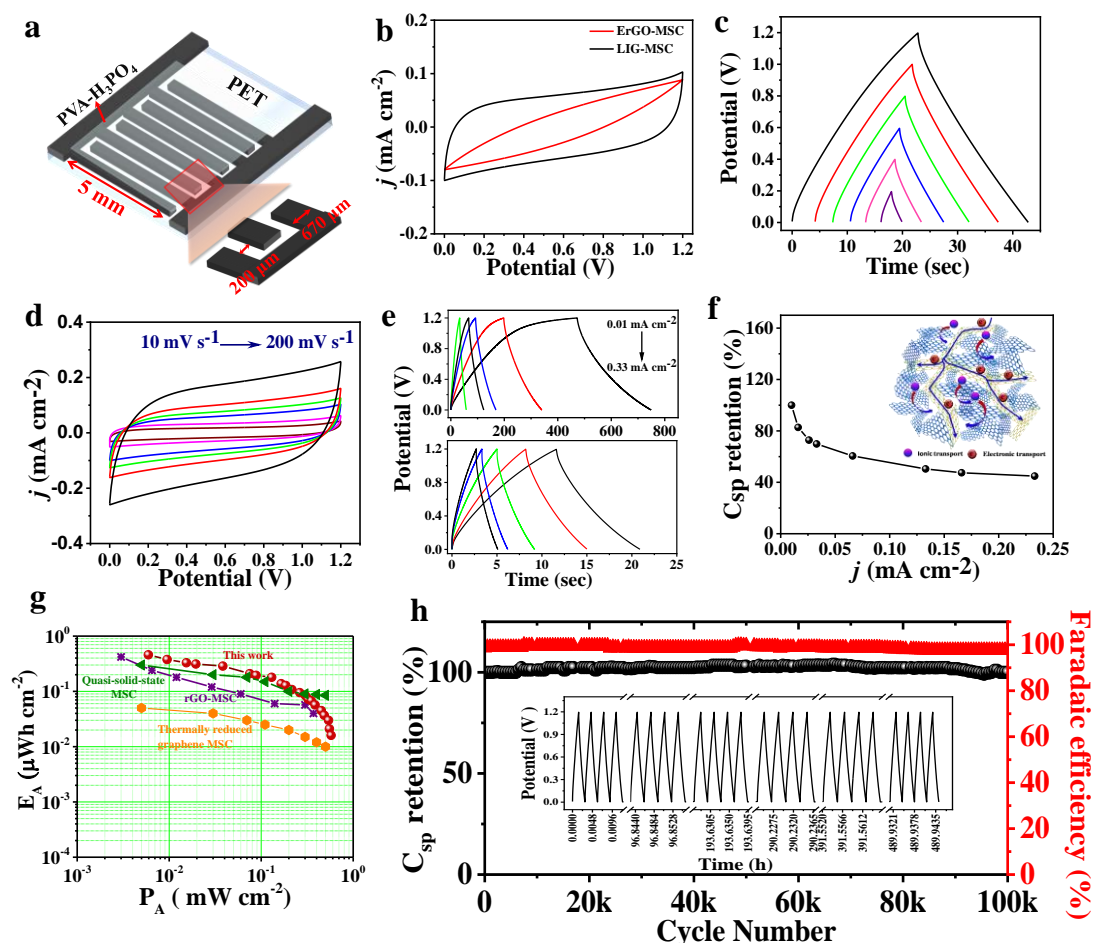
Figure 3.7. *(a) Schematic diagram of the interdigitated LIG-MSC. The cyclic voltammetry response (b) obtained from ErGO and LIG-based MSCs at 50 mV s^{-1}. Galvanostatic charge–discharge profile (c) of the LIG-MSC, used to optimize the working voltage of the device. Cyclic voltammetric response (d) of the in-plane LIG-MSC at different scan rates. Galvanostatic charge–discharge curves (e) at different current densities. (f) A plot of capacitance retention versus current density showing a 42% retention at a current density of 0.23 mA cm^{-2} of its initial capacitance, inset is the mechanistic model illustrating that the ionic and electronic transport occurs in the three-dimensional networks of the LIG material. (g) Comparative Ragone plot of LIG-MSC with various devices using results taken from the literature. (h) Cycling stability performance and faradaic efficiency of an IMSC showing the percentage retention of the initial capacitance up to 100,000 cycles. Inset shows the GCD response for three consecutive cycles of the device during the cycling test obtained after each 20,000 cycles.*

(1738 S m^{-1})[44] synthesized by El-Kady *et al*. The high conductivity of the LIG material was associated with the significant structural changes, which appeared during the LI process. As can be seen from the proposed mechanism shown in Fig. 3.1b, the reduced defect density and improved crystallinity in LIG helps the restoration of the π- electrons clouds. Furthermore, the continuous sheet-like architecture promoted faster electron transportation in the LIG material, which was responsible for the very high conductivity

of LIG. The excellent electrical conductivity value suggested that the LIG material could be a suitable choice as current collector for a supercapacitor.

3.3.2 Electrochemical characterization

Best-practice methods, cyclic voltammetry (CV) and galvanostatic charge–discharge (GCD) was conducted in the solid state with a symmetrical, interdigitated LIG-MSC device (shown schematically in Fig. 3.7a) to demonstrate the superior electric double-layer capacitor (EDLC) behaviour of the material. The CV curve of LIG-MSC (Fig. 3.7b) at 50 mV s^{-1} showed a perfect rectangular shape unlike that of the ErGO-MSC which exhibited a distorted rectangular shape because the material was less conductive, which impeded the ion transfer from the electrolyte to the electrode. The potential window of the device was optimized in aqueous-gel electrolyte to avoid the interference from oxygen evolution reaction, the corresponding GCD curve is shown in Fig. 3.7c. Interestingly, the LIG-based MSC could achieve a large working voltage of 1.2 V (0–1.2 V), which was the highest working voltage ever obtained up to now in aqueous electrolyte with carbon-based supercapacitors (Table 3.1). A dramatic change in the CV of LIG-MSC appeared after LI and the device retained a rectangular shape even at a high scan rate (Fig. 3.7d), which demonstrated the perfect electrochemical double layer formation and fast charge storage mechanism of the device. The quasi-isosceles triangular GCD profiles at different current densities further validated the ideal EDLC behaviour and the efficient mass-transport across the porous LIG fingers shown in Fig. 3.7e. A retention of 42% of its initial capacitance even at a higher current density showed that the device had a good rate capability (Fig. 3.7f) The areal capacitance (C$_A$) of the MSC, taken from the GCD curve was calculated to be 2.32 mF cm^{-2} at a current density 10 mA cm^{-2}, which was quite high compared to most of the reported graphene-based MSCs, such as methane-plasma rGO (8 μF cm^{-2}),[45] inkjet-printed graphene (0.7 mF cm^{-2}),[46] and laser written graphene (0.51 mF cm^{-2}).[47] The corresponding volumetric capacitance (C$_V$) was found to be 3.3 F cm^{-3} at 40 mA cm^{-3}. The superior performances of the device can be explained by the ionic and electronic transport through the device as shown in the inset of Fig. 3.7f. The laser irradiation method produced highly conductive graphene networks with a minimum defect density, where the graphene sheets were interconnected to each other and this facilitated the transport of the electronic current. However, the porous nature of the electrode maximized the surface area exposed to the electrolyte and this resulted in the favourable ionic transport of the electrolyte.

Combinations of these two factors expedite the accomplishment of the high energy density of the device.

The energy and power densities are powerful tools used to check the performance of the MSC. The highest area normalized energy density (E_A) and power density (P_A) of LIG-MSC were calculated to be 0.46 µW h cm^{-2} (0.65 W h cm^{-3}) and 0.57 mW cm^{-2} (822 mW cm^{-3}), respectively. The areal energy density and the power density value of the LIG device were far better than those previously reported for metal free supercapacitors as shown in Fig. 3.7g.[16,25,48–51]

To explore the commercial viability of the MSCs, the cycling performance was compared to the number of cycles and percentage retention of the specific capacitance and was one of the essential measurements. Usually, most of previously studied nanocarbon-based supercapacitors failed to show cycling performances not more than 30,000 cycles withholding 90–95% of the initial capacitance (Table 3.1). The cycling stability of the LIG-based MSC was evaluated by using continuous cycling via a GCD process at a current density of 0.166 mA cm^{-2}. Interestingly, the retention of the initial C_{sp} after 100,000 continuous cycles was ~100%, demonstrating the outstanding stability of the LIG material in an aqueous solid electrolyte (Fig. 3.7h). The inset of Fig. 3.7h
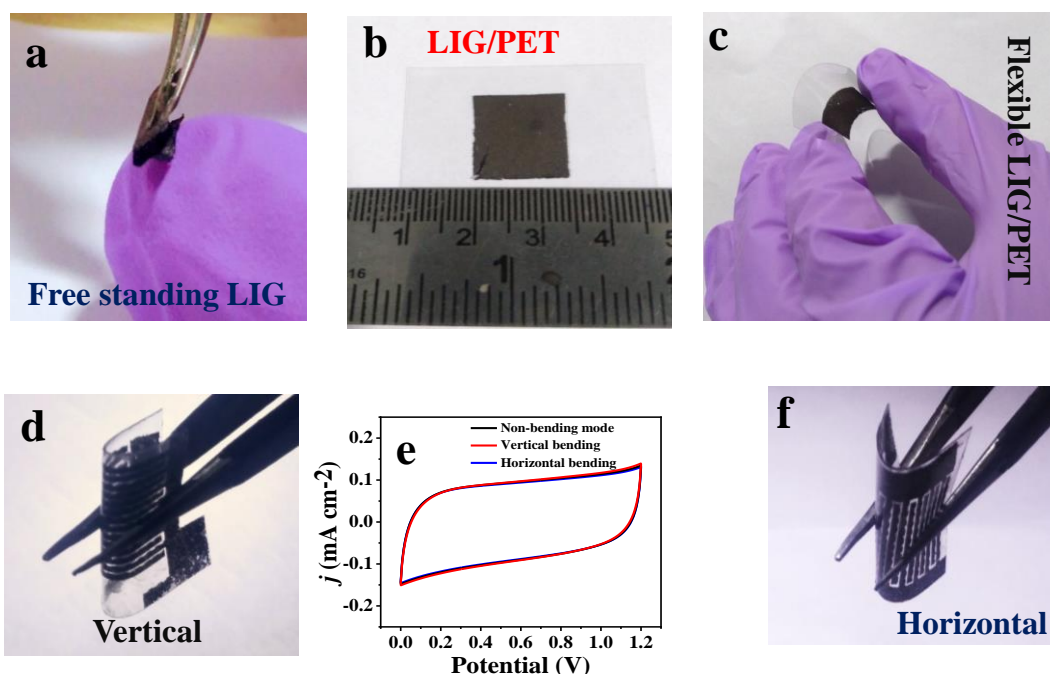
Figure 3.8. *(a) Free-standing reduced LIG film, (b) Optical image of Laser induced film (1.5 x 1.5 cm^2) deposited on PET sheet, (c) Optical image of the LIG sample on PET at bended state, (d) Patterned LIG micro device on PET in bending position, (e) Cyclic voltammetry showing flexibility of the device in vertical and horizontal bending mode, and (f) shows flexibility of the MSC device in horizontal directions.*

shows the GCD response of the LIG-MSC derived after every 20,000 cycles. As expected, a similar charge–discharge phenomenon was observed throughout the course of the 100,000 cycles, thus revealing the exceptional electrochemical stability of the material during continuous cycling. Such extraordinary cycling performances of the supercapacitor had not been achieved up to now, as far as is known (Table 3.1). The interconnected sheet-like structure of LIG and the minimum defect in its backbone are the reasons for the good electronic transport during GCD cycling. The unique porous structure and absence of metal current collector of the LIG-based MSC is the reason for the achievement of the astonishing cycling performance of the LIG-IMSC. The flexibility and durability of the LIG on PET is clearly shown in Fig. 3.8a-c and also the robustness of the LIG-MSC was evaluated using the electrochemical performances of the IMSC at bending condition (Fig. 3.8e). The electrochemical response of the device was recorded
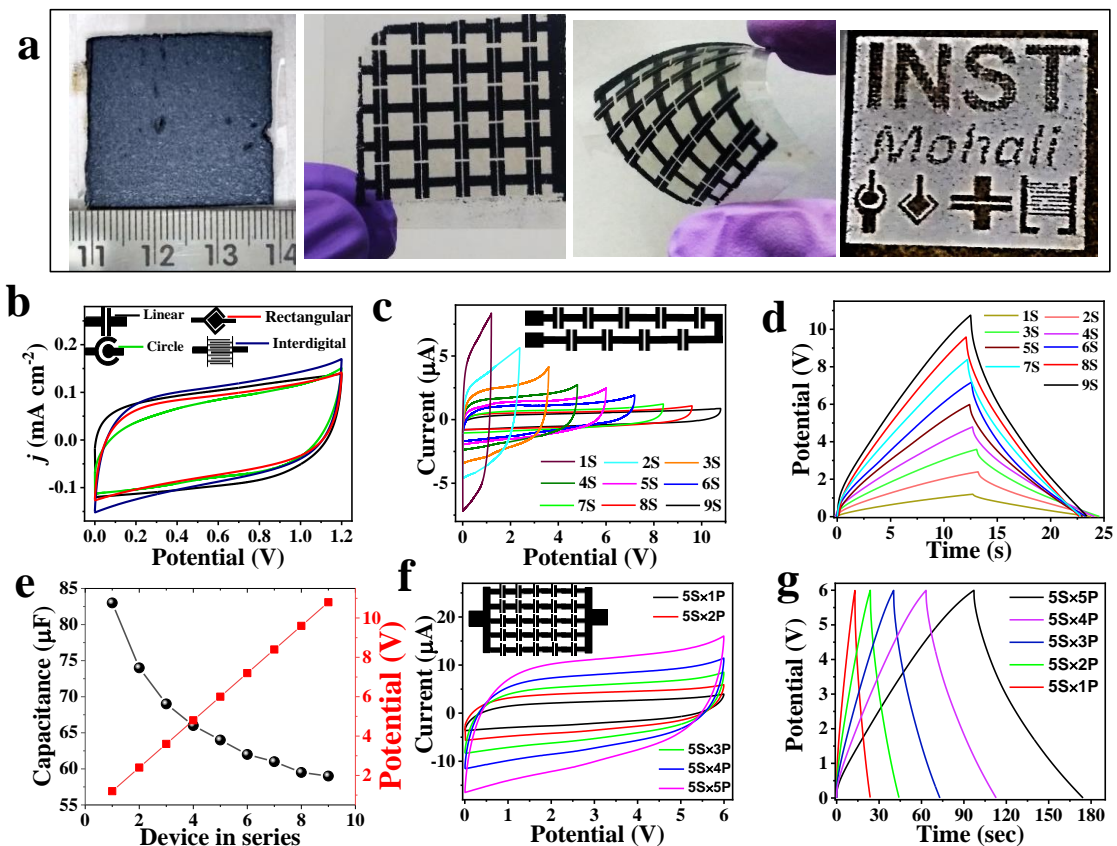
Figure 3.9. *Digital images (a) of LIG film (3×3 cm^2), patterned and flexible LIG-module, various letters and patterns written on the film. (b) CV curves for different shaped LIG-MSCs at a scan rate of 100 mV s^{-1}. The inset shows a diagram of the diverse shapes of the LIG-MSCs. (c) CV curves for linear LIG MSCs connected in series (1S to 9S) at a scan rate of 100 mV s^{-1}, and the inset shows the schematic for the series combination of the nine cells. (d) GCD profile of LIG-MSCs connected in series (1S to 9S) at a current of 10 mA. The calculated capacitance and output voltage (e) as a function of the number of devices in series. The CV response (f) and GCD (g) obtained from mS $\times$ nP (m = 5 and n = 1 to 5) configured module where m = number of cells in series and n = number of cells in parallel.*

in horizontal and vertical bending conditions, like the digital images shown in Fig. 3.8d and f. The CV curves for all the cases exhibited an almost identical current response with the non-bending or planar mode, suggesting an outstanding durability of the LIG-IMSC under mechanical bending. The excellent flexibility of the LIG-MSC shows great potential for future use in portable energy storage devices and microelectronics.

3.3.3 Structural versatility and their performance

To meet the requirements of specific voltage and capacitance rating for different portable devices, a study of the commercial supercapacitors' demand in-series and/or in-parallel connections to provide large output voltage and sufficient capacity to store energy was made.[25,52] Fig. 3.9a shows the digital images of LIG/PET (3×3 cm^2), a patterned module, a flexible LIG-module and different letters (INST Mohali) and structures written on the LIG sheet. In order to fabricate a series of complex modular LIG-MSCs, miniaturising the basic unit cell and their shape is one of the basic criteria that needs to be checked. Therefore, versatile structural LIG-MSC devices with circular, linear, rectangular and interdigitated planar geometries were fabricated with specific size parameters while keeping a constant geometrical area of the different structures. Similar CV curves (Fig. 3.9b) and approximately equal areal capacitances were observed at a scan rate of 100 mV s^{-1} for all versatile LIG-MSCs, which demonstrated an exceptionally good shape compatibility and superior suitability for further applications. Furthermore, as the linear LIG-MSC exhibited better performances in terms of specific capacitance and the shape of the CV graph, the module was patterned with linear shaped MSC.
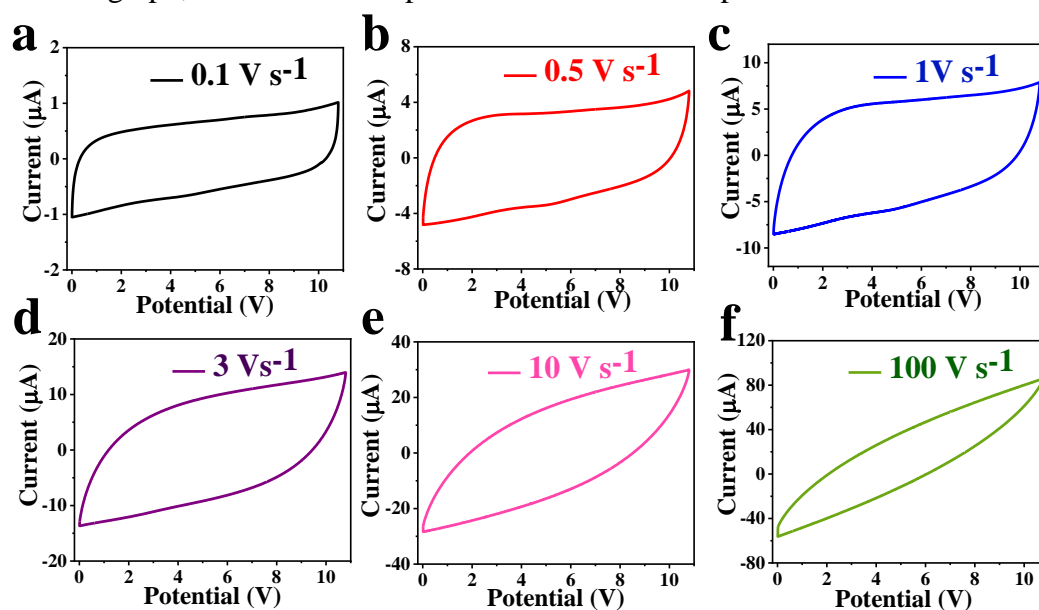
Figure 3.10. *Cyclic voltammetry response (a–f) of the LIG-module with nine devices in series at different scan rates (0.1–100 V s^{-1}).*

3.3.4 Modularization of LIG-MSC for high output voltage

To meet the demand of high voltage, number of MSC units can be connected in series, without compromising with the total current and capacitance. However, to increase the total current and capacitance, a number of supercapacitor cells in series must be
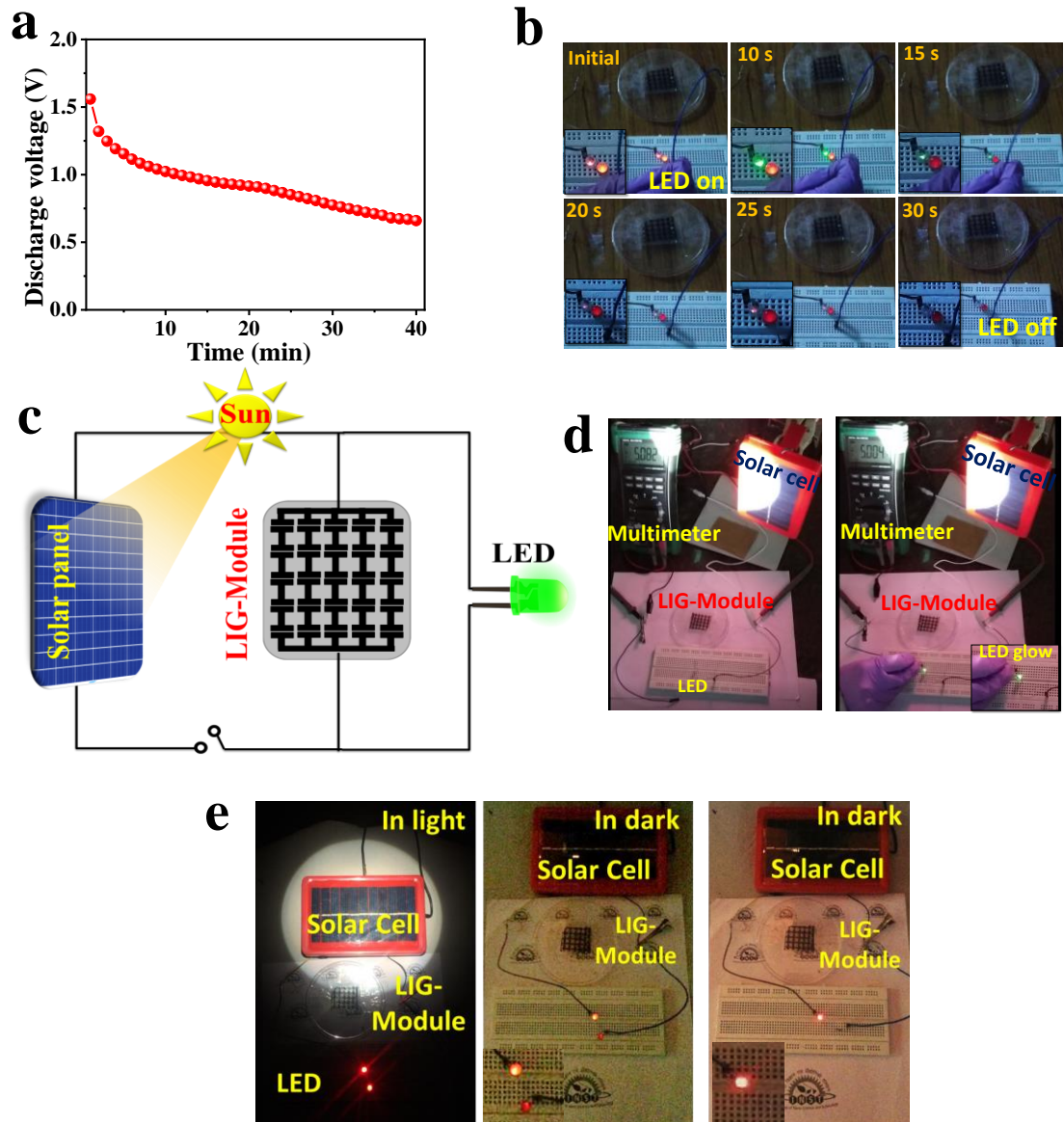
Figure 3.11. *Discharge voltage profile with time (a) obtained using the LIG-IMSC device after charging it at 2 V for 2 min. (b) Lighting the two LEDs using the LIG-module after charging the module at 5 V for 3 min. (c) Schematic representation of the solar cell/supercapacitor hybrid system. Digital images of integrated solar cell-supercapacitor system (d) LIG-Module was charged with solar cell through an open-circuit voltage of 5.082 V as can be seen on multimeter and after unplugging the solar cell, supercapacitor attain an open-circuit potential of 5.004 V. (e) Digital photograph of the assembled solar cell/supercapacitor hybrid power pack in charging mode (marked as 'in light') and lighting the LED after switching off the solar cell (marked as 'in dark').*

configured together in parallel to make an effectively powered system. The output

voltage can be increased from a few to thousands of volts from these patterned structures without compromising the capacitance.

To explore the high voltage applications of LIG-MSC, first, CV and GCD tests were performed with the linear LIG-based MSC devices both in series and in parallel as shown in Fig. 3.9c-g. As projected, all the linear LIG-MSCs connected in series, from a single device to nine devices, showed a nearly rectangular shape with EDLC behaviours (Fig. 3.9c) and exhibited a stepwise linear increase in the working voltage from 1.2 V to 10.8 V (9 × 1.2 V). Surprisingly, in the GCD curves as shown in Fig. 3.9d, the working voltage gradually increases whereas the discharge time almost remains similar in all cases. Fig. 3.9e shows that the working voltage increases and the corresponding capacitance decreases with the number of devices configured in series. To enhance the overall capacitance, five devices were assembled in parallel, which exhibited a gradual increase of current as well as capacitance. Fig. 3.9f and g show a classic demonstration of the LIG-MSC module with 25 linear devices, arranged as five in parallel rows of five serially connected devices (5S × 5P) on PET substrate. Interestingly, two (5S ×2P) and five (5S × 5P) such rows in parallel nearly doubled and increased five-fold the current and capacitance, respectively, when compared to one single row (5S × 1P), attaining a working voltage of 6 V. To evaluate the power capability of the MSC module with nine devices in series, acquiring 10.8 V cell voltage, CVs were recorded at various scan rates starting from 0.1 V s^{-1} to 100 V s^{-1} (Fig. 3.10a–f). It is worth noting that the nearly rectangular pattern was maintained up to an ultrahigh scan rate of 10 V s^{-1} and slight deformation in the shape was observed up to 100 V s^{-1}, which demonstrated the high-rate capability and instantaneous power delivery capacity of the LIG-MSC module.

3.3.5 Integrated self-powered supercapacitor with solar cell

To support the development of sustainable self-powered system for portable electronics, supercapacitors need to be hybridized with energy generation devices such as solar cells for a proper power management strategy.[53,54] The integration of solar cell and supercapacitor module, termed as "self-charging power unit" can help to compensate the power fluctuation in solar cell, yielding stable power output. Furthermore, for constant use of electric charge for consumer electronics; a renewable energy source like solar cell can be assembled in parallel with supercapacitor replacing heavy batteries.[59] At first, the discharge performance of a single device was recorded after charging a LIG-MSC for 2

Table 3.1: *A comparative study of electrochemical performance of carbon based microsupercapacitor*

S. No.	Electrode material	electrolyte	Potential Window	Capacitance C_{sp}	Energy Density	Power density	Stability (Cycle)	Retention	Ref.
1	Graphene	PVA-H_2SO_4	1V	>9 mF cm^{-2} (3.6 F cm^{-3})	0.5 mWh cm^{-3}	5 W cm^{-3}	8000	98 %	8
2	Graphene/graphite paper	1M H2SO4	1 V	15.6 mF cm^{-2}	0.001 mWh cm^{-2}	4 W cm^{-2}	10000	100%	9
3	LSG-SWCNT-MSC	PVA-H3PO4	1V	3.10 F cm^{-3}	0.84 mWh cm^{-3}	1 W cm^{-3}	5000	88.6%	10
4	Graphene foam	H3PO4	2V	38 mF cm^{-2}	3.4 mWh cm^{-2}	0.27 mW cm^{-2}	25000	68 %	11
5	3D- cellular graphene film	PVA-H3PO4	1V	2.47 mF cm^{-2}	0.22 µWh cm^{-2}	0.37 mW cm^{-2}	10000	97.6%	12
6	3D- graphene	Gel electrolyte	1V	2.63 mF cm^{-2}	0.38 µWh cm^{-2}	0.86 mW cm^{-2}	3000	90%	13
7	LIG-MSC	Ionic liquid	1V	>4mF cm^{-2}	0.8 µWh cm^{-2}	9 mW cm^{-2}	8000	100%	7
8	**LIG-MSC**	PVA-H3PO4	**1.2 V**	**2.32 mF cm^{-2} (3.3 mF cm^{-3})**	**459 µWh cm^{-2} (655 µWh cm^{-3})**	**576 mW cm^{-2} (822 W cm^{-3})**	**100000**	**100%**	**This work**

SWCNT- *single walled carbon nanotube,* **PVA**- *poly (vinyl alcohol),* **LIG**- *laser induced (irradiated) graphene*

min at 2 V. The discharge voltage was plotted with discharge time as shown in Fig. 3.11a. Surprisingly, the retention of self-discharge voltage was ~65% after 10 min and more than 50% after 30 min, indicating the excellent device performance of LIG-MSC. The device performance testing was extended by using it to light up the light-emitting diodes (LEDs) after charging the MSC-module (5S × 5P) at 5V for 3 min (Fig. 3.11b). Thereafter, in order to understand the superiority of the LIG-MSC as a hybrid system, a solar cell with an open-circuit potential of 5 V was integrated with the flexible LIG-module (5S × 5P) as schematically illustrated in Fig. 3.11c. Fig.3.11d shows the integrated solar cell/supercapacitor power pack, which was connected to the LEDs. Before charging, the open circuit voltage of the LIG-module was recorded as 0.135 V. After charging with the solar cell (open circuit voltage of 5.082 V and acting as the power source to charge the supercapacitor), the stable open circuit potential of the module was increased to 5.004 V (Fig. 3.11d) indicating the superiority of the module as a power pack unit. The solar cell was then subjected to light illumination for 10 s and then the light source was removed. The charged supercapacitor connected with solar cell was used to lighten up an LED (Fig. 3.11e) for another 35 seconds. Another demonstration of the LIG-module was obtained by using two already glowing LEDs simultaneously (Fig. 3.11e) by charging the module for 10 s with a solar panel. This demonstration of LED with a solar-powered LIG-MSC validated the concept of the self-charging unit by transferring enough energy from an energy conversion unit towards a storage system. The excellent device performances of the MSC module proved the suitability of the LIG-MSC for commercialization in the future.

3.4 Conclusions

In conclusion, a new combination of electrochemical reduction and a laser irradiation technique has been introduced for the first time for the synthesis of a highly conducting and robust graphene film. A flexible, on-chip microsupercapacitor was established for the demonstration of supercapacitive behaviour of the device with a cell voltage of 1.2 V. The notable improvement of the stability performances (100, 000 cycles) of LIG-MSC open up a new field for the development of a metal free supercapacitor. The unique structure of LIG and the interconnected highly conductive graphene sheets with fewer defects are responsible for the ion and electron transport channel with a short diffusion length. The cost-effective and environmentally friendly synthesis approach makes it a model candidate for the next generation supercapacitor electrode design. The LIG-based

MSCs were organized in series with an in parallel arrangement for the demonstration of high-voltage output without sacrificing the capacitance of the module. Furthermore, the LIG-based MSC module was integrated with a solar cell to realize its advantage for the development of a hybrid storage system. The synthetic approach, modularization and hybridization can be scaled-up with a proper electrochemical set-up and could greatly influence the field of microelectronics and wearable integrated storage devices.

3.5 References

1   Z. Cao and B. (B. Q. . Wei, *Energy Environ. Sci.*, 2013, **6**, 3183–3201.

2   Y. Fu, H. Wu, S. Ye, X. Cai, X. Yu, S. Hou, H. Kafafy and D. Zou, *Energy Environ. Sci.*, 2013, **6**, 805–812.

3   G. Lota, K. Fic and E. Frackowiak, *Energy Environ. Sci.*, 2011, **4**, 1592–1605.

4   F. Ilievski, A. D. Mazzeo, R. F. Shepherd, X. Chen and G. M. Whitesides, *Angew. Chemie Int. Ed.*, 2011, **50**, 1890–1895.

5   C. H. Wang, Y. Liu, M. Desmulliez and A. Richardson, in *2009 4th International Design and Test Workshop (IDT)*, 2009, pp. 1–6.

6   H. Tomiyasu, H. Shikata, K. Takao, N. Asanuma, S. Taruta and Y.-Y. Park, *Sci. Rep.*, 2017, **7**, 45048.

7   P. Huang, C. Lethien, S. Pinaud, K. Brousse, R. Laloo, V. Turq, M. Respaud, A. Demortiere, B. Daffos, P. L. Taberna, B. Chaudret, Y. Gogotsi and P. Simon, *Science*, 2016, **351**, 691–695.

8   M. Beidaghi and Y. Gogotsi, *Energy Environ. Sci.*, 2014, **7**, 867–884.

9   Z. Hu, Q. Liu, S. Chou and S. Dou, *Adv. Mater.*, 2017, **29**, 1700606.

10   N. Blomquist, T. Wells, B. Andres, J. Bäckström, S. Forsberg and H. Olin, *Sci. Rep.*, 2017, **7**, 39836.

11   M. Wu, Y. Li, B. Yao, J. Chen, C. Li and G. Shi, *J. Mater. Chem. A*, 2016, **4**, 16213–16218.

12   Z. S. Wu, S. Yang, L. Zhang, J. B. Wagner, X. Feng and K. Müllen, *Energy Storage Mater.*, 2015, **1**, 119–126.

13   L. Manjakkal, C. G. Núñez, W. Dang and R. Dahiya, *Nano Energy*, 2018, **51**, 604–612.

14   W. Chen, M. Beidaghi, V. Penmatsa, K. Bechtold, L. Kumari, W. Z. Li and C. Wang, *IEEE Trans. Nanotechnol.*, 2010, **9**, 734–740.

15   Q. Jiang, N. Kurra, C. Xia and H. N. Alshareef, *Adv. Energy Mater.*, 2017, **7**,

1601257.

16   Z.-S. Wu, K. Parvez, X. Feng and K. Müllen, *Nat. Commun.*, 2013, **4**, 2487.

17   D. Pech, M. Brunet, H. Durou, P. Huang, V. Mochalin, Y. Gogotsi, P. Taberna and P. Simon, *Nat. Nanotechnol.*, 2010, **5**, 651–654.

18   J. Chmiola, C. Largeot, P.-L. Taberna, P. Simon and Y. Gogotsi, *Science*, 2010, **328**, 480–483.

19   N. A. Kyeremateng, T. Brousse and D. Pech, *Nat. Nanotechnol.*, 2017, **12**, 7–15.

20   J. Chen, Y. Wang, J. Cao, Y. Liu, Y. Zhou, J. H. Ouyang and D. Jia, *ACS Appl. Mater. Interfaces*, 2017, **9**, 19831–19842.

21   Y. Shao, M. F. El-Kady, L. J. Wang, Q. Zhang, Y. Li, H. Wang, M. F. Mousavi and R. B. Kaner, *Chem. Soc. Rev.*, 2015, **44**, 3639–3665.

22   R. Raccichini, A. Varzi, S. Passerini and B. Scrosati, *Nat. Mater.*, 2015, **14**, 271–279.

23   M. Hilder, B. Winther-Jensen, D. Li, M. Forsyth and D. R. MacFarlane, *Phys. Chem. Chem. Phys.*, 2011, **13**, 9187–9193.

24   T. Purkait, G. Singh, D. Kumar, M. Singh and R. S. Dey, *Sci. Rep.*, 2018, **8**, 640.

25   M. F. El-Kady and R. B. Kaner, *Nat. Commun.*, 2013, **4**, 1475.

26   G. Hu, M. Mao and S. Ghosal, *Nanotechnology*, 2012, **23**, 395501.

27   Y. Wang, Y. Wang, P. Zhang, F. Liu and S. Luo, *Small*, 2018, 14.

28   J. Lin, Z. Peng, Y. Liu, F. Ruiz-Zepeda, R. Ye, E. L. G. Samuel, M. J. Yacaman, B. I. Yakobson and J. M. Tour, *Nat. Commun.*, 2015, **5**, 1–8.

29   V. Strong, S. Dubin, M. F. El-Kady, A. Lech, Y. Wang, B. H. Weiller and R. B. Kaner, *ACS Nano*, 2012, **6**, 1395–1403.

30   W. H. Jr and R. Offeman, *J. Am. Chem. …*, 1958, **208**, 1937.

31   R. S. Dey, H. A. Hjuler and Q. Chi, *J. Mater. Chem. A*, 2015, **3**, 6324–6329.

32   J. Lin, Z. Peng, Y. Liu, F. Ruiz-Zepeda, R. Ye, E. L. G. Samuel, M. J. Yacaman, B. I. Yakobson and J. M. Tour, *Nat. Commun.*, 2014, **5**, 5714.

33   T. N. Lin, K. H. Chih, C. T. Yuan, J. L. Shen, C. A. J. Lin and W. R. Liu, *Nanoscale*, 2015, **7**, 2708–2715.

34   Z. Wan, E. W. Streed, M. Lobino, S. Wang, R. T. Sang, I. S. Cole, D. V Thiel and Q. Li, *Adv. Mater. Technol.*, 2018, **3**, 1700315.

35   B. S. Yilbas, Z. Yilbas and M. Sami, *Opt. Laser Technol.*, 1996, **28**, 513–519.

36   C. K. N. Patel, *Phys. Rev.*, , DOI:10.1103/PhysRev.136.A1187.

37   Y. Chyan, R. Ye, Y. Li, S. P. Singh, C. J. Arnusch and J. M. Tour, *ACS Nano*,

2018, **12**, 2176–2183.

38   R. S. Dey, S. Hajra, R. K. Sahu, C. R. Raj and M. K. Panigrahi, *Chem. Commun.*, 2012, **48**, 1787.

39   M. P. Down and C. E. Banks, *ACS Appl. Energy Mater.*, 2018, **1**, 891–899.

40   A. C. Ferrari and D. M. Basko, *Nat. Nanotechnol.*, 2013, **8**, 235–246.

41   C. Thomsen and S. Reich, *Phys. Rev. Lett.*, 2000, **85**, 5214–5217.

42   R. Fossheim, *Acta Chem. Scand.*, 1985, **39**, 785–790.

43   A. G. Pandolfo and A. F. Hollenkamp, *J. Power Sources*, 2006, **157**, 11–27.

44   M. F. El-Kady, V. Strong, S. Dubin and R. B. Kaner, *Science*, 2012, **335**, 1326–1330.

45   S. Wang, Z.-S. Wu, S. Zheng, F. Zhou, C. Sun, H.-M. Cheng and X. Bao, *ACS Nano*, 2017, **11**, 4283–4291.

46   J. Li, S. Sollami Delekta, P. Zhang, S. Yang, M. R. Lohe, X. Zhuang, X. Feng and M. Östling, *ACS Nano*, 2017, **11**, 8249–8256.

47   Z.-S. Wu, K. Parvez, X. Feng and K. Müllen, *Nat. Commun.*, 2013, **4**, 2487.

48   Z. Peng, R. Ye, J. A. Mann, D. Zakhidov, Y. Li, P. R. Smalley, J. Lin and J. M. Tour, , DOI:10.1021/acsnano.5b00436.

49   F. Wen, C. Hao, J. Xiang, L. Wang, H. Hou, Z. Su, W. Hu and Z. Liu, *Carbon N. Y.*, 2014, **75**, 236–243.

50   M. F. El-Kady, V. Strong, S. Dubin and R. B. Kaner, *Science*, 2012, **335**, 1326–1330.

51   G. Nagasubramanian, R. G. Jungst and D. H. Doughty, .

52   Y. Xue, Y. Ding, J. Niu, Z. Xia, A. Roy, H. Chen, J. Qu, Z. L. Wang and L. Dai, *Sci. Adv.*, 2015, **1**, 1–10.

53   J. Kim, S. M. Lee, Y.-H. Hwang, S. Lee, B. Park, J.-H. Jang and K. Lee, *J. Mater. Chem. A*, 2017, **5**, 1906–1912.

54   X. Fu, Z. Xia, R. Sun, H. An, F. Qi, S. Wang, Q. Liu and G. Sun, *ACS Energy Lett.*, 2018, **3**, 2425–2432.

55   Z. Peng, J. Lin, R. Ye, E. L. G. Samuel and J. M. Tour, *ACS Appl. Mater. Interfaces*, 2015, **7**, 3414–3419.

56   A. Ramadoss, K. Yoon, M. Kwak, S. Kim, S. Ryu and J. Jang, *J. Power Sources*, 2017, **337**, 159–165.

57   Y. Shao, J. Li, Y. Li, H. Wang, Q. Zhang and R. B. Kaner, *Mater. Horizons*, 2017, **4**, 1145–1150.

58   G. D. Moon, J. B. Joo and Y. Yin, *Nanoscale*, 2013, **5**, 11577–11581.

59   Z. Gao, C. Bumgardner, N. Song, Y. Zhang, J. Li and X. Li, *Nat. Commun.*, 2016, **7**, 11586.

Chapter 4

Graphene/polypyrrole based metal-free microsupercapacitor using "Organic/Water-in-salt" electrolyte
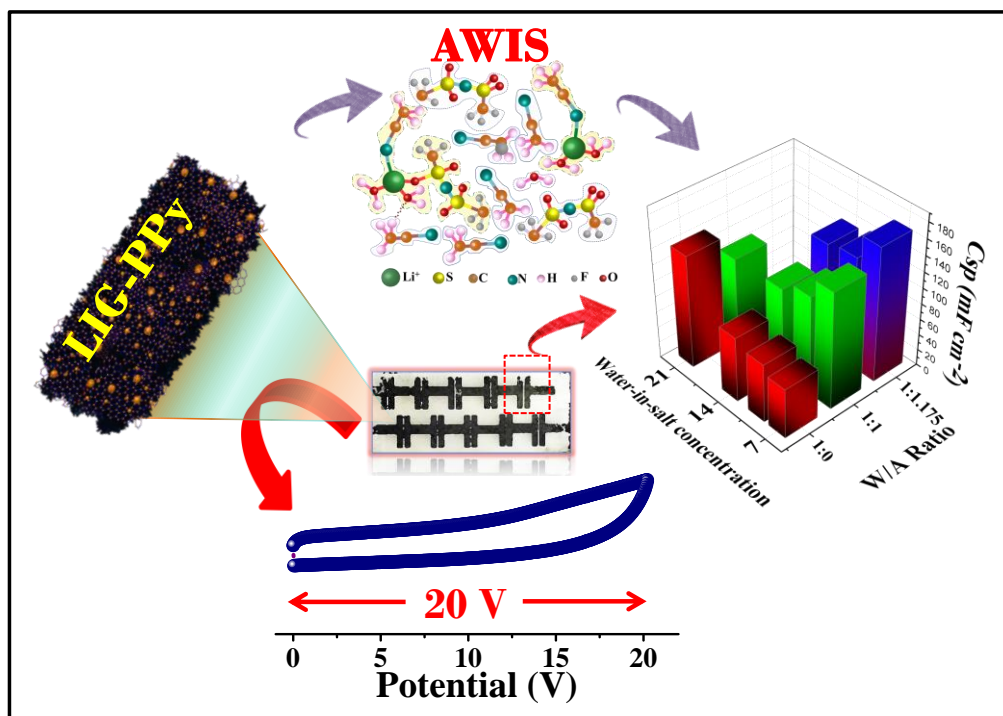
Abstract: Aqueous electrolytes are facing substantial barriers for their all-around use in high voltage electrochemical energy storage applications due to their limited operating voltage window. To overcome this issue, "Water-in-salt" electrolyte is known to be the best findings to deal with the electrochemical stability window (ESW). The present work demonstrates the fabrication of laser-irradiated graphene (LIG)-polypyrrole (PPy) hybrid material with enhanced effective surface area, electrical and electrochemical properties, which was further used to build a symmetrical metal-free microsupercapacitor (MSC) with greater electrochemical performances. The attractive feature of this work is the incorporation of a pseudocapacitive material (i.e., PPy) in LIG to increase the electrochemical storage capacity of the device in "Acetonitrile/Water-in-salt" electrolyte (AWIS) to have higher ESW up to 2.4 V. Moreover, the changes in the electrolyte solvation structure with salt concentration and different solvent dilution parameters were studied via Raman analysis in support with ^{1}H NMR measurements. The resulting symmetrical metal-free LIG-PPy$_{AWIS}$ MSC results in high specific capacitance of 124 mF cm^{-2}, the energy density of 99.2 µWh cm^{-2} and a power density of 47.75 mW cm^{-2}, shows significant progress among other graphene based MSCs. The LIG-PPy MSC module acquiring 20 V is capable to be utilised in high voltage energy applications.

4.1 Introduction

Serious environmental conditions with consumption of fossil fuels influence the scientific community to develop environmental benign energy storage technologies. Supercapacitors (SCs) are considered as a kind of fascinating energy storage system that hold high power capability, superior adaptability, fast charge-discharge kinetics and long cycle run.[1,2] Nowadays, metal-free microsupercapacitors are upgrading their field via replacing metals (current-collectors) with some other active materials that can simultaneously function both as active material and current collector. To execute the current demand, Graphene and its derivatives in the last decade, become a superior choice for the current collector and electrode material job in energy storage applications attaining so many inherent properties such as excellent electrical conductivity, higher surface area, unique porous architecture, mechanically robust and extraordinary chemical stability.[3,4] However, quite a few synthetic routes are reported so far to develop high-quality graphene sheets with less defect density and good electrical property. Recently, laser induction,[5] laser scribed[6] and laser irradiation techniques[7] are emerging as a new field for the fabrication of highly conducting graphene film with unique porosity and effective surface area. Moreover, due to its sufficient electrical conductivity graphene can function both as active electrode material as well as current collector by eliminating metals in the storage device for the fabrication of metal-free microsupercapacitors (MSCs).[4]

In spite of these advantages, it is unfortunate that electric double layer capacitance (EDLC) of graphene-based microsupercapacitors (MSCs) is not up to the mark to meet the present energy demand. The main reason behind this is unavoidable restacking of graphene sheets restrict the diffusion of electrolyte ions, that further limits the current output of graphene-based SCs.[8] Moreover, very less energy density (5–10 W h kg^{-1}) of graphene-based SCs compared to state-of-the-art supercapacitive materials (100-260 W h kg^{-1}) bound its capability towards high-end energy applications.[1] Therefore, current research interest is focused on in search of the possible ways to improve the energy density of supercapacitors. The energy density ($E = \frac{1}{2}CV^2$) of a supercapacitor is directly proportional to two parameters: one is output specific capacitance (C_{sp}) and second one is square of working voltage (V^2). Therefore, either by improving the specific capacitance *via* surface modification and/or by expanding the potential window *via*

moderation of electrolyte could results in boosting the energy density of a supercapacitor.[9]

To satisfy the high demand in energy density, one effective approach is followed by the researchers via depositing pseaudocapacitive materials such as transition metal oxides[10] (*i.e.* RuO_2, MnO_2, NiO, V_2O_5 etc.) or conducting polymers like Polypyrrole (PPy),[11] Polyaniline (PANI)[12] on the graphene surface to increase the output current of the electrode material with enhanced surface properties. The major limitation with the incorporation of metal oxides is huge volume changes occuring during charge-discharge cycles, which in turn decrease the electrochemical stability. Among all other conducting polymers, PPy has proved as a significant electrode material not only due to its large pseudocapacitive contribution, but also, it's good electrical conductivity (50–100 S cm^{-1}) and superior chemical and thermal stability. However, PPy alone is not recommended as electrode material because of its complicated charge storage mechanism that involves the insertion/de-insertion of electrolytic anions into the polymeric chains causing the volume expansion and compression, which further resulted in poor cycling stability of the device.[13,14] However, PPy can gets additional stability in conjugation with nanostructured porous carbon matrix such as graphene *via* pi-pi interaction.[15,16] This type of non-covalent conjugation chemistry not only helps to improve additional electronic transport channel but also boost the capacitive and cycling performance of the device.[17]

The second important factor that affects the energy density of a device is the electrolyte stability window (ESW), which is limited in aqueous electrolytes due to the decomposition potential of water (1.23 V) near the electrode surface.[18] Therefore, the enlargement of ESW in aqueous electrolyte is highly needed for the applicability of aqueous SCs in various applications. To resolve this issue, several approaches have been followed previously to extend the ESW such as 1) by tuning the pH of aqueous electrolytes,[19–21] 2) incorporating redox-active species in electrolyte,[22,23] 3) mass-balancing between two electrodes,[24] 4) electrode surface passivation effects and many more.[25] However, the above mentioned strategies are limited with the expansion of the ESW maximum upto 2.0 V, which is insignificant. Recently, highly concentrated (also called supersaturated) aqueous electrolytes, called "Water-in-salt" (WIS) turned out as a tropical concept for the extension of ESW up to ~3 V *via* suppressing the electrochemical stability of water molecules that is limited to 1.23 V.[26] Such a great ESW is well explained with the fact that almost all water molecules strongly coordinate to metal cations, resulting in a remarkably decreased chemical activity of water molecules near

the positive and negative electrodes. Nonetheless, WIS electrolytes are showing fantastic performance as compared to organic electrolytes in terms of safety and applicability of the device.[27] However, few challenges are still there to be overcome with WIS-type electrolytes such as high viscosity, low conductivity and salt precipitation at a low temperature. To deal with the above said challenges, researchers are recently introduced a co-solvent WIS system by mixing organic phase in water with similar typical electrolytes to create an "Organic-Water in salt" type electrolyte.[17,28]Keeping in mind above-mentioned significant aspects, herein we have fabricated a highly conducting laser-irradiated graphene (LIG) film *via* electrochemical deposition of reduced graphene oxide (rGO) followed by laser-irradiation method and in the subsequent step modification of PPy by electrochemical polymerization technique to make a hybrid electrode material. The resulting LIG-PPy hybrid material exhibits a wide potential window of 2.4 V in LiTFSI based acetonitrile-water in salt (AWIS) electrolyte. The specific capacitance of the active electrode is achieved as 168 mF cm^{-2} under optimized electrolytic conditions in three electrode system. Moreover, two parallel line symmetric metal-free microsupercapacitor is fabricated by quasi-solid-state LiTFSI-PEO based AWIS electrolyte, which shows a specific capacitance value of 124 mF cm^{-2}, energy density of 99.2 µWh cm^{-2} and power density of 47.75 mW cm^{-2}. Furthermore, the cells are combined in series and parallel configurations in order to attain maximum voltage of 20 V and a maximum current output, respectively. This work paves the way for designing and implementing high energy density supercapacitors with large cell voltage for future electronic applications.

4.2 Experimental Section

4.2.1 Preparation of Cuf@Cu *via* dynamic hydrogen bubble template (DHBT) method:

Three-dimensional copper foam (3DCuf) architecture was prepared on copper foil (2 $\times$ 2) cm^2 via DHBT method in a two-electrode system that comprises two highly pure copper foils with equal dimensions; one act as counter electrode and another as working electrode, were assembled 1 cm apart in an aqueous solution of 0.4 M CuSO$_4$. A constant current density (as maximum as 0.8 A cm^{-2}) was applied across the electrodes for 45 seconds. The applied current leads to occur two processes simultaneously: 1) the formation of hydrogen bubbles providing porous networks at the working electrode surface, 2) depositing the metal foam at a faster rate (Fig.4.1). As obtained Cuf@Cu was

cleaned several times with deionized water (DI) in order to remove any acidic impurities from the surface and stored in vacuum to avoid aerial oxidation.

4.2.2 Electrochemical growth of reduced graphene oxide (ErGO) film on Cuf@Cu substrate:

Simultaneous reduction and growth of ErGO film was carried out on 3D-Cuf@Cu network via bulk electrolysis deposition technique. The electrochemical deposition of ErGO was carried out with a three-electrode set up comprising Cuf@Cu foil as working electrode, a reference electrode (Ag/AgCl) and a counter electrode (Platinum wire) in a homogeneous solution of graphene oxide (GO) with a concentration of 3 mg ml^{-1} in 0.5 M HClO$_4$ at applied potential of -1.0 V (Fig. 4.1). The as-deposited rGO film on Cuf@Cu substrate was cleaned several times with DI water in order to eliminate unwanted physical absorbed species from the surface of ErGO@Cuf@Cu. The porous ErGO film was freed from the Cuf skeleton by leach out the Cuf@Cu with 10 wt% (NH$_4$)$_2$SO$_4$ solution and further the film was transferred onto the flexible polyethylene Terephthalate (PET) sheet after washing with DI water. As obtained ErGO film with porous structure was further laser-irradiated to obtain a highly conducting graphene sheet as described below.

4.2.3 Laser-irradiation (LI) on ErGO to obtain highly conducting graphene film:

The ErGO film is still encapsulated with many functional groups, which can further reduced via laser-irradiation method as explained in our previous work.[29] Briefly, 60 W (10.6 μm) CO$_2$ laser was used with optimum laser parameters as power of 18 W, laser speed of 0.4 m s^{-1} and the frequency of 1000 Hz exposed in one pass. The exposure was made via an automatic computer-controlled system. In our previous report, the influence of the laser parameters on the characteristic features of the graphene film was well elaborated.[7] Basically, the LI process provides a very high temperature (>2700 K) at the laser spot on the film, which leads to the rearrangement of the π-electron cloud in the carbon network *via* eliminating the oxygen functionalities. The restoration of the sp^2 carbon atoms during LI process encourage the fusion of the graphene sheets and flatten the upper surface of LIG film.

4.2.4 Formation of LIG-PPy composite via electrochemical method:

The association of LIG with PPy was done via electropolymerization technique. In order to electropolymerize as well as simultaneous deposition of PPy on LIG sheet, a constant voltage of +0.8 V was applied against Ag/AgCl (3 M KCl) for 100 seconds in 0.1 M freshly distilled pyrrole solution. The resulting composite was rinsed with DI water

several times and used as an active electrode material for designing the symmetrical on-chip microsupercapacitor (MSC) device. The incorporation of PPy into the bulk of the LIG material leads to an increase in the thickness of LIG-PPy sheet upto 20 μm as compared to the thickness of LIG sheet which is 9 μm (Fig. 4.2 a and b).

4.2.5 Fabrication of on-chip LIG-PPy composite based MSC:

A 1.06 μm near infrared (NIR) laser source was used to design the interdigitated structure of the MSC with optimum conditions as: laser power of 21 W, 0.5 m s^{-1} laser speed, 2.85-inch focal length and 20,000 Hz frequency at one pass. The LIG-PPy composite film was
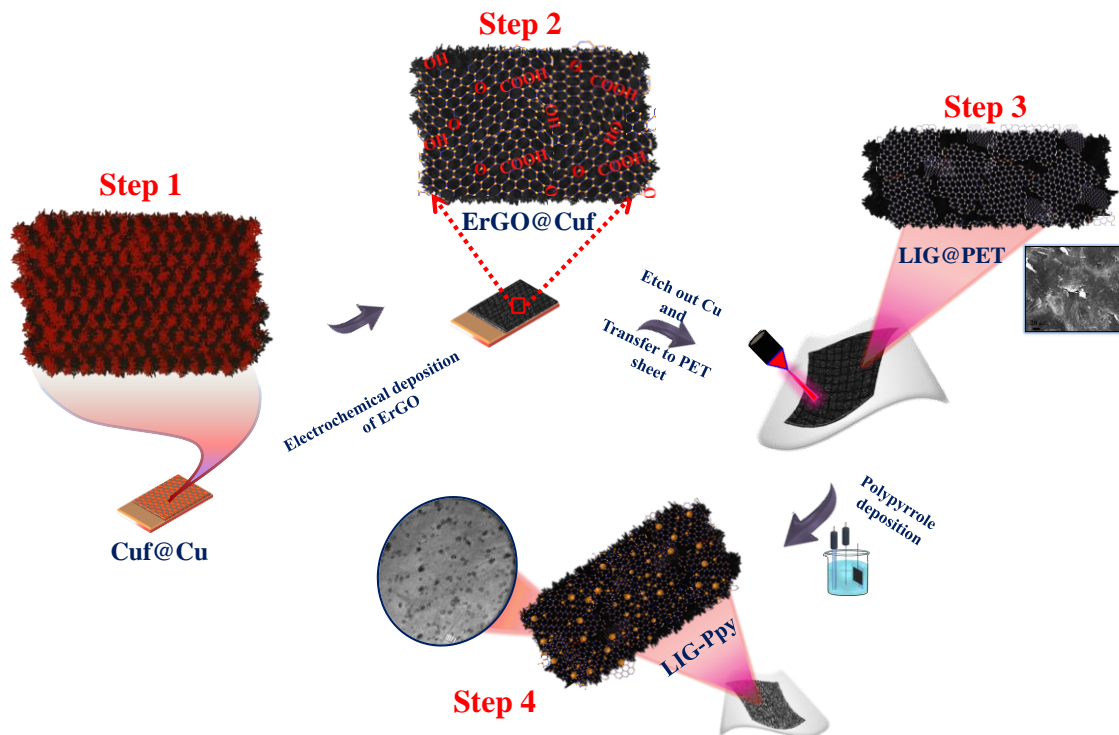
Figure 4.1. Schematic representation of synthesis of LIG-PPy composite in different steps as follows: steps: 1- Growth of copper foam on Cu foil, step:2- Electrochemical deposition of ErGO, step:3- Laser-irradiation on ErGO, step:4- Electrochemical polymerization of polypyrrole nanoparticles on the surface of LIG sheet.

patterned into different shapes to check the shape-dependent properties of the device. Finally, two linearly parallel electrodes were optimized with dimensional length of 4 mm and width of 0.5 mm for a single cell electrode and separated by a distance of 0.1 mm.

4.2.6 Quasi-solid AWIS-gel electrolyte preparation:

To make a robust MSC, a transparent quasi-solid AWIS gel electrolyte was prepared by simply adding 10 wt% PEO in 7 m acetonitrile/water-in-salt (1:1.175) solution and stir continuously for 2 hours at 80°C. The two electrodes were coated with the gel electrolyte and kept the film at oven (55°C) for overnight for drying. A LIG-PPy composite film

based MSC was also modified with PVA-H$_3$PO$_4$ gel electrolyte for the comparison.

4.2.7 Electrochemical evaluation

Electrochemical measurements like cyclic voltammetry (CV), galvanostatic charge-discharge (GCD), were performed on a CHI 760E electrochemical workstation. To electrodeposit three-dimensional (3D) reduced graphene oxide (ErGO) networks, copper foam coated copper foil (Cuf) refers to working electrode, Ag/AgCl (3 M KCl) as the reference electrode and a platinum wire as a counter electrode was used. A two-electrode
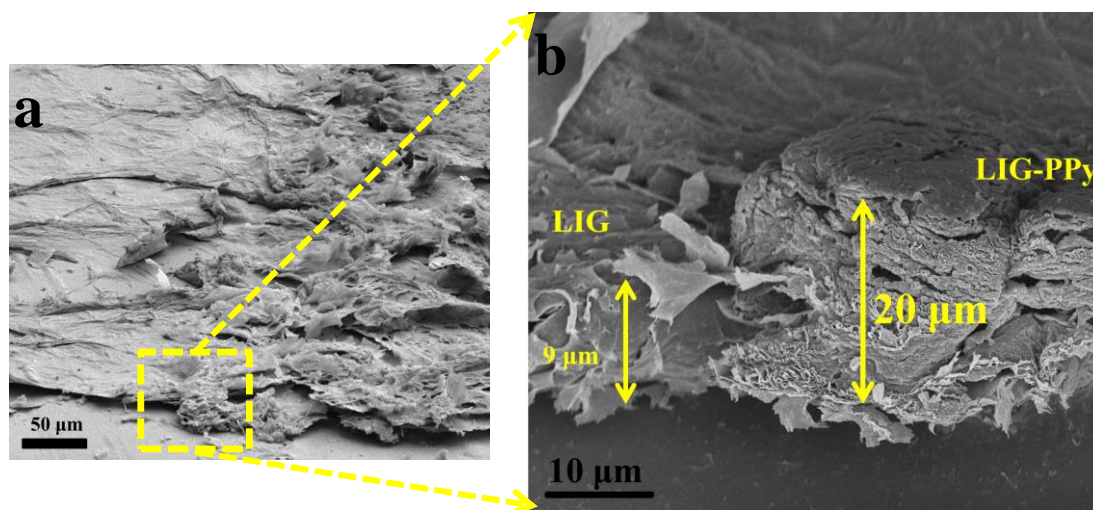
Figure 4.2. SEM image (a) showing an edge mark of LIG and LIG-PPy in the same sheet, (b) representing thickness of LIG and LIG-PPy composite material.

set up was used to measure all solid-state electrochemical performances of the in-plane microsupercapacitor device in a quasi-solid gel water-in-salt based electrolyte. Nyquist plots for both the electrodes as well as full battery system were carried out in electrolyte in the frequency range of 0.01–10 000 Hz.

4.3 Results and discussion

4.3.1 Material physicochemical characterizations:

The surface morphology and microstructure of as-prepared LIG, LIG-PPy composite films were analyzed by scanning electron microscopy (SEM) and transmission electron microscopy (TEM) techniques. The morphology of LIG as shown in Fig. 4.3a represents that the LI process encourages fusion of graphene sheets to each other. Basically, the impact of laser irradiation stimulates to interconnect the edges of the graphene sheets after eliminating the functionalities and form a continuous sheet all over the surface. Fig. 4.3b representing the TEM image of LIG which display a transparent wrinkled structure of graphene sheets. After PPy electrodeposition process, the obtained LIG-PPy

composite sheet display that the functionalized graphene sheets are uniformly decorated with tiny PPy nanospheres through π-π interactions (Fig. 4.3c-d).[30] The surface is fully covered with small size nano spheres with a diameter range of 8 nm to 20 nm that emerged from the electro- polymerization process. The smaller size nanospheres are being as beneficial for the enhancement in the electrochemical performance as an electrode in supercapacitors owing higher effective surface area. The extended π-conjugated PPy material with other conjugated graphene material is the key factor for the dispersion of PPy nanospheres into the bulk LIG structure and over the surface of the graphene sheets, which is completely justified with the SEM cross-sectional images of LIG and LIG-PPy composite (Fig. 4.2 a and b). The TEM images of the LIG-PPy composite are shown in Fig. 4.3d (and inset) and Fig. 4.3e at different resolutions
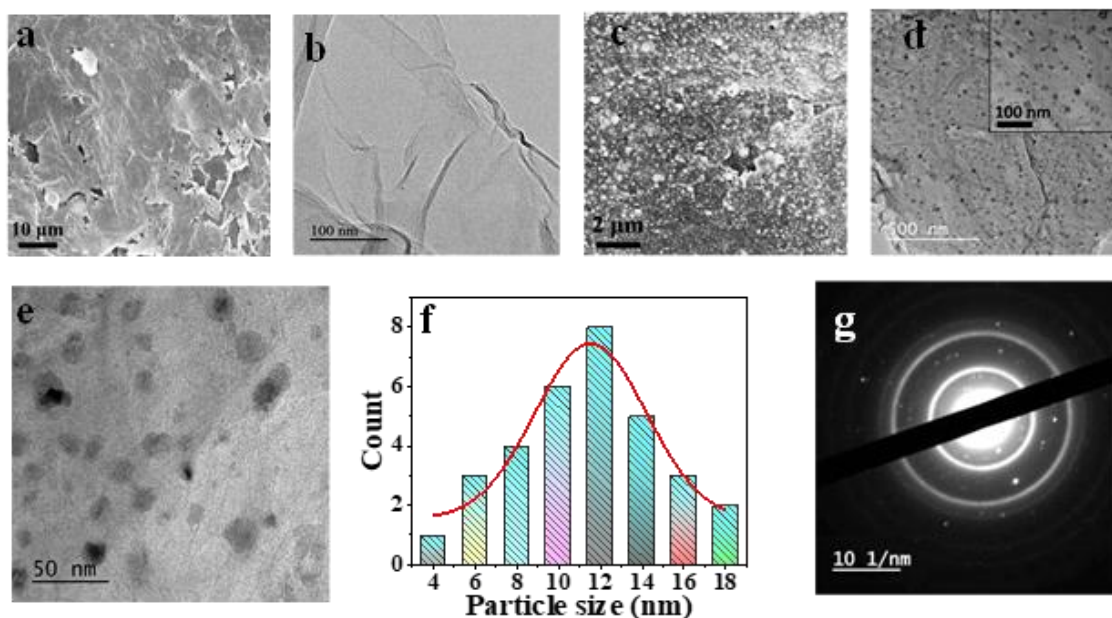
Figure 4.3. *(a) Scanning electron microscopic (SEM) image of LIG), (b) Transmission electron microscopic (TEM) image of LIG sheet, (c) SEM imege of LIG-PPy composite. images (d, e) of LIG-PPy composite at different resolutions (500 nm, 100 nm inset of d, 50 nm), showing the uniform distribution of nanoparticles decorated over graphene sheets, (f) Particle distribution over graphene sheet with different particle size, (g) the SAED pattern for LIG-PPy composite material.*

completely showing a graphene sheet functionalized with PPy nanoparticles. The PPy nanoparticles size distribution profile revealed that the frequency count for 12 nm particles is at peak of the Gaussian profile (Fig. 4.3f). Figure 4.3g shows the SAED pattern, which clearly shows the bright circles for the amorphous graphene structure and point dots represent the presence of small tiny spherical nanoparticles coated on the graphene structure.

Such kind of nanoparticle distribution can also be seen in AFM image (Fig. 4.4a) of LIG-PPy composite material and the height profile (Fig. 4.4b) represents the particles

size distribution in 1 to 8 nm range. Therefore, concluding from SEM and TEM experimental proofs, the charge transfer complex reaction mitigates between the electron acceptor *i.e.* graphene and a donor material (pyrrole monomers) which leads to the migration of PPy monomers to the surface of graphene sheets when the elecrtopolymerization takes place and the active nucleation sites allocated around the graphene sheet support the formation of polymerized pyrrole nanospheres.[31,32] The growth of the nanospheres can be easily controlled with controlled deposition parameters prohibiting the formation of any kind of array or aggregation of the nanoparticles.

In order to characterize the structure of the material, X-Ray diffraction study was carried out on GO, ErGO, LIG and LIG-PPy samples. The XRD spectrum of GO (Fig. 4.5a) shows a sharp diffraction peak (001 plane) positioned at 11.2° with a d-spacing of 0.398 nm, whereas ErGO depicts a broad diffraction peak (002 plane) at $2\theta = 26°$ (d-spacing value is 0.19 nm) that can be attributed to the graphitic structure and this peak got intensified in case of LIG. The laser irradiation process enhances the crystallinity in the graphene structure as can be seen in the XRD spectrum of LIG. A broad diffraction peak was also observed for LIG-PPy sample at $2\theta = 25.8°$ indicating the amorphous nature of the LIG-PPy composite. To attain more information about the structure changes
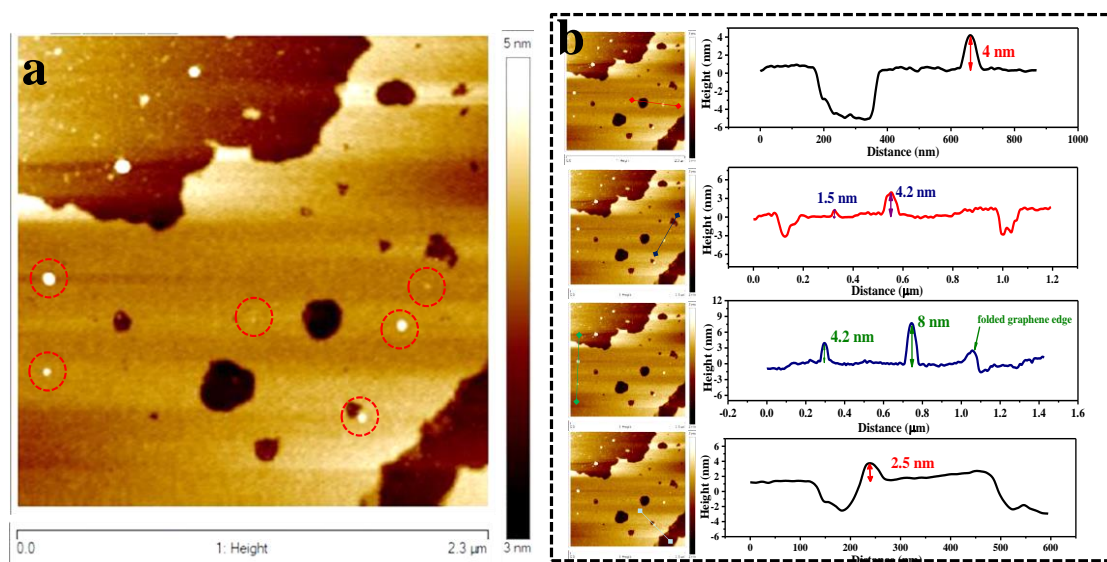
Figure 4.4. *Atomic force microscopic image (a) for LIG-PPy composite showing the distributed PPy nanoparticles all over the graphene sheet, (b) the height profile chart for the nanoparticles grown on the graphene sheet.*

during electrochemical and laser irradiated reduction of the samples; Raman characterization was performed (Fig. 4.5b). Raman spectra of LIG demonstrated the vibrational D, G and 2D band at 1350, 1582 and 2693 cm^{-1}, respectively. The D/G band intensity ratio (I_D/I_G) expresses the atomic ratio of sp^3 to sp^2 hybridized carbons, which

is a measure of the extent of disordered graphite. A very small value of I_D/I_G ratio (0.062) in case of LIG represents the reduction of oxygen functionalities among the graphene sheets. It is satisfying to note that the Raman spectrum of LIG-PPy hybrid material depicts many weak intensity peaks corresponding to different vibrations modes in addition to D and G bands indicates the functionalization of PPy to the LIG backbone. Moreover, the shifting in the G-band (1578 cm⁻¹) of LIG-PPy composites towards lower frequency region is a clear indication for the electron-donating effect of benzene
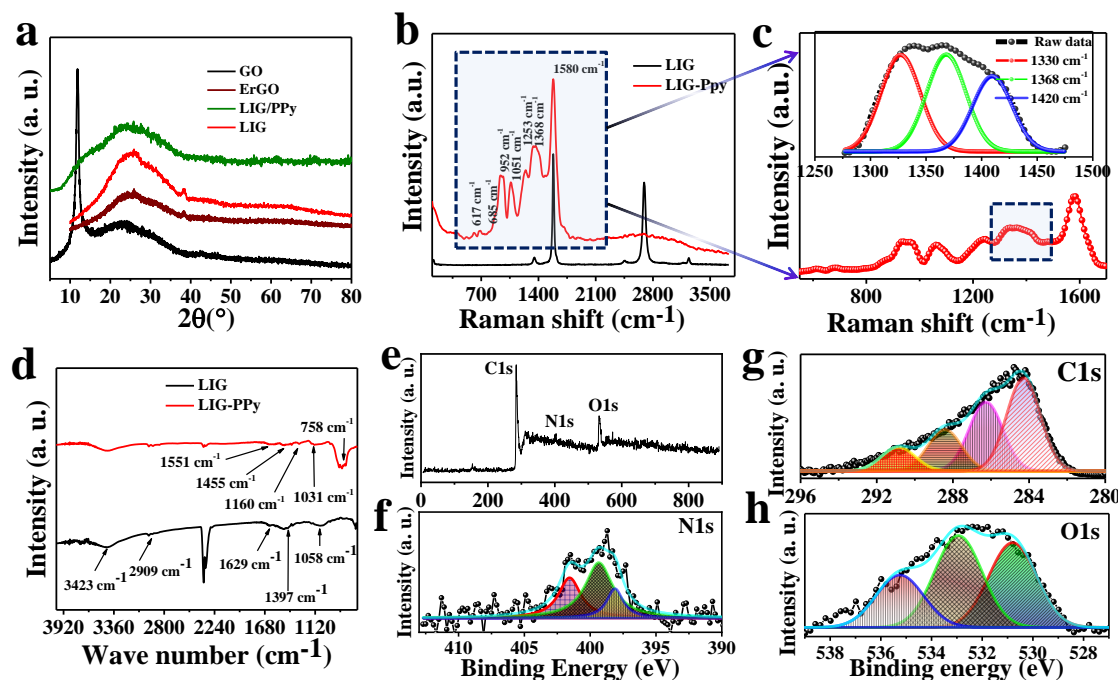
Figure 4.5. *X-Ray diffraction pattern for GO, ErGO, LIG and LIG-PPy materials, (b) Raman spectroscopic results for LIG and LIG-PPy, (c) Magnified Raman spectra for LIG-PPy composite material, inset shows the deconvoluted Raman spectra for broad G-band region, (d) corresponding FT-IR studies, (e) XPS full survey, (f) deconvoluted N 1s XPS spectra, (g) C 1s XPS spectra, (h) O 1s spectra..*

substituents, which is similar effect like molecular charge transfer mechanism with donor and acceptor molecules.[33] Figure 4.5c shows the magnified region of Raman spectrum of LIG-PPy sample and inset represents the deconvoluted spectra of G-band broad region includes three characteristics peaks at 1330, 1368 and 1420 cm⁻¹, which corresponds to the antisymmetrical in-ring C-N stretching.[34] Raman spectra of LIG-PPy also includes some more prominent bands at 617 cm⁻¹ (ring torsion), 685 cm⁻¹ (C-H wagging), 952 cm⁻¹ (ring deformation associated with the dication), 1051 cm⁻¹ (C–H in plane deformation), and 1253 cm⁻¹ (antisymmetrical C-H in-plane bending), which are characteristic Raman-active modes of PPy.[11] In order to further confirmation of hybrid nanostructure formation, Fourier transform infrared (FT–IR) spectra of LIG and LIG-PPy composite were obtained as shown in Fig. 4.5d. The two distinct peaks in the spectrum of LIG are

observed at about 1639 cm^{-1} and 2909 cm^{-1}, assigned to the C=C and C–H stretching vibrations, respectively. The FT-IR spectrum of LIG-PPy includes absorption peaks at 1455 cm^{-1}, 1160 cm^{-1}, 1030 cm^{-1} and 758 cm^{-1}, which corresponds to the C–N stretching vibration in the pyrrole ring, C–H in plane breathing vibration of pyrrole ring, N–H in plane deformation vibrations and C–H out of plane deformation vibrations, respectively.[35–37] These results indicate that PPy had been successfully functionalized on LIG.

High resolution XPS measurements were performed in order to comprehend the possible chemical bonding, including oxidation state of LIG-PPy composite film as well as to estimate their compositions as shown in Fig. 4.5 e-h. A complete XPS survey over LIG-PPy composites clearly shown in Fig. 4.5e which indicates a characteristic signal of N1s is found at 399.7 eV in addition to signals of C 1s and O 1s. The distribution of
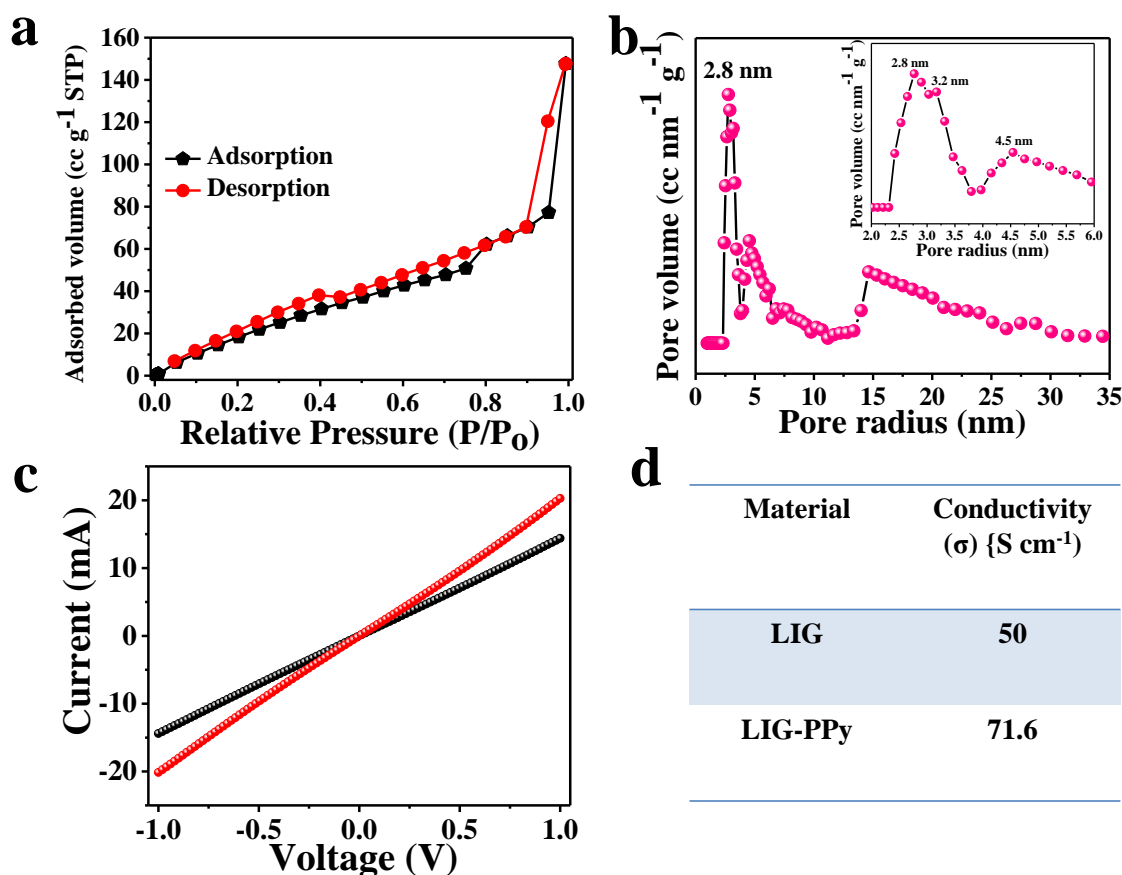
Figure 4.6. The absorption-desorption isotherm plot (a) for LIG-Ppy composite material, (b) Pore size distribution for the corresponding sample, (c) Electrical conductivity measurements for LIG and LIG-PPy composite via two-probe method and (d) the corresponding values are given in the table.

nitrogen species in LIG-PPy material was studied via deconvolution of the N1s high-resolution core level XPS spectra as shown in Fig. 4.5f. The nitrogen XPS spectra are

deconvoluted into three Gaussian peaks with the binding energies 398.2 eV, 399.3 eV and 401.1 eV, respectively. The peaks at 398.2 correspond to the neutral and the imine-like structure (-N=) can be used to estimate the defect density within the PPy, because the structure is believed to interrupt the electron hopping on the polymer chain. The peak positioned at binding energy of 399.3 eV corresponds to amine (-NH-) moieties, while peak at 401.1 eV can be ascribed to the positively charged nitrogen groups of oxidized amine and protonated imine, respectively. The C1s XPS spectra (Fig. 4.5g) are deconvoluted into four components centered at 284.2 eV, 285.9 eV, 288.6 eV, and 290.7, respectively. The main peak positioned at 284.2 eV is attributed to the C–C/C–H bond, whereas the peaks at 285.9 eV and 288.6 eV are dedicated to C–N group and O–C=O groups due to oxalate groups, which is incorporated in to the film as dopants.[38] The peak at 290.7 eV originate due the presence of C–C groups (named as "satellite peak"), respectively. The presence of the C–N C1s peak, confirms the presence of pyrrole moieties in the LIG-PPy composite sample. The deconvoluted O1s XPS spectra shown in Fig. 4.5h exhibits peaks at 530.8 eV, 532.2 eV and 535.4 eV assigned to –C–O, C–O–H and O–C=O moieties, respectively. Thus, XPS data together with XRD, SEM, TEM, FT-IR and Raman analysis results fully confirms the composite formation of LIG-PPy**.**

The effective surface area of LIG-PPy composite is calculated to be 110 m^2 g^{-1}, analysed from adsorption-desorption isotherm (Fig. 4.6a) and the particle size distribution curve indicates that LIG-PPy is mesoporous in nature as shown in Fig. 4.6b (inset shows the magnified distribution profile of nanoparticles with size <5 nm). Moreover, the electrical properties for LIG and LIG-PPy composite film were characterized *via* two-probe technique. The measured electrical conductivity for LIG is 50 S cm^{-1} and for LIG-PPy is 71.6 S cm^{-1}, respectively (see the supporting section for calculation and Fig. 4.6c and d).

4.3.2 Electrochemical characterizations:

The quantification of PPy over LIG required to enhance electrochemical performance of the electrode material can be optimized via resulting cyclic voltammetry (CV) and Galvanostatic charge-discharge (GCD) studies post deposition intervals. The CV and GCDs were taken out in acidic electrolyte (1M H_3PO_4) medium in a traditional three-electrode system. Further studies were done in AWIS electrolyte in different LiTFSI concentrations (21m, 14 m, 10 m and 7 m) in different water to ACN mixture solution denoted as $xm\ LiTFSI_{AWIS_{(1:y)}}$, where "$x$" can be LiTFSI concentration such as 21, 14,

10, 7 and "*y*" denoted the ratio of acetonitrile solution in water *i.e.,* 1:0, 1:1, 1:1.175 and 1:2, respectively. For the practical use, a quasi-solid state (PEO-AWIS-LiTFSI) symmetrical two-electrode device was designed and the corresponding output electrochemical performance was tested.

4.3.3 Polypyrrole (PPy) loading optimization on LIG:

The optimization procedure has been carried out in order to determine the optimal
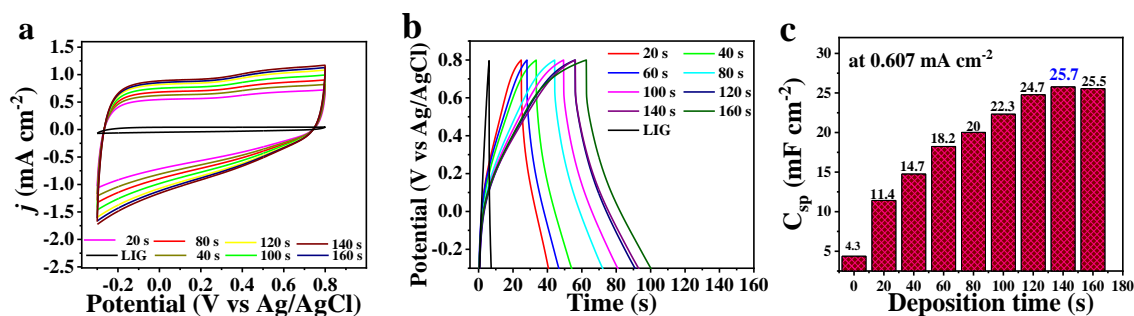
Figure 4.7. *Comparative (a) CV and GCD (b) curves to optimize the PPy deposition conditions, (c) Changes in specific capacitance with the time duration for PPy deposition.*

deposition time for uniform distribution of PPy on LIG. Figure 4.7a-c shows the comparative CV curves at 100 mV s^{-1}, almost 3-folds increment in the specific capacitance value observed after 20 seconds electrodeposition of PPy on LIG sheet. This sharp increase in the electrochemical performance can be explained with two major contributions in the capacitance: 1) electric double layer capacitance with effective high surface area and 2) is generation of faradaic pseudocapacitance from nitrogen (-N) functionalities. The capacitance increases continuously with a sustainable nucleation growth of PPy nanoparticles carried out at increased deposition intervals of time and get saturated (25.7 mF cm^{-2}) at 140 seconds deposition time maintaining a potential window of 1.1 V. Further increasing the deposition time may leads to the formation of polymer array or aggregation of nanoparticles at particular effective edge sites of graphene sheets, which increase the resistance for the ionic diffusion and hampers the storage capacity of the material.

4.3.4 Electrochemical studies in "Acetonitrile/Water-in-salt" (AWIS) hybrid electrolytes

The key obstacle of limited electrochemical stability window (ESW) for state-of-the-art aqueous electrolytes (salt-in-water) encourages the use of "Water-in-salt" electrolytes. A super higher concentration of salt (LiTFSI) in water provides the right functionalities like wide ESW and less parasitic chemical reactions involved but exhibits relatively low conductivity and higher viscosity due to the strong coordination of TFSI anions with

lithium cations, which hinders mobility of ions.[39–41] To facilitate easy ionic dynamics, some solvent addition other than water (free water reduces the stability window) is highly required to weaken the cationic-anionic bonding.[42,43] To this end, we have chosen acetonitrile as an organic co-solvent in the WIS electrolyte. The reasons for the selection of ACN over other organic solvents are 1) Its low viscosity and relatively wide ESW, 2) Higher dielectric constant to dissolve excessive amount of salt, 3) Reduces salt precipitation at lower temperature range.[44] Initially, the $^{21mLiTFSI}WIS_{(1:0)}$ electrolyte was diluted with water only in order to check the impact of excessive water with less amount of salt concentration. Conceptually, the free water molecules reduce the potential window as well as restrict the flow of electrolytic ions, which in turn hampers the output current. It is also evidenced from the experimental results as shown in Fig. 4.8 a-b and g, dilution of $^{21mLiTFSI}WIS$ electrolyte with only water, the resulting concentrations $^{14mLiTFSI}WIS_{(1:0)}$, $^{10mLiTFSI}WIS_{(1:0)}$ and $^{7mLiTFSI}WIS_{(1:0)}$, not only hampers the ESW (reduces to 2.25 V), it also reduces the storage capacity of the electrode. From the above
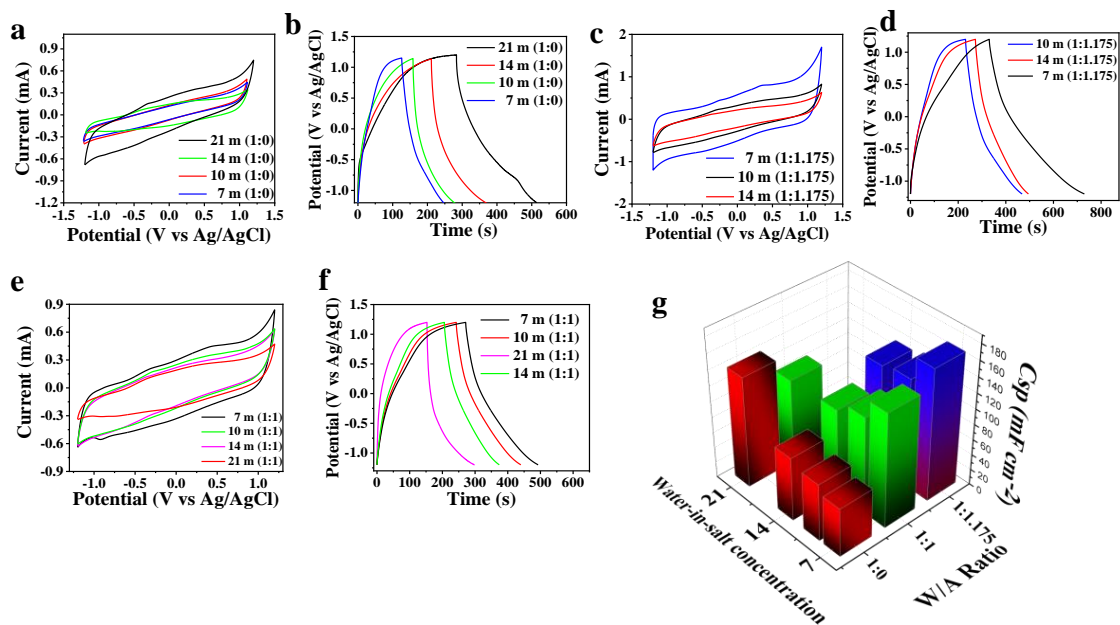
Figure 4.8. *CV curves (a, c, e) at 100 mV s^{-1} in three-electrode system, and GCD curves (b, d, f) at a current density of 1.12 mA cm^{-2} for LIG-Ppy composite electrode in different electrolyte concentrations $xm\ LiTFSI_{AWIS_{(1:0)}}$, $xm\ LiTFSI_{AWIS_{(1:1)}}$, $xm\ LiTFSI_{AWIS_{(1:1.175)}}$, $xm\ LiTFSI_{AWIS_{(1:2)}}$; where "x" can be 21, 14, 10 and 7 respectively (g) A 3D bar plot representing the best outcome for the specific capacitance value with respect to different LiTFSI concentrations in different ACN to water mixture ratios.*

discussion, it is concluded that still a complete aqueous system is not able to compete with organic one. Figure 4.9a represents two CV curves for LIG-PPy composite film in both acidic (1M H_3PO_4) as well as AWIS medium for comparative study. As expected, the ESW in 1M H_3PO_4 restricts to 1.1 V only, whereas an extended working voltage of

2.4 V and 6-folds enhanced current in AWIS medium was observed *via* maintaining perfect EDLC behaviour. Such an extraordinary high voltage feature is ascribed to the fact that water molecules are completely locked with the metal cations, resulting in a remarkably decreased chemical activity of water molecules near the electrode.[43]

Moreover, the electrochemical measurements along dilution with organic solvent
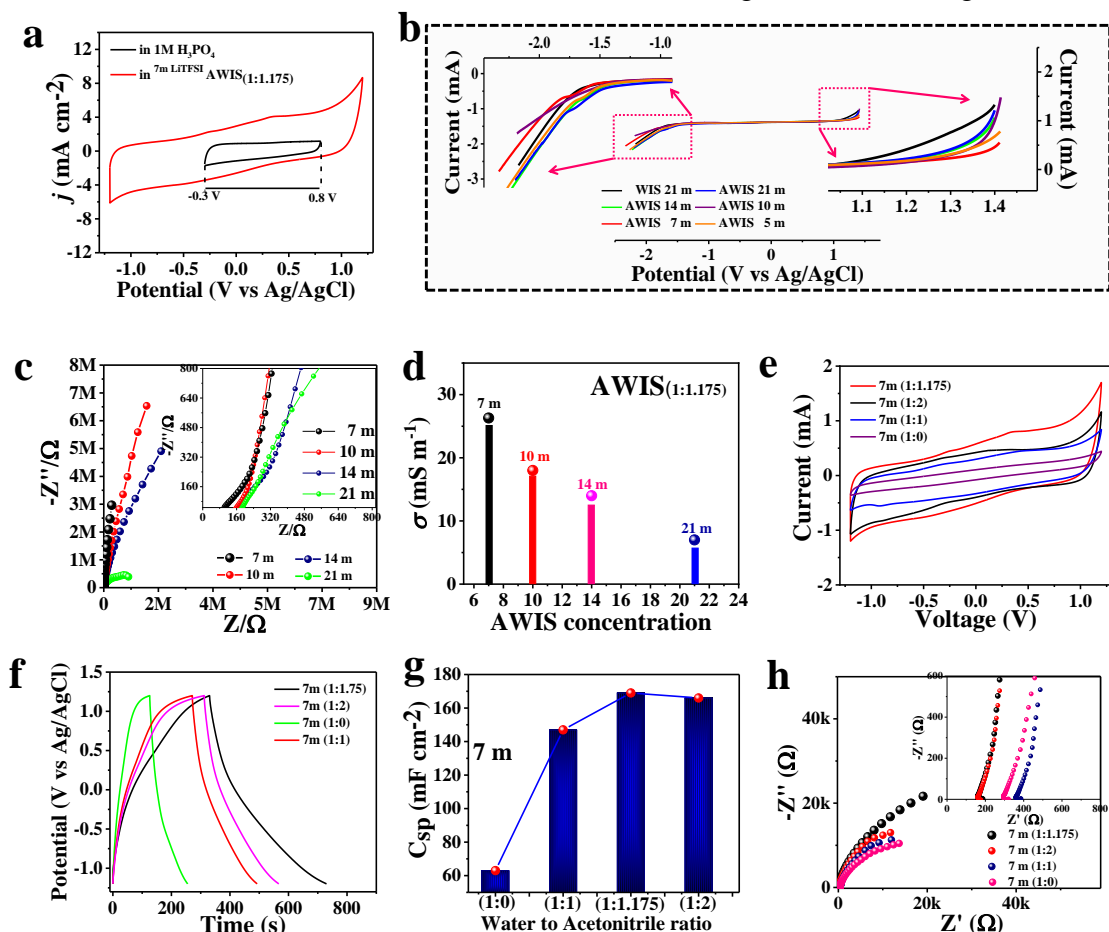
Figure 4.9. *(a) Comparative CV curves for LIG-PPy composite electrode in acidic (1 M H₃PO₄) medium and $^{7m\ LiTFSI}$AWIS electrolyte at 100 mV s⁻¹, (b) Impact of of ^{21mLiTFSI}WIS$_{(1:0)}$ and AWIS$_{(1:1.175)}$ in different LiTFSI concentrations on the electrochemical potential stability window in linear sweep voltametry experiment at a scan rate of 10 mV s⁻¹ in three-electrode system, inset shows the magnifies region from left and right side, (c) Electrochemical impedance spectroscopy (EIS) measurements for ^{LiTFSI}AWIS$_{(1:1.175)}$ electrolyte in different LiTFSI concentrations 7m, 10m, 14 m, and 21 m respectively to measure the ionic conductivity of the electrolyte in liquid state, inset shows the magnified region in the higher frequency range, (d) Variation of ionic conductivity with LiTFSI concentration in AWIS$_{(1:1.175)}$, (e) CV curves and GCD curves (f) for LIG-PPy composite electrode at 7 m LiTFSI concentration in different water to ACN mixture solvent wt% ratios (1:0, 1:1, 1:1.175 and 1:2) at 100 mV s⁻¹ in three-electrode system, (g) C$_{sp}$ versus water to ACN ratio variation, (h) Corresponding Nyquist plot.*

were carried out in different water to ACN ratio (1:1 and 1:1.175) are represented in Fig. 4.8c-f. Linear sweep voltammetry curve (Fig. 4.9b insets shows the magnified hydrogen evolution reaction region (left side) and oxygen evolution reaction region (right side) and a 3D bar plot given in Fig. 4.8g) clearly reveals that ^{7mLiTFSI}AWIS $_{(1:1.175)}$ provides the

maximum ESW of 2.4 V and corresponding high capacity of 168 mF cm^{-2} for the electrode material. The above mentioned two factors are majorly dependent upon the ionic conductivity and solvation structure of the electrolyte. Therefore, it is highly desired to examine the ionic conductivity value at different concentrations. To measure the ionic conductivity, electrochemical impedance spectra was taken at potential amplitude of 200 mV and in the frequency range of 0.05 to 100000 Hz. The corresponding Nyquist plot is provided in Fig. 4.9c, inset shows the magnified region at higher frequency range. The ionic conductivities were calculated to be 26 mS cm^{-1} for ^{7mLiTFSI}AWIS $_{(1:1.175)}$, 18 mS cm^{-1} for ^{10mLiTFSI}AWIS $_{(1:1.175)}$, 14 mS cm^{-1} for ^{14mLiTFSI}AWIS $_{(1:1.175)}$ and 7 mS cm^{-1} for ^{21mLiTFSI}AWIS $_{(1:1.175)}$, respectively as shown in Fig. 4.9d. Since, the magnitude of ions present in the electrolyte system is expected to play a significant role towards the ionic diffusion depending upon its ability to affect the solvent structure. Consequently, charge density decreases with increase in the acetonitrile amount in the solvent mixture and the ion–dipole forces between cations and water molecules weakens, which in turn helps to reduce the water solvation structure formation.

To get more insightful study about the remarkable changes in electrochemical features of the electrode material with ACN concentration variation in $^{7m~LiTFSI}$AWIS electrolyte, CV (Fig. 4.9e) and GCD (4.9f) were performed. It reflects from both the analysis that again ^{7mLiTFSI}AWIS $_{(1:1.175)}$ shows the best storage properties. The measured specific capacitance values for LIG-PPy electrode in 7 m AWIS electrolyte are 62 mF cm^{-2}, 142 mF cm^{-2}, 168 mF cm^{-2} and 160 mF cm^{-2} with respect to solvent mixture ratio of 1:0, 1:1, 1:1.175 and 1:2, respectively (Fig. 4.9g). The capacitance value increases with the increase in the acetonitrile weight percentage in the solvent is due to the increased ionic conductivity of the resulting electrolyte and also due to the reduced water molecules chemical activity at the electrode surface enabling the faster charge/discharge process. Electrode kinetic behaviour in the aforementioned electrolytic system (7 m LiTFSI in 1:0, 1:1, 1:1.175 and 1:2 H$_2$O to ACN mixture solvent) was further examined by performing the electrochemical impedance spectroscopy (EIS) as shown in Fig. 4.9h. The Nyquist plots at all the electrolytic conditions of 7m LiTFSI was recorded in the frequency range of 0.1 Hz to 100 kHz. At high frequency region, the observed pattern of this plot shows the bulk electrolyte resistance which the follows the sequence as ^{7mLiTFSI}AWIS $_{(1:0)}$ > ^{7mLiTFSI}AWIS $_{(1:1)}$ > ^{7mLiTFSI}AWIS $_{(1:2)}$ ≈ ^{7mLiTFSI}AWIS $_{(1:1.175)}$. Notably, at lower frequencies, the Nyquist plot becomes more vertical at a concentration of ^{7mLiTFSI}AWIS $_{(1:1.175)}$ suggesting it to be having the best capacitive behaviour out of four
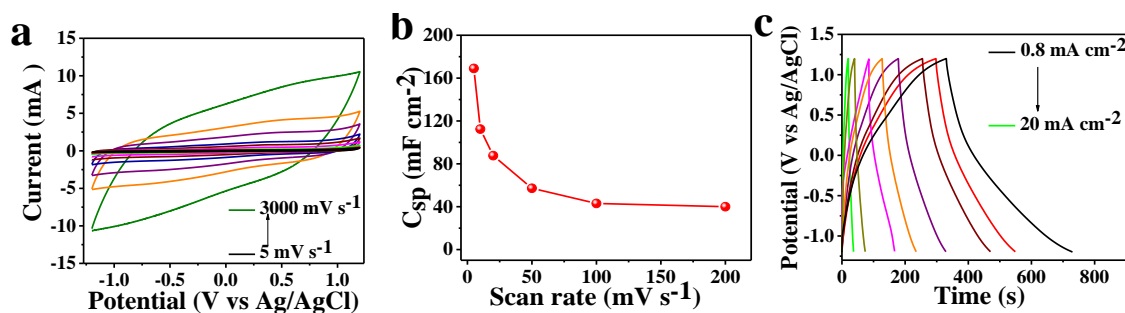
Figure 4.10. *(a) CV curves at different scan rates for LIG-PPy electrode in optimized ^{7m} $^{LiTFSI}AWIS_{(1:1.175)}$ electrolyte concentration, (b) The variation of specific capacitance of LIG-PPy electrode at different scan rate showing good rate capability of the electrode material. (c) GCD curves at different current densities, respectively.*

different concentration ratios investigated. The electrochemical response of LIG-PPy electrode at various scan rates and current densities in resulting electrolyte $^{7mLiTFSI}AWIS_{(1:1.175)}$ is illustrated in Fig. 4.10 a-c. The corresponding CV curves shows very less distortion in the rectangular shape even at very higher scan rate *i. e.,* 3000 mV s^{-1} and represents a ~40% of capacitive retention at a scan rate of 200 mV s^{-1} (Fig. 4.10b). Similarly, GCD curves (Fig. 4.10c) attain perfectly triangular geometry at very higher current densities, providing with faster power delivery characteristics. These extraordinary properties of LIG-PPy electrode in AWIS electrolyte (under optimized conditions) can be justified with electrode surface properties like wettability of the material and the changes in solvation structure of electrolyte with solvent (water and ACN) dilution. The wetting angle was analysed through contact angle measurement of ^{7m}AWIS over LIG-PPy surface as shown in Fig. 4.11a and b. The contact angle between electrolyte droplet and electrode surface is only 22.4°, suggesting the hydrophilic nature of electrode surface (Fig. 4.11b). This exact contact between electrolyte/electrode enables excellent mass-transfer and encourages easy reaction kinetics like Li$^+$ adsorption/desorption.

The concept behind the expansion of ESW was further explained via studying the molecular structure of crystalline LiTFSI, ^{21m}WIS, ^{7m}AWIS, pure water and acetonitrile through Raman spectroscopic measurements, FT-IR investigations and ^{1}H Nuclear magnetic resonance (NMR) study as shown in Fig. 4.12a-i. The Raman spectra of crystalline LiTFSI (Fig. 4.12a) includes a sharp band positioned at 745 cm^{-1} corresponds to the existence of TFSI anionic bending vibrations, which is consistent in both the crystalline LiTFSI and ^{21m}WIS electrolyte, indicating strong cation-anion interaction.[39,45] This ionic interaction weakened after the addition of organic solvent "Acetonitrile", the

Li$^+$ ions gets solvated in the ACN.[46] It is clearly evidenced in Raman spectrograph (Fig.
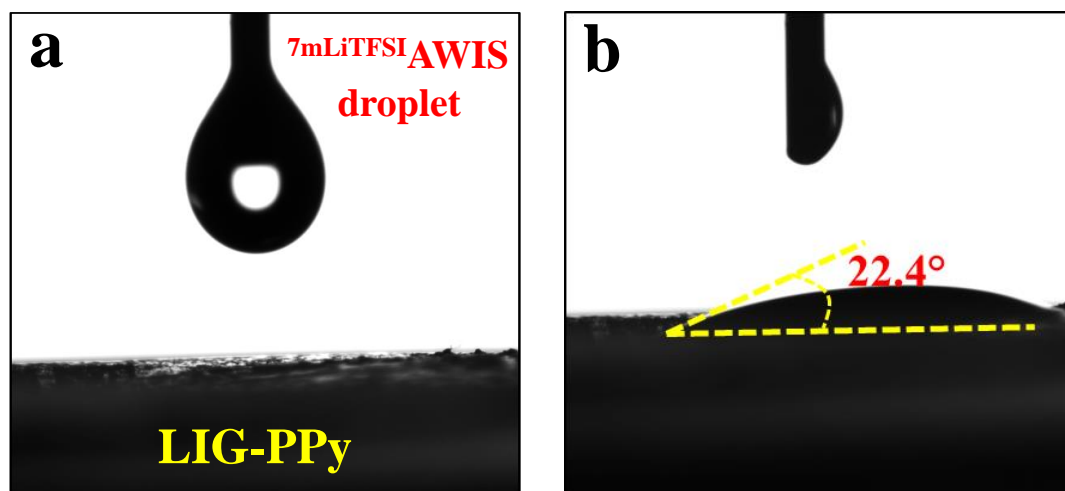
Figure 4.11 a and b *Wetting angle measurement of 7m AWIS droplet on LIG-PPy surface, representing hydrophilic surface properties.*

4.12b) of 7 m AWIS, the intense band at 745 cm^{-1} (in crystalline LiTFSI) was shifted to 739 cm^{-1} (in ^{7m}AWIS) indicates that the cation-anion aggregates diminishes to form free TFSI$^-$ anions. The Raman spectrum of pure water includes a broad Raman band in range of 3100-3530 cm^{-1} well attributed to clusters of free water molecules through H-bonding network (Fig. 4.12c).[47] The broad signal corresponding to free water clusters is disappeared in case of ^{21m}WIS and ^{7m}AWIS Raman spectra that means the whole water molecules get coordinated with Li$^+$ ions preventing the formation of water clusters. This process of removal of water clusters is the responsible fact for the reduction of water activity and widen electrolyte stability window.

How the molecular structure of ^{21m}WIS changes after addition of ACN, is clearly demonstrated schematically in Fig. 4.12d and e. Figure 4.12d display that increasing salt concentration leads to strong interaction between cations (Li$^+$) and anions (TFSI$^-$) *via* decreasing the amount of water molecule (free anions and water molecules clusters form around Li$^+$ cation in salt-in-water conditions). As explained earlier, dilution with ACN encourage the Li$^+$ and ACN molecules coordination (shown in Fig. 4.12e). The FT-IR spectra also indicate the possible changes in the solvation structure of electrolyte relative to Raman analysis (Fig. 4.12f-h).The FT-IR spectra as shown in Fig. 4.12f demonstrate that without much effecting water bending mode (positioned at 1631 cm^{-1}), the O-H stretching mode characteristic was appeared approximately at 3300 cm^{-1} in the broad signal range (3000-3700 cm^{-1}) for ^{21m}WIS and ^{7m}AWIS samples,[48] whereas the peaks at higher wavenumber region (~3420 cm^{-1} and ~3560 cm^{-1}) indicate the presence of contact

ion pair (CIPs) and ionic aggregates (AGGs).[49] The crystalline LiTFSI, [21m]WIS and [7m]WIS FT-IR spectra includes several bending and stretching modes at 737 cm^{-1}, 788 cm^{-1}, 1054 cm^{-1}, 1140 cm^{-1}, 1192 cm^{-1}, 1333 cm^{-1} and 1357 cm^{-1} corresponding to S-N stretching mode, CF_3 symmetric bending, asymmetric S-N-S stretching mode of LiTFSI, C-SO_2-N mode, asymmetric stretching mode of CF_3 in LiTFSI, C-SO_2-N bonding mode of TFSI[-] anion, asymmetric SO_2 stretching mode of LiTFSI, respectively.[50] The red shifts in asymmetric S-N-S stretching mode of LiTFSI (Fig. 4.12g) and asymmetrical stretching mode of CF_3 in LiTFSI (Fig. 4.12h) in [7m]AWIS is in good agreement with Raman explanation. To further investigation of the changes in the atomic interactions in
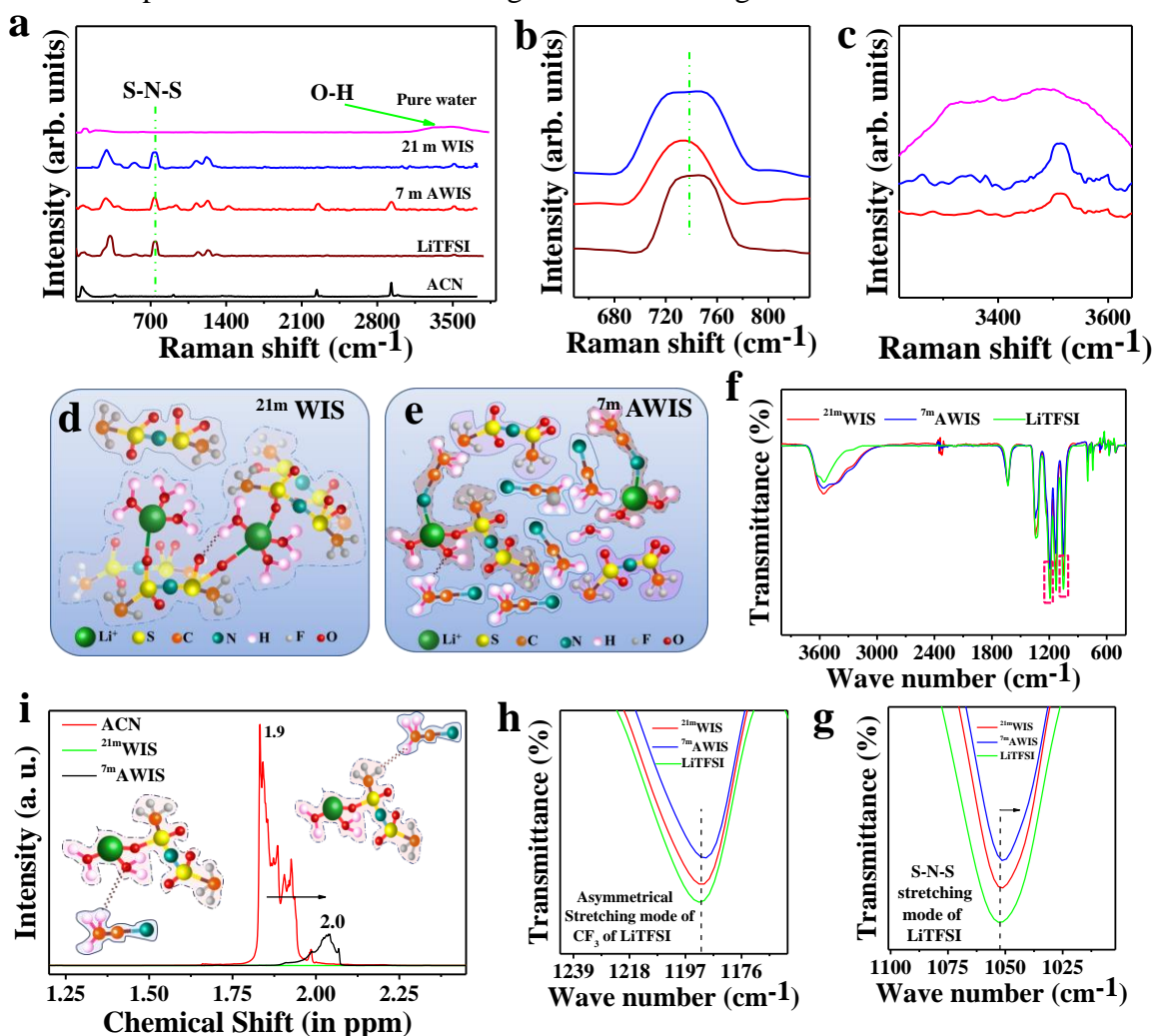
Figure 4.12 *(a) Raman study of crystalline LiTFSI, [21m]WIS, [7m]AWIS, Acetonitrile (ACN) and pure water as reference to know the molecular structure changes as LiTFSI dilution with water and ACN, Magnified Raman spectrum range indicating (b) shifting of S-N-S band, (c) comparative broad band intensity corresponding to water molecules, (d and e) [21m]WIS and [7m]AWIS molecular structure schematically representation, (f) FT-IR spectrum study of crystalline LiTFSI, [21m]WIS and [7m]AWIS, respectively, Magnified FT-IR spectrum showing the red shift of S-N-S stretching mode (g) and asymmetrical stretching mode of CF_3 (h) in [7m]AWIS, (i) 1H NMR spectrum of ACN, [7m]AWIS and [21m]WIS, inset shows the possible hydrogen bonding interactions.*

^{21m}WIS and ^{7m}AWIS, ^{1}H-NMR studies were done separately in CDCl$_3$ medium with the solvent mixtures collecting from WIS as all as AWIS and compared it with the proton NMR of pure ACN (Fig. 4.12i). WIS system does not content any ACN molecule so there is no NMR signal observed in the range of 1.8 to 2.5 ppm. But after addition of ACN (in^{7m}AWIS), we can clearly find that the protons NMR signal for -CH$_3$ group appeared at 2.04 ppm, initially presented at 1.9 ppm for pure ACN ^{1}H-NMR signal. This shifting reflects the formation of hydrogen bonding interaction with electronegative O or F atoms (come from water/TFSI$^-$) indicated in the inset of Fig.4.12i,[51] proton present in ACN might be de-shielded and may also possible due to the interaction of Li......N≡C-CH$_3$. Overall, Raman, FT-IR and NMR analysis dictates the possible steric interactions of ACN around Li$^+$ cation and TFSI$^-$ anions.

Furthermore, all the electrochemical measurements were taken for resulting linear shaped symmetrical LIG-PPy//LIG-PPy MSC in quasi solid-state electrolyte. The
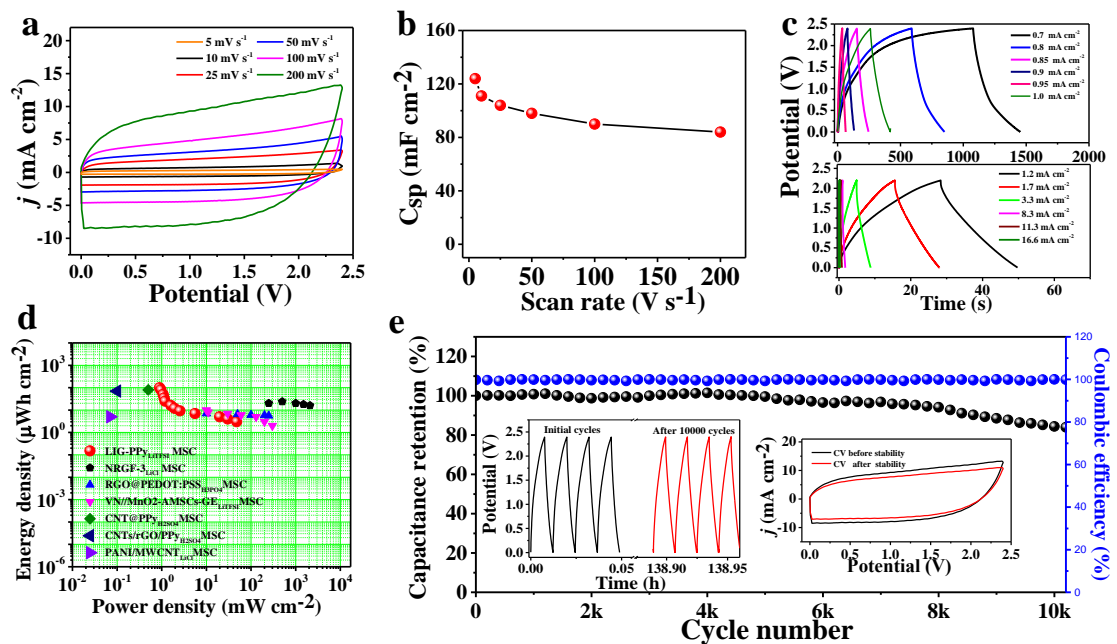
Figure 4.13. *CV curves (a) for LIG-PPy based symmetrical microsupercapacitor in quasi solid AWIS electrolyte at different scan rates, (b) Rate capability study via testing the variation of specific capacitance with scan rate, (c) GCD curves at various current densities, (d) Ragone plot representing comparison in energy density and power density of different aqueous and water-in-salt based electrolytes, (d) Electrochemical stability testing for symmetrical LIG-PPy$_{AWIS}$ MSC with continuous charge-discharge cycles, insets shows the GCD and CV curves in the initial four cycles and after 10,000*

CV curves in Fig. 4.13a retained its perfect rectangular geometry although a little polarization have emerged as the scan rate increases from 5 mV s^{-1} to 200 mV s^{-1} over the voltage window of 2.4 V (comparably higher than other reported WIS modified

MSCs as represented in Table 4.1), which is well consistent with the results of three-electrode system. All quasi solid-state LIG-PPy MSC in AWIS electrolyte delivered a
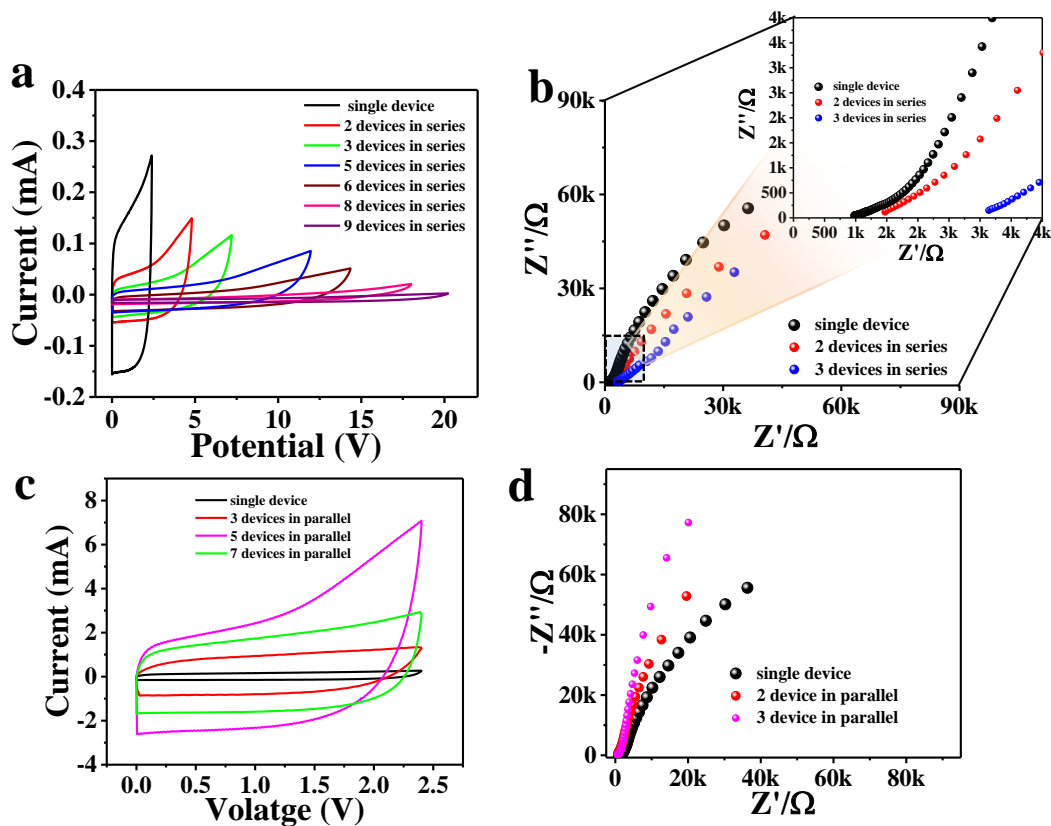
Figure 4.14 *(a) CV curves for nine solid LIG-PPy cells connected in series configuration, (b) Electrochemical impedance spectroscopic plot for the single cell, two cells in series and three cells in series configurations, respectively, (c) CV response for seven LIG-PPy cells connected in parallel configurations, (d) corresponding Nyquist plot of 3-cells in parallel configuration.*

higher reversible capacitance of 124 mF cm^{-2} at a low scan rate of 5 mV s^{-1}, which retained with sufficient capacitance value of 55 mF cm^{-2} even the scan rate increases upto 200 mV s^{-1}, showing the 45% retention of its initial capacitance (Fig. 4.13b). GCD profile (Fig. 4.13c) also gives evidence for excellent rate capability at higher current densities, which is due to the high electro-conductivity and improved reaction kinetics of LIG-PPy electrode ensuring the fast electrons transport and ions adsorption/desorption processes. The present symmetrical LIG-PPy MSC could deliver an energy density of 99.2 µWh cm^{-2} at a power density of 0.89 mW cm^{-2} and was capable of retaining energy density upto 1.68 µWh cm^{-2} at device maximum output power density of 47.75 mW cm^{-2} (Fig. 4.13d), which is comparably higher value as compared with reported water-in-salt based MSCs (Table 4.2). The energy density obtained in the LIG-PPy "AWIS" based MSC is higher than the recently reported aqueous as well as WIS based electrolyte systems.[52–57] Furthermore, to check the durability of the device, continuous charge discharge cycling

was performed at a current density of 0.9 mA cm^{-2} and the capacitance fade at a percentage of 5.8% (94.2% capacity retention) after 8000 cycles and retained capacitance of 84% as compared with its initial capacitance after 10000 cycles (as shown in Fig. 4.13e, inset represents the GCD and CV curves in initial four cycles and after 10,000

Table 4.1 *represents the electrochemical performance comparison of LIG-PPy in aqueous medium with literature reported articles*

Sr. No.	Electrode material	Type of SC	Electrolyte	Potential window	Specific capacitance	Energy density	Power density	Stability cycling (retention)	References
1	Poly(aniline-co-pyrrole)/thermally reduced graphene oxide (PAP/TrGO)	symmetrical	1 M H$_2$SO$_4$	1 V	287 F g^{-1} at 0.2 A g^{-1}	6.3 Wh Kg^{-1}	12.2 kW kg^{-1}	10,000 (103%)	58
2.	GO/PPy	Three electrodes	1 M KCl	0.9 V	633 F g^{-1}	--	--	1000 (94%)	59
3.	PPy	Three electrodes	0.5 M H$_2$SO$_4$	1 V	476 F g^{-1}	---	--	--	60
4.	Polypyrrole/graphene foam	sandwich	PVA-H$_3$PO$_4$	0.8 V	258 mF cm^{-2}	22.9 μWh cm^{-2}	6.14 mW cm^{-2}	1000 (94.8%) strain capacity	32
5.	Graphene/poly pyrrole/Cu$_2$O-Cu(OH)$_2$		0.5 M Na$_2$SO$_4$		997 F g-1 (3 electrode system)	20 Wh kg-1	19.998 kW kg^{-1}	2000 (90%)	61
6.	Graphene/poly pyrrole hydrogel		PVA-H$_3$PO$_4$	0.8 V	363 F cm^{-3}	--	--	12000 (98.6%)	62

7.	PPy/rGO/MWCNT	In-plane	4 M LiCl & PVA-H_3PO_4	0.8 V	29.5 F cm^{-3} at 10 mV s^{-1}	0.94 mWh cm^{-3}	117.12 mW cm^{-3}	3000 (84 %) under stretch condition	63
8.	Graphite flakes/polypyrrole	In-plane	1 M H_2SO_4 & PVA-H_3PO_4	0.8 V	37 mF cm^{-2} (half cell)	3.194 μW h cm^{-2}	0.842 μW cm^{-2}	5000 (99.5 %)	64
9.	PPy/PET	In-plane	PVA-H_3PO_4	0.8 V	1.64 mF cm^{-2}	4.95 mWh cm^{-3}	67.25 mW cm^{-3}	1000 (80 %)	65
10	**LIG-PPy MSC**	**In-plane**	**1 M H_3PO_4**	**1.1 V**	**25.7 mF cm^{-2}**	--	--	--	**This work**

cycles, respectively). The brief comparison of electrochemical performance of LIG-PPy MSC is given in Table 4.1 and Table 4.2 with previously reported articles in aqueous medium as well as in water-in-salt medium.

To illustrate the potential of all solid state LIG-PPy based MSC in large-scale integrated device applications; several cells were connected in series and parallel configurations in order to increase the voltage and current of the device. The voltage window can be expanded from 2.4 V to 20 V as shown in Fig. 4.14a *via* connecting nine cells in series configuration without any deformation in the rectangular and triangular shape of CV and GCD curves, respectively. It is expected the diminishing of the resistance behaviour as one cell get serially connected to another cell (indicated in the Nyquist plot Fig. 4.14b). In parallel combination the current increases while maintaining the voltage of the device constant as shown in Fig. 4.14c. Seven cells connected in parallel combination (Fig. 4.14c) imply the current output increases approximately seven times to that of the single device current and the resistance value decreases while increasing the parallel combinations is clearly visible in the EIS spectra (Fig. 4.14d). Such a high voltage (20 V) and high current features makes this quasi-solid state AWIS based symmetrical MSC a viable energy storage device for today practical energy applications.

Table 4.2 *represents a comparison of output electrochemical performance of LIG-PPy in water-in-salt medium with literature reported articles*

Sr. No.	Electrode materials	Type of SC	Electrolyte	Potential window	Specific capacitance	Energy density	Power density	Stability cycling (retention)	ref
1	MXene (-ve) Ti_3C_2 and Manganese oxide α-MnO_2 (+ve)	Asymmetrical cell	21 m CH_3COOK	2.2 V	25 F cm^{-3}	16.80 mWh cm^{-3}	137 mW cm^{-3}	10,000 (92 %)	[66]
2.	n-doped reduced graphene oxide (n-rGO)	Symmetrical	LiCL/PVA GPE	2.2 V	152.1 mF cm^{-2}	25.6 µWh cm^{-2}	2200 µW cm^{-2}	20,000 (84 %)	[57]
3.	YP-50 AC	Symmetrical	AWIS (LiTFSI)	3.0 V	27.0 F g^{-1} at 10 A g^{-1}	--	--	14,000 at 6 A g^{-1} (81 %)	[28]
4.	Polyaniline-derived carbon nanorods (PDCN)	Symmetrical	21 m LiTFSI	2.2 V	44 F g^{-1} at 1 A g^{-1}	29.6 Wh kg^{-1}	10.9 kW kg^{-1}	6,000 (73 %)	[67]
5.	N-doped graphene hydrogel	Symmetrical	24 M CH_3COOK	2.1 V	154.2 mF cm^{-2}	33.1 W h kg^{-1}	--	6000 (88.2 %)	[68]
6.	NSOC	Symmetrical	GWIS	2.3 V	51.3 F g^{-1}	20.6 Wh kg^{-1}	11500 W kg^{-1}	10,000 (85.9 %)	[69]
7.	**LIG-PPy**	**Symmetrical**	**AWIS**	**2.4 V**	**168 mF cm^{-2} (half cell), 120 mF cm^{-2} (full cell)**	**99.2 µWh cm^{-2}**	**47.75 mW cm^{-2}**	**8,000 (94.2%), 10,000 (84%)**	**This work**

*GPE- Gel polymer electrolyte, **AC**- activated carbon, **AWIS**- Acetonitrile/Water-in-Salt, **PPy** – Poly(pyrrole), **MWCNT** – multi-wall carbon nanotubes, **PET**-Poly ethylene terephthalate, LIG-laser irradiated graphene, **NSOC**- Nitrogen, sulphur, oxygen ternary doped carbon, **GWIS**- gel water in salt.*

4.4 Conclusions

In summary, metal-free, highly conducting laser-irradiated graphene electrode was modified with pseudocapacitive material (*i.e.,* PPy) to increase the current output with effective -N sites and the electrolytic environment was changed from "salt-in-water" to "Acetonitrile/water-in-salt" to increase the electrochemical stability window which provides high energy density storage cell. This work thoroughly explained the effects of LiTFSI concentration and the volume concentration variation of ACN in water over solvation structure and electrochemical response with the help of Raman and ^{1}H NMR investigations. The as-modified metal-free electrode (LIG-PPy) in ^{7mLiTFSI}AWIS $_{(1:1.175)}$ electrolytic medium shows tremendous electrical and electrochemical properties. The fabricated metal-free symmetrical LIG-PPy$_{AWIS}$ MSC results extended electrochemical stability window to 2.4 V, enhanced specific capacitance of 124 mF cm^{-2} as compared to LIG-MSC C$_{sp}$ value 2.3 mF cm^{-2} (reported previously), an energy density of 99.2 µWh cm^{-2} and a power density of 47.75 mW cm^{-2}, respectively. Consequently, this work will pave the best possible way for the development of high-voltage (upto 20 V) on-chip metal-free energy storage module with robust nature, integrated miniaturization features, greater storage capacity and corresponding high energy density for micro-electronics applications.

4.5 References

1   S. Patrice, G. Yury and D. Bruce, *Science*, 2014, **343**, 1210–1211.

2   C. Zhong, Y. Deng, W. Hu, J. Qiao, L. Zhang and J. Zhang, *Chem. Soc. Rev.*, 2015, **44**, 7484–7539.

3   A. K. Geim and K. S. Novoselov, *Nat. Mater.*, 2007, **6**, 183–191.

4   Y. Sun, Q. Wu and G. Shi, *Energy Environ. Sci.*, 2011, **4**, 1113–1132.

5   N. A. Kyeremateng, T. Brousse and D. Pech, *Nat. Nanotechnol.*, 2017, **12**, 7–15.

6   W. Gao, N. Singh, L. Song, Z. Liu, A. L. M. Reddy, L. Ci, R. Vajtai, Q. Zhang, B. Wei and P. M. Ajayan, *Nat. Nanotechnol.*, 2011, **6**, 496.

7   N. Kamboj, T. Purkait, M. Das, S. Sarkar, K. S. Hazra and R. S. Dey, *Energy Environ. Sci.*, 2019, **12**, 2507–2517.

8   J. Mao, J. Iocozzia, J. Huang, K. Meng, Y. Lai and Z. Lin, *Energy Environ. Sci.*, 2018, **11**, 772–799.

9   K. Naoi, S. Ishimoto, J. Miyamoto and W. Naoi, *Energy Environ. Sci.*, 2012, **5**, 9363–9373.

10   L. Peng, P. Xiong, L. Ma, Y. Yuan, Y. Zhu, D. Chen, X. Luo, J. Lu, K. Amine

and G. Yu, *Nat. Commun.*, 2017, **8**, 15139.

11   T. Purkait, G. Singh, N. Kamboj, M. Das and R. S. Dey, *J. Mater. Chem. A*, 2018, **6**, 22858–22869.

12   J. Wu, Q. Zhang, J. Wang, X. Huang and H. Bai, *Energy Environ. Sci.*, 2018, **11**, 1280–1286.

13   G. A. Snook, P. Kao and A. S. Best, *J. Power Sources*, 2011, **196**, 1–12.

14   C. Peng, J. Jin and G. Z. Chen, *Electrochim. Acta*, 2007, **53**, 525–537.

15   V. Khomenko, E. Frackowiak and F. Béguin, *Electrochim. Acta*, 2005, **50**, 2499–2506.

16   Q. Wu, Y. Xu, Z. Yao, A. Liu and G. Shi, *ACS Nano*, 2010, **4**, 1963–1970.

17   Q. Nian, W. Zhu, S. Zheng, S. Chen, B.-Q. Xiong, Z. Wang, X. Wu, Z. Tao and X. Ren, *ACS Appl. Mater. Interfaces*, 2021, **13**, 51048–51056.

18   J. Durst, A. Siebel, C. Simon, F. Hasché, J. Herranz and H. A. Gasteiger, *Energy Environ. Sci.*, 2014, **7**, 2255–2260.

19   M. P. Bichat, E. Raymundo-Piñero and F. Béguin, *Carbon N. Y.*, 2010, **48**, 4351–4361.

20   Y. Wen, B. Wang, C. Huang, L. Wang and D. Hulicova-Jurcakova, *Chem. – A Eur. J.*, 2015, **21**, 80–85.

21   M. Yu, D. Lin, H. Feng, Y. Zeng, Y. Tong and X. Lu, *Angew. Chem. Int. Ed. Engl.*, 2017, **56**, 5454–5459.

22   S.-E. Chun, B. Evanko, X. Wang, D. Vonlanthen, X. Ji, G. D. Stucky and S. W. Boettcher, *Nat. Commun.*, 2015, **6**, 7818.

23   J. Y. Hwang, M. Li, M. F. El-Kady and R. B. Kaner, *Adv. Funct. Mater.*, 2017, **27**, 1605745.

24   V. Khomenko, E. Raymundo-Piñero and F. Béguin, *J. Power Sources*, 2010, **195**, 4234–4241.

25   Q. Gao, L. Demarconnay, E. Raymundo-Piñero and F. Béguin, *Energy Environ. Sci.*, 2012, **5**, 9611–9617.

26   N. Feng, B. Wang, Z. Yu, Y. Gu, L. Xu, J. Ma, Y. Wang and Y. Xia, *ACS Appl. Mater. Interfaces*, 2021, **13**, 7396–7404.

27   M. J. R. and S. Patrice, *Science*, 2008, **321**, 651–652.

28   Q. Dou, S. Lei, D.-W. Wang, Q. Zhang, D. Xiao, H. Guo, A. Wang, H. Yang, Y. Li, S. Shi and X. Yan, *Energy Environ. Sci.*, 2018, **11**, 3212–3219.

29   N. Kamboj, T. Purkait, M. Das, S. Sarkar, K. S. Hazra and R. S. Dey, *Energy*

Environ. Sci., 2019, **12**, 2507–2517.

30   S. Kulandaivalu, N. Suhaimi and Y. Sulaiman, *Sci. Rep.*, 2019, **9**, 4884.

31   I. J. Gómez, M. Vázquez Sulleiro, D. Mantione and N. Alegret, *Polym.* , 2021, 13.

32   J. Ren, R. Ren and Y.-K. Lv, *Chem. Eng. J.*, 2018, **349**, 111–118.

33   X. Zhang, J. Wang, J. Liu, J. Wu, H. Chen and B. Hong, *Carbon N. Y.*, 2017, **115**, 134–146.

34   Y.-C. Liu, *J. Electroanal. Chem. - J ELECTROANAL CHEM*, 2004, **571**, 255–264.

35   Y. Chen, K. Cai, C. Liu, H. Song and X. Yang, *Adv. Energy Mater.*, 2017, **7**, 1701247.

36   L. Fu, X. Fu and G. Zhao, *Chem. Phys. Lett.*, 2021, **765**, 138290.

37   Z. Wang, X. Xiong, L. Qie and Y. Huang, *Electrochim. Acta*, 2013, **106**, 320–326.

38   R. Rajagopalan and J. O. Iroh, *Appl. Surf. Sci.*, 2003, **218**, 58–69.

39   L. Suo, O. Borodin, T. Gao, M. Olguin, J. Ho, X. Fan, C. Luo, C. Wang and K. Xu, *Science*, 2015, **350**, 938–943.

40   L. Suo, O. Borodin, W. Sun, X. Fan, C. Yang, F. Wang, T. Gao, Z. Ma, M. Schroeder, A. von Cresce, S. M. Russell, M. Armand, A. Angell, K. Xu and C. Wang, *Angew. Chemie Int. Ed.*, 2016, **55**, 7136–7141.

41   A. C. Forse, J. M. Griffin, C. Merlet, J. Carretero-Gonzalez, A.-R. O. Raji, N. M. Trease and C. P. Grey, *Nat. Energy*, 2017, **2**, 16216.

42   W. Liu, X. Yan, J. Lang and Q. Xue, *J. Mater. Chem.*, 2012, **22**, 8853–8861.

43   Y. Yamada, K. Usui, K. Sodeyama, S. Ko, Y. Tateyama and A. Yamada, *Nat. Energy*, 2016, **1**, 16129.

44   Y. Sun, Y. Wang, L. Liu, B. Liu, Q. Zhang, D. Wu, H. Zhang and X. Yan, *J. Mater. Chem. A*, 2020, **8**, 17998–18006.

45   D. M. Seo, O. Borodin, S.-D. Han, P. D. Boyle and W. A. Henderson, *J. Electrochem. Soc.*, 2012, **159**, A1489–A1500.

46   J. Zheng, J. Lochala, A. Kwok, Z. Deng and J. Xiao, *Adv. Sci.*, 2017, **4**, 1700032.

47   Y.-H. Zhang and C. K. Chan, *J. Phys. Chem. A*, 2003, **107**, 5956–5962.

48   D. Strmcnik, M. Uchimura, C. Wang, R. Subbaraman, N. Danilovic, D. van der Vliet, A. P. Paulikas, V. R. Stamenkovic and N. M. Markovic, *Nat. Chem.*, 2013,

5, 300–306.

49   O. Borodin, L. Suo, M. Gobet, X. Ren, F. Wang, A. Faraone, J. Peng, M. Olguin, M. Schroeder, M. S. Ding, E. Gobrogge, A. von Wald Cresce, S. Munoz, J. A. Dura, S. Greenbaum, C. Wang and K. Xu, *ACS Nano*, 2017, **11**, 10462–10471.

50   S. Liumin, B. Oleg, G. Tao, O. Marco, H. Janet, F. Xiulin, L. Chao, W. Chunsheng and X. Kang, *Science*, 2015, **350**, 938–943.

51   C. H. Giammanco, P. L. Kramer and M. D. Fayer, *J. Phys. Chem. B*, 2016, **120**, 9997–10009.

52   C. Choi, J. M. Lee, S. H. Kim, S. J. Kim, J. Di and R. H. Baughman, *Nano Lett.*, 2016, **16**, 7677–7684.

53   R. Hu and J. Zheng, *J. Power Sources*, 2017, **364**, 200–207.

54   S. Wang, Y. Liang, W. Zhuo, H. Lei, M. S. Javed, B. Liu, Z. Wang and W. Mai, *Mater. Chem. Front.*, 2021, **5**, 1324–1329.

55   J. Qin, S. Wang, F. Zhou, P. Das, S. Zheng, C. Sun, X. Bao and Z.-S. Wu, *Energy Storage Mater.*, 2019, **18**, 397–404.

56   G. Qu, J. Cheng, X. Li, D. Yuan, P. Chen, X. Chen, B. Wang and H. Peng, *Adv. Mater.*, 2016, **28**, 3646–3652.

57   Q. Liu, J. Zhou, C. Song, X. Li, Z. Wang, J. Yang, J. Cheng, H. Li and B. Wang, *Energy Storage Mater.*, 2020, **24**, 495–503.

58   A. Moyseowicz, Z. Arias, R. Menéndez and G. Gryglewicz, *Compos. Part B Eng.*, 2018, **145**, 232–239.

59   J. Li and H. Xie, *Mater. Lett.*, 2012, **78**, 106–109.

60   D. P. Dubal, S. V Patil, W. B. Kim and C. D. Lokhande, *Mater. Lett.*, 2011, **65**, 2628–2631.

61   P. Asen and S. Shahrokhian, *J. Phys. Chem. C*, 2017, **121**, 6508–6519.

62   X. Wu and M. Lian, *J. Power Sources*, 2017, **362**, 184–191.

63   S. Wang, N. Liu, J. Su, L. Li, F. Long, Z. Zou, X. Jiang and Y. Gao, *ACS Nano*, 2017, **11**, 2066–2074.

64   C. J. Raj, B. C. Kim, W.-J. Cho, W. Lee, S.-D. Jung, Y. H. Kim, S. Y. Park and K. H. Yu, *ACS Appl. Mater. Interfaces*, 2015, **7**, 13405–13414.

65   X. Jiao, C. Zhang and Z. Yuan, *ACS Appl. Mater. Interfaces*, 2018, **10**, 41299–41311.

66   H. Avireddy, B. W. Byles, D. Pinto, J. M. Delgado Galindo, J. J. Biendicho, X. Wang, C. Flox, O. Crosnier, T. Brousse, E. Pomerantseva, J. R. Morante and Y.

Gogotsi, *Nano Energy*, 2019, **64**, 103961.

67   D. Xiao, Q. Wu, X. Liu, Q. Dou, L. Lingyang, Y. Bingjun and H. Yu, *ChemElectroChem*, , DOI:10.1002/celc.201801342.

68   Y. Deng, H. Wang, K. Zhang, J. Shao, J. Qiu, J. Wu, Y. Wu and L. Yan, *Nanoscale*, 2021, **13**, 3010–3018.

69   Z. Song, H. Duan, D. Zhu, Y. Lv, W. Xiong, T. Cao, L. Li, M. Liu and L. Gan, *J. Mater. Chem. A*, 2019, **7**, 15801–15811.

Chapter 5

Electrochemically synthesized highly crystalline single-phase Ni₃P superstructure for rechargeable Ni-Zn battery
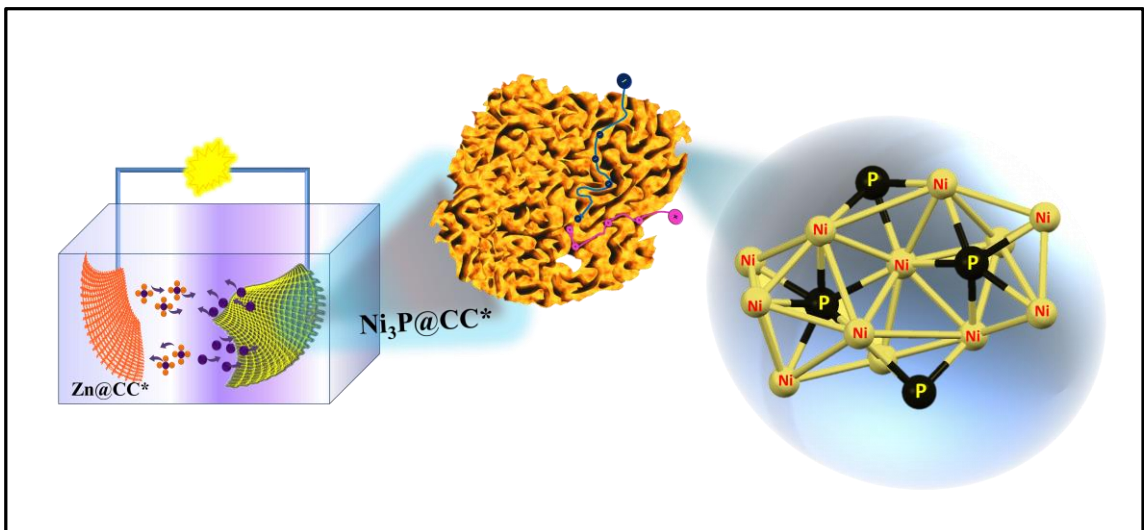
Abstract: Zn-based aqueous batteries have become a highlighted field in worldwide research on rechargeable energy storage systems due to their significant merits as safe and cost-effective technology. However, the lack of proper cathode materials having sufficient accessible channels for ionic diffusion in order to achieve excellent power delivery, higher energy storage capacity and good cycle stability challenge their use in practical application. Herein, we demonstrate electrodeposited porous Ni_3P superstructures on activated carbon cloth (CC*) as a robust cathode material towards enhanced Ni-Zn aqueous battery technology. The as-deposited Ni_3P exhibiting internal porous network with fully exposed active sites accelerates the electrode kinetics by providing affluent channels for electron transfer. This unique structure of Ni_3P electrode offers remarkable specific capacity of 258 mA h g^{-1} along with tremendous high-rate capability (maintains 81% at 11 A g^{-1}). Moreover, the $Ni_3P@CC*//Zn@CC*$ battery is capable of showing a record-high specific capacity of 322 mA h g^{-1}, power density 17.5 kW kg^{-1} and imposing energy density of 661.98 Wh kg^{-1}. These results open a new avenue for developing an easy synthesis strategy for cathode materials of Ni-Zn batteries with boosted electrochemical activity toward affordable and practical energy storage.

5.1 Introduction

High energy/power density and intrinsically safe renewable energy storage systems have become a foremost essential in advancement of microelectronics and electric vehicle technologies. [1–4] Among all the energy storage systems, highly energetic Lithium ion batteries (LIBs) dominate in the rechargeable battery trade with their omnipresence in consumer electronic applications.[5] However, high cost and safety concern associated with the limited resources of Li and the corresponding production technology,[6,7] limited rate capability and ionic conductivities of Li^+ in aprotic electrolytes, restricts the scope of LIB in high-power applications.[8,9] Nowadays, multivalent ions (such as Zn^{2+}, Mg^{2+}, Al^{3+}) based batteries are emerging as new generation battery systems to replace LIBs for energy storage technologies. Alternative aqueous batteries such as rechargeable Zn-ion batteries can offer a possible solution to the storage technology due to their worldwide reserve, lower redox potential, enlarged theoretical capacity of 825 mAh g^{-1},[10] intrinsically protection with incombustible aqueous electrolytes and comparable or higher specific energies than Li-ion batteries.[11] During preliminary research, various Zn-based secondary batteries were used such as $Zn-MnO_2$, $Zn-Co_3O_4$, $Zn-Ni_3Se_2$, Zn-NiCo hydroxide and so on.[12–17]

It is well understood that the overall performance of Ni-Zn battery depends upon the characteristic features of the cathodic electrode materials. In particular, various Ni-based cathodic materials like nickel oxides, hydroxides, selenides and phosphides have been explored due to their multiple features like high output working voltage window (~1.8 V) compared to other aqueous batteries, which is of mostly $\leq$ 1.2 V [18–20], abundant reserve, good reversibility and high specific capacity. However, very low electrical conductivity and confined interfacial kinetics of the nickel oxides, hydroxides, sulphides and selenides prohibit their higher theoretical specific capacity at high rates of charge/discharge process.[21] Recently, considerable attempts have been made in designing the hybrid nanostructured of Ni-based materials such as a) conductive reinforcements (carbon fiber, metal nanowire array), b) tuning the morphology and composition such as cobalt-doped $Ni(OH)_2$ on nickel nanowires arrays (NAA@CNH), nanoflakes of NiO, Ni_3S_2 nanosheet[14,17,22,23] c) hetero-structured nanosheets (Ni-NiO),[17] and d) other Ni-based compounds like NiAlCo-LDH (layered double hydroxide) nanoplates coupled with few-walled carbon nanotubes (NiAlCo LDH/CNT),[24] for efficient cathode development. It can be concluded that three- dimensional (3D) porous

nanoarchitecture with large surface area, sufficient exposed active sites, seamless inter-connectivity and shorten ionic diffusion path length would facilitate the fast charge transport kinetics and accelerates the ionic diffusion that can be a game-changer for the best upgradation in Ni-Zn battery systems.[25,26] Despite a few achievements, Ni-Zn battery is still far from the commercialization standards due to the limited capacity and poor cycling stability compared to most of the reported Ni-Zn batteries. Moreover, complicated synthesis procedure involving some ambient conditions, long duration and harsh chemicals restrict their use as large-scale energy storage applications.[24,27–29] Therefore, a facile synthetic route is an urgent need to explore the novel Ni-based cathode material with good reversibility, low polarization, high conductivity and unique structural features to increase the active site density.

Recently, transition metal phosphides, particularly Nickel phosphides have been meticulously used as electrode material in energy storage applications for their metalloid properties, excellent electrocatalytic activity, high chemical stability and reversible electrochemical properties.[30–33] Among all existing phases of Nickel phosphides (NiP, Ni_2P, Ni_3P, Ni_5P_4 etc.), the Ni_3P phase shows excellent electrochemical performance for their low polarization, good reversibility in alkaline medium.[34] Thus, a nanoporous Ni_3P based cathode electrode should be rationally designed for improving the performance of alkaline battery system.

Electrochemical synthesis has several advantages, such as 1) this is a facile one-step process, 2) does not require high temperature, 3) low-cost and less chemical consumption, 4) considered as green approach and 5) porous all-in-one catalyst can be prepared on the current collector in a short duration. However, comparing with literature, there are no such reports till date for the electrochemically synthesized Ni_3P directly on the carbon cloth current collector that was explored for Ni-Zn battery. Herein, we report a scalable, simple and inexpensive strategy to prepare a single-phase 3D hierarchical porous structure of Ni_3P on pre-treated carbon cloth (denoted as $Ni_3P@CC^*$) *via* a single-step electrochemical deposition method with enhanced electrochemical activity as the state-of-the-art cathode for aqueous Ni-Zn battery. The resultant Ni_3P nanostructure seamlessly constructs a 3D porous network with large active site density, which not only offers a high surface area but also can afford 3D electron transfer networks and ion diffusion channels. These metrics endows this $Ni_3P@CC^*$ electrode with an extraordinary specific capacity of 258 mA h g^{-1} at 1 A g^{-1} and excellent rate performance.

Moreover, $Ni_3P@CC^*$ as cathode and $Zn@CC^*$ as an anode were used to build a high-performance Ni-Zn battery, delivering a maximum capacity of 322 mA h g^{-1} at a current density of 1 A g^{-1}, high energy density 661.98 W h kg^{-1}, the power density 17.5 kW kg^{-1} and excellent rate capability.

5.2 Experimental Section

5.2.1 Activation of carbon cloth as a flexible substrate.

Commercial carbon cloth (CC) was cut into (2×3) cm^2 dimensional area. Before use, the cloths were cleaned with acetone followed by distilled water under constant ultrasonication for 5 minutes. The CC is then soaked into a mixture solution of concentrated H_2SO_4 (98%) and concentrated HNO_3 (69%) with a ratio of 2:1 for 30 min.
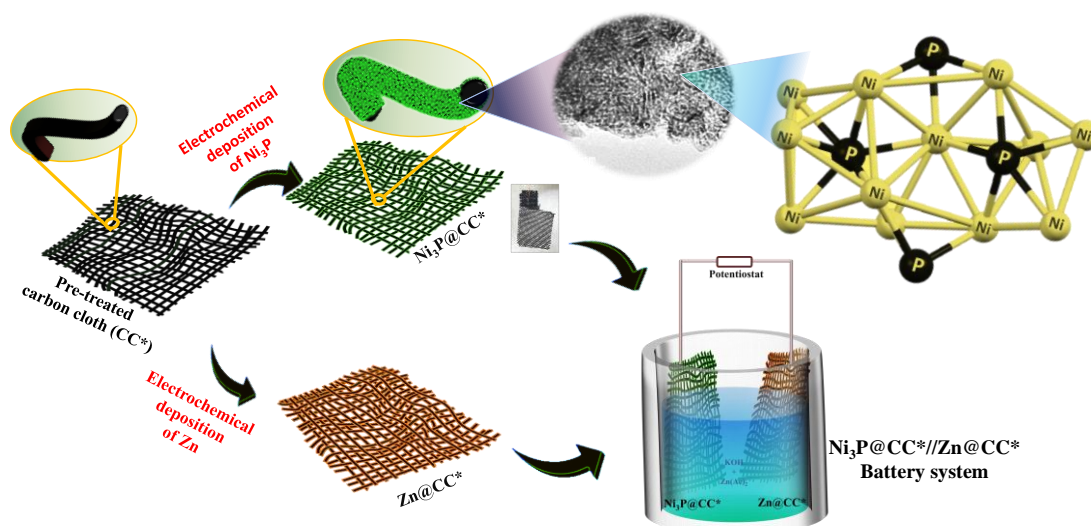
Figure 5.1. *A schematic representation of electrochemical deposition process of Ni_3P on activated carbon cloth (CC*).*

Then, the reaction was further proceeded with the addition of strong oxidizing agent $KMnO_4$ to the above mixture under vigorously stirring at room temperature. After 1 hour, 100 ml distilled water (DI) was slowly added to the mixture followed by drop wise addition of H_2O_2 until the solution become transparent. The CC was washed with DI water and transferred into the vacuum for overnight for drying. Finally, after calcination of the cloth at 950˚C for 1 hour at a temperature ramp rate of 5˚C/min, the pre-treated carbon cloth (CC*) was obtained for use.

5.2.2 Synthesis of $Ni_3P@CC^*$ *via* electrodeposition method.

A three-electrode set-up was used for the electrodeposition of Ni_3P over the CC*, which comprises CC* as a working electrode, a reference electrode Ag/AgCl (3M KCl) and a counter electrode (Platinum wire). In this method, a precursor mixture solution was

prepared from $NiCl_2.6H_2O$, $NaH_2PO_2.H_2O$ and NaH_2PO_4 with concentration values of 60 mM, 50 mM and 0.5 M, respectively. The electrochemical deposition of Ni_3P was done on CC* at constant potential (-0.8 V)bulk electrolysis method for 5400 seconds (Fig. 5.1).[33] Then, as-deposited Ni_3P on CC* was washed several times with Millipore water and stored under vacuum condition. The loaded mass of the active material was calculated to be 1 mg cm^{-2}. The electrode was then subjected to the electrochemical analysis which was performed in both three-electrode as well as in two-electrode system between a potential window of 0–0.5 V in 1 M KOH electrolyte.

5.2.3 Preparation of Zn@CC* via electrodeposition method.

Zn was electrodeposited on CC* using two-electrode system at a fixed current density (5 mA cm^{-2}) in a mixture solution of $ZnSO_4$ (0.6 M) and $(NH_4)_2SO_4$ (0.1 M) for 5000 seconds using a working CC* electrode and a counter Zinc plate (Fig 5.1). The Zn deposited carbon cloth (Zn@CC*) was washed with distilled water to extract any physically absorbed impurities on the surface and vacuum dried for overnight.

5.2.4 Electrochemical evaluation

The electrochemical techniques like cyclic voltammetry (CV), galvanostatic charge-discharge (GCD), and the electrochemical impedance spectroscopic techniques (EIS) were employed for the electrochemical investigation of the prepared samples on a CHI 760E electrochemical workstation. The cyclic voltametric testing of zinc electrode and Ni_3P on carbon cloth was performed in a three-electrode cell with a platinum wire and an Ag/AgCl as the counter and reference electrodes respectively. The Zn@CC* was assembled with Ni_3P@CC* in 15 ml 1 M KOH and 10×10^{-3} M Zn(Ac)$_2$. The two-electrode cell was used to test the cycling and charge– discharge behavior. Nyquist plots for both the electrodes as well as full battery system were carried out in electrolyte in the frequency range of 0.01–10 000 Hz.

5.2.5 Calculation of proton diffusion coefficient

In CV method, the proton diffusion coefficient D_H can be calculated based on the Sevick equations 4 and 5:

$$i_P = 0.4463 \, nFAC \left(\frac{nFvD}{RT}\right)^{1/2} \qquad \text{..........................(4)}$$

$$i_P = 2.69 \times 10^5 n^{3/2} A \, D^{1/2} C \, v^{1/2} \qquad \text{..........................(5)}$$

where $"i_P"$ is the peak current (A), "v" is the scan rate (V s^{-1}), "n" is the electron transfer number, "A" is the surface area of the electrode (cm^{-2}), and "C" is the proton

concentration (mol cm^{-3}), *"D"* Diffusion co-efficient in cm^2 s^{-1}, *"R'* Gas constant, "T" is temperature.

5.3 Result and discussion

5.3.1 Structural and morphological characterizations of Ni₃P.
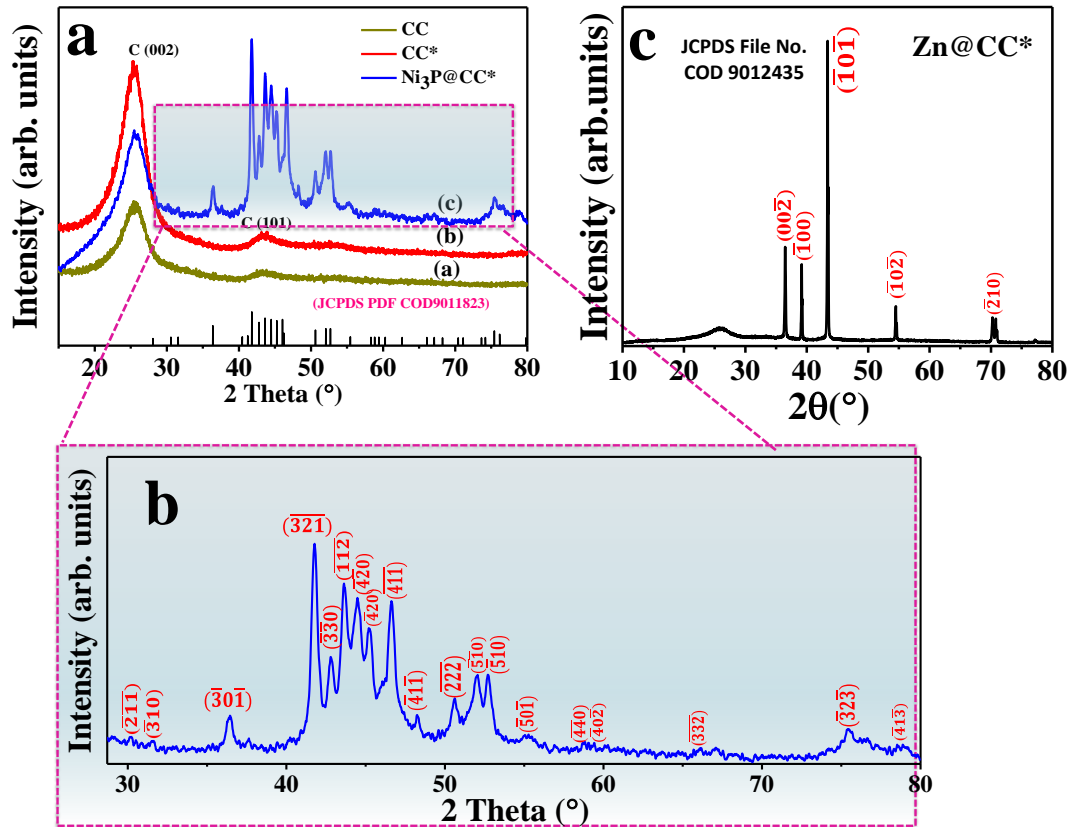
Figure 5.2. *(a) A comparative X-Ray diffraction pattern for carbon cloth (CC), pre-treated carbon cloth (CC*) and Ni₃P@CC*, (b) the magnified XRD spectra in 2θ range (28°–80°), (c) XRD pattern for Zn@CC*.*

Crystal structure and chemical composition of Ni₃P on CC* was firstly characterized via XRD analysis. The XRD pattern exhibits spectra corresponding to CC, CC* and the crystalline phase of Ni₃P, respectively is shown in Fig. 5.2a. The XRD pattern for both CC and CC* display two broad diffracted peaks at 26° and 43°, which is assigned for the (002) and (101) planes of graphite, respectively.[35] It should be noted that the (002) peak of CC* move to the higher angle with enhanced peak intensity as compared with CC which indicates improved graphitization in CC* upon pre-treatment.[36] These graphitic sites are believed to be involved in adsorption of ionic species on charged electrode during the electrodeposition process providing adequate electrical conducting pathways.[37] In the XRD spectrum of electrodeposited Ni₃P@CC*, a broad peak at around 26° originate from the CC* substrate is significantly weaker in intensity than the features
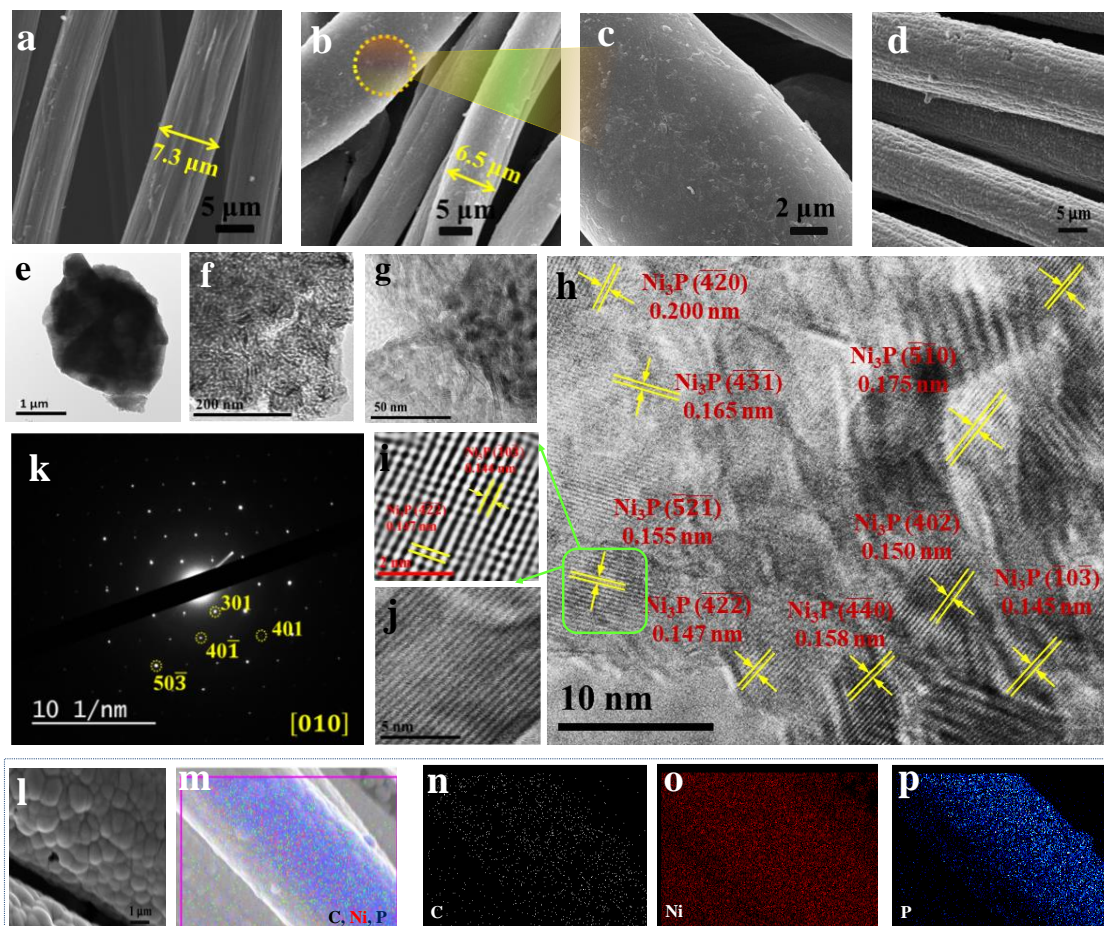
Figure 5.3 *SEM image of carbon cloth (a) before pre-treatment, (b) After pre-treatment, (c) the zoom version showing the rough surface of the carbon fibre. SEM images of (d) electrochemical deposited Ni₃P@CC*, shows the dense spheres on each and every carbon fibre, (e) TEM image of Ni₃P@CC* at a magnification of 1 µm (f, g) TEM images of a Ni₃P micro sphere, showing the porous structure at a magnification of 200 nm and 50 nm, respectively. (h) High magnification TEM image comprising various planes with corresponding d-spacing values, (i and j) HRTEM images at a magnification of 5 nm and 2 nm, respectively (k) SAED pattern for Ni₃P, illustrating the lattice pattern of [010] zone-axis, (l-p) showing EDS elemental mapping of Ni₃P@CC* sample which confirms the presence of C, Ni and P in the material.*

of Ni_3P which clearly indicates that the porous network structured of Ni_3P are well spread on the carbon cloth substrate. All the characteristic diffracted peaks of electrodeposited $Ni_3P@CC^*$ are very well assigned to the single-phase Ni_3P (JCPDS file no. COD9011823). The zoom version of the XRD spectrum of $Ni_3P@CC^*$ is shown in Fig. 5.2b from the 2θ range 28° to 80°. As expected, there were no additional diffraction peaks other than pure Ni_3P phase and carbon cloth observed, indicating excellent purity of the electrodeposited Ni_3P single-phase material. The XRD pattern for electrodeposited Zn

on CC* is shown in Fig. 5.2c, which is exactly matched with JCPDS file no. COD 9012435.

The morphology of as-prepared $Ni_3P@CC^*$ was characterized by SEM and TEM imaging as shown in Fig. 5.3. The microscopic images shown in Fig. 5.3a-c reveals that the smoothed surfaces of the carbon cloth change to rough surfaced carbon fibre with reduced diameter after pre-treatment. The severe depth of the activation conditions results in the disintegration and roughness over the surface of the fibres. Figure 5.3d
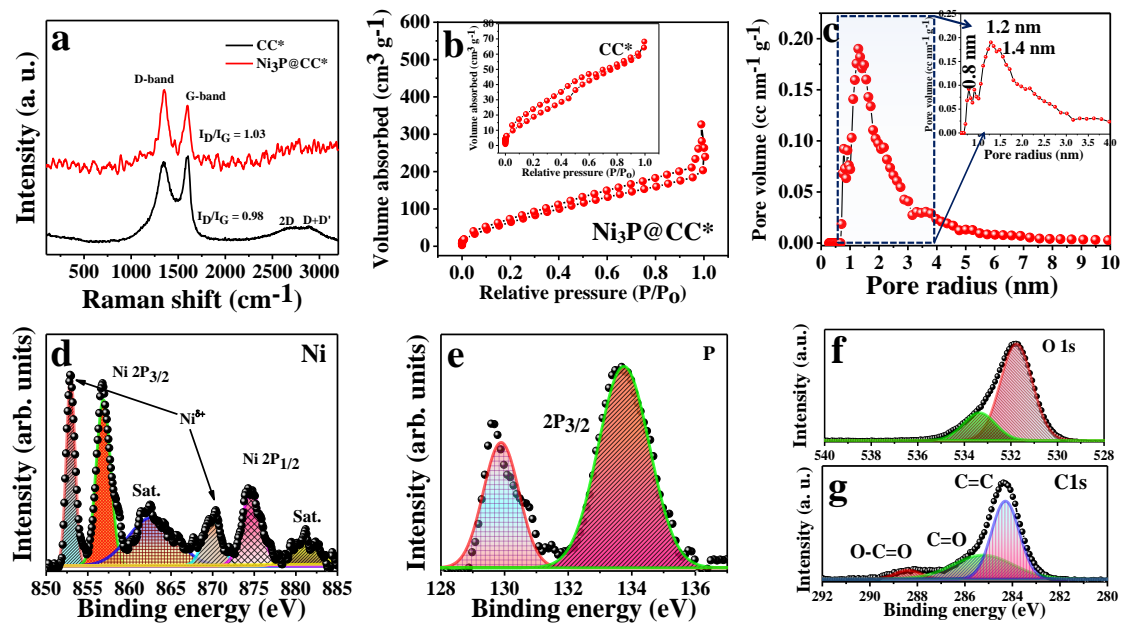
Figure 5.4*. (a) Raman spectrum for CC* and $Ni_3P@CC^*$, (b) The absorption-desorption isotherm plot for $Ni_3P@CC^*$ and CC* (in inset) sample to calculate the active surface area, (c) Pore size distribution of $Ni_3P@CC^*$ sample, (d) Deconvoluted XPS spectra of Ni 2p, (e) P 2p, (f) O 1s, (g) C 1s, respectively.*

depicts the SEM image $Ni_3P@CC^*$, a well-defined hierarchical radial structure of Ni_3P was observed. The SEM image elaborates the uniform distribution of the densely packed Ni_3P over the fibres (Fig. 5.3d). The TEM images shown in Fig. 5.3e exhibits an aggregated porous cluster of Ni_3P, which was extracted from CC* by ultrasonication in DI water. The TEM micrographs in Fig. 5.3g and h further reveals the internal structure of Ni_3P that exhibits a hierarchical porous network-like structure. This kind of hierarchical structure advantageous over solid structures for the electrolytic ions permeation and electronic transportation.[38] The HRTEM image (Fig. 5.3h-j) confirms the formation of different planes of Ni_3P phase highlighted with their d-spacing values, which fitted very well with different facets of tetragonal Ni_3P. The selected area electron diffraction (SAED) spots (Fig. 5.3k) are splendidly indexed to the diffraction pattern of a particular zone axis [010]. It can be seen from Ni_3P SAED pattern, the material has

excellent crystallinity with enlarged grain alignments along [010] zone axis. The appearance of forbidden spots with less intensity is probably due to the multiple electron scattering. The presence of carbon, nickel and phosphorous in the sample (Fig.5.3 l-p), was quantified by means of elemental mapping.

Furthermore, to explore more structural and electronic properties of $Ni_3P@CC^*$ and CC^*, Raman spectroscopy was utilised (Fig. 5.4a). The D-band is related to disordered carbon and the corresponding defects sites, while G-band is associated with the sp^2 hybridized carbon atoms, is clearly asymmetric. The relative intensity ratio of D to G-band (I_D/I_G) is proportional to the number of defects degree of the material. The D and G bands were observed at positions 1349 cm^{-1}, 1591 cm^{-1} for CC^* and 1346 cm^{-1}, 1596 cm^{-1} for $Ni_3P@CC^*$, respectively. The I_D/I_G ratio for $Ni_3P@CC^*$ increases to 1.03 from 0.98 (for CC^*), indicating that the material has sufficient defects sites to provide sufficient reaction sites. In addition, a combination of 2D band and D+D' of the graphitic carbon is allocated as weak and the broad peaks at around 2693 and 2800 cm^{-1}, respectively.[39,40] It is evident from the reported literature that there is no vibrational active Raman modes corresponding to Ni_3P Phase.[41,42] The BET measurement results for CC^* and $Ni_3P@CC^*$ obtained from N_2 adsorption–desorption isotherms are presented in Fig. 5.4b and inset of Fig. 5.4b. The calculated active surface area of the $Ni_3P@CC^*$ is 78.6 $m^2\ g^{-1}$ which is quite higher than CC^* effective surface area value *i.e.,* 56.2 $m^2\ g^{-1}$. The mesoporous range (from 0.5 to 2 nm) of Ni_3P (Fig. 5.4c) favours the ionic transportation resulting increased rate performance.

To get insight into chemical states, the fine scanned X-Ray photoelectron spectra (XPS) for Ni, P, O and C were fitted as shown in Fig. 5.4d-g. To find out the Ni 2p and P 2p bonding states, a deconvolution procedure with a Gaussian profile was utilised. The fitted peaks of Ni $2p_{3/2}$ (Fig. 5.4d) located at binding energy 852.9 eV are indexed to $Ni^{\delta+}$ in the Ni_3P,[43,44] whereas the peak at 856.5 eV arise due to Ni^{2+} to phosphate ions interactions.[45–47] A satellite peak (indicated at "Sat.") is indicated at binding energy of 861.9 eV.[48] Three more peaks are also observed which corresponds to the Ni $2p_{1/2}$ at around 871.14, 874.601 and 880.4 eV, which are attributed to the $Ni^{\delta+}$ in the Ni_3P and Ni^{2+} in the nickel oxide and a satellite peak (indicated as "Sat."), respectively.[33,49] The P $2p_{3/2}$ spectrum (Fig. 5.4e) display that the peak at binding energy of 129.8 eV corresponds to $P^{\delta-}$ in Ni_3P.[50] The peak of P $2p_{3/2}$ positioned at 133.8 eV may due to oxidation of phosphorous from air oxygen and converts into phosphates ions.[51] The O1s spectrum (Fig. 5.4f) consisting of two-component curves at 531.7 eV and 533.3 eV, which is due

to the metal-oxygen bond, oxygen in defects and multiplicity of physi- and chemi-sorbed water. Figure 5.4g shows the C1s spectrum consisting of three fitted peaks is allocated at 284.6 eV, 285.7 eV and 288.5 eV which are assigned to C–C bonding (sp^2 carbon), C–O of epoxy and O–C=O groups.

5.3.2 Electrochemical performance of cathode material (Ni₃P@CC*)

To examine the electrochemical response of cathodic electrode material, Ni₃P@CC*,
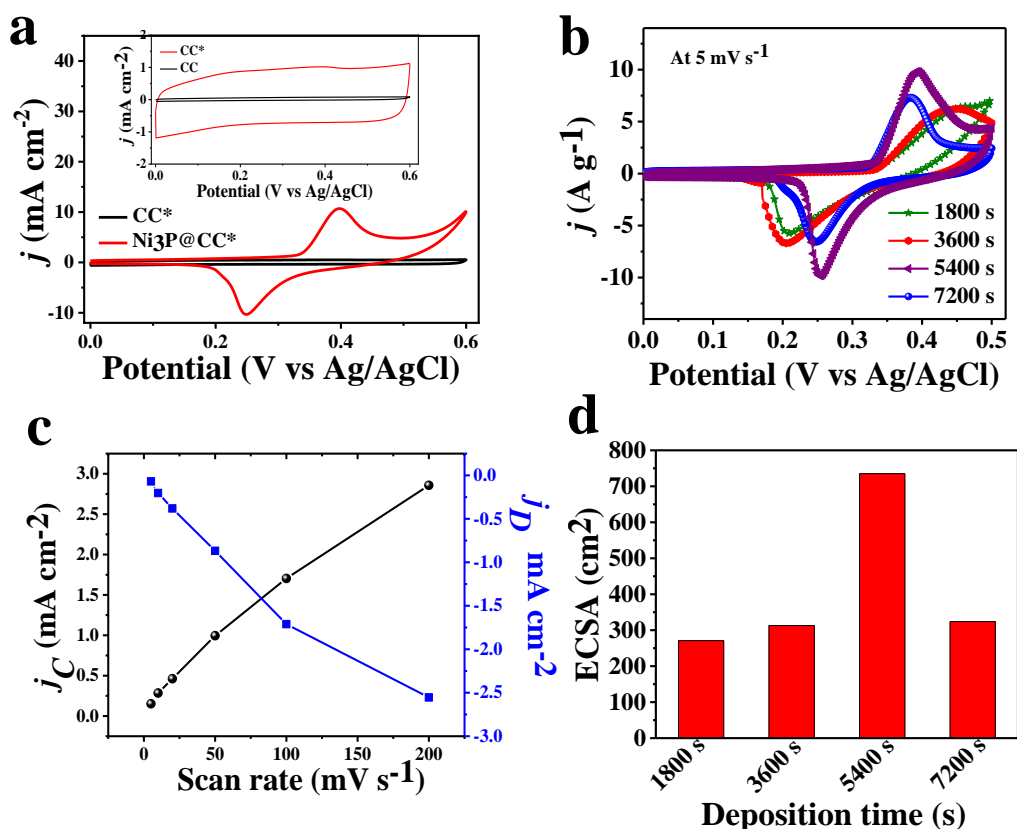
Figure 5.5. *(a) A comparative CV response of Ni₃P@CC*compared to CC* at a scan rate of 50 mV s⁻¹, inset shows CV curves of carbon cloth before and after pre-treatment at a scan rate of 100 mV s-1 in 1 M KOH, (b) Cyclic voltammetry curves showing optimization for the increase in the capacity of the electrode with the deposition time, (c) Charge/Discharge current density versus scan rate response calculated from CV response of the Ni₃P electrode deposited for 5400 seconds in 0.5 M H₂SO₄ to calculate the electrochemical surface area of the electrode, (d) The calculated electrochemical surface area at different deposition times.*

electrochemical measurements were performed in 1M KOH aqueous electrolyte by applying them as working electrode in a three-electrode set-up. Inset of Fig. 5.5a displayed a contrast of the classic cyclic voltammetry (CV) profile of CC and CC* at 100 mV s⁻¹ scan rate, respectively. The pre-treated carbon cloth presents improved electrochemical response over the carbon cloth due the surface modification after pre-treatment. From the cyclic voltammogram curve shown in Fig 5.5a, Ni₃P@CC* delivered the most significant electrochemical response when compared with the CV area

of pre-treated carbon cloth at a scan rate of 50 mV s^{-1}. Figure 5.5b represents the CV curves for Ni$_3$P electrochemical deposition optimizations, which clearly demonstrate that the current density increases with the deposition time (1800 seconds to 5400 seconds). Once the maximum surface of pre-treated carbon cloth covered by the Ni$_3$P materials, further deposition may lead to the aggregation, which restricts the ionic path and also
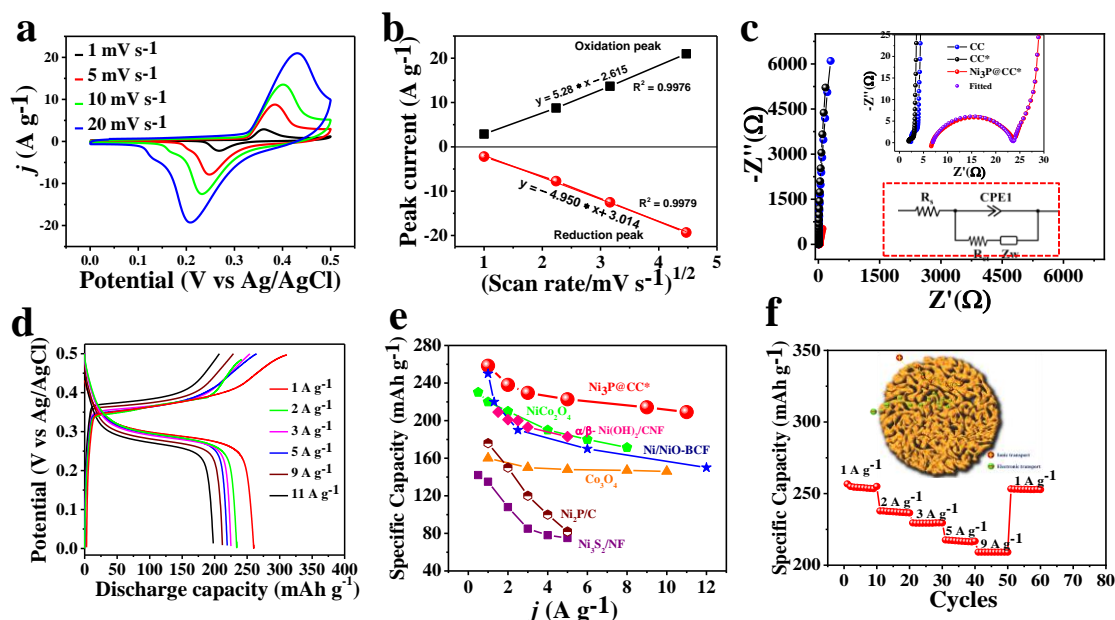
Figure 5.6. *(a) CV response of Ni$_3$P@CC* at different scan rates, (b) The peak current density obtained from the CV curves as a function of square root of scan rate, (c) Nyquist plot for CC, CC* and Ni$_3$P@CC* electrode in three-electrode system, inset shows the magnified view of the impedance spectra at higher frequency region and equivalent circuit corresponding to Ni$_3$P@CC*, (d) Galvanostatic charge-discharge response at various current densities, (e) Specific capacity versus current density response showing the excellent rate capability of the electrode as compared to many reported Ni, Co-based electrodes, (f) A rate capability study with continuous charge-discharge cycles by varying current density in each 10 cycles, inset shows a schematic representation of internal structure of Ni$_3$P exhibiting the porous network for easy ionic transport and the active channels for the electronic transport.*

diminish the electrical response to the Ni$_3$P surface. The scan rate dependence of the current density for Ni$_3$P@CC* (Fig. 5.5c) was employed to calculate the electrochemical active surface area (ECSA). The Ni$_3$P deposited for 5400 seconds shows the highest ECSA value i.e., 735 cm^2 (Figs 5.5d). CV tests of Ni$_3$P@CC* at different scan rates were also conducted (Fig. 5.6a) in the window of 1 mV s^{-1} to 20 mV s^{-1}. It can be seen that there are two redox peak potentials (oxidation and reduction potentials) at 1 mV s^{-1}, which are located at 0.36 V and 0.26 V (vs Ag/AgCl), respectively. As scan rate increases, the gap between the peaks also increases due to the polarization factor. The shape of CV curves is unaltered along with high current density, indicating an excellent power delivery capability of the Ni$_3$P@CC* electrode. Moreover, the dependence of

peak current (i, A g^{-1}) from the charged and discharged states over square root of scan rate ($v^{1/2}$) is linear (Fig. 5.6b) revealing a diffusion-controlled process based on the equation $\boldsymbol{i = a\,v^b}$, where a and b values are simply adjustable parameters for the material.[52,53] Furthermore, proton diffusivity (D$_H$) value of Ni$_3$P@CC* electrode was
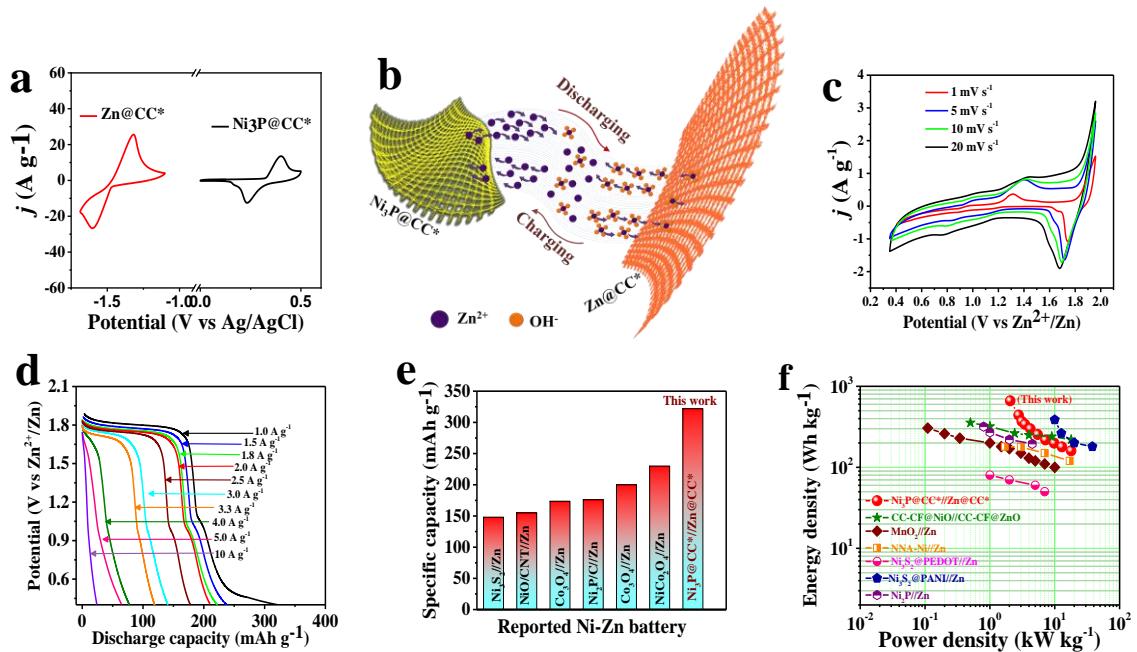
Figure 5.7. *Electrochemical performance of assembled Ni$_3$P@CC*//Zn@CC* battery, (a) Cyclic voltammetry curve of Zn@CC* in 1 M KOH and 10 mM Zn(Ac)$_2$ and of Ni$_3$P@CC* in 1M KOH electrolyte at 10 mV s^{-1} scan rate, respectively, (b) Schematic illustration of the redox process for the Ni$_3$P@CC*//Zn/CC* battery during charge-discharge process, (c) Cyclic voltammetry curves for alkaline Ni–Zn battery (Ni$_3$P@CC*//Zn@CC*) in 1 M KOH + 10 mM Zn(Ac)$_2$ electrolyte at different scan rates, (d) Galvanostatic charge discharge response as as-prepared battery at different current densities, (e) A comparison of the specific capacity values with reported Ni–Zn based batteries, (f) Ragone plot of Ni$_3$P@CC*//Zn@CC* battery.*

calculated by Randles-Sevick equation,[54] which is found to be 7.69×10^{-11} cm^2 s^{-1}. Such amplified electrochemical kinetics is very well confirming with electrochemical impedance spectroscopy (EIS) data at different stages of Ni$_3$P@CC* fabrication as shown in Fig. 5.6c. Figure 5.6c inset shows the equivalent circuit that consists of a solution resistance (R$_s$), the charge-transfer resistance (R$_{ct}$), the resistance belongs to the ionic diffusion (Z$_w$), a constant phase element (CPE). EIS curve of Ni$_3$P@CC* shows a semi-circle in the high-frequency range which was not initially present in either CC or CC*. The nyquist plot of Ni$_3$P@CC* shows smaller R$_s$ of 6.9 Ω, less R$_{ct}$ (16 Ω) and the low-frequency regions exhibit a slope related to diffusion-limited electron transfer process of the electrode. EIS fitting results indicates the elevated electrochemical kinetics and prompted ionic diffusion rate of the electrolytic ions towards the electrode surface.

To assure the high-rate delivery capabilities of $Ni_3P@CC^*$ electrode, the electrodes were first charged and subsequently discharged at numerous current densities (from 1 A g^{-1} to 11 A g^{-1}). All the GCD profiles had relatively flat potential plateaus (Fig. 5.6d), which further confirm the presence of faradic redox reactions at same peak potential positions signified to be of battery behaviour. The variation of specific capacity with current density (Fig. 5.6e) represents that the specific capacity for $Ni_3P@CC^*$ electrode is very high *i.e.* 258 mA h g^{-1} at a current density of 1 A g^{-1}, which decreases to 209 mA h g^{-1} at high current density of 11 A g^{-1}, delivers the excellent rate capability over many reported Ni-Zn batteries.[23,32,55–58] Encouragingly, the $Ni_3P@CC^*$ electrode maintains phenomenal capacity retention of 80.9% even there is an 11-fold amplification in current density which indicates $Ni_3P@CC^*$ as a powerful electrode for storage applications with best rate capabilities (Fig. 5.6e). The inferior rate capabilities of aqueous rechargeable batteries become a progressive barrier for their broad commercialization. In this term, the rate capacity of the Ni_3P electrode was investigated by continual GCD measurements at various current densities. On the contrary, the electrode exhibited a stable high-rate performance along with remarkable specific capacity of 258 mA h g^{-1} at 1 A g^{-1} to 214 mA h g^{-1} at 9 A g^{-1}. When the current density changes to 1 A g^{-1} after 50 cycles, the recover specific capacity of $Ni_3P@CC^*$ electrode is 257.6 mA h g^{-1} demonstrating the superior electrochemical reversibility of $Ni_3P@CC^*$ electrode (Fig. 5.6f). Such advanced electrochemical kinetics can be easily understood from the TEM (Fig. 5.3g-h) results that demonstrates the Ni_3P hierarchical porous structure with increased effective surface area which further provides rich channels and easy pathways for electrolyte ions permeation as well as for electron transfer to the electrode surface. It is well explained from the schematic shown in the inset of Fig. 5.6f, which illustrates the easy and effective pathways for both ions and electron transport as said. Therefore, the $Ni_3P@CC^*$ electrode possesses extraordinary electrochemical activity and high-rate capability utilising the improved charge-transfer kinetics.

Furthermore, evaluating the application of $Ni_3P@CC^*$ cathode in Ni-Zn battery, a battery (indicated as $Ni_3P@CC^*//Zn@CC^*$) was fabricating by using $Zn@CC^*$ as anode and $Ni_3P@CC^*$ as cathode in 1M KOH+10 mM $Zn(Ac)_2$ as mixed aqueous electrolyte. Figure 5.7a presents cyclic voltammetric curves for $Zn@CC^*$ in 1M KOH+ 10 mM $Zn(Ac)_2$ and $Ni_3P@CC^*$ electrode in an aqueous electrolyte (1M KOH) at 10 mV s^{-1}. Zinc acetate was introduced into the electrolyte to improve the reversibility and to stabilize of the zinc anode. In the CV curve of $Zn@CC^*$, a set of redox peaks positioned

at $-1.35/-1.55$ V (vs Ag/AgCl) explains a redox reaction of Zn/Zn(OH)$_4{}^{2-}$.[59] Ni$_3$P@CC*
and Zn@CC* electrodes assembled into a battery system acquiring a large potential
difference and the flow of ionic and electronic charges during charging and discharging
processes is schematically shown in Fig. 5.7b. Their electrode and cell reactions are
simplified as the following (1), (2) and (3) equations:

At Anode (–ve electrode):

$$[Zn(OH)_4]^{2-} + 2\,e^- \longleftrightarrow Zn + 4OH^- \qquad\qquad (1)$$

At Cathode (+ve electrode):

$$Ni_3P + 2OH^- \longleftrightarrow Ni_3PO + H_2O + 2e^- \qquad\qquad (2)$$

Overall reaction:

$$Ni_3P + [Zn(OH)_4]^2 \longleftrightarrow Ni_3PO + Zn + 2OH^- \qquad (3)$$
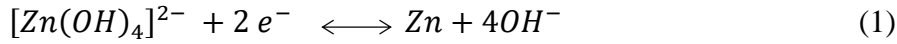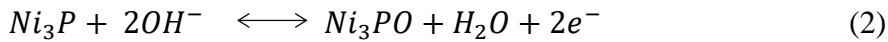
During the charging process, the $[\boldsymbol{Zn(OH)_4}]^{2-}$ release OH$^-$ and covert into Zn and
during the charge process, Zn again reacts with OH$^-$ to form such kind of
complex $[\boldsymbol{Zn(OH)_4}]^{2-}$. The good reversibility occurs at Zn surface with the addition of
Zn(Ac)$_2$ in the electrolyte solution. At cathode, Ni$_3$P bonds to OH$^-$ ions via weak Van-
der Waals interactions from alkaline electrolyte and again release the OH$^-$ ions during
discharge, shows excellent reversibility reaction at the surfaces.

The electrochemical stability window of Ni$_3$P@CC*//Zn@CC* battery system in
alkaline electrolyte is evaluated using CV and GCD characterizations. The CV curves of
Ni$_3$P@CC*//Zn@CC* at a range of scan rate values are shown in Fig. 5.7c, which
displayed a voltage window of about 1.9 V (vs Zn/Zn^{2+}) and all distinct redox peaks,
which is attributed to Ni (I) to Ni (II) conversion reaction. The voltage plateau during
charge and discharge in GCD curves (Fig. 5.7d) also corresponds to the above said
chemical reaction. Moreover, Ni$_3$P@CC*//Zn@CC* battery in alkaline electrolyte
exhibits a remarkable rate capability, showing the discharge capacities of 322 mAh g^{-1},
242 mAh g^{-1}, 221 mAh g^{-1}, 209 mAh g^{-1}, 165 mAh g^{-1}, 138 mAh g^{-1}, 119 mAh g^{-1}, 78
mAh g^{-1}, 66 mAh g^{-1} and 24 mAh g^{-1} recorded at rates of 1, 1.5, 1.8, 2, 2.5, 3, 3.3, 4, 5
and 10 A g^{-1}, respectively (Fig. 5.7d). Figure 5.7e shows that the capacity of
Ni$_3$P@CC*//Zn@CC* battery (322 mAh g^{-1} at 1 A g^{-1}) is higher than that of maximum
reported capacity values in several Ni-Zn battery systems, such as Ni$_3$S$_2$//Zn (148 mAh

g[-1] at 0.2 A g^{-1}),[23] NiO/CNTs//Zn (155 mAh g^{-1} at 1 A g^{-1}),[17] Co_3O_4//Zn (173.6 mAh g^{-1} at 1 A g^{-1}),[60] Ni_2P/C//Zn (176 mAh g^{-1} at 1 A g^{-1}),[61] solid state Co_3O_4//Zn (200 mAh g^{-1} at 0.5 A g^{-1}),[16] and $NiCo_2O_4$//Zn (230 mAh g^{-1} at 0.5 A g^{-1}).[58]

The as-fabricated battery delivers maximum specific energy density of 661 A h kg^{-1}
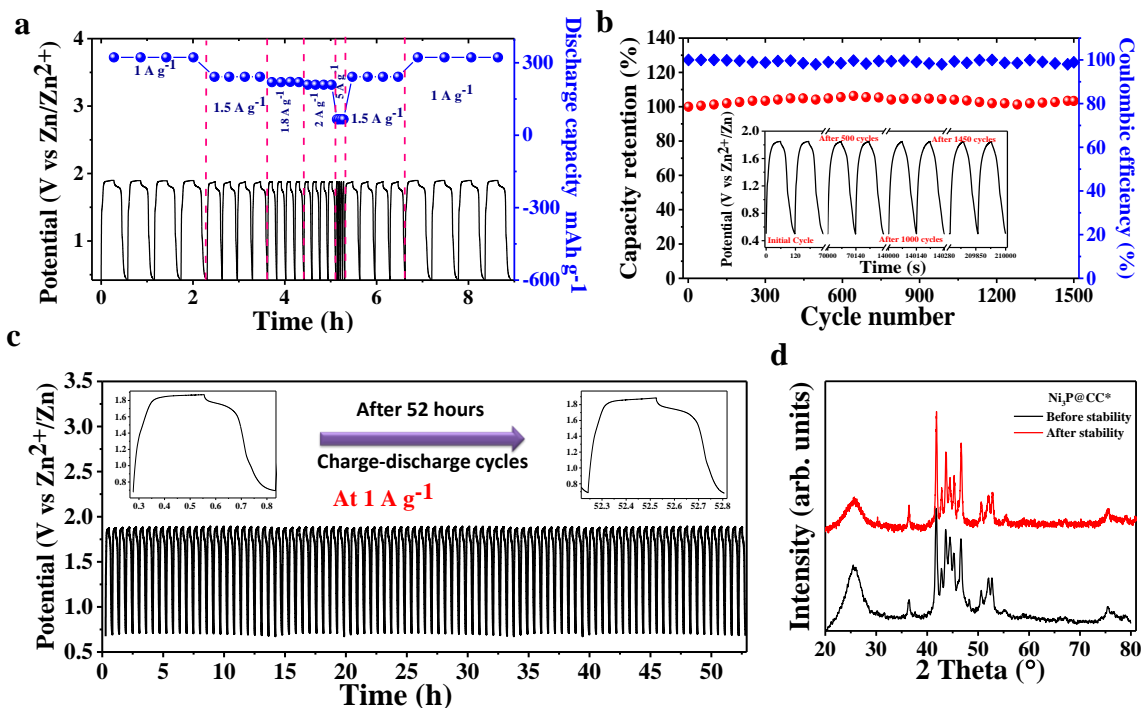
Figure 5.8 *(a) The rate performance of the battery upon cycling with step increase and decrease in the current density, (b) Cycling stability of Ni_3P@CC*//Zn@CC* battery with continuous charge-discharge cycles at a current density of 3.3 A g^{-1}, inset demonstrates the charge-discharge curves for initial cycle and after each 500 cycles, (c) stability study for Ni_3P@CC*//Zn@CC* battery at a very low current density of 1 A g^{-1} shows excellent stable charge-discharge profile continuously run for 55 h, inset have the initial charge-discharge cycle and after 55 h stability cycle, (d) XRD pattern of Ni_3P@CC* electrode before and after stability.*

and power density of 17.5 kW kg^{-1}, which are considerably better to those of numerous reported Ni-Zn battery,[14] Co-Zn battery,[62] Li thin-film battery[63] and asymmetric supercapacitors (Fig. 5.7f).[64,65] The Ni_3P@CC*//Zn@CC* battery system shows an outstanding overall performance in comparison with many other Zn-based batteries reports (Table 5.1). As aforementioned, the porous structure and excellent conductivity of nickel phosphide electrode contributes to the superior performance of as modified Ni-Zn battery.

To check the rate capabilities of as-fabricated Ni-Zn battery, continuous charge-discharge was carried out at different current densities. While the current rate increases in steps from 1 A g^{-1} to 5 A g^{-1}, the capacity values change accordingly via maintaining 100 % coulombic efficiency. When the rate alters to 1 A g^{-1}, the capacity value again

Table 5.1 *A comparative table showing the different parameters variations like potential window, specific capacity, energy density, power density, cycling stability with the different electrode materials.*

Sr. No.	Cathode	Anode	Electrolyte	Potential window (V)	Specific capacity (mAh g^{-1})	Energy density	Power density	Cycle stability	Retention	Reference
1.	NiSe$_2$	Zn	6M KOH+saturated ZnO	1.35- 2.2 V	245.1 mAh g^{-1}	328.8 Wh kg^{-1}	91.22 kW kg^{-1}	10,000	-	54
2.	Ultrathin Ni(OH)$_2$ nanosheet array	Holey α-Fe$_2$O$_3$ nanorod array	6 M KOH gel	0- 2 V	210 mAh g^{-1}	28.1 mWh cm-3	10.6 mW cm-3	10,000	91.3%	66
3.	Ni-MOF nanosheet	Zn	2M KOH+ZnO saturated	1.2-1.86 V	0.4 mAh cm-2	0.71 mWh cm-2	-	1000	90.3%	29
4.	Al-CoNiDH	Zn@CC	Gel PVA+KOH	1- 2 V	264 MAh g-1 (electrode) 152 mAh g-1 (battery)	-	-	500	62%	67
5.	Ni/NiO 3D-network	Zn	6 M KOH+0.5 mM Zn(Ac)$_2$	1.2 – 2.2 V	296 mAh g-1	313 Wh kg-1	-	1000	100%	55
6.	Ni-NiO/CC	Zn	6 M KOH+0.5 M Zn(Ac)$_2$	1.3 -2.2 V	184 mAh g-1	441.7 Wh kg-1	41.6 kW kg-1	2000	80%	68
7.	Commercial Ni	3D flower-like calcium zincate	6 M KOH+0.5 M LiOH saturated with ZnO	1.2 -1.9 V	297.mAh g^{-1} at 2C	-	-	400	-	69

No.	Material		Electrolyte	Voltage	Capacity	Energy density	Power density	Cycles	Retention	Ref.
8.	Zn-doped Co_3O_4	Zn	$ZnSO_4$+$CoSO_4$	0.8-2.4 V	1.25 mAh cm^{-2}	772.6 mWh cm^{-3}	-	5000	-	70
9.	$NiMoO_4$-NC	Zn	6 M KOH+0.2 M $Zn(Ac)_2$ with K_2MoO_4 additive	1.5-1.8 V	229.2 mAh g^{-1}	-	-	3000	85.9 %	28
10.	Ni_3S_2@PEDOT	Zn	1 M KOH+ 20 mM $Zn(Ac)_2$	1.5 V-2.0 V	261.9 mAh g^{-1}	456.4 Wh kg^{-1}	5.45 kW kg^{-1}	2000	73%	15
11.	$Co(OH)_2$ nanosheet on Co foam	Zn	6M KOH+$Zn(Ac)_2$	1 V-1.9 V	0.265 mAh cm^{-2}	6.09 mWh cm^{-3}	1.75 W cm^{-3}	10,000	83.3 %	71
12.	$NiMn_xO_y$ nanosheet	Zn	1M KOH+ 20 mM $ZnSO_4$	1.4 V-1.95 V	0.68 mAh cm^{-2}	1.13 mW cm^{-2}	3.34 mW	5500	88.5 %	27
13.	Co_3O_4@NiO nanostrips@nanorod array	Zn@Cu foil	6M KOH + ZnO (saturated)	1.4 – 1.9 V	182 mAh g^{-1}	215.51 Wh kg^{-1}	3.45 kW kg^{-1}	500	89%	72
14.	**Ni_3P@CC***	**Zn@CC***	**1 M KOH+ 10 mM $Zn(Ac)_2$**	**0.4 V-1.9 V**	**322 mAh g^{-1}**	**661.98 Wh kg^{-1}**	**17.5 kW kg^{-1}**	**1500**	**100 %**	**This work**

***Ni(OH)₂** – Nickel hydroxide, **MOF**- Metal oxide framework, **CC**- Carbon cloth, **PEDOT**- poly(3, 4-ethylenedioxythiophene), **PVA**- Poly(vinylalcohol)*

restored back to 322 mAh g^{-1}, showing an excellent stability towards ultrafast conversion reaction (Fig. 5.8a). Such extraordinary rate performance is well describing to a stabilized Ni_3P electrode with astonishing electrochemical kinetics.

Furthermore, the Ni_3P@CC*//Zn@CC* battery cycling performance at a current density 3.3 A g^{-1} was investigated as shown in Fig. 5.8b and c. The capacity of the Ni_3P@CC*//Zn@CC* battery is very well preserved and reached 100% capacity retention after 1500 GCD cycles without any capacity fading. In addition, the columbic efficiency remained approximately 99% during whole cycling process. The rising of the battery capacity after 500 cycles results from the complete activation of the Ni_3P electrode active sites. The capacitive retention for Ni_3P@CC*//Zn@CC* system was

consistently high or comparable to that of many reported batteries (Table 5.1). Figure 5.8c shows the galvanostatic charge-discharge profile at a very low current density value (1 A g^{-1}) to investigate the long-run cycling stability. The Fig. 5.8c insets clearly revealed that there is negligible loss between the initial and final GCD curves, CV curves and impedance spectra. There is no phase change even after battery cycling for long time as shown in the XRD spectrum (Fig. 5.8d), indicates excellent stability of the device. Obviously, the reversible capacity of Ni$_3$P@CC*//Zn@CC* battery retains 321 mAh g^{-1} with capacity retention of 99.6% over continuous charge-discharge cycles run for 55 hours. High environmental suitability endows our flexible Ni$_3$P@CC*//Zn@CC* battery with great feasibility towards robust and lightweight electronic applications.

5.4 Conclusions

In this work, an easy and one-step synthesis strategy *i. e.* electrochemical deposition method is adopted for the development of cathode (Ni$_3$P@CC*) and anode (Zn@CC*) materials in order to fabricate a homemade Ni-Zn battery. As a potential cathode for Ni-Zn battery, Ni$_3$P@CC* exhibits excellent electrochemical performance with good reversibility during the charge-discharge processes. The structural characterizations and electrochemical kinetics analysis for the charge-discharge process demonstrates that the three-dimensional porous network of Ni$_3$P electrode possess separate channels for the electronic and ionic transport. The Ni$_3$P@CC*//Zn@CC* battery delivers a high specific capacity of 322 mAh g^{-1}, high energy density of 661 Wh kg^{-1} and a power density of 17.5 kW kg^{-1}. The Ni$_3$P@CC*//Zn@CC* battery system exhibits high-capacity retention of almost 100% after 1500 continuous charge-discharge cycles. This work demonstrates a new material Ni$_3$P as a highly promising cathode material in Ni-Zn batteries that can be a great motivation for further research on nickel phosphides for high performance energy storage solutions.

5.5 References

1   P. Simon and Y. Gogotsi, *Nat. Mater.*, 2008, **7**, 845–854.

2   X. Lu, M. Yu, G. Wang, Y. Tong and Y. Li, *Energy Environ. Sci.*, 2014, **7**, 2160–2181.

3   S. Zheng, H. Huang, Y. Dong, S. Wang, F. Zhou, J. Qin, C. Sun, Y. Yu, Z.-S. Wu and X. Bao, *Energy Environ. Sci.*, 2020, **13**, 821–829.

4   D. R. S. Dey, T. Purkait, N. Kamboj and M. Das, *Carbonaceous Materials and Future Energy: Clean and Renewable Energy Sources*, CRC Press, 2019.

5   Y. Ding, Z. P. Cano, A. Yu, J. Lu and Z. Chen, *Electrochem. Energy Rev.*, 2019, **2**, 1–28.

6   D. Chao, W. Zhou, F. Xie, C. Ye, H. Li, M. Jaroniec and S.-Z. Qiao, *Sci. Adv.*, 2020, **6**, eaba4098.

7   K. Liu, Y. Liu, D. Lin, A. Pei and Y. Cui, *Sci. Adv.*, 2018, **4**, eaas9820.

8   G. Zubi, R. Dufo-López, M. Carvalho and G. Pasaoglu, *Renew. Sustain. Energy Rev.*, 2018, **89**, 292–308.

9   M. Song, H. Tan, D. Chao and H. J. Fan, *Adv. Funct. Mater.*, 2018, **28**, 1802564.

10   H. Kim, G. Jeong, Y.-U. Kim, J.-H. Kim, C.-M. Park and H.-J. Sohn, *Chem. Soc. Rev.*, 2013, **42**, 9011–9034.

11   Y. Zeng, Y. Han, Y. Zhao, Y. Zeng, M. Yu, Y. Liu, H. Tang, Y. Tong and X. Lu, *Adv. Energy Mater.*, 2015, **5**, 1402176.

12   G. G. Yadav, J. W. Gallaway, D. E. Turney, M. Nyce, J. Huang, X. Wei and S. Banerjee, *Nat. Commun.*, 2017, **8**, 14424.

13   C. Li, Q. Zhang, J. Sun, T. Li, S. E, Z. Zhu, B. He, Z. Zhou, Q. Li and Y. Yao, *ACS Energy Lett.*, 2018, **3**, 2761–2768.

14   J. Liu, C. Guan, C. Zhou, Z. Fan, Q. Ke, G. Zhang, C. Liu and J. Wang, *Adv. Mater.*, 2016, **28**, 8732–8739.

15   Y. He, P. Zhang, H. Huang, X. Li, X. Zhai, B. Chen and Z. Guo, *Electrochim. Acta*, 2020, **343**, 136140.

16   L. Ma, S. Chen, H. Li, Z. Ruan, Z. Tang, Z. Liu, Z. Wang, Y. Huang, Z. Pei, J. A. Zapien and C. Zhi, *Energy Environ. Sci.*, 2018, **11**, 2521–2530.

17   X. Wang, M. Li, Y. Wang, B. Chen, Y. Zhu and Y. Wu, *J. Mater. Chem. A*, 2015, **3**, 8280–8283.

18   F. Beck and P. Rüetschi, *Electrochim. Acta*, 2000, **45**, 2467–2482.

19   G. Bronoel, A. Millot and N. Tassin, *J. Power Sources*, 1991, **34**, 243–255.

20   J. Jindra, *J. Power Sources*, 2000, **88**, 202–205.

21   D. Khalafallah, M. Zhi and Z. Hong, *Top. Curr. Chem.*, 2019, **377**, 29.

22   C. Xu, J. Liao, C. Yang, R. Wang, D. Wu, P. Zou, Z. Lin, B. Li, F. Kang and C.-P. Wong, *Nano Energy*, 2016, **30**, 900–908.

23   P. Hu, T. Wang, J. Zhao, C. Zhang, J. Ma, H. Du, X. Wang and G. Cui, *ACS Appl. Mater. Interfaces*, 2015, **7**, 26396–26399.

24   M. Gong, Y. Li, H. Zhang, B. Zhang, W. Zhou, J. Feng, H. Wang, Y. Liang, Z. Fan, J. Liu and H. Dai, *Energy Environ. Sci.*, 2014, **7**, 2025–2032.

25   H. Zhang, R. Wang, D. Lin, Y. Zeng and X. Lu, *ChemNanoMat*, 2018, **4**, 525–536.

26   S. Bhardwaj, A. Biswas, M. Das and R. S. Dey, *Sustain. Energy Fuels*, 2021, **5**, 2393–2414.

27   X. Liang, X. Zou, X. Ren, B. Xiang, W. Li, F. Chen, J. Hao, Q. Hu and L. Feng, *J. Colloid Interface Sci.*, 2020, **578**, 677–684.

28   L. Zhou, S. Zeng, D. Zheng, Y. Zeng, F. Wang, W. Xu, J. Liu and X. Lu, *Chem. Eng. J.*, 2020, **400**, 125832.

29   C. Li, Q. Zhang, T. Li, B. He, P. Man, Z. Zhu, Z. Zhou, L. Wei, K. Zhang, G. Hong and Y. Yao, *J. Mater. Chem. A*, 2020, **8**, 3262–3269.

30   R. Zhang, V. Raveendran, Y. He, A. Yau, A. Chang, C. Chi, S. Bong, F. Cheng, W. Ma and J. Chen, *Energy Mater. Adv.*, 2021, **2021**, 2124862.

31   J. Cheng, D. Zhao, L. Fan, X. Wu, M. Wang, N. Zhang and K. Sun, *J. Mater. Chem. A*, 2017, **5**, 14519–14524.

32   J. Li and C. Chen, *Mater. Res. Express*, , DOI:10.1088/2053-1591/aaa103.

33   M. Das, N. Jena, T. Purkait, N. Kamboj, A. De Sarkar and R. S. Dey, *J. Mater. Chem. A*, 2019, **7**, 23989–23999.

34   P. Sun, M. Qiu, J. Huang, J. Zhao, L. Chen, Y. Fu, G. Cui and Y. Tong, *Chem. Eng. J.*, 2019, **380**, 122621.

35   Q. Wang, W. Ren, F. Gao, C. Qiu, Q. Wang, F. Gao and C. Zhao, *ChemElectroChem*, 2019, **6**, 1768.

36   S. Xiong, J. Fan, Y. Wang, J. Zhu, J. Yu and Z. Hu, *J. Mater. Chem. A*, 2017, **5**, 18242–18252.

37   A. Thamilselvan, A. S. Nesaraj, M. Noel and E. J. James, *J. Electrochem. Sci. Technol.*, 2015, **6**, 139–145.

38   R. Zou, K. Xu, T. Wang, G. He, Q. Liu, X. Liu, Z. Zhang and J. Hu, *J. Mater. Chem. A*, 2013, **1**, 8560–8566.

39   S. K. T. Aziz, B. Malik, H. K. Sadhanala, A. Gedanken, M. Noked and G. D. Nessim, *ACS Appl. Nano Mater.*, 2020, **3**, 10914–10921.

40   N. Kamboj, T. Purkait, M. Das, S. Sarkar, K. S. Hazra and R. S. Dey, *Energy Environ. Sci.*, 2019, **12**, 2507–2517.

41   S. He, S. He, X. Bo, Q. Wang, F. Zhan, Q. Wang and C. Zhao, *Mater. Lett.*, 2018, **231**, 94–97.

42   F. Yang, S. Huang, B. Zhang, L. Hou, Y. Ding, W. Bao, C. Xu, W. Yang and Y.

Li, *Nanomater. (Basel, Switzerland)*, , DOI:10.3390/nano9071022.

43   Y. Okamoto, Y. Nitta, T. Imanaka and S. Teranishi, *J. Chem. Soc. Faraday Trans. 1 Phys. Chem. Condens. Phases*, 1979, **75**, 2027–2039.

44   J. F. Deng, J. Yang, S. S. Sheng, H. G. Chen and G. X. Xiong, *J. Catal.*, 1994, **150**, 434–438.

45   S. T. Oyama, X. Wang, Y.-K. Lee, K. Bando and F. G. Requejo, *J. Catal.*, 2002, **210**, 207–217.

46   S. J. Sawhill, K. A. Layman, D. R. Van Wyk, M. H. Engelhard, C. Wang and M. E. Bussell, *J. Catal.*, 2005, **231**, 300–313.

47   T. I. Korányi, Z. Vít, D. G. Poduval, R. Ryoo, H. S. Kim and E. J. M. Hensen, *J. Catal.*, 2008, **253**, 119–131.

48   Z. Yu, Y. Wang, Z. Sun, X. Li, A. Wang, D. M. Camaioni and J. A. Lercher, *Green Chem.*, 2018, **20**, 609–619.

49   H. Zhang, Y. Lu, C.-D. Gu, X.-L. Wang and J.-P. Tu, *CrystEngComm*, 2012, **14**, 7942–7950.

50   J. Tian, Q. Liu, A. M. Asiri and X. Sun, *J. Am. Chem. Soc.*, 2014, **136**, 7587–7590.

51   S. Zhang, S. Zhang, L. Song, X. Wu and S. Fang, *Mater. Res. Bull.*, 2014, **53**, 158–162.

52   T. Purkait, Dimple, N. Kamboj, M. Das, S. Sarkar, A. De Sarkar and R. S. Dey, *J. Mater. Chem. A*, 2020, **8**, 6740–6756.

53   L. Zhou, X. Zhang, D. Zheng, W. Xu, J. Liu and X. Lu, *J. Mater. Chem. A*, 2019, **7**, 10629–10635.

54   W. Zhou, J. He, D. Zhu, J. Li and Y. Chen, *ACS Appl. Mater. Interfaces*, 2020, **12**, 34931–34940.

55   L. Jiang, L. Li, S. Luo, H. Xu, L. Xia, H. Wang, X. Liu, Y. Wu and Y. Qing, *Nanoscale*, 2020, **12**, 14651–14660.

56   X. Wang, F. Wang, L. Wang, M. Li, Y. Wang, B. Chen, Y. Zhu, L. Fu, L. Zha, L. Zhang, Y. Wu and W. Huang, *Adv. Mater.*, 2016, **28**, 4904–4911.

57   Y. Jian, D. Wang, M. Huang, H.-L. Jia, J. Sun, X. Song and M. Guan, *ACS Sustain. Chem. Eng.*, 2017, **5**, 6827–6834.

58   W. Shang, W. Yu, P. Tan, B. Chen, H. Xu and M. Ni, *J. Power Sources*, 2019, **421**, 6–13.

59   X. Fan, Z. Yang, W. Long, Z. Zhao and B. Yang, *Electrochim. Acta*, 2013, **92**,

365–370.

60   P. Tan, B. Chen, H. Xu, W. Cai, W. He and M. Ni, *Appl. Catal. B Environ.*, 2019, **241**, 104–112.

61   J. Li and C. Chen, *Mater. Res. Express*, 2018, **5**, 15502.

62   C. Guan, W. Zhao, Y. Hu, Q. Ke, X. Li, H. Zhang and J. Wang, *Adv. Energy Mater.*, 2016, **6**, 1601034.

63   D. Yu, K. Goh, H. Wang, L. Wei, W. Jiang, Q. Zhang, L. Dai and Y. Chen, *Nat. Nanotechnol.*, 2014, **9**, 555–562.

64   J. Xu, Q. Wang, X. Wang, Q. Xiang, B. Liang, D. Chen and G. Shen, *ACS Nano*, 2013, **7**, 5453–5462.

65   X. Wang, B. Liu, R. Liu, Q. Wang, X. Hou, D. Chen, R. Wang and G. Shen, *Angew. Chemie Int. Ed.*, 2014, **53**, 1849–1853.

66   D. Kong, Y. Wang, S. Huang, B. Zhang, Y. Von Lim, G. J. Sim, P. Valdivia y Alvarado, Q. Ge and H. Y. Yang, *ACS Nano*, 2020, **14**, 9675–9686.

67   X. Zhu, Y. Wu, Y. Lu, Y. Sun, Q. Wu, Y. Pang, Z. Shen and H. Chen, *J. Colloid Interface Sci.*, 2021, **587**, 693–702.

68   L. Li, L. Jiang, Y. Qing, Y. Zeng, Z. Zhang, L. Xiao, X. Lu and Y. Wu, *J. Mater. Chem. A*, 2020, **8**, 565–572.

69   E. Shangguan, L. Li, C. Wu, P. Fu, M. Wang, L. Li, L. Zhao, G. Wang, Q. Li and J. Li, *J. Alloys Compd.*, 2021, **853**, 156965.

70   Q. Li, Q. Zhang, Z. Zhou, W. Gong, C. Liu, Y. Feng, G. Hong and Y. Yao, *Nano Res.*, 2021, **14**, 91–99.

71   J. Wu, Y. Lin, R. Qin, Y. Zeng and X. Lu, *ACS Sustain. Chem. Eng.*, 2020, **8**, 1464–1470.

72   J. Zhao, J. He, M. Sun, M. Qu and H. Pang, *Inorg. Chem. Front.*, 2015, **2**, 129–135.

Chapter 6

Mix-phase SnO-SnO₂ nanoparticles decorated on reduced graphene oxide as an excellent anode material for Li-ion battery
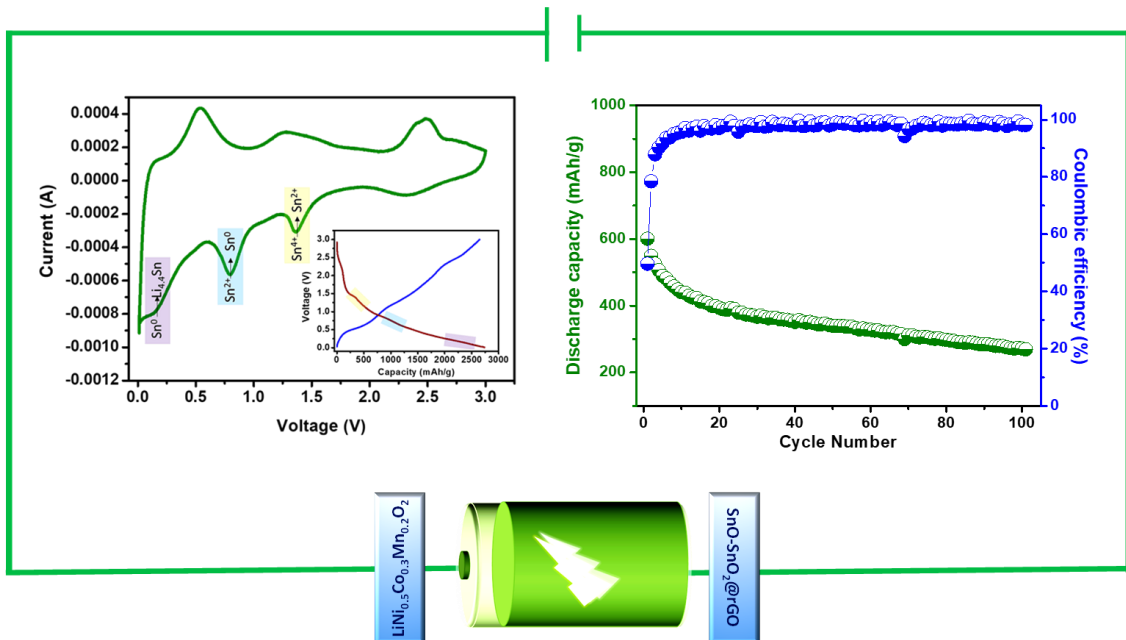
Abstract: Tin–based materials with high specific capacity have been studied as high-performance anodes for Li-ion storage devices. Herein, a mix-phase structure of SnO-SnO$_2$@rGO was designed and prepared *via* simple chemical method, which leads to the growth of tiny nanoparticles of a mixture of two different tin oxide's phases on the crumbled graphene nanosheets. The three-dimensional structure of graphene forms the conductive framework. The as-prepared mix phase SnO-SnO$_2$@rGO exhibits large BET surface area of 255 m^2 g^{-1} and excellent ionic diffusion rate. When the resulting mix-phase material was examined for Li-ion battery (LIB) anode application, the SnO-SnO$_2$@rGO was noted to deliver an ultrahigh reversible capacity of 2604 mA h g^{-1} at a current density of 0.1 A g^{-1}. It also exhibited superior rate capabilities and more than 82 % retention of capacity after 150 charge-discharge cycles at 0.1 A g^{-1}; lasting till 500 cycles at 1 A g^{-1} with very good retention of the initial capacity. Owing to the uniform functional group's defects on the rGO matrix, formation of LiOH upon lithiation has been suggested to be the primary cause of this very high reversible capacity in addition to the contribution from the material itself, which is beyond the theoretical limit. A Li-ion full cell was assembled using LiNi$_{0.5}$Mn$_{0.3}$Co$_{0.2}$O$_2$ (NMC-532) as a high-capacity cathodic counterpart, which showed a very high reversible capacity of 570 mA h g^{-1} (based on the anode weight) at an applied current density of 0.1 A g^{-1} with more than 50% retention of capacity after 100 cycles. This work offers a highly promising new design of electrode material, namely mix-phase tin oxide-nanocarbon matrix, rendering an outstanding performance for Li storage applications.

6.1 Introduction

Li-ion batteries (LIBs) are one of the most powerful sources to be widely used in daily life, ranging from small portable mobile electronic devices to electrical vehicles because of their high energy density, high voltage, and light weight.[1–4] Due to various limitations of conventional graphitic anode such as limited theoretical capacity (372 mAh g^{-1}), inferior rate performance, poor energy and power densities and lithium dendrites formation on the electrode surface, comparatively stable anodic materials with notably high energy and power density value are need of the hour. With the availability of high voltage stable cathodic systems like $LiNi_xCo_yMn_{1-(x+y)}O_2$ (NMC) and $LiNi_xCo_yMn_{1-(x+y)}O_2$ (NCA), anodes are indeed the bottleneck as far as next-generation Li-ion batteries are concerned. In this regard, several anodes beyond graphite starting from intercalation (various carbonaceous and layered systems) to alloying systems (Si, Sn, Ge, Sb etc.)[5] to conversion systems such as various oxides and sulfide [6–8] have gained huge research interest since past two decades.[9,10] However, getting a real anode, which can stand sufficiently tall in battling the abovementioned bottlenecks are still far from reality. The insertion-type anodes such as layered transitional metal dichalcogenides (TMDs), 2D layered carbides such as MXenes have some specific limitations in energy density and these do undergo unstable electrochemical kinetics with fast charging issues.[11–12] Owing to the very high-volume change under electrochemical cycling condition and thereby eventual cell failure, alloying systems are also out of consideration to be used on their own.[14] On the other hand, conversion systems although challenged with several drawbacks like high voltage polarization and thereby low energy efficiency, are still being researched extensively due to high specific capacity, reasonably good rate performance, and fair cyclic stability.[15]

Tin oxides (like SnO_2 and SnO)-based nanostructured materials have absolutely marked their presence in the Li-ion battery community as high capacity negative electrodes.[17] These systems, having a very unique combination of alloying and conversion reaction mechanism involved in the lithiation and de-lithiation process; lithium can be repeatedly released and stored, and thus can offer very high theoretical (1494 mAh g^{-1}) capacity.[18,19] Moreover, tin oxides are earth-abundant, intrinsically non-toxic, possess-easy with low-cost material processability, and have high chemical stability. These indeed make these systems as one of the most sustainable choices as far as anodes are concerned.[20] Despite their several advantages, tin oxide-based anodes

intrinsically suffer from low conductivity, large volume change under electrochemical cycling and unsatisfactory cycling stability that makes them a not-to-go anode for a Li-ion full cell system.[21] To address these issues, researchers have been focusing either on reducing strain during volume expansion by introducing nanostructured materials or by integrating SnO_2 with nanocarbon materials. Reduced graphene oxide could be a good choice of anchoring material for tin oxide nanoparticles due to many factors such as high surface area, enhanced electrical conductivity, high flexibility, and pronounced chemical stability.[22,23] Although, there are various methods available in the literature such as chemical, hydrothermal etc. for the synthesis of SnO_2-rGO composites for various energy applications, most of the methods involve either hazardous reagents or multistep process to get the desired materials. Furthermore, to the best of our knowledge, there are no methods are available for the mix-phase Sno-SnO_2 decorated rGO hybrid materials for Li-ion storage applications.

Tremendous efforts have been expended to overcome the problem of using SnO_2 as anode of Li-ion battery in the past few years. We propose herein a simple yet worthwhile strategy to prepare the mix phase of tin oxides, SnO_2 and SnO, uniformly decorated on reduced graphene oxide matrix (named as "SnO-SnO_2@rGO") using hydrothermal reduction of GO with Sn powder with an absolutely optimized ratio of GO to Sn powder. The method has dual role; first Sn is acting as reducing agent to convert GO to rGO in the acidic medium[24] and further *in situ* formed tin chloride is converted to mix-phase tin oxides that is decorated on three-dimensional crumpled rGO nanosheets upon hydrothermal reaction conditions. This material was designed and synthesized to overcome the drawbacks of SnO_2 or SnO individual systems since the matrix could provide adequate conductivity. At the same time, this uniformly decorated mix-phase material could withstand the volume change during electrochemical cycling as the rGO matrix could act as a stress-absorbing cushion. Our hypothesis was indeed validated by the noted performance of the material as an anode for LiB systems; with a very high reversible capacity of 2604 mA h g^{-1} at an applied current density of 0.1 A g^{-1}. Moreover, it showed more than 82 % retention of capacity after 150 charge-discharge cycles at 0.1 A g^{-1} and could last till 500 cycles at 1 A g^{-1} with very good cyclic stability. The rate performance data was also very impressive, which showed a reversible capacity of ~500 mAh g^{-1} at 2 A g^{-1}. It is interesting to note that due to a high voltage polarization and low energy efficiency, there exists a very few literature reports on impressive full cell using similar systems. Herein, taking advantages of unique mix-phase system with

conducting rGO matrix support, the SnO-SnO$_2$@rGO material could not only perform well in a full cell, but could also couple with LiNi$_{0.5}$Mn$_{0.3}$Co$_{0.2}$O$_2$ (NMC-532) as a high-capacity cathodic counterpart in the full cell for the very first time to the best of our knowledge. The full cell offered a very high reversible capacity of 570 mA h g^{-1} (based on the anode weight) at an applied current density of 0.1 A g^{-1} with more than 50% retention of capacity after 100 cycles.

6.2 Experimental Section

6.2.1 Preparation of mix phase SnO-SnO$_2$ nanoparticles on reduced graphene oxide (SnO-SnO$_2$@rGO):

Graphene oxide (GO) was prepared by the modified Hummer's method from graphite powder as reported earlier.[42] In a typical synthesis method, GO was dispersed in 4M HCl followed by ultrasonication and was subjected to chemical reduction with Sn powder with (1:10 GO to Sn ratio). Typically, solid Sn powder (1g) was added slowly in GO homogenous dispersion solution and then stirred vigorously for 4 hours at room temperature. The brown colored GO solution gradually turned black during the reaction, suggesting the reduction of GO and forming a metal oxide-reduced graphene oxide (rGO) composite. After the reduction treatment, the homogenous black suspension was transferred to a 50 mL Teflon-lined autoclave for the hydrothermal reaction. The whole hydrothermal process was allowed to carry out at 180°C for 10 hours. After cooling, the black product was thoroughly washed with DI water till the solution becomes pH neutral. The resultant product was then dried at 70°C to obtain mix phase tin oxide nanoparticles scattered on graphene sheets (Fig. 6.1). Similarly, control samples were synthesized at different GO to Sn ratios; (a) 1:0 abbreviated as S$_0$ (rGO), (b) 1:5 named as "S$_1$", (c) 1:20 as "S$_2$".

6.2.2 Electrodes and coin cell fabrication:

The electrodes for the mix phase sample (SnO-SnO$_2$@rGO) was prepared by mixing the active material, conducting carbon (Super P) and polyvinylidene difluoride (PVDF) binder (Sigma–Aldrich; weight ratios were maintained as 7.5:1.5:1) in N-methyl-2-pyrrolidone (NMP) solvent followed by coating the slurry onto a Cu foil (Current collector). The electrodes were dried in an oven at 80°C overnight under vacuum. The dried electrodes were then cut into round electrodes by using a disc-cutter. 2032-type coin cells were made in an Ar-filled glove-box. For all the studies, LiPF$_6$ electrolyte was used in a solvent combination of 1:1ethylene carbonate (EC) and dimethyl carbonate

(DMC) along with 5wt% fluoroethylene carbonate (FEC;SigmaAldrich) as an additive. Celgard 2500 was used as the separator.

6.2.3 Full cell fabrication:
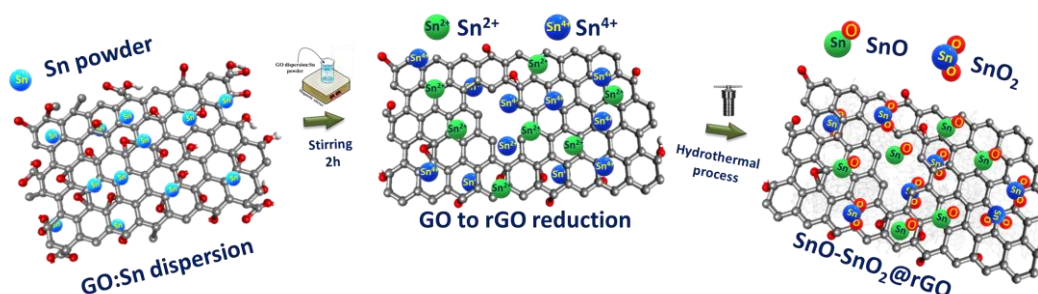
Figure 6.1. *A schematic illustration for the synthesis of mix phase SnO-SnO$_2$@rGO via hydrothermal method.*

A Li-ion full battery was fabricated using LiNi$_{0.5}$Mn$_{0.3}$Co$_{0.2}$O$_2$ (NMC-532) as cathode. A full cell was prepared by employing the electrochemical activation method. First, both the cathode and anode were activated electrochemically for one charge–discharge cycle followed by fabrication of the full cell. The anode to cathode mass ratio was being kept as 1:15. The operating potential window was kept at 2–4 V. LiPF$_6$ in EC/DMC (1:1 v/v) was used as the electrolyte with 5 vol% of FEC additive. A total amount of 150 µL of electrolyte was used. The capacity of the full cell was calculated based on the total weight (which included the weight of the anode and cathode).

6.3 Result and discussion

6.3.1 Structural characterizations of the material

In this work, we adopted a convenient in-situ method to synthesize rGO decorated with SnO and SnO$_2$ nanoparticles. The overall fabrication procedure is illustrated in the supporting information and schematically represented in Fig. 6.1 The basal plane of GO nanosheets exists with a number of functional groups like epoxy, hydroxyl groups and carboxylic groups presumably located at the sheets' edge points. A homogenously dispersed solution of GO in 4M HCl is formed due to these oxygenate species. Moreover, the addition of metallic Sn powder (with a mass ratio 10 times larger than GO concentration) is responsible for the fast reduction process of GO and its conversion it into rGO. The *in situ* generated Sn^{2+}/Sn^{4+} get selectively bonded with the oxygenated groups through electrostatic force and form unstable Sn(OH)$_4$ nuclei in the solution

mixture. After hydrothermal treatment at 180˚C, the rGO nanosheets anchored Sn^{2+} and
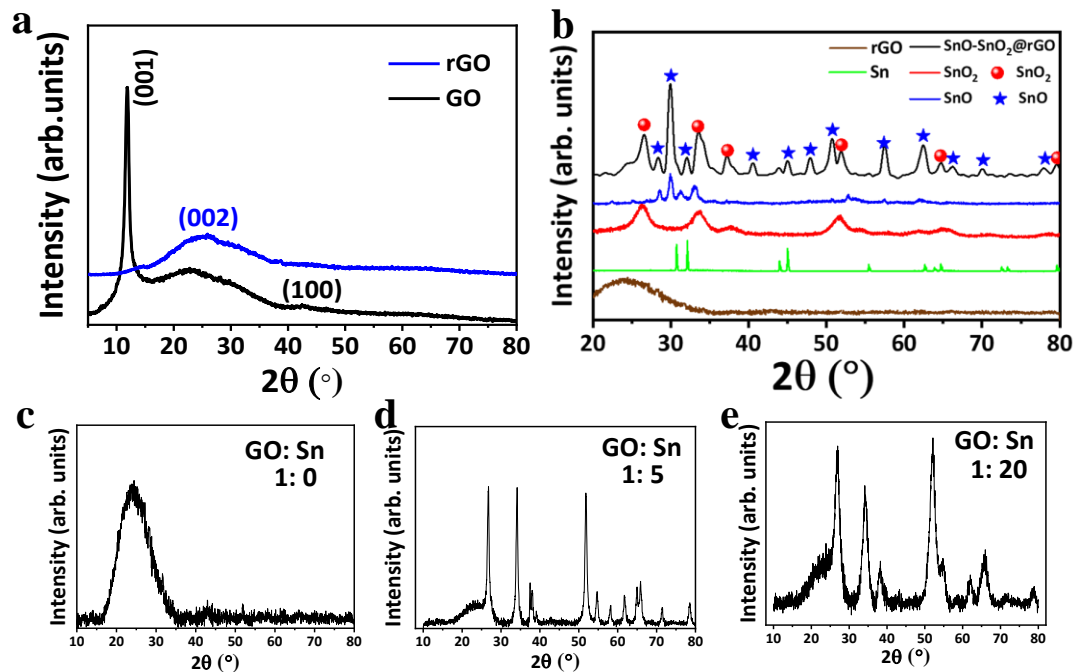
Figure 6.2. *X-Ray diffraction pattern for (a) GO, rGO (b) mix-phase SnO-SnO₂@rGO, XRD of control samples, (c-e) GO to Sn variant concentration ratios (1:0) - S₀, (1:5)-S₁ and (1:20)-S₂, respectively.*

Sn^{4+} ions are converted into tiny SnO and SnO_2 nanoparticles, respectively. This *in situ* reduction of GO and co-fabrication of nanoparticles has distinct advantages toward alleviating any serious stacking of rGO sheets and preventing the agglomeration of metal oxide nanoparticles.

A systematic microstructure study of GO to rGO and GO to mix-phase SnO-SnO_2@rGO was carried out via X-Ray diffraction and Raman analysis. The XRD pattern of as-prepared products SnO-SnO_2@rGO and control samples GO, rGO samples named as S_0, S_1, S_2 (samples with different GO:Sn concentration) are illustrated in Fig. 6.2a-e, respectively. As expected, the XRD pattern for GO displayed a sharp characteristic peak at 11.6° (Fig. 6.2a), which represents the weak van der Waals forces between the GO layers. Whereas, the intense peak corresponding to GO does not appear in the XRD spectrum of rGO and SnO-SnO_2@rGO as shown in Fig. 6.2a (blue coloured curve) and Fig. 6.2b, indicating that metallic Sn is effectively converted GO to its reduced form during the reduction process. The two broad diffraction peaks at 26° and 43° angle, are assigned to (002) and (101) planes of rGO.[25] The XRD spectrum of mix phase SnO-SnO_2@rGO (Fig. 6.2b) includes all the distinguishable diffraction peaks corresponding to SnO and SnO_2 phases. The lattice planes $(\bar{1}0\bar{1}), (\bar{1}\bar{1}0), (00\bar{2}), (\bar{1}\bar{1}\bar{1}), (10\bar{2}), (\bar{1}\bar{1}\bar{2}), (\bar{2}\bar{1}\bar{1}), (\bar{2}\bar{1}\bar{2})$ correspond to rutile SnO

tetragonal phase (JCPDS file no. COD2104754) and the lattice planes $(\bar{1}\bar{1}0), (\bar{1}0\bar{1}), (\bar{2}00), (\bar{1}\bar{1}\bar{2}), (00\bar{2}), (\bar{2}\bar{1}0), (\bar{2}\bar{1}\bar{1})$ correspond to rutile SnO_2 tetragonal phase (JCPDS file no. COD9008956). The diffraction peak corresponding to the rGO component is absent in the XRD spectra SnO-SnO_2@rGO, which further explains the homogenous dispersion of SnO_2 and SnO nanoparticles throughout the graphene layers. [26–29] It can be concluded from the comparative XRD curves of samples with different GO to Sn ratios as shown in Fig.6.2c-e; the only sample with a GO to Sn weight ratio of 1:10 provides the mix phase hybrid material i.e., our SnO-SnO_2@rGO material.

Further, Raman spectra of all the three samples (GO, rGO and SnO-SnO_2@rGO)
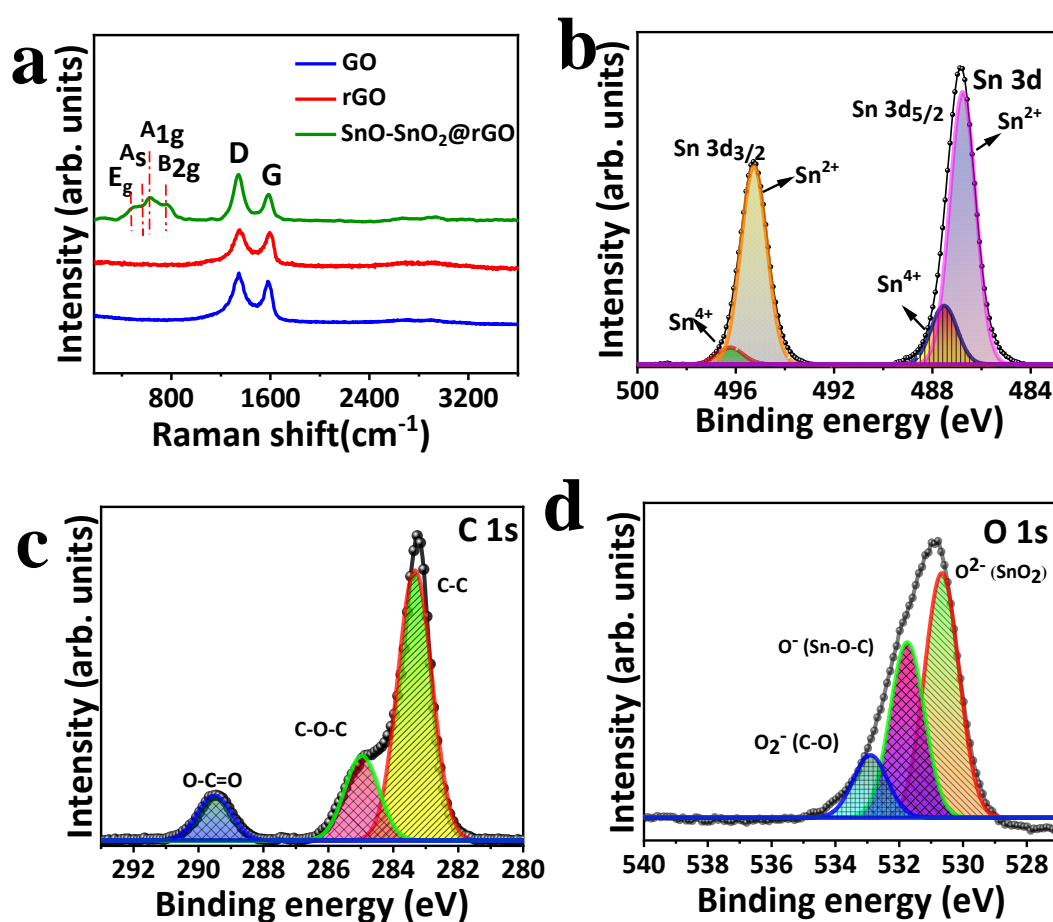
Figure 6.3. *Raman spectra (a) for SnO-SnO$_2$@rGO; Deconvoluted XPS spectrum for (b) Sn 3d, (c) C 1s, and (d) O 1s in mix phase SnO-SnO$_2$@rGO sample, respectively.*

were recorded (Fig. 6.3a) to further analyse the reduction of GO and formation of mixed oxides of tin via chemical reaction. The Raman spectrum of GO shows two sharp bands located at 1340 cm^{-1} and 1580 cm^{-1} that are assigned to D- and G-band, respectively. The relevant origin behind the occurrence of G-band is vibrations corresponding to sp^2-hybridized carbon atoms, while the D band is associated with existence of oxygen functional groups as defects; forming disordered lattice in the GO graphitic layers. [30] The

defect band (I_D) to graphitic band (I_G) intensity ratio *i.e.* I_D/I_G decreased to 1.06 (rGO) as compared to I_D/I_G ratio of 1.14 in the case of GO, indicating the improved degree of graphitization.[31] However, it is exciting to see that the rGO component in the mix phase composite material yields a higher I_D/I_G (=1.42) ratio. This can be attributed to the decrease in the average size of the sp^2 domains and increase in the defect domains during
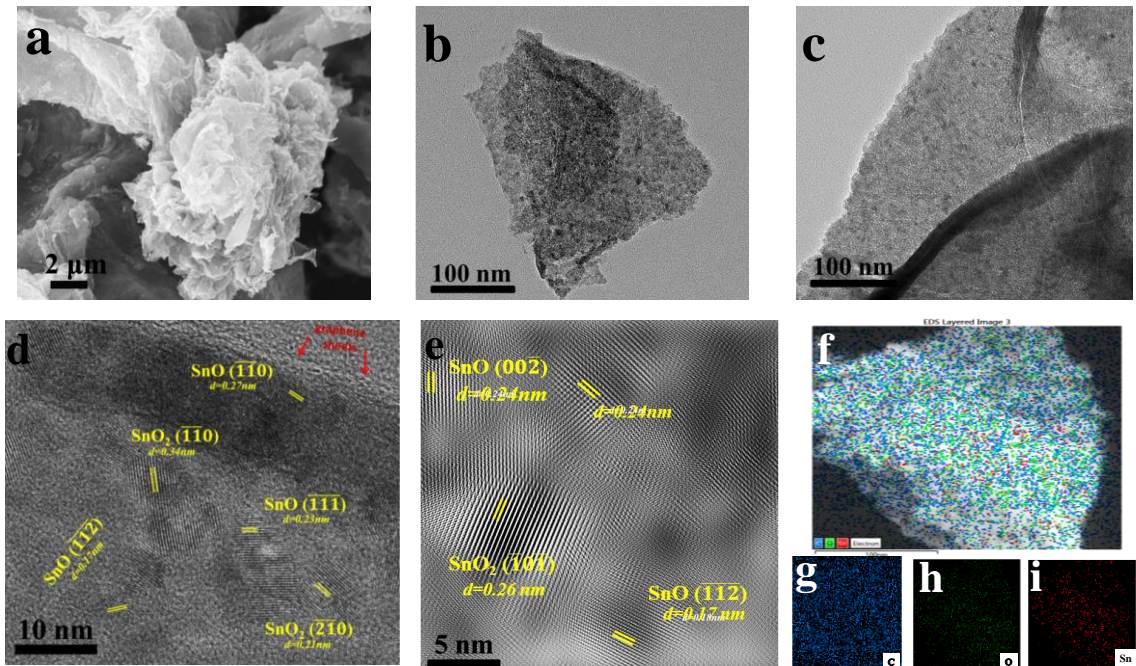
Figure 6.4. *Scanning electron microscopic image (a) and Transmission electron microscopic image (b) for mix phase SnO-SnO₂@rGO showing SnO and SnO₂ nanoparticles are well decorated all over the graphene sheets, (c) TEM image from the edge of graphene sheets representing the folded graphene sheets with uniformly distributed nanoparticles, (d and e) HRTEM and FFT images showing the fringe pattern for SnO and SnO₂ mix phase at a resolution of 10 nm and 5 nm, respectively, Energy dispersive cumulative elemental mapping (f) represents the existence of C (g), O (h) and Sn (i) in 50.2%, 38.7% and 11.0% ratio, respectively.*

the chemical reaction between Sn precursor and graphene sheets.[32] Generally, these defect domains enhance the electrochemical reaction, which also contributes to the overall capacity of LIB cell.[33] The Raman spectrum of mix phase material occupied four active vibrational bands in the Raman shift range of 200 nm to 800 nm. The two peaks B_{1g}, and B_{2g} positioned at 316 cm^{-1} and 782 cm^{-1} correspond to the active modes indexed to the SnO phase.[34] The two other modes were also found at 632 cm^{-1} and 491 cm^{-1} corresponding to the A_{1g} (non-degenerate mode) and E_g (doubly degenerate mode) vibrational sites of SnO₂ nanoparticles.[35] The E_g mode vibrates in the direction of the c-axis corresponding to the oxygen vibrations.[36,37][34]
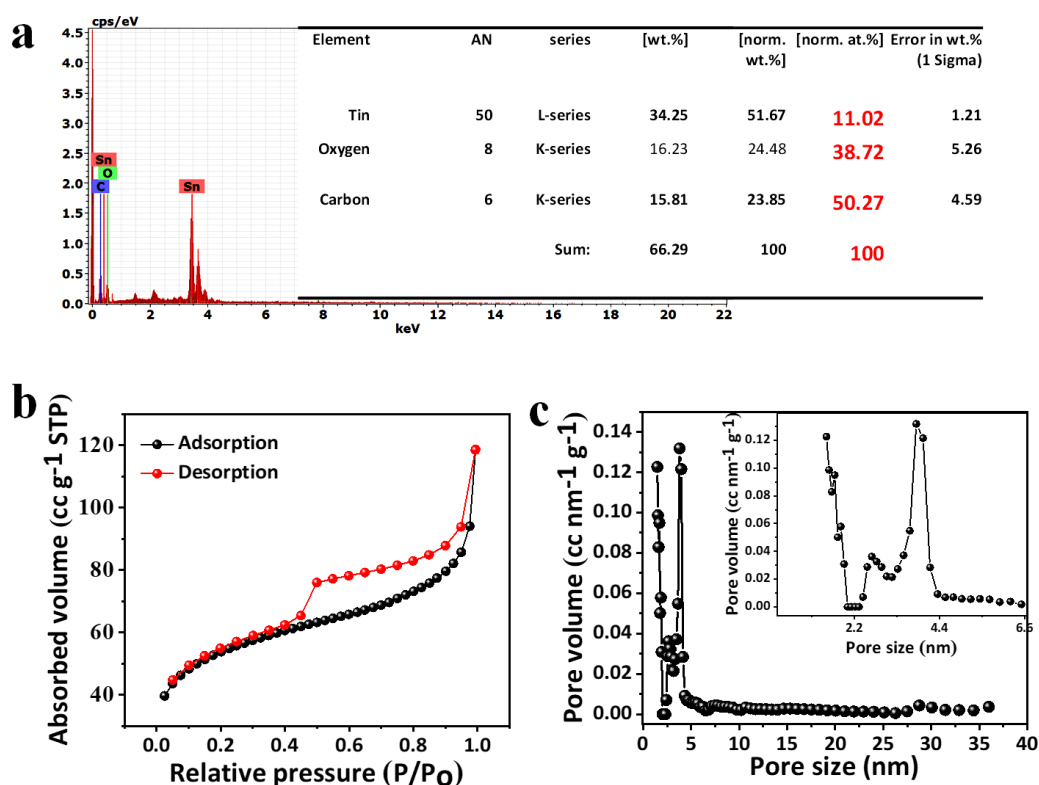
Figure 6.5. *(a) Energy Dispersive X-Ray spectrum for mix phase SnO-SnO₂@rGO composite, (b) Adsorption-desorption isotherm for SnO-SnO₂@rGO material for the calculation of effective surface area, (c) pore –size distribution curve, inset shows the magnified version of region 0 to 5 nm, respectively.*

To know the chemical state of the resulting materials, X-ray photoelectron spectra (XPS) analysis was performed. The core-level XPS spectra of Sn 3d, O 1s and C 1s are shown in Fig. 6.3b-d. The XPS spectra of Sn 3d (Fig. 6.3b) include two primitive peaks corresponding to Sn $3d_{3/2}$ and $3d_{5/2}$ orbitals, which are further deconvoluted. The deconvoluted peaks under Sn $3d_{5/2}$ at binding energies of 485.9 eV, 486.8 eV correspond to Sn^{2+} and Sn^{4+}, respectively, and the peaks under Sn $3d_{3/2}$ positioned at 495.2 eV, 496.2 eV correspond to Sn^{2+}, Sn^{4+} state, respectively.[33] Figure 6.3c represents the binding energies of 283.35 eV, 284.6 eV and 288.8 eV in C 1s deconvoluted XPS spectrum related to C–C, C–O–C and O–C=O bonding in the SnO-SnO₂@rGO material, respectively. The O 1s XPS spectrum is shown in Fig. 6.3d displays three peaks at 530.4 eV (O^{2-} configuration), 531.7 eV (Sn–O–C bonding) and 532.7 eV (C–O bond).[38] The Sn–O–C bond initiates a good synergistic effect between the carbon matrix and tin oxides nanoparticles, which trigger the superior electrochemical properties.

6.3.2 Morphological characterizations

The morphology of SnO-SnO$_2$@rGO was characterized by scanning electron microscopy (SEM) and transmission electron microscopy (TEM), as shown in Fig. 6.4a-e. SEM image of SnO-SnO$_2$@rGO depicts corrugated graphene nanosheets and these are well expanded in three-dimensional (3D) flower-like nanostructures, as shown in Fig. 6.4a. The TEM images shown in Fig. 6.4b and 6.4c reveals that the wrinkled graphene nanosheets are densely packed with tiny nanoparticles of SnO and SnO$_2$ nanoparticles and the 3D structure of the composite is preserved during in-situ nucleation and growth of two phase's metal-oxide nanoparticles, respectively. It is worth mentioning that there are no bigger agglomerates of tin oxide of any phase have been found in the sample. It is suggested that GO can prevent the agglomeration of nanoparticles effectively. It can be seen from the lattice resolved high-resolution TEM images (Fig.6.4d and e) at different magnifications of 10 nm and 5 nm, the calculated crystal lattice fringes d-spacing values with their crystal lattice planes are 0.17 nm $(\overline{1}\overline{1}2)_{SnO}$, 0.23 nm $(\overline{1}\overline{1}1)_{SnO}$, 0.210 nm $(\overline{2}\overline{1}0)_{SnO2}$, 0.27 nm $(\overline{1}\overline{1}0)_{SnO}$, and 0.34 nm $(\overline{1}\overline{1}0)_{SnO2}$, respectively. Figure 6.4d also indicates the presence of approximately 3 to 5 graphene layers as marked with arrow. This kind of structure is known to be advantageous for the excellent electron transfer pathway and accommodation of the strains of Li$^+$ insertion/extraction, resulting in excellent Li$^+$ storage properties. The spatial distribution of Sn, O and C elements in SnO-SnO$_2$@rGO sample was further measured by EDAX elemental mapping (Fig. 6.4f-i). The images in Fig 6.4f-i shows the cumulative and individual C, O, and Sn elemental mapping, respectively. It reveals that the Sn, O and C elements are evenly distributed in atomic weight percentage ratio of 11.02, 38.72 and 50.27, respectively (elemental dispersive spectra is shown in Fig. 6.5a). Moreover, the effective surface area and pore size distribution of the resulting mix phase composite materials was obtained using Brunauer-Emmett-Teller (BET) method as shown in Fig. 6.5b and c. The effective surface area is calculated to be 255 m^2 g^{-1} (Fig. 6.5b) and pore sizes range from 1.5 nm to 5 nm, which is helpful for easy ionic diffusion kinetics (Fig. 6.5c).

6.3.3 Electrochemical characterizations:

A series of electrochemical experiments were carried out to check the lithium storage performance of SnO-SnO$_2$@rGO material in LiPF$_6$ medium. First, a Li-ion half-cell was tested with SnO-SnO$_2$@rGO as cathodic counterpart considering Li metal as reference anode. The cyclic voltammetry of SnO-SnO$_2$@rGO (vs Li$^+$/Li) at 0.05 mv s^{-1} shows three clear reversible anodic peaks approximately at 1.38 V, 0.8 V and 0.17 V, which indicates

the reductions of Sn^{4+} to Sn^{2+}, Sn^{2+} to Sn^0 and subsequent Li_xSn alloy formation, respectively (Fig. 6.6a and b). The reaction mechanism is as follows:

$$SnO_2 + 4\,Li^+ + 4\,e^- \rightleftharpoons Sn + 2\,Li_2O \ldots\ldots\ldots\ldots(\sim1.38\,V)$$

$$SnO + 2\,Li^+ + 2\,e^- \rightleftharpoons Sn + Li_2O \ldots\ldots\ldots\ldots(\sim0.8\,V)$$

$$Sn + x\,Li^+ + x\,e^- \rightleftharpoons Li_xSn\,(0 \le x \le 4.4) \ldots (\sim0.17\,V)$$

$$C + y\,Li^+ + y\,e^- \rightleftharpoons Li_yC \ldots\ldots\ldots\ldots(0.02-0.05\,V)$$
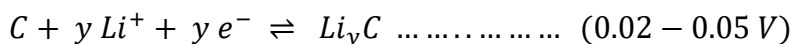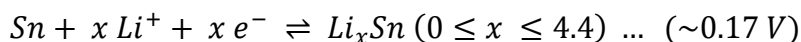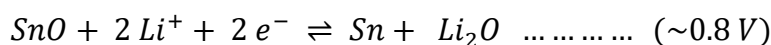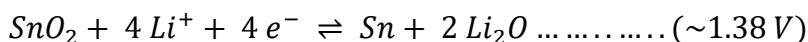
The charge-discharge profile and cycling performance was tested and the results are shown in Fig. 6.6c. The charge-discharge plateaus did show a one-to-one correlation with the CV peaks (Fig. 6.6b inset). Surprisingly, the half-cell unveiled extremely high initial
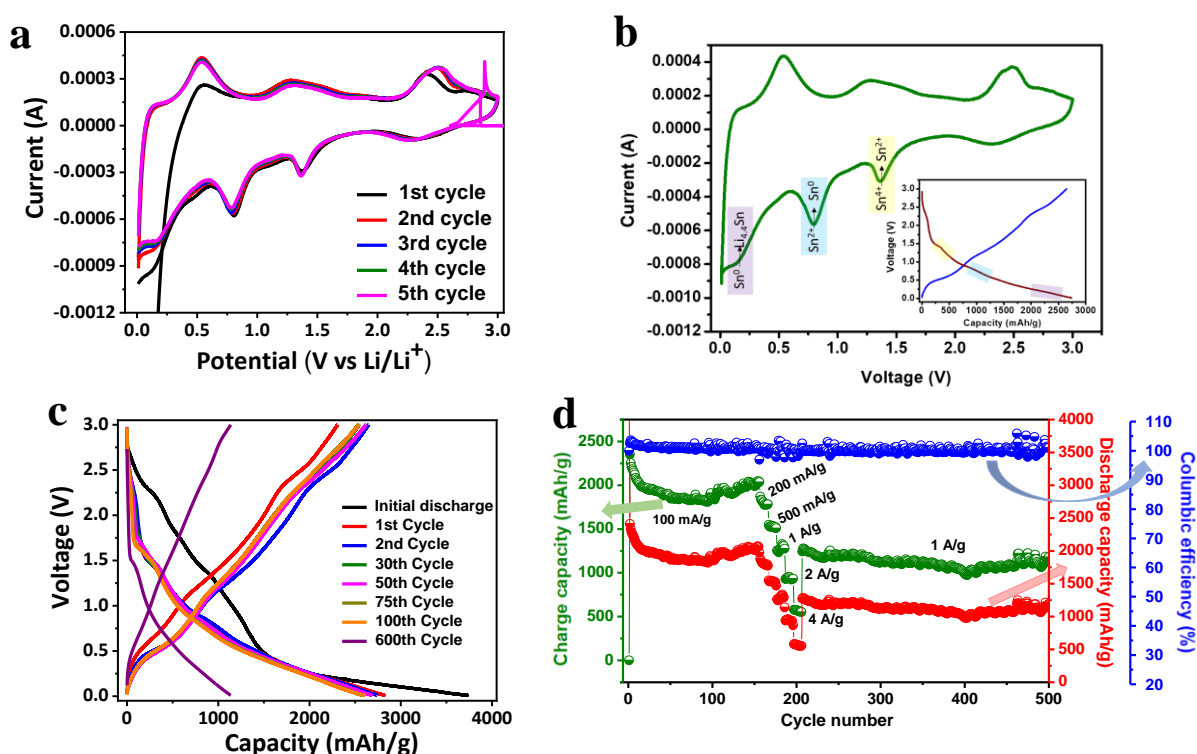
Figure 6.6. *(a) Cyclic voltammetry data (b) comparison of the redox mechanism between the CV and the charge-discharge, (c)Charge-discharge profile in the half cell configuration (d) Stability, efficiency and rate performance.*

discharge capacity of 3744 mAh g^{-1} followed by a stable reversible capacity of 2604 mA h g^{-1} at an applied current density of 100 mA g^{-1} (Fig. 6.6c), which is the highest reversible capacity for SnO_x based Li-ion battery system till date, to the best of our knowledge (a comparative study is given in Table 6.1). A very impressive cyclic stability of 500 cycles was observed with an average columbic efficiency of ~99.7 %. The material proved itself capable of providing high power since it could show a reasonably high capacity of ~500 mA h g^{-1} at a very high current density of 2 A g^{-1} (Fig. 6.6d).
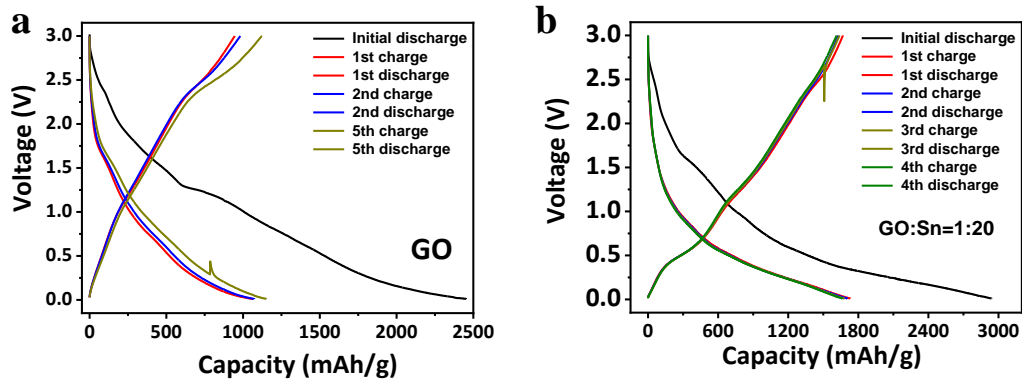
Figure 6.7. *(a) Charge discharge profile of the as synthesized GO without the Sn precursor (sample "S0"), (b) GO with Sn in ratio (1:20), respectively*

The contribution from rGO during lithiation was also found to be significant. A control experiment showed that the reversible capacity of synthesized rGO via the same process (without the addition of the Sn precursor) is ~1300 mAh g^{-1} at a current density of 100 mA g^{-1} (Fig. 6.7a). The lithiation in rGO was found to be occurring in the potential window of 0.02 to 0.05 V. Similarly, we did another control experiment so as to understand the role of the composition of the system. A control experiment where we changed the ratio of Sn powder to rGO rendered a much lesser capacity of ~1770 mAh g^{-1} which indeed justifies the fact that the optimum composition of the starting material
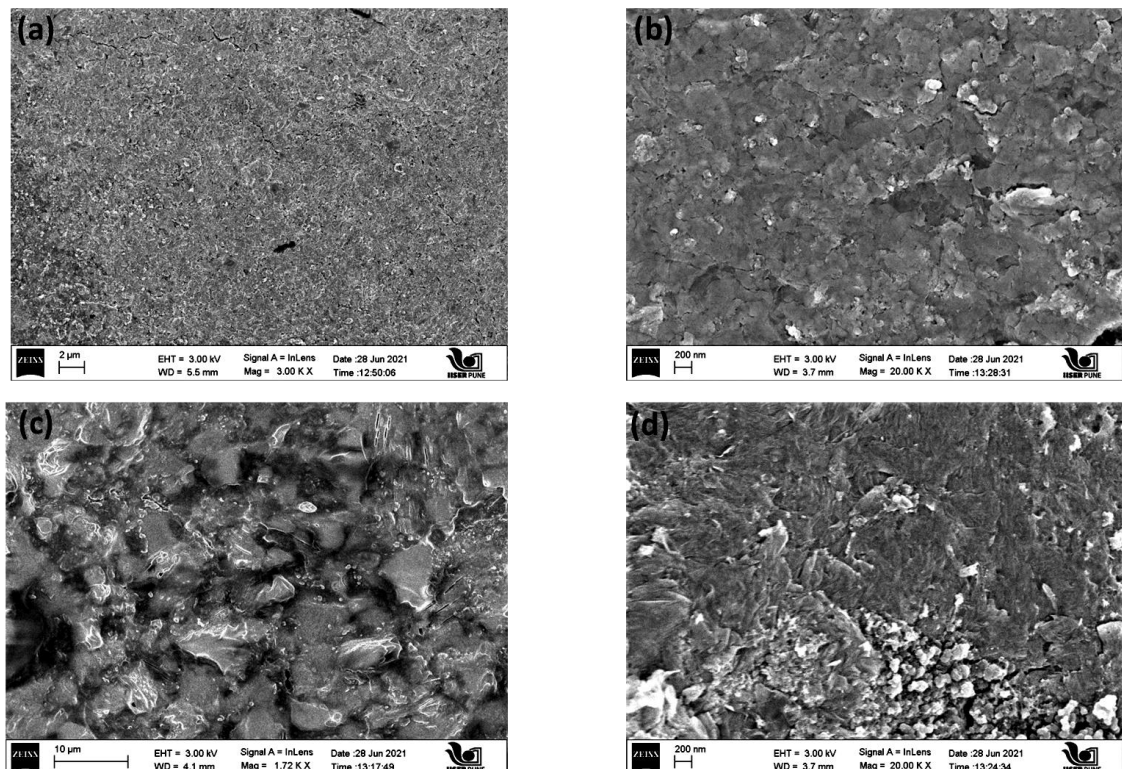
Figure 6.8. *FESEM images of (a and b) Fresh as-made SnO-SnO$_2$@rGO electrodes, and (c and d) Cycled electrodes.*

is required for the best performance (Fig. 6.7b). Fattakhova-Rohlfing and co-worker[39]

had pointed out that intermediate Li-Sn-O phases etc. largely depend on the composition and morphology of the active SnO_2 material, which in-turn depends on the crystallinity, defects, stoichiometry, impurities etc. According to them, all of these factors have major
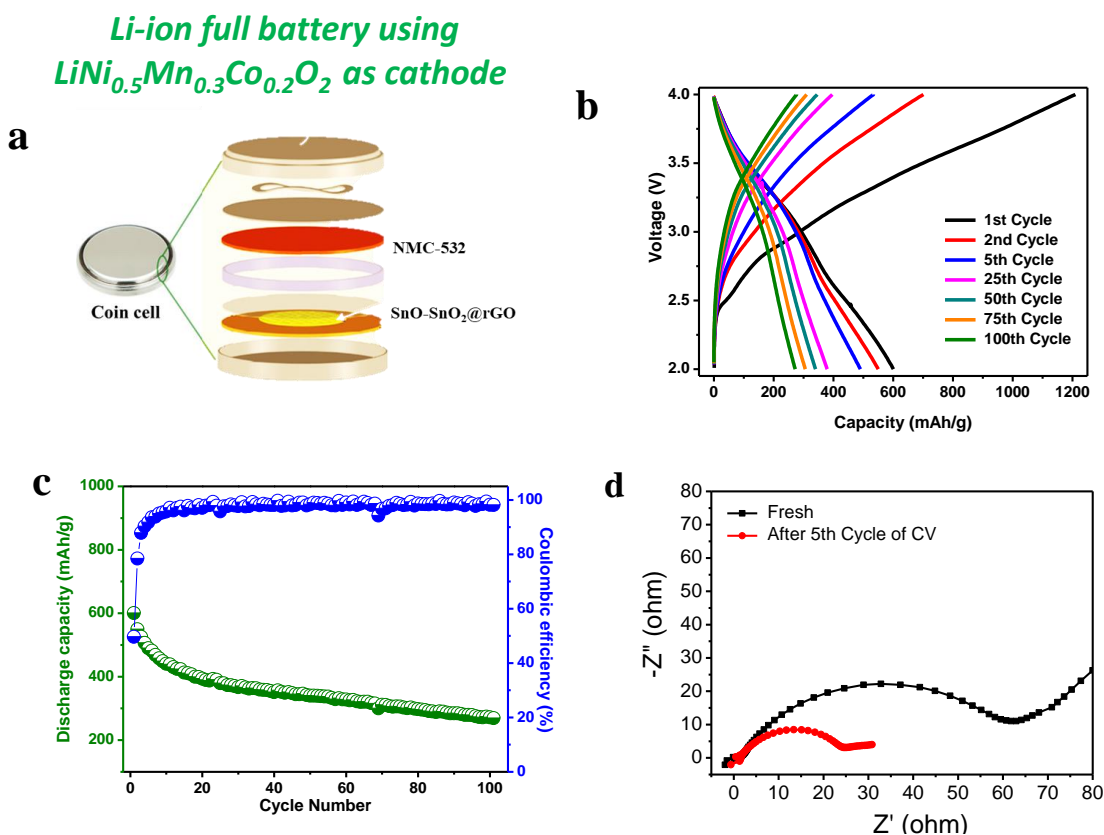
Figure 6.9. *Li-ion full cell battery electrochemical performance. (a) Schematic shows the Li-ion coin cell configuration, (b) Charge-discharge profile in the full cell configuration using NMC-532 as the cathode (c) Stability and efficiency data for the full cell, (d) Electrochemical impedance spectroscopic analysis for the cell (fresh cell and after 5 cycle).*

dependence on the synthesis protocol and the choice of precursor, and these become deciding factors in the overall capacity and electrochemical stability.[39] It is very much essential to tune the synthetic methodology in order to engineering of the active material so as to have 1) concurrent SnO and SnO_2 phase formation, 2) sufficient defect density and 3) homogeneous distribution of the crystalline nanoparticles across the conductive rGO matrix. In this study, uniform distribution of both SnO and SnO_2 on the reduced graphene oxide matrix is turned out to be the primary factor responsible for extremely high capacity and superior cyclic stability (Fig. 6.4b, 6.4c and 6.4f). Furthermore, the conducting rGO matrix also serves as a stress-absorbing cushion so as to stabilize the material by taking into consideration the volume expansion and contraction that occurs during the lithiation and de-lithiation process; providing adequate conductivity alongside. It is very much evident from the comparison ex-situ SEM images of fresh

(Fig. 6.8a and b) and post-cycling samples (Fig. 6.8c and d) (that no major cracks were found after lithiation and de-lithiation. Moreover, the overall voltage polarization between charging and discharging get reduced to a significant extent making the overall battery material energy-efficient and very stable.

Taking into consideration of the above-mentioned advantages of the material, we fabricated a practical Li-ion battery (LIB), where SnO-SnO_2@rGO acts as anode and a high voltage $LiNi_{0.5}Mn_{0.3}Co_{0.2}O_2$ (NMC-532) acts as cathode (Fig. 6.9a). It is noteworthy to mention that this LIB achieved a very high reversible capacity of 570 mA h g^{-1} (based on the anode weight) at an applied current density of 0.1 A g^{-1} with more than 50% retention of capacity after 100 cycles as depicted from Fig. 6.9b and c. The electrochemical impedance spectroscopy reveals that the charge transfer resistance (R_{ct}) was reduced to a considerable extent even after post-cycling (Fig. 6.9d) of LIB. This essentially proves that a uniform conducting solid-electrolyte interphase (SEI) layer has formed at the electrode-electrolyte interface with the help of the conducting support matrix of rGO, which makes the interfacial Li diffusion very much facile.

The extraordinary capacity value achieved with the material encouraged us to further investigate the origin of it. The SnO_2 has a theoretical capacity of ~1500 mA h g^{-}
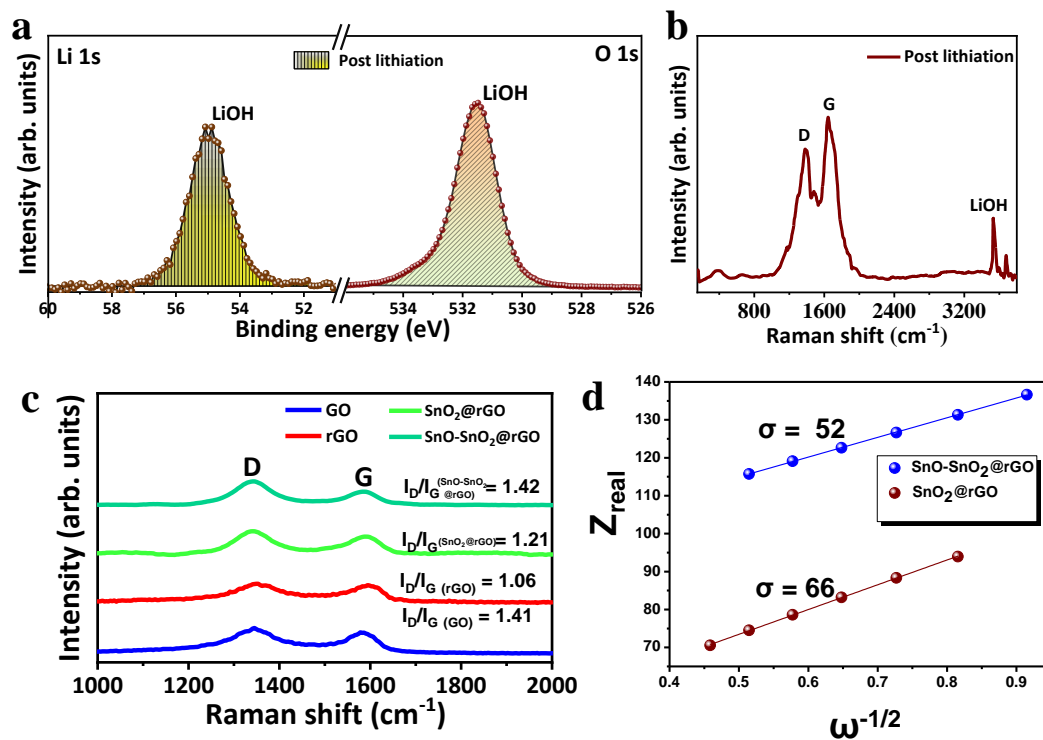
Figure 6.10. *Post cycling (a) ex-situ Li1s and O1s XPS spectra and (b) Raman spectra revealing the formation of LiOH in the lithiated state, (c) Raman spectra of GO, rGO, SnO$_2$@rGO and mix phase SnO-SnO$_2$@rGO materials (d) ω$^{-1/2}$ vs Z$_{real}$ plot.*

[1], while SnO has it at ~1300 mA h g^{-1}. The control experiment had shown an experimental capacity of ~1300 mA h g^{-1} for the as-prepared rGO. However, it is onerous to quantify the accurate composition of the individual components in SnO-SnO$_2$@rGO hybrid material and thus it would be preposterous to calculate the theoretical capacity of the overall system. Thus, using any reasonable estimate based on the theoretical capacity values one could not reasonably project much higher experimental capacity unless one
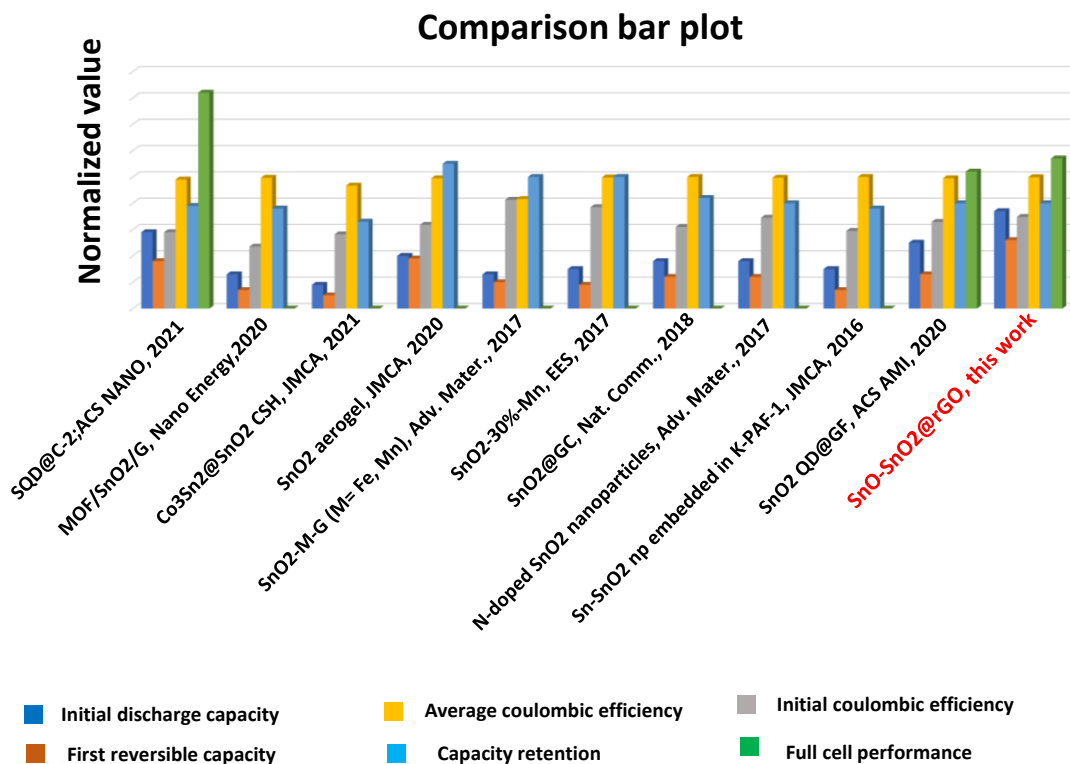
Figure 6.11. A bar diagram showing the comparison of electrochemical performances of different SnO$_x$ based Li-ion batteries reported in literature and compared with our work (mix phase SnO-SnO$_2$@rGO based LIB).

envisions some interesting synergistic effects. Interestingly, Grey et al. have mentioned that the formation of LiOH and its reaction with Li further transforming the phase to Li$_2$O and LiH could account for the extra capacity in conversion anodes (especially in oxide and fluoride systems).[40,41] Along this line, we have performed post-cycling ex-situ Raman and XPS to check the formation of LiOH. During lithiation, a clear formation of LiOH is noticed both in Raman and XPS data (Fig. 6.10a and b) Therefore, the extra capacity can indeed be attributed to the formation of LiOH in the system.

To have a better understanding the rationale for significantly higher capacity of SnO-SnO$_2$@rGO hybrid material, some control experiments were performed. Based on different GO to Sn ratio, we obtained different compositions of SnO$_x$ dispersed on the rGO matrix. Since LiOH formation is an established cause of the origin of the extra

Table 6.1. *A comparative study for the output electrochemical performances with reported SnO₂-based half-cell and full cell.*

Sr. No.	Electrode material	Synthesis protocol	Initial discharge capacity (mAh g⁻¹)	First reversible capacity (mAh g⁻¹)	Cycle stability	Capacity retention (%)	Capacity at highest reported current density	Columbic efficiency	Full cell reversible capacity (mAh g⁻¹)	References
1	SQD@C-2	Chemical synthesis	2948	1824	100 (0.2 A g-1)	78%	850 mAh g⁻¹ (5 A g⁻¹)	Initial C.E = 58% Average = 98%	817 mAh g⁻¹ (based on anode mass)	*43*
2	MOF/SnO₂/G	MOF (hydrothermal method), SnO2 (chemical method)	1332	660	100 (at 0.1 A g⁻¹),	75.5% (at 0.1 A g⁻¹)	324 mAh g⁻¹ (1 A g⁻¹)	Initial C.E = 47% Average = 99.5%	Not reported	*44*
3	Co₃Sn₂@SnO₂ CSH	Diffusion based nanocrystal conversion method	881.5	520	500 (0.1 A g⁻¹)	65%	350 mAh g⁻¹ (5 A g⁻¹)	Initial C.E = 56.4% Average = 93.3%	Not reported	*45*
4	SnO₂@C	Stober's method (two step hydrothermal reaction)	1058	650	200	66%	420 mAh g⁻¹ at 1 A g⁻¹	Initial C.E = 50% Average = 99%	Not reported	*46*
5	Chemically engineered SnO₂ aerogel	Shape anisotropy method followed by chemical growth of SnO₂	2031	1295	5000 (at 10 C)	110% (at 10 C)	505 mAh g⁻¹ (1.58 A g⁻¹)	Average = 99%	Not reported	*47*
6	SnO₂-M-G (M = Fe or Mn)	Ball Milling	1300	940	150 (0.2 A g⁻¹)	100%	720 mAh g⁻¹ (3.4 A g⁻¹)	Initial = 82.5% Average = 83.2%	0.45 mAh cm⁻²	*48*

7	SnO₂@TiO₂ composites	chemical reaction	799	397	50	79%	110 mA h g⁻¹ at 0.8 A g⁻¹	Initial = 49.7% Average = 89%	Not reported	**49**
8	SnO₂ QD@GF	Hydrothermal treatment	2500	1300	1000 (5 Ag⁻¹), 5000 (10 A g⁻¹)	58% (5 A g⁻¹), {79% (10 A g⁻¹)	134 mAh g⁻¹ (10 A g⁻¹)	Initial = 65.9% Average = 99%	516 mAh g⁻¹	**50**
9	SnO₂-30%-Mn	Ball milling	1500	850	400 (0.2 A g⁻¹), {900 (2 A g⁻¹)}	100 % (0.2 A g⁻¹), {100 % (2 A g⁻¹)}	700 mAh g⁻¹ (2 A g⁻¹)	Initial = 77% Average = 99.5%	Not reported	**51**
10	SnO₂@GC	Hydrothermal treatment	1805	1200	300 (1 A g⁻¹)	84%	599 mAh g⁻¹ (1 A g⁻¹)	Initial = 62% Average = ~100%	152 mAh g⁻¹	**52**
11	ZnWO₄/SnO₂ @rGO	Chemical reaction method	1486	600	500	98%	436 mAh g⁻¹ at 0.5 A g⁻¹	Initial = 92% Average = ~99%	Not reported	**53**
12	SnO₂/Mxene	ALD technique	1264	897	50 (0.5 A g⁻¹)	50%	--	Initial = 78%	Not reported	**54**
13	SnO₂/BG	Hydrogen assisted reduction method	1639	848	100 (0.1 A g⁻¹)	92.4%	191 mAh g⁻¹ (2 Ag⁻¹)	Initial = 50% Average = 92.3%	Not reported	**55**
14	Porous SnO₂@C	Chemical reaction	1452	1020	250	96%	773 mAh g⁻¹ at 3 A g⁻¹	Initial = 68% Average = 98%	Not reported	**56**
15	SnO₂@HPC @NC	Chemical reaction	1450	1082	100 (at 0.1 A g⁻¹)	100%	310 mAh g⁻¹ (5 A g⁻¹)	Initial = 75.2% Average = 95.3%	Not reported	**57**

16	Sn-SnO$_2$ np embedded in K-PAF-1	Thermal treatment	1500	760	400 (0.4 A g^{-1})	76%	152 mAh g^{-1} (3 A g^{-1})	Initial = 59% Average = ~100%	Not reported	*58*
17	N-doped SnO$_2$ nanoparticles	Laser pyrolysis synthesis	1830	1241	300 (1.4 A g^{-1})	522 (10 A g^{-1})	80%	Initial = 69% Average = ~99.3%	Not reported	*59*
18	SnO-SnO$_2$	Spray pyrolysis system	1500	652	300 (1 A g^{-1})	86%	379 mAh g^{-1} (10 A g^{-1})	Initial = 51%	Not reported	*60*
19	SnO$_2$	--	1250	1220	200 (at 1/5 C rate)	70%	--	Initial = 95.5%	Not reported	*61*
20	Sn-SnO$_2$ nanoclusters @CNTs	Hydrothermal treatment	1450	1187	200 (0.2 A g^{-1}), {1000 (0.5 A g^{-1})	96% (0.2 A g^{-1}), {86% (0.5 A g^{-1})	960 mAh g^{-1} (5 A g^{-1})	Initial = 71% Average = 98%	Not reported	*62*
21	G@p-SnO$_2$@C composite	Chemical reaction followed by calcination	1455	1000	200 (0.2 A g^{-1})	>100%	405 mAh g^{-1} (5 A g^{-1})	Initial = 68% Average = 99%	Not reported	*63*
22	RGO/SnO$_2$ composite	Hydrothermal reaction	1380	718	200 (0.1 A g^{-1})	71.8%	512 mAh g^{-1} (1 A g^{-1})	Initial = 57%	Not reported	*64*
23	**SnO-SnO$_2$@rGO**	**Hydrothermal treatment**	**3744**	**2604**	**200 (0.1 A g^{-1}) 500 (1 A g^{-1})**	**80%**	**500 (2 A g^{-1})**		**570 mAh g^{-1} (Based on anode weight)**	**This work**

SQD- Tin quantum dot, MOF- metal-organic framework, CSH- core-shell heterostructures, BG- Boron doped graphene, QD- quantum dots, GF- graphene framework, HPC- hierarchical porous graphene, NC-N-doped carbon, CNTs- carbon nanotubes, ALD- atomic layer deposition, G-graphene, np-nanoparticles, PAF 1- porous aromatic framework, GC- graphene cage

capacity in the conversion systems (beyond their theoretical limit), we hypothized that rGO matrix is serving as the source of the functional groups that can essentially form LiOH upon electrochemical lithiation. Hence, we performed Raman analysis on different systems to have a good understanding of the defect to graphitization (I_D/I_G) ratio, with the results provided in Fig. 6.10c. We found the highest I_D/I_G ratio in SnO-SnO_2 mixed phase system as compared to bare rGO and the SnO_2@rGO composite (Fig. 6.10c). Higher I_D/I_G ratio essentially signifies higher concentration of defects in the rGO matrix; thereby elevated formation of LiOH. This ultimately leads to significantly higher amount of reversible lithium storage in the mixed phase system compared to the SnO_2@rGO system.

Furthermore, we also found that the SnO-SnO_2@rGO system offers much better rate performance compared to single phase SnO_2@rGO. To elucidate this further, we calculated Warburg coefficient (σ) and it was found that the σ value for SnO-SnO_2@rGO composite system is less than that of single-phase system (Fig. 6.10d). Since σ is inversely proportional to the diffusion coefficient, it can be inferred that the mixed phase system could offer a much more facile interfacial diffusion pathway as compared to that of the single-phase system. These experiments prove the superiority of the SnO-SnO_2 mixed phase nanostructured material over the single-phase system both in terms of stable reversible specific capacity and power density. Figure 6.11 shows a comparative bar diagram of different electrochemical parameter, which reveals that the capability of the SnO-SnO_2 mix phase composite system stands taller than most of the similar Li-storage material reported in the literature.

6.4 Conclusions

To conclude, this report provides a unique way of synthesizing SnO_2 and SnO mix phase system in a conducting matrix of reduced graphene oxide, which could host high quantity of Li in a very facile manner and that too beyond theoretical limit. The SnO-SnO_2@rGO system provides a half-cell reversible capacity of 2604 mAh g^{-1} at an applied current density of 0.1 A g^{-1}. It showed more than 82 % retention of capacity after 150 charge-discharge cycles at 0.1 A g^{-1} and could last till 500 cycles at 1 A g^{-1} with very good cyclic stability. The rate performance was also found to be impressive as it showed a reversible capacity of ~500 mAh g^{-1} at 2 A g^{-1}. We have also fabricated a Li-ion full battery using $LiNi_{0.5}Mn_{0.3}Co_{0.2}O_2$ (NMC-532) as the cathode and thereby, we have a Li-ion battery that is able to deliver a very high reversible capacity of 570 mAh g^{-1} (based on the anode

weight) at an applied current density of 0.1 A g^{-1} with more than 50% retention of capacity after 100 cycles. The extraordinarily high capacity beyond the theoretical limits is suggested to arise from the magnificent formation of LiOH due to defect-enriched mix-phase SnO-SnO$_2$@rGO material via synthetic control.

6.5 References

1   K. Kang, Y. S. Meng, J. Bréger, C. P. Grey and G. Ceder, *Science*, 2006, **311**, 977–980.

2   C. K. Chan, H. Peng, G. Liu, K. McIlwrath, X. F. Zhang, R. A. Huggins and Y. Cui, *Nat. Nanotechnol.*, 2008, 3, 31–35.

3   V. Etacheri, R. Marom, R. Elazari, G. Salitra and D. Aurbach, *Energy Environ. Sci.*, 2011, **4**, 3243–3262.

4   J. Li, R. Yao and C. Cao, *ACS Appl. Mater. Interfaces*, 2014, **6**, 5075–5082.

5   B. Wang, X. Li, T. Qiu, B. Luo, J. Ning, J. Li, X. Zhang, M. Liang and L. Zhi, *Nano Lett.*, 2013, **13**, 5578–5584.

6   B. Yin, X. Cao, A. Pan, Z. Luo, S. Dinesh, J. Lin, Y. Tang, S. Liang and G. Cao, *Adv. Sci.*, 2018, **5**, 1800829.

7   K. Roy, M. Wahid, D. Puthusseri, A. Patrike, S. Muduli, R. Vaidhyanathan and S. Ogale, *Sustain. Energy Fuels*, 2019, **3**, 245–250.

8   Z. Hu, Z. Zhu, F. Cheng, K. Zhang, J. Wang, C. Chen and J. Chen, *Energy Environ. Sci.*, 2015, **8**, 1309–1316.

9   J. B. Goodenough and K.-S. Park, *J. Am. Chem. Soc.*, 2013, **135**, 1167.

10   H. Li, Z. Wang, L. Chen and X. Huang, *Adv. Mater.*, 2009, **21**, 4593.

11   T. Stephenson, Z. Li, B. Olsen and D. Mitlin, *Energy Environ. Sci.*, 2014, **7**, 209–231.

12   B. Chen, D. Chao, E. Liu, M. Jaroniec, N. Zhao and S.-Z. Qiao, *Energy Environ. Sci.*, 2020, **13**, 1096–1131.

13   K. Roy, T. Li, S. Ogale and N. Robertson, *J. Mater. Chem. A*, 2021, **9**, 2689–2693.

14   J. Hassoun, K.-S. Lee, Y.-K. Sun and B. Scrosati, *J. Am. Chem. Soc.*, 2011, **133**, 3139.

15   J. Y. Huang, L. Zhong, C. M. Wang, J. P. Sullivan, W. Xu, L. Q. Zhang, S. X. Mao, N. S. Hudak, X. H. Liu, A. Subramanian, H. Fan, L. Qi, A. Kushima and J. Li, *Science*, 2010, **330**, 1515.

16   K. Roy, V. Chavan, S. M. Hossain, S. Haldar, R. Vaidhyanathan, P. Ghosh and S. B. Ogale, *ChemSusChem*, 2020, **13**, 196–204.

17   D.-C. Zuo, S.-C. Song, C.-S. An, L.-B. Tang, Z.-J. He and J.-C. Zheng, *Nano Energy*, 2019, **62**, 401.

18   X. W. D. Lou, C. M. Li and L. A. Archer, *Adv. Mater.*, 2009, **21**, 2536–2539.

19   C. Wu, J. Maier and Y. Yu, *Adv. Funct. Mater.*, 2015, **25**, 3488.

20   R. Hu, D. Chen, G. Waller, Y. Ouyang, Y. Chen, B. Zhao, B. Rainwater, C. Yang, M. Zhu and M. Liu, *Energy Environ. Sci.*, 2016, **9**, 595–603.

21   L. P. Wang, Y. Leconte, Z. Feng, C. Wei, Y. Zhao, Q. Ma, W. Xu, S. Bourrioux, P. Azais, M. Srinivasan and Z. J. Xu, *Adv. Mater.*, 2017, **29**, 1603286.

22   Y. Sun, Q. Wu and G. Shi, *Energy Environ. Sci.*, 2011, **4**, 1113–1132.

23   N. Kamboj, T. Purkait, M. Das, S. Sarkar, K. S. Hazra and R. S. Dey, *Energy Environ. Sci.*, 2019, **12**, 2507–2517.

24   R. S. Dey, S. Hajra, R. K. Sahu, C. R. Raj and M. K. Panigrahi, *Chem. Commun.*, 2012, **48**, 1787.

25   Q. Wang, W. Ren, F. Gao, C. Qiu, Q. Wang, F. Gao and C. Zhao, *ChemElectroChem*, 2019, **6**, 1768.

26   L. Liu, M. An, P. Yang and J. Zhang, *Sci. Rep.*, 2015, **5**, 9055.

27   J. Yao, X. Shen, B. Wang, H. Liu and G. Wang, *Electrochem. commun.*, 2009, **11**, 1849–1852.

28   H. Liu, J. Huang, X. Li, J. Liu, Y. Zhang and K. Du, *Phys. E Low-dimensional Syst. Nanostructures*, 2012, **44**, 1931–1935.

29   D. Pan, S. Wang, B. Zhao, M. Wu, H. Zhang, Y. Wang and Z. Jiao, *Chem. Mater.*, 2009, **21**, 3136–3142.

30   N. Kamboj, T. Purkait, M. Das, S. Sarkar, K. S. Hazra and R. S. Dey, *Energy Environ. Sci.*, 2019, **12**, 2507–2517.

31   K. N. Kudin, B. Ozbas, H. C. Schniepp, R. K. Prud'homme, I. A. Aksay and R. Car, *Nano Lett.*, 2008, **8**, 36–41.

32   C. Botas, D. Carriazo, G. Singh and T. Rojo, *J. Mater. Chem. A*, 2015, **3**, 13402–13410.

33   Y. Zhang, D. Yan, Z. Liu, Y. Ye, F. Cheng, H. Li and A.-H. Lu, *ACS Nano*, 2021, **15**, 7021–7031.

34   C. Meier, S. Lüttjohann, V. G. Kravets, H. Nienhaus, A. Lorke, P. Ifeacho, H. Wiggers, C. Schulz, M. K. Kennedy and F. E. Kruis, *J. Appl. Phys.*, 2006, **99**,

113108.

35   J. Kaur, J. Shah, R. K. Kotnala and K. C. Verma, *Ceram. Int.*, 2012, **38**, 5563–5570.

36   R. S. Katiyar, P. Dawson, M. M. Hargreave and G. R. Wilkinson, *J. Phys. C Solid State Phys.*, 1971, **4**, 2421–2431.

37   A. Diéguez, A. Romano-Rodríguez, A. Vilà and J. R. Morante, *J. Appl. Phys.*, 2001, **90**, 1550–1557.

38   S. M. Jung, D. W. Kim and H. Y. Jung, *J. Mater. Chem. A*, 2020, **8**, 8244.

39   F. Zoller, D. Böhm, T. Bein and D. Fattakhova-Rohlfing, *ChemSusChem*, 2019, **12**, 4140–4159.

40   T. Liu, Z. Liu, G. Kim, J. T. Frith, N. Garcia-Araez and C. P. Grey, *Angew. Chemie Int. Ed.*, 2017, **56**, 16057–16062.

41   Y.-Y. Hu, Z. Liu, K.-W. Nam, O. J. Borkiewicz, J. Cheng, X. Hua, M. T. Dunstan, X. Yu, K. M. Wiaderek, L.-S. Du, K. W. Chapman, P. J. Chupas, X.-Q. Yang and C. P. Grey, *Nat. Mater.*, 2013, **12**, 1130–1136.

42   T. Purkait, G. Singh, D. Kumar, M. Singh and R. S. Dey, *Sci. Rep.*, 2018, **8**, 640.

43   Y. Zhang, D. Yan, Z. Liu, Y. Ye, F. Cheng, H. Li and A.-H. Lu, *ACS Nano*, 2021, **15**, 7021–7031.

44   C. Gao, Z. Jiang, P. Wang, L. R. Jensen, Y. Zhang and Y. Yue, *Nano Energy*, 2020, **74**, 104868.

45   T. T. Salunkhe, A. N. Kadam, W. G. Kidanu, S.-W. Lee, T. L. Nguyen and I. T. Kim, *J. Mater. Chem. A*, 2021, **9**, 14991–15002.

46   Y. Wang, W. Guo, Y. Yang, Y. Yu, Q. Li, D. Wang and F. Zhang, *Electrochim. Acta*, 2018, **262**, 1–8.

47   S. M. Jung, D. W. Kim and H. Y. Jung, *J. Mater. Chem. A*, 2020, **8**, 8244–8254.

48   R. Hu, Y. Ouyang, T. Liang, H. Wang, J. Liu, J. Chen, C. Yang, L. Yang and M. Zhu, *Adv. Mater.*, 2017, **29**, 1605006.

49   J. Liang, L. Zhang, D. XiLi and J. Kang, *Electrochim. Acta*, 2020, **341**, 136030.

50   L. Gao, G. Wu, J. Ma, T. Jiang, B. Chang, Y. Huang and S. Han, *ACS Appl. Mater. Interfaces*, 2020, **12**, 12982–12989.

51   R. Hu, Y. Ouyang, T. Liang, X. Tang, B. Yuan, J. Liu, L. Zhang, L. Yang and M. Zhu, *Energy Environ. Sci.*, 2017, **10**, 2017–2029.

52   J. Han, D. Kong, W. Lv, D.-M. Tang, D. Han, C. Zhang, D. Liu, Z. Xiao, X. Zhang, J. Xiao, X. He, F.-C. Hsia, C. Zhang, Y. Tao, D. Golberg, F. Kang, L. Zhi and Q.-H. Yang, *Nat. Commun.*, 2018, **9**, 402.

53   K. Brijesh, S. Vinayraj, P. C. Dhanush, K. Bindu and H. S. Nagaraja, *Electrochim. Acta*, 2020, **354**, 136676.

54   B. Ahmed, D. H. Anjum, Y. Gogotsi and H. N. Alshareef, *Nano Energy*, 2017, **34**, 249–256.

55   M. Sahoo and S. Ramaprabhu, *Carbon N. Y.*, 2018, **127**, 627–635.

56   Q. Tian, Y. Chen, Z. Sui, J. Chen and L. Yang, *Electrochim. Acta*, 2020, **354**, 136699.

57   Y. Hong, W. Mao, Q. Hu, S. Chang, D. Li, J. Zhang, G. Liu and G. Ai, *J. Power Sources*, 2019, **428**, 44–52.

58   Y. Dong, S. Das, L. Zhu, T. Ben and S. Qiu, *J. Mater. Chem. A*, 2016, **4**, 18822–18831.

59   L. P. Wang, Y. Leconte, Z. Feng, C. Wei, Y. Zhao, Q. Ma, W. Xu, S. Bourrioux, P. Azais, M. Srinivasan and Z. J. Xu, *Adv. Mater.*, 2017, **29**, 1603286.

60   J. H. Kim, K. M. Jeon, J.-S. Park and Y. C. Kang, *J. Power Sources*, 2017, **359**, 363–370.

61   R. Hu, D. Chen, G. Waller, Y. Ouyang, Y. Chen, B. Zhao, B. Rainwater, C. Yang, M. Zhu and M. Liu, *Energy Environ. Sci.*, 2016, **9**, 595–603.

62   L. Sun, H. Si, Y. Zhang, Y. Shi, K. Wang, J. Liu and Y. Zhang, *J. Power Sources*, 2019, **415**, 126–135.

63   Y. Zhao, L. P. Wang, S. Xi, Y. Du, Q. Yao, L. Guan and Z. J. Xu, *J. Mater. Chem. A*, 2017, **5**, 25609–25617.

64   L. Wang, D. Wang, Z. Dong, F. Zhang and J. Jin, *Nano Lett.*, 2013, **13**, 1711–1716.

Chapter 7

A metal-free on-chip battery-supercapacitor hybrid system using laser-irradiated graphene decorated with MnO_2 nanoflower as a cathode material and polypyrrole as an anode material

Abstract: Battery-supercapacitor hybrid (BSH) devices generally provide both high energy and power density, but usually suffer from the serious electrochemical kinetics mismatch of cathodes and anodes mainly due to complex faradaic reactions of the unmatched battery-type electrodes used for charge storage, which inevitably degrade the rate capability and power density. In this work, we have grown MnO_2 nanoflowers and PPy nanoparticles uniformly on laser-irradiated graphene (LIG) network. This work also demonstrates a high-performing rechargeable $Zn-MnO_2$ battery system based on zinc anode, $LIG@MnO_2$ cathode in a mild acidic aqueous electrolyte and delivers a high storage capacity with extreme stability. Finally, a BSH system was designed utilising $LIG@PPy$ as a supercapacitive electrode and $LIG@MnO_2$ as a battery electrode in a mild electrolyte system of 1M $ZnSO_4$ + 0.2 M $MnSO_4$. The full cell of BSH system exhibited enhanced energy density, and promising Zn-ion storage capability that can bridge the energy density gap between the conventional zinc-ion batteries and supercapacitors. As result, the designed on-chip BSH cell exhibits high capacity (2.4 mAh cm^{-2}) and a cell voltage of 1.9 V. Furthermore, the assembled $LIG@MnO_2//LIG@PPy$ BSH system delivers a total energy density of 5.8 mWh cm^{-2}, among the highest value achieved in aqueous battery technologies

7.1 Introduction

The widespread endorsement of carbon-free energy resources for the production of electricity and to make self-reliant transportation sectors such as airlines, railways, logistic firms, trucking etc., development of new technology and emerging energy storage materials must be explored.[1,2] Electrochemical energy storage (EES) systems like batteries and supercapacitors (SCs) with an immense combination of high power and energy density, ultralong cycling stability, cheap and secure systems are trading exceedingly in the high energy electric vehicles market.[3–5] However, batteries do suffer from poor power delivery response and SCs bear lower energy densities.[6] Hence, integrating the superior properties of batteries and SCs into a battery-supercapacitor hybrid (BSH) system possesses the target values of energy density and remarkable power density simultaneously.[7] The positively charged cathode material i.e., battery-type electrode materials follow the strong faradaic reaction to store the charges, whereas capacitive anode materials undergo three charge storage mechanisms: electric double layer capacitance (EDLC) at the electrode surface, surface-controlled redox pseudocapacitance and diffusion-controlled intercalation pseudocapacitance.[8,9] The complex faradaic reaction involved at battery-type electrode may imbalance of the electrochemical charge storage kinetics between the electrodes, which in response will definitely diminish the rate capability and power delivery. Therefore, looking into the horizon of innumerable applications of electronic devices, it is indeed to look after the particular choice for a cathode (battery-type) and anode (supercapacitor-type) material, which can result a compensated electrochemical kinetics in BSH system.

Till now, numerous approaches have been followed to develop low-cost cathodes with unique morphologies and superior electrochemical properties for high performance BSH devices.[10,11] Transition metal oxides (TMOs) like manganese dioxide (MnO_2) have drawn considerable attention as one of the promising cathode material for rechargeable Zn-ion battery owing to its ultrahigh theoretical energy density i.e., ~308 Wh kg^{-1}, elemental abundance, and environmental friendliness in mild electrolytic conditions.[12] In recent studies, the mild electrolytes have been chosen to improve the rechargeability of Zn-MnO_2 battery system. However, the low conductivity of MnO_2 put a constraint over battery design to touch its theoretical energy density.[13] The typical charge-discharge mechanism involves the changes in the chemical state of Mn between +3 to +4 and the

dissolution of MnO_2, which in turn hampers the cycling stability. The stability of MnO_2 cathode material should not be affected in order to make a device commercially viable.

To resolve the aforementioned problem of low electrical conductivity of MnO_2 and the dissolution of MnO_2 carbonaceous material such as graphene is widely used as a conducting supporting material to which MnO_2 nanostructures are attached, thereby improving the stability of the material and provides ultra-high energy density.[14] To make a flexible device, a self-supported with extreme electrical conductivity graphene sheet is highly demanding. On the basis of recent studies, graphene film prepared through single step laser processing technique directly from graphene oxide (GO) exhibits extraordinary properties such as unique morphology and electrical response[15–17] But the resulting laser-irradiated graphene (LIG) film gain poor mechanical strength and also the greater chances for the restacking of graphene sheets upon laser irradiation. To avoid such restacking of graphene layers and in order to improve the mechanical robustness of the film, GO is mixed with gel polymer like poly(vinyl alcohol) (PVA) under optimized GO to PVA concentration and laser irradiated to get a robust graphene film.

Herein, we present a three-dimensional (3D) laser-irradiated graphene (LIG) decorated with flower-like morphology of MnO_2, was used as a battery-type cathode material in rechargeable Zn-MnO_2 system as well as in BSH system. A LIG-Polypyrrole (PPy) composite structure will act as a supercapacitive anode material in BSH system. Such integrated architecture of LIG@MnO_2 provides large electrode to electrolyte interfaces, a mutual combination of intercalation and interfacial Zn^{2+} storage, shorter path length for the diffusion of Zn^{2+} and electrons and *vice versa*, which in results gives highly reversible conversion reactions in Zn-MnO_2 system and in the BSH system. Finally, a solid state on-chip BSH system was made which delivers a high reversible capacity of 2.4 mAh cm^{-2}exhibited, enhanced energy density of 5.8 mWh cm^{-2}, and promising Zn ion storage capability that can bridge the energy density gap between the conventional zinc ion batteries and supercapacitors.

7.2 Experimental section

7.2.1 Fabrication of laser-irradiated graphene structure

A suspension of graphene oxide (GO) was prepared by modified Hummer's method as reported by our group previously.[18] GO was taken as a starting material and mixed with PVA in different concentration ratios (GO:PVA = 5:1, 4:1, 3:1, 2:1, 1:0) at 90 °C under vigorous stirring conditions for 1 h. A glass slide was cleaned with isopropyl alcohol

solution followed DI water and then dried to remove the dust particles on it before use. Then, mixture of GO and PVA was uniformly dropcasted on the glass slide within a fixed dimension of (1×2) cm^2 and keep the slides for drying at 70 °C in oven for 2 hours (Fig. 7.1a).

7.2.2 Preparation of LIG and patterning into the device configuration

The dried films were directly subjected to laser-irradiation process by CO$_2$ laser of wavelength 10.6 μm, maximum power of 60 W, maximum acceleration speed of 2.8 ms^{-1} and a focal length of 2 inches. The optimized laser source parameters for irradiation are: 19 W power (30% of maximum power), 0.98 m s^{-1} (35% of maximum acceleration speed), a frequency of 1000 Hz in a single pass. All the optimizations were carried out in order to achieve the highest electrical conductivity via maintaining the mechanical robustness of the film. The LIG sheet having GO:PVA ratio of 5:1 shows very less sheet resistance and good flexibility under optimized parameters of laser-irradiation. The near infrared flex laser of wavelength 1.06 μm was used for patterning the LIG sheet into a linear shape geometry. The LIG sheet was patterned into two linear electrodes with same dimensions (1.2 mm × 5 mm) and separated by a spacing distance of 0.3 mm.

7.2.3 Electrochemical deposition of MnO$_2$ on LIG

Electrochemical deposition of MnO$_2$ on resulting one side LIG electrode was carried out under a constant current density of 7 mA cm^{-2} in a three-electrode electrochemical cell. LIG film on glass slide as a working electrode, graphite rod as a counter electrode and Ag/AgCl as reference electrode was utilized in 3-electrode set-up configurations. An aqueous solution of 0.02 M manganese (II) sulfate monohydrate (MnSO$_4$.H$_2$O) and 0.1 M sodium sulfate (Na$_2$SO$_4$) was taken as precursor solution for the electrochemical deposition of MnO$_2$ (Fig. 7.1b). The deposition was conducted in an electrochemical cell for different time spans (15, 30, 60, and 90 minutes). The deposition time was optimized as per the best electrochemical response having sufficient mass loading. The final sample (LIG@MnO$_2$) was cleaned with millipore water several times and can directly use as cathode material in BSH system. An another LIG@MnO$_2$ (1×1.5) cm^2 was prepared to assemble Zn-MnO$_2$ rechargeable battery system in mild electrolyte conditions.

7.2.4 Electrochemical deposition of PPy on LIG

Firstly, the distillation of pyrrole was carried out before use for the electrodeposition purpose. A constant potential of 0.8 V was applied in order to deposit polypyrrole (PPy) on the LIG electrode by oxidative co-polymerization method in an aqueous solution of

0.1 M pyrrole in 0.4 M HCl (Fig. 7.1). The as deposited LIG@PPy was washed with Millipore water many times to remove the acidic contents from the surface and used as anode material in BSH system.

7.2.5 Fabrication of solid state on-chip battery-supercapacitor system
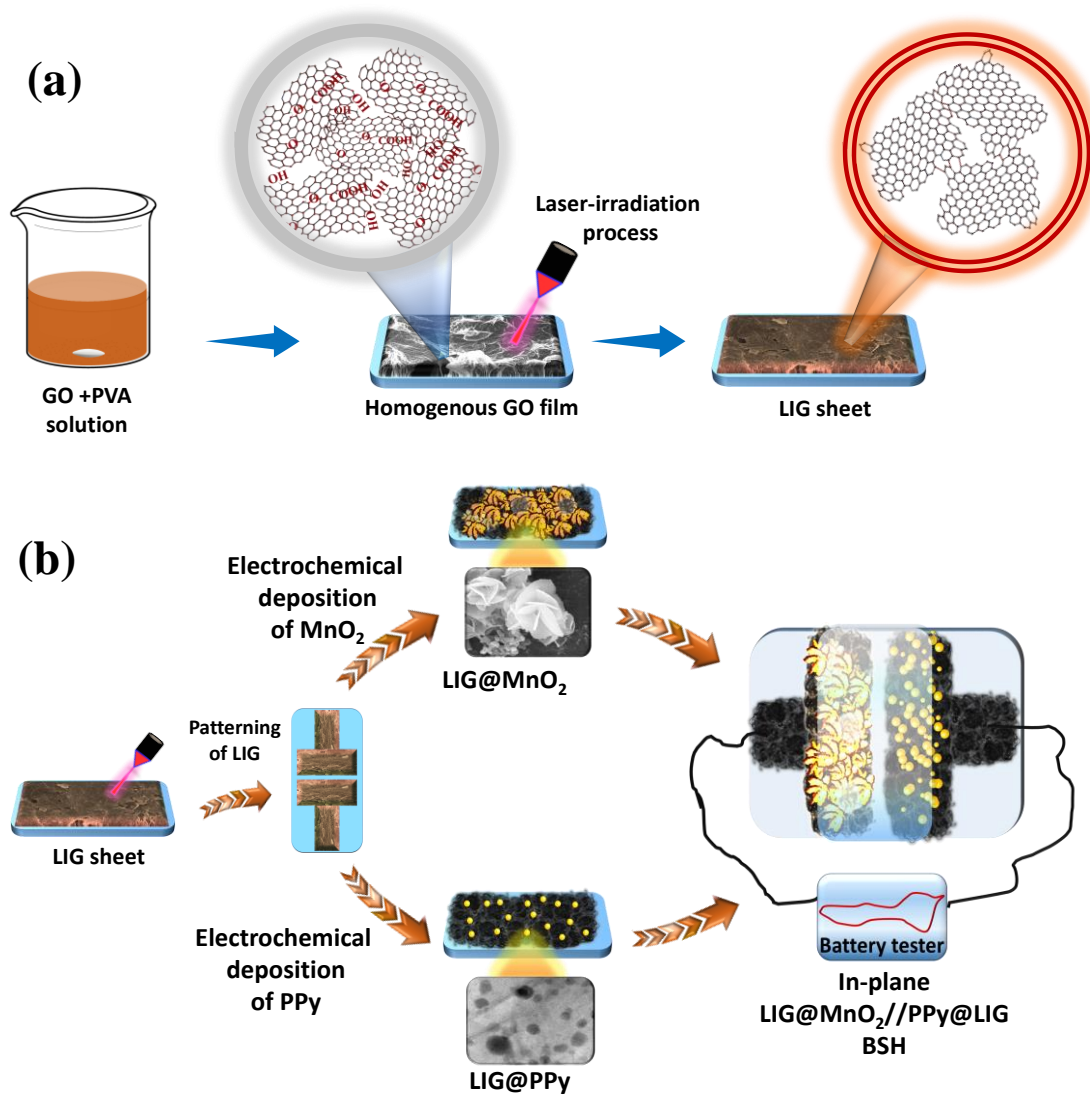
Figure 7.1. *(a) A schematic representation for the synthesis process from GO to LIG, and (b) towards electrochemical deposition process for the deposition of MnO_2 and PPy on LIG sheet.*

The two electrodes LIG@MnO_2 and LIG@PPy on a glass slide were assembled together with a spacing distance of 0.3 mm as a cathode and an anode material in BSH system, respectively. The electrodes were coated with a gel electrolyte of PVA mixed with 1M $ZnSO_4.H_2O$ and 0.2 M $MnSO_4.H_2O$ (the optimized electrolytic concentrations) at a temperature of 90 °C and keep it for drying for overnight in desiccator (Fig. 7.1b). The finally fabricated on-chip BSH device was tested under electrochemical evaluations in a battery tester system.

7.2.6 Electrochemical measurements

The electrochemical performances of the as synthesized cathode or anode material were tested primarily in a three-electrode system using LIG@MnO2 or LIG@PPy as a
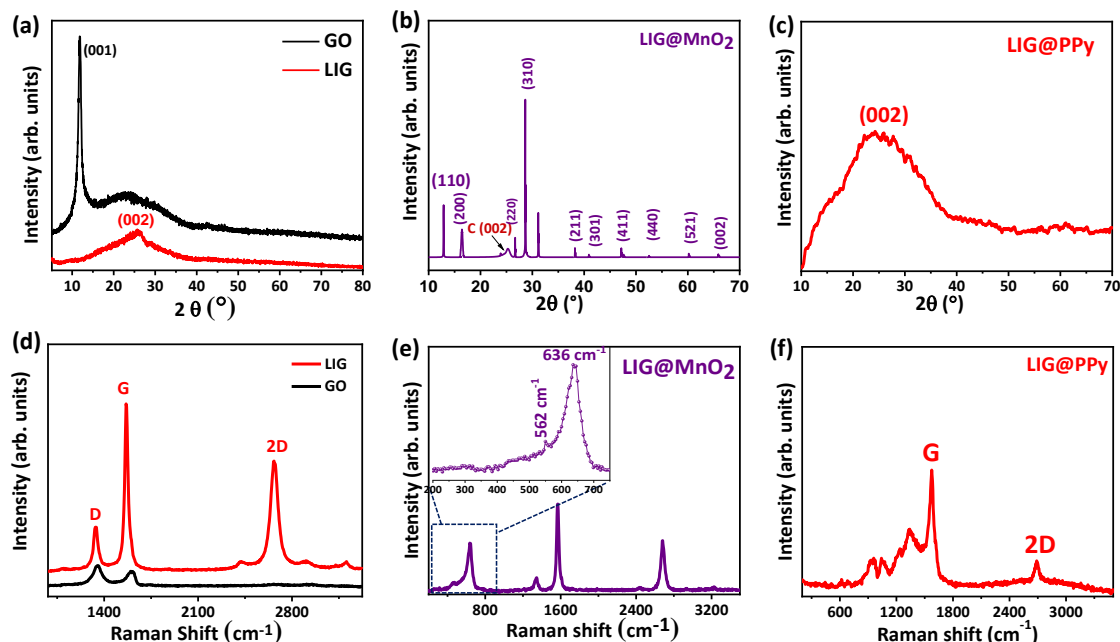
Figure 7.2. *(a-c) X-Ray diffraction pattern of GO, LIG, LIG@MnO₂ and LIG@PPy, (d-f) Raman spectra of GO, LIG, LIG@MnO₂ (inset is the magnified version in the Raman shift range 200 cm⁻¹ to 780 cm⁻¹) and LIG@PPy, respectively.*

working electrode, Ag/AgCl as the reference electrode and platinum wire as the counter electrode in 1 M KOH solution under ambient conditions. Then, a BSH device performance was evaluated in a two-electrode configuration where LIG@MnO₂ acts as positive electrode and LIG@PPy as negative electrode. To check the electrochemical performance, cyclic voltammetry (CV) at different scan rates, Galvanostatic charge-discharge (GCD) profile was taken at various current densities. For the analysis of stability and durability of the device, GCD profile was taken at a very low current density. The electrochemical impedance spectroscopy (EIS) was conducted at a potential of 1 V in the frequency range of 10^5-10^{-2} Hz in order to check the sheet resistance (R_s), charge-transfer resistance (R_{ct}) in the device.

7.3 Results and discussion

7.3.1 Phase, microstructure and chemical state evaluation of the samples (LIG@MnO₂ and LIG@PPy)

In order to characterize the structure of the materials, X-Ray diffraction study was carried out on GO, LIG, LIG@MnO₂ and LIG@PPy samples. The XRD spectrum of GO (Fig.

7.2a) shows a sharp diffraction peak (001 plane) positioned at 11.2˚ with a d-spacing of 0.398 nm, whereas LIG depicts a broad diffraction peak (002 plane) at 2θ = 26˚ (d-spacing value is 0.19 nm) that can be attributed to the graphitic structure. The laser irradiation process enhances the crystallinity in the graphene structure as can be seen in the XRD spectrum of LIG. The XRD patterns of the LIG@MnO$_2$ is shown in Fig. 6.2b. A number of diffraction peaks appeared at 2θ = 12.7°, 18.1°, 26.9°, 28.7°, 29.2°, 38.5°, 39.1°, 41.9°, 42.1°, 48.3°, 53.2°,60.3° and 65.9° matched well with the diffraction peaks of (110), (200), (220), (310), (211), (301), (411), (440), (521) and (002) crystal planes of crystalline α-MnO$_2$ standard data (JCPDS card PDF file no. 44-0141)[19,20] A broad peak is also appeared at 2θ = 26.1° which corresponds to the graphitic carbon plane (002).[21] No other peak related to any impurity or any other phase was observed which means the resulting product have single α-MnO$_2$ phase only. Figure 7.2c comprises X-Ray
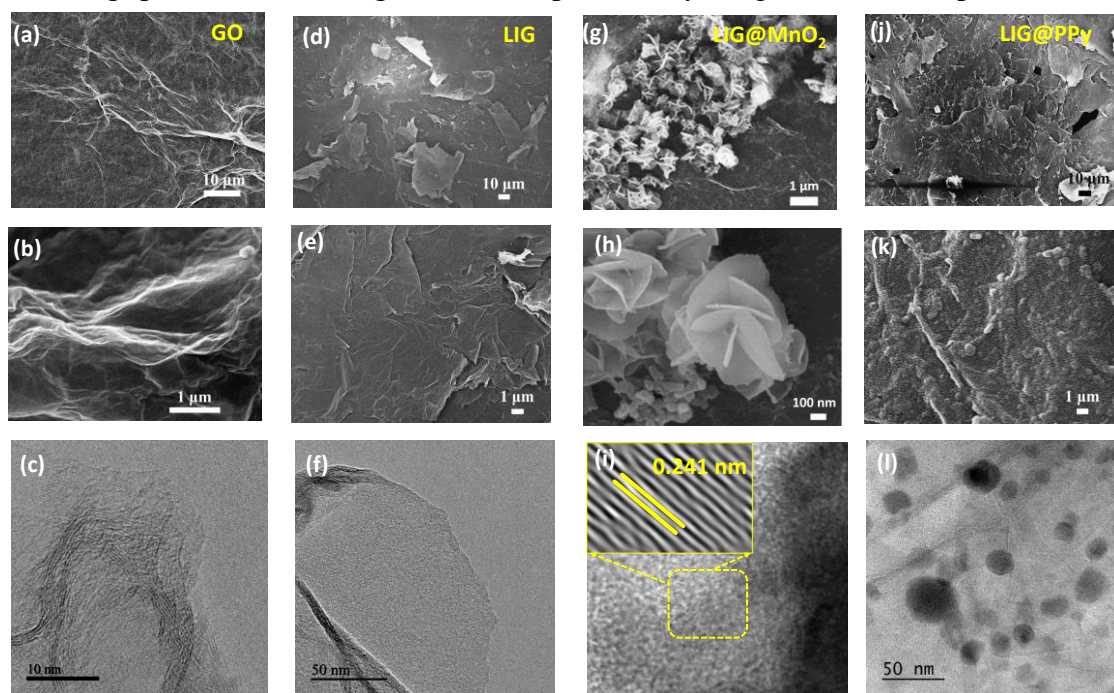
Figure 7.3. *Field emission scanning electron microscopic images (a-b) GO, (d-e) LIG, (g-h) LIG@MnO$_2$, (j-k) LIG@PPy at magnifications of 10 μm, 1μm and 100 nm, respectively. Transmisson electron microscopic (TEM) images of (c)GO, (f) LIG, (i)LIG@MnO$_2$, (l) LIG@PPy, respectively.*

diffraction pattern for LIG@PPy material, which shows a broad diffraction peak at 2θ = 25.8˚ indicating the amorphous nature of the LIG-PPy composite as shown in Fig. 7.2 c. To attain more information about the structure changes before and after laser irradiated reduction, Raman characterization was performed on GO and LIG samples (Fig. 7.2d). Raman spectra of GO demonstrated the vibrational D and G-bands at 1350 and 1582 cm^{-1}, respectively. The D/G band intensity ratio (I$_D$/I$_G$) expresses the atomic ratio of sp^3 to sp^2 hybridized carbons, which is a measure of the extent of disordered graphite. The I$_D$/I$_G$

ratio is 1.04 in cased on GO, which means the corresponding material comprises many oxygen functionalities like -COOH, -OH group and -C=O etc.[22,23] Whereas, a very small value of I_D/I_G ratio (0.062) is observed in case of LIG (Fig.7.2d) that represents the reduction of oxygen functionalities among the graphene sheets and a sharp 2D appears at position 2693 cm^{-1}. The Raman spectra of the LIG@MnO$_2$ materials show peaks at 636 and 562 cm^{-1} (shown in inset of Fig. 7.2e) together with the D-, G-, 2D- bands of graphitic LIG (Fig. 7.2e). The predominant peak at 636 cm^{-1} corresponding to stretching vibration of Mn–O and a very less intense peak at 562 cm^{-1} corresponds to symmetric
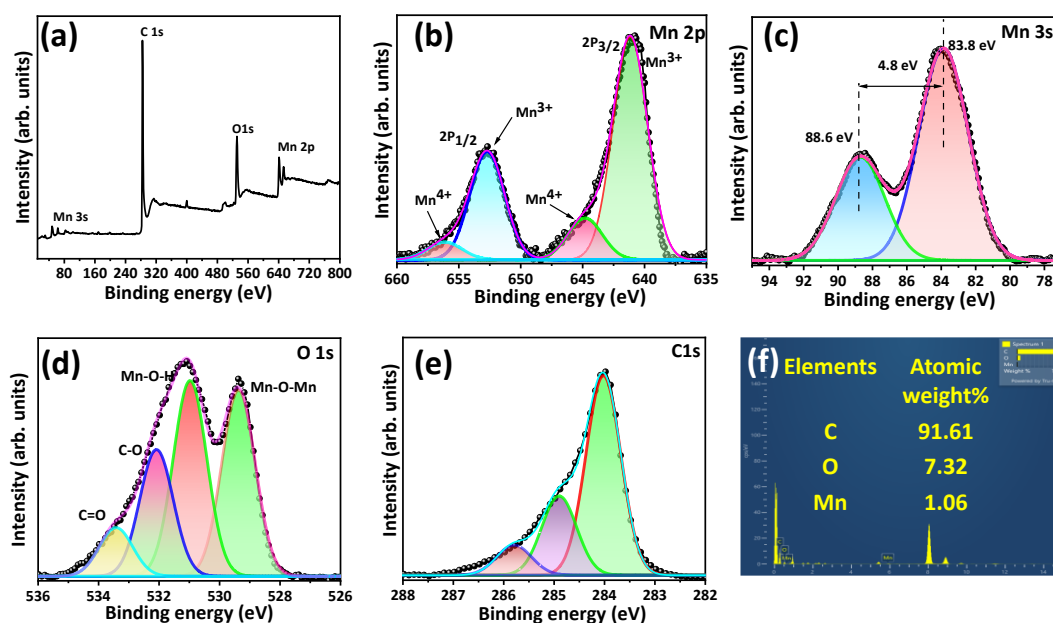
Figure 7.4. *X-Ray photoelectron spectra of LIG@MnO$_2$ sample, (a) full XPS spectra, (b and c) Deconvoluted Mn 2p and Mn 3s spectra, (d) Deconvoluted O1s and (e) C1s spectra, respectively, (f) Elemental composition detection in LIG@MnO$_2$ sample, inset gives a table showing atomic weight percent of C, O and Mn, respectively.*

stretching vibration of the basal MnO$_6$ octahedral group in MnO$_2$.[24] It is satisfying to note that the Raman spectrum of LIG-PPy hybrid material depicts many weak intensity peaks corresponding to different vibrations modes in addition to D and G bands indicates the functionalization of PPy to the LIG backbone.[25] Moreover, the shifting in the G-band (1578 cm^{-1}) of LIG-PPy composites towards lower frequency region is a clear indication for the electron-donating effect of benzene substituents, which is similar effect like molecular charge transfer mechanism with donor and acceptor molecules (Fig. 7.2f).[26] The broad D-band region includes three characteristics peaks at 1330, 1368 and 1420 cm^{-1}, which corresponds to the antisymmetrical in-ring C-N stretching.[27] Raman spectra of LIG-PPy also includes some more prominent bands at 617 cm^{-1} (ring torsion), 685 cm$^-$

[1] (C-H wagging), 952 cm^{-1} (ring deformation associated with the dication), 1051 cm^{-1} (C–H in plane deformation), and 1253 cm^{-1} (antisymmetrical C-H in-plane bending), which are characteristic Raman-active modes of PPy.[28]

The morphology of the corresponding samples was investigated through field emission scanning electron microscopic (FESEM) and transmission electron microscopic (TEM) technique as shown in Fig. 7.3a-l. Graphene oxide have wrinkled flakes throughout the surface as shown in Fig. 7.3a-b. The TEM image for GO is represented in Fig. 7.3c which clearly shows the crumbed graphene sheets and the number of graphene layers can be calculated from the fringe pattern shown at the edges. The wrinkled edges of graphene
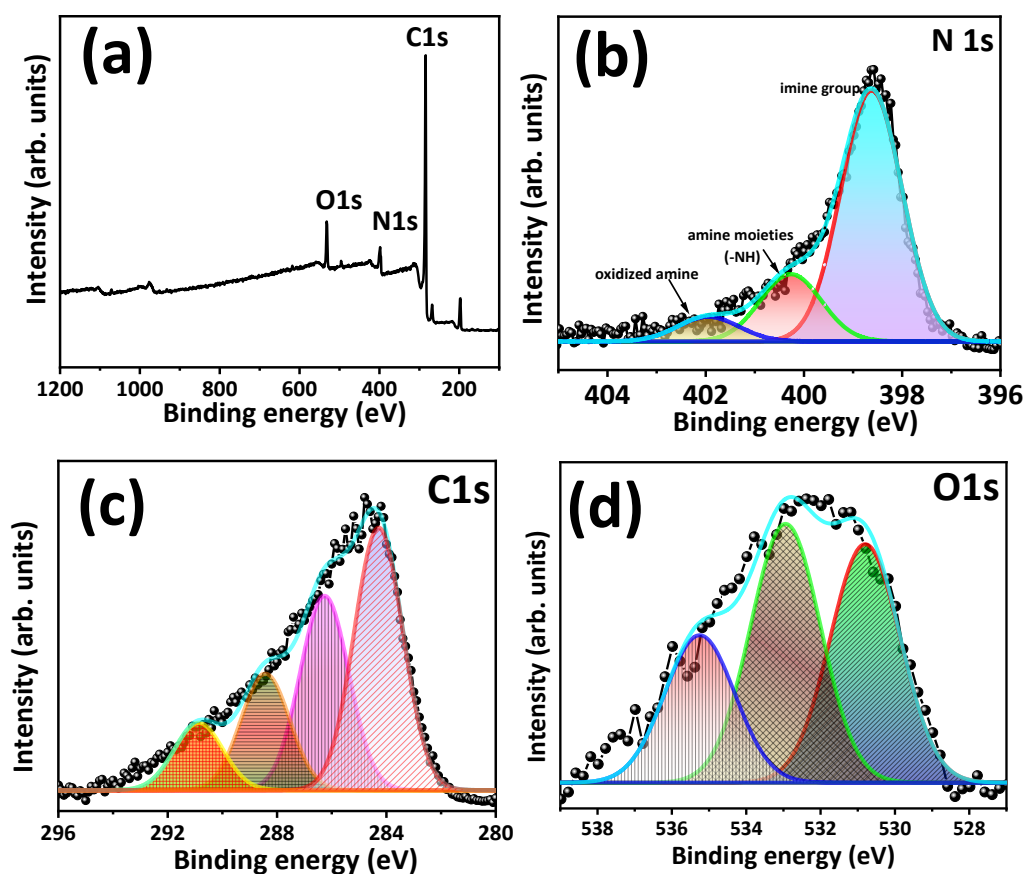
Figure 7.5. X-Ray photoelectron spectra of LIG@PPy sample, (a) full XPS survey spectra, (b) Deconvoluted N 1s, (c) C 1s, (d) O 1s XPS spectra, respectively.

sheets in GO get fused after laser-irradiation and get flattened morphology of the LIG surface (Fig. 7.3d-e). A single graphene flake is shown in the TEM image (Fig. 7.3f). The electrodeposition of MnO_2 on LIG surface shows flower-like hierarchical porous morphology and the flower spheres are stacked by thin nanosheets as it can be seen from FESEM image in Fig. 7.3g-h. These nanosheets interconnected to make a porous surface

morphology, which is beneficial for the easy ionic dynamics during electrochemical measurements.[29] The HRTEM image and FFT image (inset) in Fig. 7.3i shows the fringe pattern with a lattice spacing of 0.241 nm corresponding to lattice plane of MnO_2 phase. Figure 7.3j-k shows FESEM images of as-synthesized LIG@PPy material, where well-defined graphene sheets functionalized with spherical shaped PPy nanoparticles were observed. The distribution of PPy nanoparticles on graphene sheet network is clearly visible in TEM image of LIG@PPy (Fig. 7.3l).

The elemental composition and chemical state of LIG@MnO2 and LIG@PPy was investigated by X-Ray photoelectron spectroscopy in Fig. 7.4 and Fig. 7.5, respectively. A full survey XPS spectra of LIG@MnO_2 is shown in Fig. 7.4a which indicates the
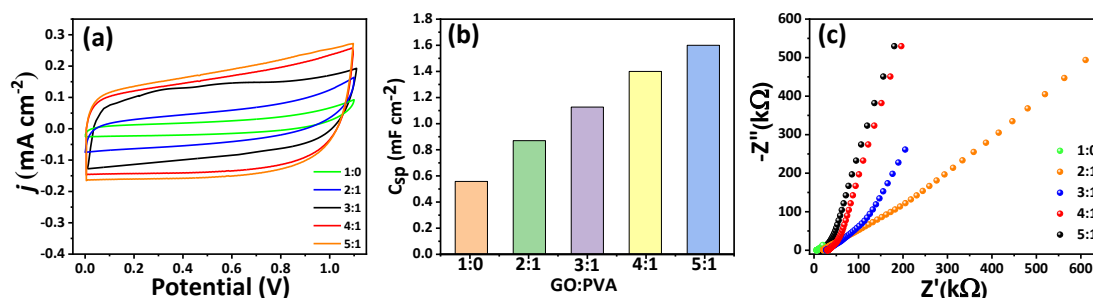
***Figure 7.6.** (a) Cyclic voltammetry characterization to optimize the concentration ratio of GO and PVA, (b)A bar diagram showing the specific capacitance (mF cm^{-2}) at different GO to PVA ratios, (c) corresponding electrochemical impedance spectra.*

presence of elements carbon (C), oxygen (O) and manganese (Mn). The high-resolution deconvoluted XPS spectra of Mn 2p is represented in Fig. 7.4b and exhibits four peaks located at 641.60, 644.1, 652.80, and 656.20 eV were obtained by peak-differentiating technique. These peaks were assigned to the Mn^{3+} ($2p_{3/2}$), Mn^{4+} ($2p_{3/2}$), Mn^{3+} ($2p_{1/2}$), and Mn^{4+} ($2p_{1/2}$) species, respectively.[30] The mixed valent manganese system (Mn^{4+}/ Mn^{3+}) indicate the existence of oxygen vacancies on the surface of α-MnO_2.[31] Moreover, it has been observed the higher content of Mn^{3+} as confirmed from the peak areas of Mn^{3+} and Mn^{4+}. A higher content of Mn^{3+} in MnO_2 can lead to a better electrochemical performance due to the single electron occupation in the σ*-orbital (e_g) of Mn^{3+}.[32] Moreover, the deconvoluted Mn 3s spectrum comprises two peaks at 83.8 and 88.6 eV with a separation of 4.8 eV (Fig. 7.4c), which further proved that Mn existed in the form of MnO_2. The O 1s spectrum (Fig. 6.4d) of LIG@MnO_2 is quite broad and contains at least four different contributions. The peak located at 529.3 eV corresponds to Metal-O bond (Mn-O-Mn). The other contributions at 530.8 eV, 532.0 eV and 533.4 eV correspond to Mn-OH bond, organic C-O and organic C=O bond, respectively. Figure

7.4e represents the binding energies of 283.35 eV, 284.6 eV and 285.8 eV in C 1s deconvoluted XPS spectrum related to C–C, C–O–C and O–C=O bonding in LIG@MnO$_2$ material, respectively. The elements C, O and Mn are presented in LIG@MnO2 in atomic weight percent ratio of 91.6: 7.3: 1.06, respectively (Fig. 6.4f). High-resolution XPS measurements were performed in order to comprehend the possible chemical bonding in LIG@PPy composite as shown in Fig. 7.5. A complete XPS survey over LIG-PPy composites clearly shown in Fig. 7.5a, which indicates a characteristic signal of N 1s is found at 399.7 eV in addition to signals of C 1s and O 1s. The distribution
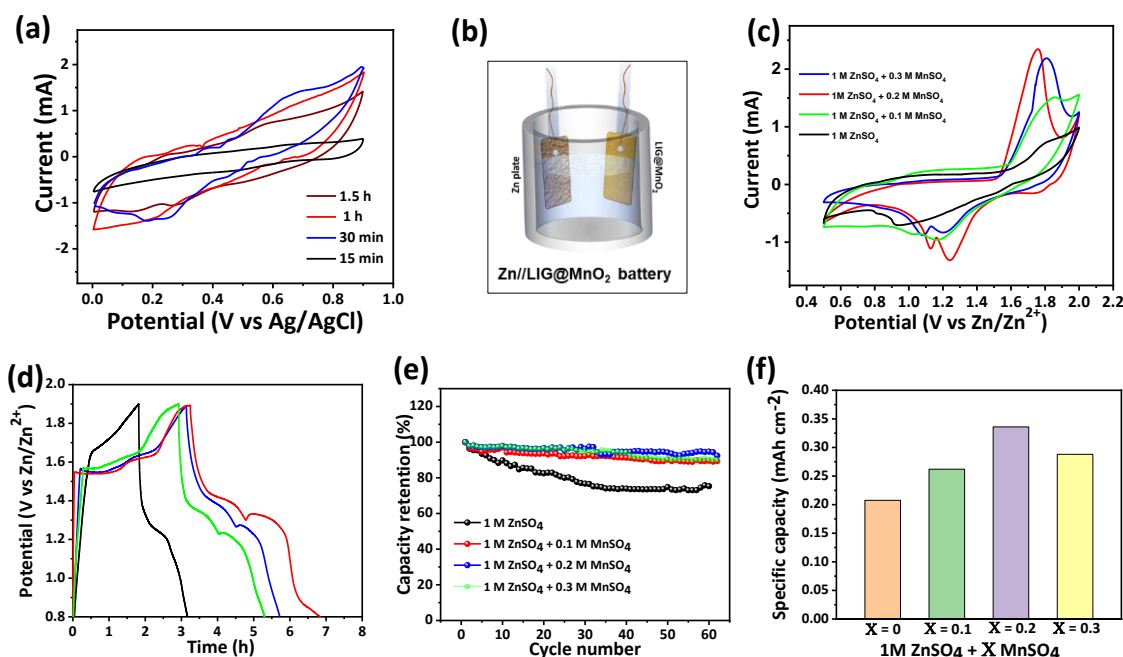
Figure 7.7. (a) Mass loading optimization of MnO$_2$ on LIG via cyclic voltammetry close area evaluation, (b)Schematic of two electrode system Zn//LIG@MnO$_2$ battery system, (c) CV curves for Zn//LIG@MnO$_2$ system at different electrolyte concentrations at a scan rate of 5 mV s^{-1}, (d) corresponding galvanostatic charge discharge profile, (e) Stability testing via continuous charge/discharge cycling at a low current density of 0.1 mA cm^{-2}, (f)A bar diagram showing the specific capacitance (mAh cm^{-2}) of Zn//LIG@MnO$_2$ system at different electrolyte concentrations.

of nitrogen species in LIG-PPy material was studied via deconvolution of the N1s high-resolution core level XPS spectra as shown in Fig. 7.5b. The nitrogen XPS spectra are deconvoluted into three Gaussian peaks with the binding energies 398.7 eV, 401.3 eV and 402.5 eV, respectively. The peaks at 398.7 eV correspond to the neutral and the imine-like structure (-N=) can be used to estimate the defect density within the PPy, because the structure is believed to interrupt the electron hopping on the polymer chain. The peak positioned at binding energy of 401.3 eV corresponds to amine (-NH-) moieties, while peak at 402.5 eV can be ascribed to the positively charged nitrogen

groups of oxidized amine and protonated imine, respectively. The C1s XPS spectra (Fig. 7.5c) are deconvoluted into four components centered at 284.2 eV, 285.9 eV, 288.6 eV, and 290.7, respectively. The main peak positioned at 284.2 eV is attributed to the C–C/C–H bond, whereas the peaks at 285.9 eV and 288.6 eV are dedicated to C–N group and O–C=O groups due to oxalate groups, which is incorporated in to the film as dopants.[33] The peak at 290.7 eV originate due the presence of C–C groups (named as "satellite peak), respectively. The presence of the C–N peak in C 1s spectra confirms the presence of pyrrole moieties in the LIG-PPy composite sample. The deconvoluted O1s XPS spectra is shown in Fig. 7.5d exhibits peaks at 530.8 eV, 532.2 eV and 535.4 eV assigned to –C–O, C–O–H and O–C=O moieties, respectively.

7.3.2 Electrochemical characterizations

7.3.2.1 Electrochemical measurements of LIG films made through different GO to PVA concentration ratio

To analyze the impact of PVA in GO solution, the five LIG films prepared via different GO to PVA ratio are characterized through electrochemical techniques. The LIG films prepared through purely GO solution is completely discontinuous and full of cracks in the layers, which results decrease in the electrical conductivity of the film. The diminish electrical response of LIG film with only GO depicts very small area under cyclic voltammetry curve and very less specific capacitance of 0.58 mF cm^{-2} (Fig. 7.5 a and b). After adding PVA in GO at a ratio of 2:1, although the electrical conductivity is hampered due to insulated polymer binder but after laser-irradiation process, the resulting LIG film exhibits interconnected graphene sheets in more compact form and is responsible for improved electrochemical response. An optimum concentration of PVA in GO i.e.,$(\frac{1}{5}:1)$ gives the best specific capacitance value of 1.6 mF cm^{-2} and a very less sheet resistance of 10 Ω in EIS spectra as can be seen in Fig. 7.5c.

7.3.2.2 Electrochemical performance of battery-electrode i.e., LIG@MnO$_2$

In order to optimize the loading of MnO$_2$ on LIG, cyclic voltammetry was performed in 1M KOH after MnO$_2$ deposition at different time scales (15 min, 30 min, 1 h and 1.5 h) as shown in Fig. 7.7a and found 30 minute of MnO$_2$ deposition gives the best electrochemical storage capacity. Then, the battery kind behaviour of LIG@MnO$_2$ was tested *via* assembling it with Zn plate in a mild electrolyte medium (1M ZnSO$_4$) and forming a Zn//LIG@MnO$_2$ cell (Fig. 7.7b). As shown in Fig. 7.7c, the cyclic voltammetry curve exhibits two reversible oxidation and reduction redox peaks

corresponding to the diffusion-dominated H^+ intercalation process and intercalation pseudocapacitance process of Zn^{2+}, respectively.[34] The addition of $MnSO_4$ in the mild electrolyte (1M $ZnSO_4$) leads to an increase in the charge storage capacity and stabilize the electrode under two-electron reaction process. Figure 7.7c and d shows CV and GCD profiles of Zn//LIG@MnO_2 battery in mild electrolyte, with and without $MnSO_4$, revealing a similar redox behaviour that indicates the $MnSO_4$ additive did not affect the redox reactions in the LIG@MnO_2 electrodes. The two pairs of redox peaks are consistent with the two plateaux in the charge/discharge curves shown in Fig. 7.7d.
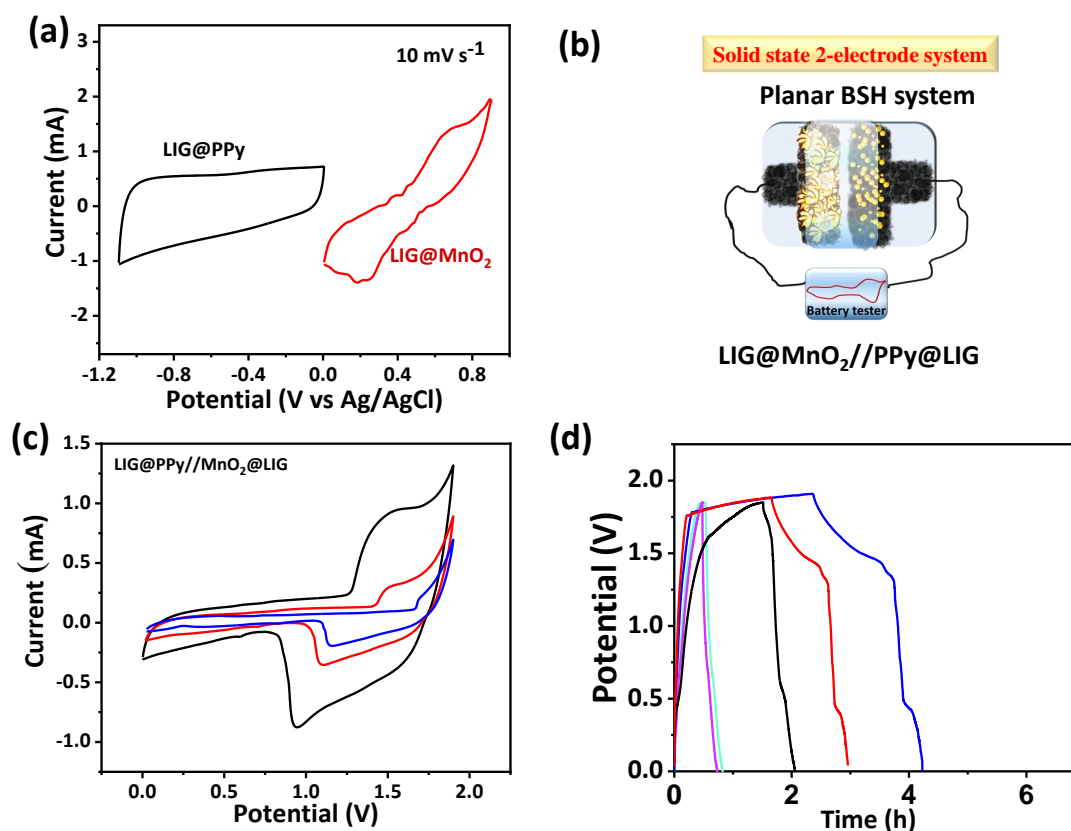
Figure 7.8. (**a**) *CV curves for LIG@PPy and LIG@MnO₂ in 1M KOH solution representing the capacitive and redox active processes in the corresponding electrode materials, respectively, (b) Assembled all solid-state metal-free on-chip LIG@PPy//LIG@MnO₂ BSH system, (c) CV curves at different scan rates (0.5 mV s⁻¹ to 5 mV s⁻¹), (d) GCD profile at different current densities (10 μA to 70 μA) of the BSH system.*

However, with the $MnSO_4$ additive in the electrolyte, the cycling performance of the LIG@MnO_2 electrode is significantly improved (Fig. 7.7e). It is highly likely that the addition of 0.2 M Mn^{2+} will provide an appropriate equilibrium between Mn^{2+} dissolution (from the electrode to the electrolyte) and the re-oxidation of Mn^{2+} in the electrolyte, leading to high stability of the electrode.[35] The combination of a highly reversible Zn anode and a LIG@MnO_2 cathode in a mild aqueous electrolyte (that is, 1 M $ZnSO_4$ with

0.2 M MnSO₄) presents a potentially high-capacity (Fig. 7.7f) aqueous battery chemistry with high reversibility and high cycling stability, that is both environmentally benign and safe.

To further prove the feasibility of designed LIG@MnO$_2$ nanoflowers for practical applications, a full cell BSH device was assembled with LIG@MnO$_2$ as a cathode material (positive electrode) and LIG@PPy as an anode (negative electrode) in 1 M ZnSO$_4$ + 0.2 M MnSO$_4$ electrolyte and was subjected to electrochemical performance testing. The CV curves in Fig. 7.8a depict the potential range of the LIG@MnO$_2$ electrode (0-0.9 V) and LIG@PPy electrode (-1.1-0 V), indicates the wide potential window of 0-2.5 V can be achieved in the resulting BSH device. Figure 7.8a presents the rectangular and symmetric CV curves of LIG@PPy indicating the double layer capacitance characteristics. Figure 7.8b shows the schematic representation of planar full cell (LIG@MnO$_2$//LIG@PPy). The cyclic voltammetry curves of prepared BSH system were collected at various scan rates in which the potential range of 0-1.9 V was selected for further electrochemical characterizations (Fig. 7.8c). The CV response is a combination of capacitive response originate from LIG@PPy and redox reactions involved at LIG@MnO$_2$ electrode. The GCD profile was collected at different current densities range 0.1 mA cm^{-2} to 2 mA cm^{-2} which shows a voltage plateau at 1.89 V. The calculated capacity for the full cell BSH system is to be 2.4 mAh cm^{-2} and achieved a high cell voltage of 1.9 V. Based on the above calculations and corresponding experimental results, it can be deduced that the root of the excellent reaction kinetics and high capacity of the BSH system is the combination of lower energy barriers for H$^+$ diffusion and enhanced surface adsorption/intercalation of H$^+$/Zn^{2+}.

7.4 Conclusions

In conclusion, we have successfully fabricated highly conducting graphene film directly from graphene oxide as starting material and utilised as a metal-free current collector in energy storage system. The MnO$_2$ nanoflowers and PPy nanoparticles have been grown uniformly on LIG network. This work also demonstrate a high-performing rechargeable Zn-MnO$_2$ battery system based on zinc anode, LIG@MnO$_2$ cathode in a mild acidic aqueous electrolyte. Finally, a BSH system was designed utilising LIG@PPy as a supercapacitive electrode and LIG@MnO$_2$ as a battery electrode in a mild electrolyte system of 1 M ZnSO$_4$ + 0.2 M MnSO$_4$. The full cell BSH system exhibited enhanced energy density, and promising Zn ion storage capability that can bridge the energy

density gap between the conventional zinc ion batteries and supercapacitors. As result, the designed on-chip BSH cell exhibits high capacity (2.4 mAh cm^{-2}) and a cell voltage of 1.9 V. Furthermore, the assembled LIG@MnO$_2$//LIG@PPy BSH system delivers a total energy density of 5.8 mWh cm^{-2}, among the highest value achieved in aqueous battery technologies. The present BSH system holds great promise for potential applications in large scale energy storage, in view of the remarkable electrochemical performance and other advantages such as low materials cost, easy manufacturing, high safety, and environmental friendliness.

7.5 References

1   N. Armaroli and V. Balzani, *Energy Environ. Sci.*, 2011, **4**, 3193–3222.

2   A. S. Aricò, P. Bruce, B. Scrosati, J.-M. Tarascon and W. van Schalkwijk, *Nat. Mater.*, 2005, **4**, 366–377.

3   P. Simon and Y. Gogotsi, *Nat. Mater.*, 2008, **7**, 845–854.

4   P. Simon and Y. Gogotsi, *Acc. Chem. Res.*, 2013, **46**, 1094–1103.

5   S. Patrice, G. Yury and D. Bruce, *Science*, 2014, **343**, 1210–1211.

6   F. Cheng, J. Liang, Z. Tao and J. Chen, *Adv. Mater.*, 2011, **23**, 1695–1715.

7   H. Kim, M.-Y. Cho, M.-H. Kim, K.-Y. Park, H. Gwon, Y. Lee, K. C. Roh and K. Kang, *Adv. Energy Mater.*, 2013, **3**, 1500–1506.

8   E. Lim, C. Jo, H. Kim, M.-H. Kim, Y. Mun, J. Chun, Y. Ye, J. Hwang, K.-S. Ha, K. C. Roh, K. Kang, S. Yoon and J. Lee, *ACS Nano*, 2015, **9**, 7497–7505.

9   G. K. Veerasubramani, K. Krishnamoorthy and S. J. Kim, *J. Power Sources*, 2016, **306**, 378–386.

10   F. Zhang, T. Zhang, X. Yang, L. Zhang, K. Leng, Y. Huang and Y. Chen, *Energy Environ. Sci.*, 2013, **6**, 1623–1632.

11   H. Liu, K. Hu, D. Yan, R. Chen, Y. Zou, H. Liu and S. Wang, *Adv. Mater.*, 2018, **30**, 1800295.

12   H. Pan, Y. Shao, P. Yan, Y. Cheng, K. S. Han, Z. Nie, C. Wang, J. Yang, X. Li, P. Bhattacharya, K. T. Mueller and J. Liu, *Nat. Energy*, 2016, **1**, 16039.

13   M. Huang, F. Li, F. Dong, Y. X. Zhang and L. L. Zhang, *J. Mater. Chem. A*, 2015, **3**, 21380–21423.

14   B. Wu, G. Zhang, M. Yan, T. Xiong, P. He, L. He, X. Xu and L. Mai, *Small*, 2018, **14**, 1703850.

15   M. F. El-Kady, V. Strong, S. Dubin and R. B. Kaner, *Science*, 2012, **335**, 1326–

1330.

16   J. Ye, H. Tan, S. Wu, K. Ni, F. Pan, J. Liu, Z. Tao, Y. Qu, H. Ji, P. Simon and Y. Zhu, *Adv. Mater.*, 2018, **30**, e1801384.

17   N. Kamboj, T. Purkait, M. Das, S. Sarkar, K. S. Hazra and R. S. Dey, *Energy Environ. Sci.*, 2019, **12**, 2507–2517.

18   T. Purkait, G. Singh, D. Kumar, M. Singh and R. S. Dey, *Sci. Rep.*, 2018, **8**, 640.

19   A. Khan, H. Wang, Y. Liu, J. Ali, J. Ifthikar, Z. Liao, T. Wang and Z. Chen, *J. Mater. Chem. A*, , DOI:10.1039/C7TA07942G.

20   Z. Y. Leong and H. Y. Yang, *ACS Appl. Mater. Interfaces*, 2019, **11**, 13176–13184.

21   Y. Wang, Y. Wang, P. Zhang, F. Liu and S. Luo, *Small*, 2018, 14.

22   A. C. Ferrari and D. M. Basko, *Nat. Nanotechnol.*, 2013, **8**, 235–246.

23   C. Thomsen and S. Reich, *Phys. Rev. Lett.*, 2000, **85**, 5214–5217.

24   T. Gao, H. Fjellvåg and P. Norby, *Anal. Chim. Acta*, 2009, **648**, 235–239.

25   T. Purkait, G. Singh, N. Kamboj, M. Das and R. S. Dey, *J. Mater. Chem. A*, 2018, **6**, 22858–22869.

26   X. Zhang, J. Wang, J. Liu, J. Wu, H. Chen and B. Hong, *Carbon N. Y.*, 2017, **115**, 134–146.

27   Y.-C. Liu, *J. Electroanal. Chem. - J ELECTROANAL CHEM*, 2004, **571**, 255–264.

28   T. Purkait, G. Singh, N. Kamboj, M. Das and R. S. Dey, *J. Mater. Chem. A*, 2018, **6**, 22858–22869.

29   X. Zhong, Z. Lu, W. Liang, X. Guo and B. Hu, *Environ. Sci. Nano*, 2020, **7**, 3303–3317.

30   E. Pargoletti, G. Cappelletti, A. Minguzzi, S. Rondinini, M. Leoni, M. Marelli and A. Vertova, *J. Power Sources*, 2016, **325**, 116–128.

31   V. P. Santos, M. F. R. Pereira, J. J. M. Órfão and J. L. Figueiredo, *Appl. Catal. B Environ.*, 2010, **99**, 353–363.

32   Z. H. Wei, T. Zhao, X. B. Zhu and P. Tan, *J. Power Sources*, 2016, **306**, 724–732.

33   R. Rajagopalan and J. O. Iroh, *Appl. Surf. Sci.*, 2003, **218**, 58–69.

34   K. Han, F. An, F. Yan, H. Chen, Q. Wan, Y. Liu, P. Li and X. Qu, *J. Mater. Chem. A*, 2021, **9**, 15637–15647.

35   M. Chamoun, W. R. Brant, C.-W. Tai, G. Karlsson and D. Noréus, *Energy*

Storage Mater., 2018, **15**, 351–360.

Chapter 8

Conclusions and future perspectives

Abstract: In this chapter, a brief summary of the important finding of all the work in the thesis is provided. This thesis aims the exploration of various graphene and its hybrid nanostructures based active electrodes for the energy storage applications. The unique and tuneable features of graphene occupy wide latitude range to encourage the alternative energy supplier of things and therefore, a facile, economical and a scalable synthesis technique with excellent properties is very much imperative for the development of graphene and its hybrid nanostructures. This has motivated us to tune the structural features of graphene *via* exploring new synthesis strategies. These custom-made graphene nanostructures are utilised in supercapacitor to fulfil the power need and in battery system to enhance the working voltage and the capacity of the cell, which in turn gives high energy density. We are expecting that this thesis work provides a new pathway for exploring the advanced graphene-based electrode materials for a wide range of integrated, sustainable and commercial power-pack applications.

8.1 Conclusion

The present thesis work concentrates on the development of highly conducting graphene and its hybrid nanostructures with conducting polymers, metal-oxides for surface-controlled and diffusion-controlled kinetics. A detailed step-by-step improvement was attempted in the electrochemical performance of supercapacitor as well as the battery. The combination or hybrid structure of both kinds of kinetics accelerates the charge storage capacity, energy density and power output of the cell.

The first part of the thesis **(chapter 1)** describes the numerous universal challenges arise due to the current energy scenario and the need for alternative energy resources to fulfill the current demand. The basic understanding of the storage mechanism in electrochemical energy storage systems such as supercapacitors and batteries is provided. The device performance is also affected by the device's geometrical configurations such as stacked structure or planar geometry. The planar geometry is beneficial to fasten the ionic charge transport and reduce the ionic path length, which in turn increases the stability of the device. Carbonaceous material is the most pronounced material to be used as active material as well as a current collector replacing metals from the device. A complete literature survey of carbonaceous materials, pseudocapacitive materials, battery type materials and their electrochemistry in electrochemical cell and their implementation for the storage applications is very well elaborated. The motivation and perspective to approach the next-generation energy technology *i.e.,* hybrid structure of battery and supercapacitor (BSH) system is impactfully interpreted based on previous literature reports.

In **chapter 2**, a brief description of various synthesis techniques like electrochemical deposition method and hydrothermal route; the instrumentation used material characterizations such as X-ray diffraction (XRD), transmission electron microscopy (TEM), Scanning electron microscopy (SEM) etc.; the material electrochemical performance techniques like cyclic voltammetry (CV), galvanostatic charge-discharge (GCD), electrochemical impedance spectroscopy techniques, is provided.

The experimental work has been started with the exploration of a new synthesis scheme for highly conducting graphene sheets in order to replace metals from supercapacitor devices in **chapter 3.** A two-step reduction process was introduced *i.e.,* the electrochemical deposition method followed by laser-irradiation method, which helps

to grow a conductive three-dimensional (3D) graphene network which has the ability to replace metals from the energy device and exhibits high effective surface area that gives rise to the charge storage capacity. The unique structural and morphological features of fused graphene sheets are well explained with Raman and SEM analysis. The resulting laser-irradiated graphene (LIG) based metal-free microsupercapacitor (MSC) exhibits an electric double layer capacitance (EDLC) feature and offers a large working voltage window of 1.2 V, an energy density of 0.46 μWh cm^{-2}, a power density of 0.57 mW cm^{-2} and extreme stability of 1,00,000 continuous stability cycling with 100% capacitive retention and opens up a new field for the development of a metal-free microsupercapacitor. The unique structure of LIG and the interconnected highly conductive graphene sheets with fewer defects are responsible for the ion and electron transport channel with a short diffusion length. The cost-effective and environmentally friendly synthesis approach makes it a model candidate for the next generation supercapacitor electrode design. The LIG-based MSCs were organized in series with an in parallel arrangement for the demonstration of high-voltage output without sacrificing the capacitance of the module. Furthermore, the LIG-based MSC module was integrated with a solar cell to realize its advantage for the development of a hybrid storage system.

Despite being so stable MSC device, the specific capacitance and energy density of the metal-free LIG MSC were not sufficient. Therefore, to improve the charge storage capacity, the first work was extended in **chapter 4** with the addition of a conductive polymer *i.e.,* polypyrrole (PPy) in LIG *i.e* LIG-PPy *via* gaining pseudocapacitive and the EDLC features both. Moreover, an "Organic/Water-in-salt" (WIS) type electrolyte was chosen to increase the electrochemical stability window. The complete solvation structure mechanism of WIS electrolytes was studied by Raman analysis and nuclear magnetic resonance (NMR) spectra. The prepared quasi solid-state LIG-PPy based MSC was performed with an extended potential window of 2.4 V and enhanced energy density of 99.2 μWh cm^{-2} as compared to LIG-MSC. The LIG-PPy MSC module acquires a 20 V voltage window applicable for high voltage energy applications.

Batteries are the classic energy storage systems working under a diffusion-controlled process that exhibits high charge storage capacity and energy density. Lithium-ion batteries and aqueous batteries such as rechargeable Zn-ion batteries have the ability to offer a possible solution to the storage technology. Transition metal oxides (TMOs) and phosphides (TMPs) are the other class of nanomaterials in battery applications owing to their distinct abundant active sites, short diffusion pathways, low

synthesis cost, and distinct reaction mechanisms. Transition metal phosphides, particularly Nickel phosphides have meticulous characteristics like their metalloid properties, excellent electrochemical activity, high chemical stability, and reversible electrochemical kinetics. Among all existing phases of Nickel phosphides, the Ni_3P phase shows excellent electrochemical performance for their low polarization, good reversibility in an alkaline medium. Thus, in **chapter 5**, we have prepared a single-phase 3D hierarchical porous structure of Ni_3P on carbon cloth (denoted as $Ni_3P@CC^*$) through a single-step electrochemical deposition method with enhanced electrochemical performance as the state-of-the-art cathode for aqueous Ni-Zn battery. The resultant Ni_3P 3D porous network nanostructure occupying with huge active site density offers a high surface area, 3D electron transfer networks and ionic diffusion channels. These multiple featured $Ni_3P@CC^*$ electrode endows an extraordinary specific capacity of 258 mA h g^{-1} at 1 A g^{-1} and excellent rate performance. Moreover, the Ni-Zn battery system assembled with $Ni_3P@CC^*$ as cathode and $Zn@CC^*$ as an anode delivers a maximal capacity of 322 mA h g^{-1}, high energy density 661.98 W h kg^{-1}, the power density 17.5 kW kg^{-1}. Since, the stability performance of Ni-Zn battery system was not as remarkable as that of Li-ion batteries. Therefore, in **chapter 6**, a Li-ion system was designed with mix phase $SnO-SnO_2@rGO$ material as an anode and investigated the electrochemical performance in both half and full cells. The resulting LIB shows the tremendous reversible specific capacity of 2604 mAh g^{-1} and an outstanding rate capability of more than 82 % capacity retention after 150 charge-discharge cycles at 0.1 A g^{-1} which lasts till 500 cycles at 1 A g^{-1} with very good retention of the initial capacity.

In order to approach the high energy storage technology, a hybrid structure of battery and supercapacitor i.e BSH system was designed in **chapter 7**, utilising $LIG@MnO_2$ as Zn-ion battery electrode and LIG@PPy as a capacitive electrode. The BSH system shows the potential electrochemical performance involving extreme reaction kinetics between the battery and supercapacitor electrode. This versatile system gives a new avenue for the development of efficient energy storage systems for the commercial trade.

Table 8.1 *Overall summary of all the projects carried out under thesis work.*

Synthesized electrode material	Highlights of the experiment	Result obtained	Opportunities for electrochemical enhancement
Work 1: Laser-irradiated graphene film	Highly conducting graphene; interconnected fused graphene network; metal-free microsupercapacitor	Cell voltage - 1.2 V; Stability; 10,000 continuous GCD cycling (~100% retention)	The development of battery is highly needed for the enhancement in specific capacitance and energy density values
Work 2: LIG-PPy	Incorporation of pseudocapacitance features; use of "organic/water-in-sat" electrolytic medium	Cell voltage – 2.4 V; Module voltage – 20 V C_{sp}- 122 mF cm^{-2}	Further increase in energy density can be done via making a hybrid structure of battery and supercapacitor
Work 3: Ni$_3$P@CC* as cathode Zn@CC* as anode	Development of rechargeable Ni-Zn battery system in alkaline medium	Cell voltage- 1.85; Csp- 322 mAh g^{-1}, ~100% stability after continuous GCD cycling	Still capacity needs to be improved with Li-ion battery system
Work 4: Mix phase SnO-SnO$_2$@rGO as anode	Importance of mix phase system on achieving high specific capacity and excellent rate capability; LiOH formulation to add up an extra capacity to the system	Cell voltage- 3V; C_{sp} – 2604 mAh g^{-1}; extraordinary stability and extreme full cell performance	To achieve a balance between energy and power density; a hybrid structure of battery and supercapacitance i.e., BSH system
Work 5: LIG@MnO$_2$ and LIG@PPy	Formation of LIG directly from graphene oxide; Hybrid structure of LIG@MnO$_2$ (battery electrode) and LIG@PPy (capacitive electrode)	Cell voltage – 1.9 V; C_{sp} – 2.4 mF cm^{-2}	Modification in the battery electrode can be done to enhance the capacitive response

8.2 Future perspectives

The main objective of the thesis is to fabricate a hybrid BSH device with sufficient charge storage capacity and its delivery at a faster extent. It was tried hard to achieve the final goal of the thesis with good electrochemical results. There is still huge scope in the modulation of battery type (cathode) electrodes to enhance the electrochemical storage properties of the hybrid system.

The following points are a few scopes in the direction of future possibilities of the work that can be extended as:

❖ Making a hybrid system of Li-ion battery and supercapacitor in order to develop a highly stable BSH system with extended storage properties.

❖ Modification of the system in bi-redox type of electrolytic system to enhance the electrochemical performance of the device.

❖ Development of a hybrid system of energy conversion devices like solar cell, nanogenerator etc. with energy storage system (supercapacitor, battery and BSH system) to make a self-sufficient power pack system for the sustainable power supply.

❖ Utilization of laser-irradiated graphene material for second-generation battery i.e.; sodium-ion, magnesium-ion battery etc.

Appendix A

List of Publications

1. **N Kamboj,** T Purkait, M Das, S Sarkar, K S Hazra, R S Dey*, Ultralong cycle life and outstanding capacitive performance of a 10.8 V metal free micro-supercapacitor with highly conducting and robust laser-irradiated graphene for an integrated storage device. ***Energy Environ. Sci.***, 2019**,**12**,** 2507-2517

2. **N Kamboj,** R S Dey*, Electrochemically grown highly crystalline single-phase Ni_3P superstructure accelerating ionic diffusion in rechargeable Ni-Zn battery. ***J. Power. Sources,*** 2021, 512, 230527

3. **N Kamboj,** R S Dey*, Graphene-polypyrrole based metal-free microsupercapacitor module achieved 20 V working voltage using "Organic/Water-in-salt" electrolyte. ***Electrochimica Acta**, 2022, 421, 140499*

4. **N Kamboj,**[†] B Debnath,[†] S Bhardwaj, S. Ogale, * K Roy, * R S Dey*, Ultrafine mix-phase $SnO-SnO_2$ nanoparticles anchored reduced graphene oxide boosting Li-ion storage capacity with improved cyclic stability. **(Revision submitted)**

5. **N Kamboj**, N Kumar, R S Dey*, Rational designing of highly conducting laser-irradiated graphene anchored MnO_2 nanoflakes/nanowalls as a cathode material for on-chip battery-supercapacitor hybrid system. **(Communicated)**

6. T Goswami,[†] **N Kamboj,**[†] A Bheemaraju, A Kataria, R S Dey*, Supercapacitive behavior of a novel nanocomposite of 3,4,9,10-perylenetetracarboxylic acid incorporated captopril-Ag nanocluster decorated on graphene nanosheets. ***Mater. Adv.***, 2021, 2, 1358-1368.

7. T Purkait, G Singh, **N Kamboj,** M Das, R S Dey*, All-porous heterostructure of reduced graphene oxide polypyrrole-nanoporous gold for planar flexible supercapacitor showing outstanding volumetric capacitance and energy density. ***J. Mater. Chem. A,*** 2018, 6, 22858 – 22869.

8. M Das, N Jena, T Purkait, **N Kamboj**, A De Sarkar, R S Dey*, Single-phase Ni_5P_4-Copper foam superhydrophilic and aerophobic core-shell nanostructures for efficient hydrogen evolution reaction. ***J. Mater. Chem. A,*** 2019, 7, 23989-23999.

9. M Das, **N Kamboj**, T Purkait, S Sarkar, R S Dey*, Revealing the Structural Aspect of Ultrastable Self-Supportive Bifunctional Electrocatalyst for Solar-Driven Water Splitting. ***J. Phys. Chem. C,*** 2020, 124, 13525−13534.

10. S Sarkar, **N Kamboj**, M Das, T Purkait, A Biswas, R S Dey*, Universal Approach for Electronically Tuned Transition-Metal-Doped Graphitic Carbon Nitride as a Conductive Electrode Material for Highly Efficient Oxygen Reduction Reaction. *Inorganic Chemistry*, 2020, 59, 1332-1339

11. S Sarkar, S S Sumukh, K Roy, **N Kamboj,** T Purkait, M Das, R S Dey*, Facile one step synthesis of Cu-g-C$_3$N$_4$ electrocatalyst realized oxygen reduction reaction with excellent methanol crossover impact and durability. *Journal of Colloid and Interface Science*, 2020, 558, 182–189

12. S Sarkar, A Biswas, T Purkait, M Das, **N Kamboj,** R S Dey*, Unravelling the Role of Fe–Mn Binary Active Sites Electrocatalyst for Efficient Oxygen Reduction Reaction and Rechargeable Zn-Air Batteries. *Inorganic Chemistry,* 2020, 59 (7), 5194-5205

13. T Purkait, Dimple, **N Kamboj**, M Das, S Sarkar, A De Sarkar, R S Dey* Electrochemically customized assembly of a hybrid xerogel material via combined covalent and non-covalent conjugation chemistry: an approach for boosting the cycling. *Journal of Materials Chemistry A,* 2020, 8 (14), 6740-6756

14. A Biswas, S Sarkar, M Das, **N Kamboj**, R S Dey*, A No-Sweat Strategy for Graphene-Macrocycle Co-assembled Electrocatalyst toward Oxygen Reduction and Ambient Ammonia Synthesis. *Inorganic Chemistry* 59 (22), 16385-16397

15. S Sarkar, A Biswas, **N Kamboj,** R S Dey*, Unveiling the potential of an Fe Bis(terpyridine) complex for precise development of an Fe-NC Electrocatalyst to promote the Oxygen Reduction Reaction. *Inorganic Chemistry*, 2020, 59, 18, 13453-13464.

16. A Biswas, S Nandi, **N Kamboj,** J Pan, A Bhowmik, R S Dey*, Alteration of electronic band structure via a metal-semiconductor interfacial effect enables high faradaic efficiency for electrochemical nitrogen fixation. *ACS Nano*, 2021, 15, 12, 20364-20376.

17. **Book publication:** Carbonaceous Materials and Future Energy: Clean and Renewable Energy Sources, by R S Dey, T Purkait, **N Kamboj**, M Das CRC Press, Taylor & Francis Group, 2019, DOI: 10.1201/9781351120784, ISBN:-978-0-8153-4788-0.

18. **Conference proceedings:** T Purkait, P Pandey, **N Kamboj,** R S Dey*, Co$_3$O$_4$ Nanocube- 3DrGO Hybrid structure: Efficient Non-Noble- Metal Electrocatalyst with High-performance for oxygen evolution reaction. *ECS Meeting Abstracts*, 2019, 2093.

19. **N Kamboj**, Athira K, R S Dey*, Laser-irradiated graphene-polymer contact electrification as a sustainable power source in metal-free triboelectric nanogenerator, *Materials today: proceeding,* 2022, 57, 239-244.

20. A Sharma, [†] V Panwar, [†] B Mondal, D Prasher, M K Bera, J Thomas, A Kumar, **N Kamboj**, D Mandal, * Deepa Ghosh, * Electrical Stimulation Mediated by Piezo-Driven Triboelectric Nanogenerator and Electroactive Hydrogel Encourage Wound Repair. *Nano Energy,* 2022, 99, 107419.

21. M Das, Z Khan, **N Kamboj**, M Banerjee, R S Dey, * Facile single-step electrochemical growth of Ni_3P on carbon cloth for highly efficient hydrogen evolution reaction. *(**Revision submitted in journal of Electrochemical Society**)*

Appendix B

Awards/Achievements/conferences/workshops

Awards and Recognitions:

1. The work entitled as "Ultralong cycle life and outstanding capacitive performance of a 10.8 V metal-free microsupercapacitor with highly conducting and robust laser-irradiated graphene for an integrated storage device" was **highlighted by DST** followed by the link: https://dst.gov.in/inst-mohali-develops-corrosion-free-high-voltage-integrated-energy-storage-device

2. Our article published in energy and environmental science was amongst **the top 5% (capped at top 100 papers)** across Royal Society of Chemistry journals in terms of citations in 2020.

3. **Awarded by travel grant** from CSIR to attend the MRS conference, 2019.

4. **Best Poster Award** in Joint CRICK Symposium organised at Indian Institute of Science Education and Research Mohali on 2nd- 3rd November 2019.

5. **Best Poster Award** in RSC sponsored chemical science virtual symposium organised by Indian Institute of Science Education and Research Kolkata on 7th -10th December 2020.

6. **Best Oral presentation award** at 1st annual meeting of Energy and Environmental unit organized at INST Mohali on 11th-12th September, 2021.

7. **Best Oral presentation award** at international conference on multidisciplinary aspects of materials in engineering 2021 organised at Panjab university on 8th-9th October, 2021.

Conferences/workshops:

India International Science Festival (IISF 2020), Government of India (online)	*2020*
CRICK Chemistry Symposium, IISER Mohali	*2019*
RSC sponsored chemical science virtual symposium, IISER Kolkata	*2020*
1st annual meeting of Energy and Environmental unit organized at INST Mohali (Oral presentation)	*2021*
International Conference on Multidisciplinary Aspects of Materials in Engineering (ICMAME-2021) Oral presentation.	*2021*
International conference on recent developments in chemistry (RDC-2021), NIT Durgapur	*2021*
International Symposium on materials of the Millennium Emerging Trends and Future Prospects, PDEU Gandhinagar (Oral presentation)	*2021*
Arduino program learning course from National Institute of Electronics & Information Technology	*2019*